

# Applications of Network Physiology in Neonatology

**Dries Hendrikx**

Supervisors:

Prof. dr. ir. S. Van Huffel

Prof. dr. G. Naulaers

Prof. dr. ir. A. Caicedo Dorado

Dissertation presented in partial  
fulfillment of the requirements for the  
degree of Doctor of Engineering  
Science (PhD): Electrical Engineering

December 2021



# Applications of Network Physiology in Neonatology

**Dries HENDRIKX**

Examination committee:

Prof. dr. ir. J. Berlamont, chair

Prof. dr. ir. S. Van Huffel, supervisor

Prof. dr. G. Naulaers, supervisor

Prof. dr. ir. A. Caicedo Dorado, supervisor

Prof. dr. ir. D. Schreurs

Prof. dr. K. Jansen

Prof. dr. ir. J. Suykens

Prof. dr. ir. L. Faes

(University of Palermo)

Prof. dr. G. Pichler

(Medical University of Graz)

Dissertation presented in partial fulfillment of the requirements for the degree of Doctor of Engineering Science (PhD): Electrical Engineering

December 2021

© 2021 KU Leuven – Faculty of Engineering Science  
Uitgegeven in eigen beheer, Dries Hendrikx, Kasteelpark Arenberg 10, B-3001 Leuven (Belgium)

Alle rechten voorbehouden. Niets uit deze uitgave mag worden vermenigvuldigd en/of openbaar gemaakt worden door middel van druk, fotokopie, microfilm, elektronisch of op welke andere wijze ook zonder voorafgaande schriftelijke toestemming van de uitgever.

All rights reserved. No part of the publication may be reproduced in any form by print, photoprint, microfilm, electronic or any other means without written permission from the publisher.

# Preface

‘Here is a broom, go and sweep the floors.’ ‘But I have a PhD ...’ ‘Oh sorry, give me the broom, I’ll show you how it’s done.’ Hoewel ik alles relativeer, besef ik dat ik vandaag trots mag zijn. Trots op het behalen van mijn doctoraat. De laatste vier jaar waren hobbelig, het gekende verhaal van de *ups* en *downs*. Maar uiteindelijk zijn we er toch geraakt, aan de finish, daar waar de bloemen worden uitgereikt. Dat zou niet gelukt zijn zonder de hulp en steun van vele mensen, bewust of onbewust. Ik spendeer dan ook graag de eerste pagina’s van dit boekje aan een dankwoord.

Eerst en vooral wil ik mijn promotor, prof. Sabine Van Huffel, bedanken. Sabine, jouw passie voor het verwerken en interpreteren van biomedische data is werkelijk aanstekelijk. Na jouw vak te hebben gevolgd, was ik snel overtuigd dat mijn interessegebied ook lag in biomedisch toepassingen. Na mijn master gaf jij mij de kans om een doctoraat te starten over een interessant en klinisch relevant onderwerp: jij geloofde in mij en in mijn capaciteiten vanaf dag één. Ik waardeer dat je me de volledige vrijheid gaf om mijn project zelf in te vullen, terwijl je onderweg waardevolle suggesties en advies gaf. Jij bent een *people manager* als geen ander: als kapitein van het schip zorgde je steeds voor een uitstekende sfeer in de groep, door de organisatie van pizza-avonden en kerstfeestjes, waarop je de hele groep bij jouw thuis verwelkomde, en nog vele andere activiteiten.

Ik wil ook mijn co-promotor, prof. dr. Gunnar Naulaers, bedanken. Gunnar, vanaf onze eerste ontmoeting, toen nog een verlegen master student die erg onder de indruk was van de ziekenhuisomgeving, was het meteen duidelijk dat jij niet alleen enorm intelligent, maar ook een heel warme persoon bent. Jij geloofde als geen ander in het potentieel van mijn onderzoek en dat gaf me veel motivatie om eraan te werken: dag in, dag uit. Bedankt voor jouw positieve ingesteldheid, jouw constructieve feedback op al mijn presentaties, jouw complimenten wanneer het goed ging, en alle aanmoedigingen op momenten dat de resultaten niet helemaal waren wat we ervan gedacht hadden. Dankjewel voor je vertrouwen en alle steun tijdens de afgelopen jaren: het was een voorrecht om zo intensief

met jou samen te mogen werken.

Third, I would like to express my gratitude towards prof. Alexander Caicedo. Alex, I don't exaggerate when I write that you were one of my greatest inspirations over the last five years. You never seem to run out of ideas of things we could try and implement. You were one of the reasons I decided to start my PhD, since I really enjoyed our teamwork. Not just on the workfloor, but also in free time: from dancing *the V* in the pubs of Oude Markt to spicing up your ginto with an entire jar of nutmeg: it was an absolute pleasure to experience all of those moments together with you.

Next, I would like to thank the members of my jury for their feedback during the last four years. Prof. Katrien Jansen, bedankt voor je gerichte feedback en je enthousiasme: jij toonde altijd veel interesse in mijn werk, en gaf vele waardevolle suggesties. Prof. Dominique Schreurs, bedankt voor je heldere blik op mijn werk en mijn thesis. Prof. Johan Suykens, jouw feedback heeft mijn werk aanzienlijk verbeterd. In addition, I would like to thank prof. Gerhard Pichler and prof. Luca Faes for completing my examination committee. Thank you for taking the time to read my thesis, and to provide me with feedback. Tot slot wil ik ook de voorzitter, prof. Jean Berlamont, bedanken om mijn doctoraatsverdediging in goede banden te leiden.

This PhD is the product of an intense collaboration with the University Hospitals Leuven. Gunnar, Katrien, Anneleen, Liesbeth, Anne, Kate, and Jan†: thank you for the numerous interesting discussions we had during our biweekly meetings and thank you for helping me with the interpretation of my results. I learned many things, from each and every one of you.

Special thanks goes out to all (ex-)colleagues of the BIOMED group. I truly believe that this is one of the nicest groups at KU Leuven. Abhi, we shared a passion for football; our trip to Genk–Liverpool was a true highlight. Amalia, my office mate, thank you for your positive vibes, and for making our office feel like home by taking care of the many plants. Carolina, you are such a lovely person: I enjoyed every single conversation we had. Dorien en Griet, de voortrekkers van de sfeer en gezelligheid. Jasper, samen met de nodige ironie de actualiteit van het dagelijks bestaan analyseren: beter wordt het niet! John, my other office mate, your work ethic is truly remarkable: thank you for being so kind and welcoming. Jonathan M, de man met de eeuwige glimlach, tenzij de computer niet meewerkt (*gij zijt zelf nen error!*). Mario, thanks for showing me what a fake Italian looks like. Nico, de man in het blauwe shirt, altijd op de loer om te dribbelen, en altijd paraat voor eerste hulp bij problemen. Ofelie, *moa ven toh*, hartelijk, gezellig, joviaal, oprecht, sympathiek, warm: jij bent een topper. Rob, *Du hast die Haare schön* (echt hé), merci voor de sfeer en gezelligheid, op en naast de dansvloer. Simon G, de man van duizend en één wijsheden: van

jou heb ik veel geleerd, over het werk en over het leven. Simon VE, de andere man in het blauwe shirt, heel gezellig, maar let op voor dat afstandschot! Stijn D, samen de zaken eens goed relativeren, schoner wordt het niet. Stijn H, het Genk gevoel in Leuven, merci voor de ritjes van en naar het werk. Tim, het vat vol moppen geraakt maar niet leeg, het vat pils in café Sport spijtig genoeg wel. In addition, I would like to thank Adrian, Alexander, Amir, Angeliki, Barath, Bavo, Bori, Cem, Charles, Christos, Elisabeth, Iustina, Jingwei, Jonathan D, Joran, Kaat, Kenneth, Konstantinos, Laura, Lieven, Maarten, Margot, Martijn, Matthias, Miguel, Neetha, Nick, Nicolas, Omer, Pooya, Servaas, Thomas DC, Thomas S, and Zhenxiang for the nice moments we shared during the past years.

Thank you to Fonds voor Wetenschappelijk Onderzoek (FWO) Vlaanderen, which provided me with funding in the form of a Strategic Basic Research grant. I am also very grateful to Ida, Elsy, John, Wim and Maarten to guide me through the administrative tasks and for the support with IT.

Daarnaast wil ik mijn familie en vrienden bedanken voor alle steun en de leuke momenten die we gedeeld hebben de afgelopen jaren. Onze hechte familieband is er een om te koesteren. Jullie interesse in mijn doctoraat werkte altijd motiverend. Mijn vrienden zijn misschien wel de beste vrienden ter wereld, maar dat beweert wellicht iedereen over zijn eigen vriendengroep. Jullie visie op mijn doctoraat – dik betaald worden om wat prentjes te maken – hielp me om alles te relativeren, zeker op momenten dat goede resultaten even uitbleven.

Ik wil ook mijn gezin bedanken voor de onvoorwaardelijke steun. Bedankt Niels, Stan en Joorn voor de interesse in alles wat mij bezighoudt in het leven. Bedankt mama en papa: jullie hebben mij doorheen mijn hele leven gesteund, jullie willen altijd het allerbeste voor mij en staan altijd voor iedereen klaar. Niets is te veel gevraagd, en dat weet iedereen die jullie kent.

Tot slot wil ik Julia, mijn vriendin en tegelijk ook mijn grootste supporter bedanken. Juul, dank je dat je er altijd voor mij was, niet alleen gedurende dit doctoraat, maar ook al lang daarvoor. Jouw steun was er altijd: in goede en slechte dagen. Zonder jou was dit doctoraat simpelweg niet mogelijk geweest. Ik kijk er naar uit om ons nieuwe huis een echte thuis te maken, en samen verder te bouwen aan een lange toekomst samen.

Bedankt iedereen, voor alles.  
Thanks everyone, for everything.

Dries  
24 november 2021



# Abstract

Every year, an estimated 15 million babies are born preterm, that is, before 37 weeks of gestation. This number is rising in all countries and currently represents more than 1 in 10 babies, affecting families all over the world. During the last decades, the survival rate of prematurely born neonates has steadily increased, mainly as a result of medical and technical progress in neonatal intensive care. The very preterm infants, which represent up to 10% of the preterm infants in the EU, remain at risk for adverse outcome and neurodevelopmental disability. These maladaptive outcomes have a severe effect on the children's quality of life and a huge economic impact on society. In order to reduce this burden and improve neonatal care in general, appropriate tools need to be developed to identify the neonates with a higher risk of adverse outcomes.

Brain damage in neonates is complex, since brain abnormality is caused by a complex combination of destructive and developmental mechanisms rather than a mere summation of different brain lesions. In addition, brain abnormality has to be studied over time, since some infants normalize over time while others remain abnormal. In general, brain damage often results from maladaptive perfusion of the brain, since both hypo- and hyperperfusion can cause significant neurologic injury. In a properly functioning brain, there are various regulation mechanisms in place to keep cerebral blood flow (CBF) within the accepted range to support brain function. Modeling the status of these CBF regulation mechanisms and the maturation thereof will allow clinicians to identify neonates at risk for brain injury in an early stage, allowing therapeutic intervention.

In clinical practice, the neonatal brain can be monitored using a combination of two signal modalities: electroencephalography (EEG) to measure brain activity and near-infrared spectroscopy (NIRS) to measure cerebral tissue oxygenation. Both modalities can be measured continuously at the bedside in a non-invasive way. The diagnostic value of both modalities has been studied heavily over the last years. The automated integration of both modalities, together with numerous systemic variables allows to create a coordinated overview of the major

components of CBF regulation. In this thesis, we developed a computational model for this automated analysis, and validated this model in various clinical settings.

The first part of this thesis focuses on a univariate analysis. Such an analysis largely corresponds to how medical doctors currently use signals in clinical practice. Two anesthetic approaches were compared during non-cardiac-major surgery: a sedative-agent based versus an anesthetic-based strategy. The anesthetic-based strategy resulted in adequate anesthesia, as indicated by the decrease in heart rate variability, and the shift in sympathovagal balance, in combination with increased cerebral oxygenation and decreased brain activity. The sedative-based strategy, on the other hand, resulted in alarmingly low cerebral tissue oxygenation and increased EEG power, which might indicate the conscious experience of pain.

In the second part, we study a new methodology to integrate EEG and NIRS measurements. From a physiological point of view, both measurements are tightly coupled, since increases in brain activity trigger consequent changes in CBF. We quantified the coupling between both signals and observed that neonates with a small injury had lower coupling values, suggesting a less functional regulation of CBF. Brain abnormalities thus alter CBF regulation and this change in regulation can be captured using signal processing techniques.

The third and final part extends the bivariate analysis to a multivariate analysis. Instead of focusing on one component of CBF regulation, we integrated various regulation mechanisms in one straightforward, visual model, which we call the *neurocardiovascular graph*. This model was studied in three different clinical settings. In a first study, we analyzed the model during immediate transition after birth, and observed that heart rate and arterial saturation significantly coupled with cerebral tissue oxygenation, and that this coupling changes with age. Our second study indicated that the model reflects the dynamics of propofol, a frequently used anesthetic. Propofol administration destroyed all interaction, which consequently restored to baseline. In the third and final study, the neonate's clinical condition and the surgical and anesthesiological approach were observed to affect neonatal physiology and CBF regulation mechanisms at different levels.

In summary, the neurocardiovascular graph provides a new way to look at the effect of drugs, surgery and perioperative management on the neonate. This new direction of monitoring could assist clinicians in making patient-specific decisions, aiming to prevent brain injury and impaired neurodevelopmental outcome.

# Beknopte samenvatting

Elk jaar worden naar schatting 15 miljoen baby's te vroeg geboren, voor 37 weken zwangerschap. Dit aantal stijgt wereldwijd en vertegenwoordigt momenteel meer dan 1 op de 10 baby's. In de laatste decennia is de overlevingskans van premature baby's gestaag toegenomen, voornamelijk als gevolg van de medische en technische vooruitgang in de neonatale intensieve zorg. De extreem premature vroeggeborenen, die tot 10% van de totale populatie aan premature baby's in de EU vertegenwoordigen, blijven risico lopen op een nadelige uitkomst en neurologische ontwikkelingsstoornissen. Dit heeft ernstige gevolgen op de levenskwaliteit van het kind en een grote economische impact op de samenleving. Geschikte instrumenten moeten ontwikkeld worden om baby's met een hoger risico op een nadelige uitkomst te identificeren, om zo neonatale zorg verder te verbeteren.

Hersenbeschadiging bij pasgeborenen wordt veroorzaakt door een complexe combinatie van destructieve en ontwikkelingsmechanismen. Bovendien moet hersenbeschadiging in de tijd worden bestudeerd, aangezien sommige baby's na verloop van tijd normaliseren, terwijl andere abnormaal blijven. Over het algemeen is hersenbeschadiging vaak het gevolg van een onaangepaste perfusie van de hersenen, aangezien zowel hypo- als hyperperfusie een aanzienlijk neurologisch letsel kunnen veroorzaken. In een goed functionerend brein zijn er verschillende regelmechanismen aanwezig om de cerebrale bloedstroom binnen het fysiologisch bereik te houden, zodat de hersenfunctie ten allen tijde ondersteund kan worden. Door deze regulatiemechanismen en de maturatie ervan te modelleren kunnen klinici in een vroeg stadium pasgeborenen met een risico op hersenletsel identificeren, waardoor therapeutische interventie mogelijk wordt.

De hersenen van neonaten kunnen gemonitord worden met behulp van een combinatie van twee signaalmodaliteiten: elektro-encefalografie (EEG) om de hersenactiviteit te meten en nabij-infrarood spectroscopie (NIRS) om de zuurstofsaturatie van het hersenweefsel te meten. Beide modaliteiten kunnen

op een continue, niet-invasieve manier gemeten worden tijdens het verblijf in de couveuse. De geautomatiseerde integratie van beide modaliteiten, samen met tal van systeemvariabelen, maakt het mogelijk om een gecoördineerd overzicht te creëren van de belangrijkste componenten van de cerebrale bloedstroom regulatie. In dit proefschrift werd een model ontwikkeld voor deze geautomatiseerde analyse en vervolgens gevalideerd in verscheidene klinische contexten.

Het eerste deel van dit proefschrift richt zich op een univariate analyse. Een dergelijke analyse komt in grote lijnen overeen met hoe artsen momenteel signalen gebruiken in de praktijk. Twee anesthesische benaderingen werden vergeleken: een strategie met focus op pijnstillers en een strategie met focus op verdooving. De strategie gebaseerd op verdooving resulteerde in adequate anesthesie met een afname in hartslagvariabiliteit en een verschuiving van het sympathovagale evenwicht, in combinatie met een verhoogde cerebrale oxygenatie en verminderde hersenactiviteit. De strategie gebaseerd op verdooving daarentegen resulteerde in een alarmerend lage cerebrale zuurstofsaturatie en een verhoogd EEG vermogen, wat zou kunnen wijzen op de bewuste ervaring van pijn.

In het tweede deel bestuderen we een nieuwe methodologie om EEG en NIRS metingen te integreren. Vanuit een fysiologisch oogpunt staan beide metingen nauw met elkaar in contact, aangezien een toename in hersenactiviteit een toename in cerebrale bloedstroom veroorzaakt. In dit proefschrift hebben we de koppeling tussen beide signalen berekend. Hierbij viel op dat neonaten met een klein hersenletsel lagere koppelingswaarden hebben, wat een minder sterke functieregulatie van de cerebral bloedstroom suggereert. Hersenafwijkingen veranderen dus de regulatie van cerebrale bloedstroom en deze verandering in regulatie kan worden vastgelegd met behulp van signaalverwerkingstechnieken.

Het derde en laatste deel breidt de bivariate analyse uit tot een multivariate analyse. In plaats van ons te concentreren op één component van cerebrale bloedstroom regulatie, hebben we verschillende regulatiemechanismen geïntegreerd in een visueel model dat we de *neurocardiovasculaire graaf* noemen. Dit model werd bestudeerd in drie verschillende klinische contexten. In een eerste studie analyseerden we het model net na de geboorte. We stelden vast dat hartslag en arteriële zuurstofsaturatie gekoppeld waren met cerebrale weefseloxygenatie, en dat deze koppeling verandert met de leeftijd. Onze tweede studie gaf aan dat het model de dynamiek van propofol, een veelgebruikt anestheticum, weerspiegelt. Toediening van propofol vernietigde alle interactie, die bijgevolg terugkeerde naar de basislijn. De derde en laatste studie leerde dat de klinische toestand van de pasgeborene en de chirurgische en anesthesiologische benadering de neonatale fysiologie en cerebrale bloedstroom regulatiemechanismen op verschillende niveaus beïnvloeden.

Samenvattend biedt de neurocardiovasculaire grafiek een nieuwe kijk op het

effect van medicijnen, chirurgie en perioperatieve behandeling van de neonaat. Deze nieuwe manier van monitoring kan klinici helpen bij het nemen van patiëntspecifieke beslissingen, gericht op het voorkomen van hersenletsels en het verminderden neurologische ontwikkelingsstoornissen.



# List of Abbreviations

<b>aEEG</b>	amplitude integrated EEG
<b>AIC</b>	Akaike information criterion
<b>ANS</b>	autonomic nervous system
<b>ApEn</b>	approximate entropy
<b>BRS</b>	baroreflex sensitivity
<b>BW</b>	birth weight
<b>CAR</b>	cerebral pressure autoregulation
<b>CBF</b>	cerebral blood flow
<b>CFM</b>	cerebral function monitor
<b>CNS</b>	central nervous system
<b>CO</b>	cardiac output
<b>CPR</b>	cardiopulmonary resuscitation
<b>CRIB</b>	clinical risk index for babies
<b>cUS</b>	cranial ultrasound
<b>CVR</b>	cerebrovascular resistance
<b>CWS</b>	continuous wave spectroscopy
<b>CWT</b>	continuous wavelet transform
<b>CytOx</b>	cytochrome c oxidase
<b>DFT</b>	discrete Fourier transform
<b>DPF</b>	differential path length factor
<b>DWT</b>	discrete wavelet transform
<b>EA</b>	esophageal atresia

---

<b>ECG</b>	electrocardiogram
<b>ECMO</b>	extracorporeal membrane oxygenation
<b>EEG</b>	electroencephalography
<b>EU</b>	European Union
<b>fmRI</b>	functional magnetic resonance imaging
<b>FTOE</b>	fractional tissue oxygen extraction
<b>GA</b>	gestational age
<b>GLS</b>	generalized least squares
<b>HbO<sub>2</sub></b>	oxyhemoglobin
<b>HF</b>	high frequency band, in HRV analysis
<b>HHb</b>	deoxyhemoglobin
<b>HIE</b>	hypoxic-ischemic encephalopathy
<b>HR</b>	heart rate
<b>HRP</b>	heart rate passivity
<b>HRV</b>	heart rate variability
<b>IAAFT</b>	iterative amplitude adjusted Fourier transform
<b>IBI</b>	interburst interval
<b>ICP</b>	intracranial pressure
<b>ICU</b>	intensive care unit
<b>INSURE</b>	intubation, surfactant, extubation
<b>IQR</b>	interquartile range
<b>IRDS</b>	infant respiratory distress syndrome
<b>IV</b>	intravenous
<b>IVH</b>	intraventricular hemorrhage
<b>KDE</b>	kernel density estimation
<b>LF</b>	low frequency band, in HRV analysis
<b>LME</b>	linear mixed effects model
<b>MABP</b>	mean arterial blood pressure
<b>MI</b>	mutual information
<b>MRI</b>	magnetic resonance imaging

<b>NE</b>	neonatal encephalopathy
<b>NICU</b>	neonatal intensive care unit
<b>NIRS</b>	near-infrared spectroscopy
<b>NREM</b>	non-rapid eye movement
<b>NVC</b>	neurovascular coupling
<b>OLS</b>	ordinary least squares
<b>OR</b>	operating room
<b><math>P_a\text{CO}_2</math></b>	atrial pressure of carbox dioxide
<b>PDA</b>	patent ductus arteriosus
<b>PDF</b>	probability density function
<b>PET</b>	positron emission tomography
<b>PICU</b>	pediatric intensive care unit
<b>PMA</b>	postmenstrual age
<b>PNA</b>	postnatal age
<b>PNS</b>	peripheral nervous system
<b>PPHN</b>	persistent pulmonary hypertension
<b>PSD</b>	power spectral density
<b>PVL</b>	periventricular leukomalacia
<b>REM</b>	rapid eye movement
<b>rScO<sub>2</sub></b>	regional cerebral oxygen saturation (%)
<b>SampEn</b>	sample entropy
<b>SDNN</b>	standard deviation of the NN intervals
<b>SNS</b>	sympathetic nervous system
<b>SpO<sub>2</sub></b>	arterial oxygen saturation
<b>SRS</b>	spatially resolved spectroscopy
<b>TA</b>	tracé alternant
<b>TCD</b>	transcranial Doppler ultrasound
<b>TE</b>	transfer entropy
<b>TOI</b>	tissue oxygenation index
<b>TRS</b>	time resolved spectroscopy

<b>VIF</b>	variance inflatable factor
<b>VIS</b>	vasoactive inotropic scores
<b>VLf</b>	very low frequency band, in HRV analysis

# List of Symbols

$\alpha$	EEG frequency band: 8–12 Hz
$\alpha$	statistical significance
$\bar{x}$	mean of $x$
$\beta$	EEG frequency band: 12–30 Hz
$\delta$	EEG frequency band: 0.5–4 Hz
$\delta(G)$	average degree of graph $G$
$\mathbf{x}_k^-$	embedding vector
$\mathcal{N}$	normal distribution
$\psi$	mother wavelet
$\sigma$	RBF kernel bandwidth
$\theta$	EEG frequency band: 4–8 Hz
$A$	adjacency matrix
$d_i$	vertex degree
$E$	finite set of distinct unordered pairs of $V$
$G$	weighted graph
$H(X)$	Shannon entropy
$H_0$	null hypothesis
$H_1$	alternative hypothesis

---

$I(X;Y)$	mutual information
$k_{xy}$	RBF kernel function
$P_i$	$i$ -th percentile ( $0 < i \leq 100$ )
$r$	tolerance in ApEn and SampEn
$R^2$	coefficient of determination
$r_{xy}$	sample correlation coefficient
$s(x_i)$	Silhouette score
$S_i$	cluster $i$
$s_x^2$	variance of $x$
$S_{xx}(f)$	power spectral density
$T_{X \rightarrow Y}^n$	normalized transfer entropy
$T_{X \rightarrow Y}$	transfer entropy from $X$ to $Y$
$V$	nonempty finite set of vertices
$v_i$	vertex
$w_{ij}$	edge weight

# Contents

<b>Abstract</b>	<b>v</b>
<b>Beknopte samenvatting</b>	<b>vii</b>
<b>List of Abbreviations</b>	<b>xiv</b>
<b>List of Symbols</b>	<b>xvi</b>
<b>Contents</b>	<b>xvii</b>
<b>List of Figures</b>	<b>xxiii</b>
<b>List of Tables</b>	<b>xxxi</b>
<b>Part I: Introduction</b>	<b>1</b>
<b>1 Introduction</b>	<b>6</b>
1.1 Problem statement . . . . .	7
1.2 Outline of the thesis . . . . .	10
1.2.1 Part I: Introduction . . . . .	11
1.2.2 Part II: Univariate analysis . . . . .	12

1.2.3	Part III: Bivariate analysis . . . . .	12
1.2.4	Part IV: Multivariate analysis . . . . .	13
1.2.5	Part V: Conclusion . . . . .	13
1.3	Collaborations . . . . .	13
1.4	Conclusion . . . . .	15
<b>2</b>	<b>Physiology and monitoring of the neonatal brain</b>	<b>18</b>
2.1	The neonatal brain . . . . .	19
2.1.1	Nervous system . . . . .	19
2.1.2	Building blocks of the brain . . . . .	20
2.1.3	Brain development . . . . .	22
2.2	Brain monitoring . . . . .	23
2.2.1	Overview of neonatal brain monitoring . . . . .	23
2.2.2	Near-infrared spectroscopy . . . . .	24
2.2.3	EEG . . . . .	31
2.2.4	Matching NIRS and EEG . . . . .	34
2.3	Regulation of cerebral blood flow . . . . .	38
2.3.1	Cerebral autoregulation . . . . .	41
2.3.2	Neurovascular coupling . . . . .	43
2.3.3	Other aspects of regulation . . . . .	47
2.3.4	Integrating CBF regulation using graphs . . . . .	48
2.4	Brain pathology . . . . .	49
2.4.1	Hypoxia . . . . .	49
2.4.2	Intraventricular hemorrhage . . . . .	52
2.4.3	Periventricular leukomalacia . . . . .	53
2.5	Conclusion . . . . .	55

<b>3</b>	<b>Signal processing pipeline</b>	<b>58</b>
3.1	Data processing pipeline . . . . .	59
3.2	Artifact removal . . . . .	59
3.3	Univariate analysis . . . . .	61
3.3.1	Descriptive statistics . . . . .	62
3.3.2	Power spectral density . . . . .	62
3.3.3	Approximate and sample entropy . . . . .	64
3.4	Bivariate analysis . . . . .	66
3.4.1	Linear correlation . . . . .	67
3.4.2	Regression correlation . . . . .	68
3.4.3	RBF kernel function . . . . .	69
3.4.4	Transfer entropy . . . . .	71
3.4.5	Surrogate analysis . . . . .	78
3.5	Multivariate analysis . . . . .	80
3.5.1	Signal interaction graph . . . . .	80
3.5.2	Clustering . . . . .	81
3.6	Statistics . . . . .	85
3.6.1	Statistical hypothesis tests . . . . .	85
3.6.2	Regression . . . . .	92
3.7	Conclusion . . . . .	97
<b>4</b>	<b>Datasets</b>	<b>100</b>
4.1	Propofol dataset . . . . .	101
4.2	Congenital diaphragmatic hernia dataset . . . . .	103
4.3	Esophageal atresia dataset . . . . .	106
4.4	Neonatal dataset . . . . .	108
4.5	Conclusion . . . . .	110

<b>Part II: Univariate analysis</b>	<b>113</b>
<b>5 Heart rate variability during non-cardiac-major surgery</b>	<b>116</b>
5.1 Introduction . . . . .	117
5.2 Dataset . . . . .	118
5.3 Methods . . . . .	119
5.4 Results . . . . .	121
5.5 Discussion . . . . .	124
5.6 Conclusion . . . . .	129
<b>6 Cerebral oxygenation and activity during surgical repair of neonates with congenital diaphragmatic hernia</b>	<b>132</b>
6.1 Introduction . . . . .	133
6.2 Dataset . . . . .	134
6.3 Methods . . . . .	134
6.4 Results . . . . .	136
6.5 Discussion . . . . .	143
6.6 Conclusion . . . . .	147
<b>Part III: Bivariate analysis</b>	<b>149</b>
<b>7 Transfer entropy as a measure for neurovascular coupling</b>	<b>152</b>
7.1 Introduction . . . . .	153
7.2 Dataset . . . . .	154
7.3 Methods . . . . .	154
7.4 Results . . . . .	155
7.5 Discussion . . . . .	156
7.6 Conclusion . . . . .	158

<b>Part IV: Multivariate analysis</b>	<b>161</b>
<b>8 Coupling between regional oxygen saturation of the brain and vital signs during immediate transition after birth</b>	<b>164</b>
8.1 Introduction . . . . .	165
8.2 Dataset . . . . .	166
8.3 Methods . . . . .	166
8.4 Results . . . . .	167
8.5 Discussion . . . . .	170
8.6 Conclusion . . . . .	176
<b>9 The neurocardiovascular graph reflects propofol dynamics</b>	<b>180</b>
9.1 Introduction . . . . .	181
9.2 Dataset . . . . .	183
9.3 Methods . . . . .	184
9.4 Results . . . . .	189
9.5 Discussion . . . . .	190
9.6 Conclusions . . . . .	196
<b>10 Neurocardiovascular coupling; revealing insight in perioperative physiology</b>	<b>200</b>
10.1 Introduction . . . . .	201
10.2 Dataset . . . . .	202
10.3 Methods . . . . .	202
10.4 Results . . . . .	206
10.5 Discussion . . . . .	213
10.6 Conclusions . . . . .	218

<b>Part V: Conclusion</b>	<b>221</b>
<b>11 Conclusion and future directions</b>	<b>224</b>
11.1 Conclusions . . . . .	225
11.1.1 Marker for neurovascular coupling . . . . .	225
11.1.2 Model for (neuro)cardiovascular interactions . . . . .	225
11.1.3 Other findings . . . . .	226
11.2 Future directions . . . . .	227
11.2.1 Artifact removal . . . . .	227
11.2.2 Multiscale analysis . . . . .	228
11.2.3 Detection and removal of spurious connections . . . . .	231
11.2.4 Validation . . . . .	232
11.2.5 Functional growth charts of neural development . . . . .	232
11.2.6 Clinical support system . . . . .	233
<b>Bibliography</b>	<b>235</b>
<b>Curriculum vitae</b>	<b>283</b>
<b>List of publications</b>	<b>285</b>

# List of Figures

1.1	Preterm birth is defined as a delivery before 37 completed weeks of gestation. Different age terminology is used in neonatal care: the gestational age, postnatal age, postmenstrual age, and corrected age. . . . .	8
1.2	This thesis is split up in five main parts: the introduction is followed by the univariate, bivariate, and multivariate analysis. At the end, the conclusive part describes the main conclusions and the future research directions. . . . .	11
2.1	The nervous system of vertebrates consists of two parts: the central nervous system and the peripheral nervous system. . . .	20
2.2	A neuron is made up of four key parts: the cell body, the dendrites, the axon, and the axon terminals. . . . .	21
2.3	During the last trimester of pregnancy, the brain significantly increases in volume, roughly triples in weight, undergoes cortical folding and improves (functional) connectivity. Due to the cortical folding, the surface area of the brain increases 30-fold in the last 16 weeks of pregnancy. . . . .	23
2.4	Absorption spectra for the three main chromophores that cause absorption in NIRS monitoring: cytochrome c oxidase (CytOx), oxyhemoglobin (HbO <sub>2</sub> ) and deoxyhemoglobin (HHb). . . . .	25
2.5	The Beer-Lambert law states that the attenuation of light in a nonscattering medium is proportional to the length of the path traveled in the medium and the concentration of the absorbing species. The modified Beer-Lambert law corrects for scattering.	27

2.6	Propagation of near-infrared light in the brain: due to scattering, the light follows a path inside the brain that resembles a banana shape. . . . .	28
2.7	In SRS, photons are measured at multiple spacings from the source, improving the precision. In addition, the SRS system design enhances contribution of deeper tissues, while reducing the contribution of more superficial tissue like skin and adipose tissue to the NIRS signals. . . . .	30
2.8	EEG provides a noninvasive measurement of the electrical activity of the cerebral cortex via electrodes attached to the scalp. . . .	32
2.9	The international 10-20 montage of EEG guarantees uniform and consistent monitoring of different brain regions. . . . .	33
2.10	Biomedical time series are associated with different time scales of operation. . . . .	36
2.11	The EEG of premature neonates alternates between periods of high activity (bursts, or burst intervals, in gray) and periods of suppressed activity (interburst intervals), making its morphology discontinuous. . . . .	37
2.12	EEG preprocessing based on a time-frequency representation (CWT) can be used to obtain a time-average estimate of the PSD or an estimate of the power in time. . . . .	39
2.13	Cerebral blood flow is tightly regulated. Overperfusion (too much flowing through vascular bed) might lead to hemorrhage, while underperfusion (too little blood flowing to brain) might lead to ischemic damage. . . . .	41
2.14	Schematic drawing of the relation between cerebral blood flow and mean arterial blood pressure in the preterm newborn during normal cerebral circulation. . . . .	42
2.15	At the microscopic level, neurovascular coupling consists of neurons, astrocytes and pericytes that secrete various chemical signals causing vasodilation and vasoconstriction of arterioles and capillaries, which directly affects cerebral blood flow. . . .	44
2.16	Different types of NVC response: functional hyperemia, oxygen consumption only in absence of functional hyperemia, and vasoconstriction or decrease in capillary bed volume. . . . .	45

2.17	A multimodal dataset can be translated in various types of signal interaction graphs, including a simple graph (a link is present or not), a weighted graph (each link carries a certain weight) and a directed graph (each link carries a weight and has a direction).	50
2.18	The neurocardiovascular graph allows to study various aspects of CBF regulation at the same time in one model. These regulation mechanisms include CAR, NVC, HRP, and BR. . . . .	51
2.19	Three classes of hypoxia are reported in literature: hypoxic hypoxia, anemic hypoxia, and ischemic hypoxia. . . . .	52
2.20	PVL is a brain injury characterized by damage to the white matter around the fluid-filled areas of the brain (ventricles). IVH is a brain injury that includes a bleeding into the ventricles of the brain. The severity of the bleeding is graded from I to III, with or without periventricular infarction. . . . .	54
3.1	Schematic overview of the data processing pipeline used to compute the coupling between biomedical time series. . . . .	60
3.2	Sample entropy is based on the conditional probability that two sequences of length $m$ matching at a tolerance $r$ will still be matching for a length $m + 1$ . . . . .	66
3.3	Schematic overview of coupling measures, which fall apart in two categories: functional (no directionality) and effective (directionality) measures. Both categories contain linear and nonlinear techniques. . . . .	67
3.4	Illustration of linear and nonlinear $k$ -nearest neighbors regression on a toy example. . . . .	70
3.5	The kernel bandwidth $\sigma$ has a profound influence on the coupling values obtained from the RBF kernel function. . . . .	71
3.6	Shannon entropy: building block of information theory, illustrated on one thousand samples from different distributions. . . . .	72
3.7	Effect of the number of quantization levels $Q$ and the embedding dimension $d$ on the resulting TE values (left) and computational time (right). . . . .	74

3.8	Robust estimation of Shannon entropy strongly depends on a proper choice of bin width. When the bin size is too low or too high, we obtain an underestimation and an overestimation of Shannon entropy, respectively. . . . .	76
3.9	Various techniques to estimate the probability density function from data: binning, KDE using a tophat and Gaussian kernel, and nearest-neighbors statistics. . . . .	77
3.10	Different methods to generate surrogates: random noise sources, time-shuffled surrogates, time-shifted surrogates and surrogates generated using the IAAFT. . . . .	79
3.11	Hierarchical clustering using different numbers of clusters, illustrated on toy data of 100 samples generated from isotropic Gaussian blobs with three centers . . . . .	84
3.12	Schematic overview of the statistical hypothesis tests used throughout this thesis. . . . .	87
3.13	Graphical illustration of the permutation test. . . . .	91
3.14	The OLS regression model is based on four assumptions: linearity in the coefficients, normality of the error terms, homoscedasticity, and independence of the error terms. . . . .	93
3.15	Visual representation of the coefficient of determination, which can be defined using the total sum of squares, the explained sum of squares, and the residual sum of squares. . . . .	94
4.1	A six hour long segment of multimodal data for one patient (PMA: 27 weeks, PNA: 2 days) in the propofol dataset (raw data, as received). . . . .	104
4.2	A seven hour long segment of multimodal data for one patient (GA: 38 weeks, PNA: 2 days, BW: 3500 grams, liver up, Boston C, open surgery at OR, measured in Rotterdam) in the CDH dataset (processed). . . . .	107
4.3	A 15 min long segment of multimodal data for four patients (GA: 37+2, 39, 34+1, 38+5 weeks from left to right, respectively) in the neonatal dataset (raw data, as received) . . . . .	110

5.1	Data processing pipeline used to translate ECG to tachogram to various time-domain, frequency-domain and nonlinear HRV metrics. . . . .	120
5.2	HRV metrics in a cohort with baseline data (seven neonates) changed significantly when transitioning from awake to sevoflurane-based anesthesia. . . . .	123
5.3	GA age significantly alters absolute power in the VLF and LF band, as well as the LF/HF ratio. . . . .	125
5.4	End expired sevoflurane concentration (%) significantly alters the mean RR interval, the sample entropy, and the absolute power in the HF band. . . . .	126
5.5	VIS significantly alters the mean RR interval, the sample entropy, and the absolute power in the VLF band. . . . .	127
6.1	Overview of the medication administered to the neonates before, during and after surgery. . . . .	138
6.2	Longitudinal overview of the perioperative changes in HR, MABP, SpO <sub>2</sub> , rScO <sub>2</sub> , FTOE, time in hypoxia, EEG slow delta ( $\delta_1$ ), EEG fast delta ( $\delta_2$ ), and EEG gamma ( $\gamma$ ). . . . .	139
6.3	Cerebral activity during surgery: $\delta_1$ , $\delta_2$ and $\gamma$ power in time. . . . .	142
6.4	A higher maximum dose of midazolam was associated with a significant decrease in rScO <sub>2</sub> and EEG $\delta_1$ power during surgery. The same trends were observed for the maximum end expired sevoflurane concentration, although these trends were not significant. . . . .	143
6.5	Intraoperatively, rScO <sub>2</sub> significantly correlated with cerebral activity in the midazolam group ( $R^2 = 0.41$ , $p = 0.01$ ). . . . .	144
6.6	In the sevoflurane group, rScO <sub>2</sub> negatively correlated with VIS ( $R^2 = 0.23$ , $p = .004$ ) and FTOE positively correlated with VIS ( $R^2 = 0.21$ , $p = .04$ ) during surgery. The same correlations were found after surgery for rScO <sub>2</sub> ( $R^2 = 0.35$ , $p = .001$ ) and FTOE ( $R^2 = 0.32$ , $p = .001$ ). . . . .	145

7.1	Two features were computed from the TE curves to quantify the effect of propofol: the minimal value $M$ and the maximal deviation $\Delta$ from baseline, which was defined as the median value of the last 3 hours of the analysis window. . . . .	156
7.2	TE curves after administration of propofol at $t = 0$ ; $T_{\text{rScO}_2 \rightarrow \text{EEG}}$ and $T_{\text{EEG} \rightarrow \text{rScO}_2}$ . . . . .	157
7.3	Comparison of feature and baseline values between the normal and abnormal neonates. . . . .	157
8.1	The signal processing pipeline used to study neonates during immediate transitional after birth. . . . .	168
8.2	Linear and nonlinear correlation curves for both clusters. The main differentiation between both clusters can be observed in the $\text{SpO}_2\text{-rScO}_2$ and the $\text{SpO}_2\text{-FTOE}$ curves. . . . .	171
8.3	The Silhouette scores indicate that the main difference in coupling curves between the two clusters is observed for the linear and non nonlinear correlation $\text{SpO}_2\text{-rScO}_2$ , and the linear correlation $\text{SpO}_2\text{-FTOE}$ . . . . .	173
8.4	Asymmetry of the nonlinear correlation coefficient measures the degree of nonlinearity. The asymmetry was highest for coupling pairs involving HR. A significant between-cluster difference was observed for the $\text{SpO}_2\text{-rScO}_2$ coupling. . . . .	174
9.1	Illustration of various features computed from the EEG signal: the running RMS value, and the running RMS and running duration values for bursts and IBIs. . . . .	185
9.2	Method used to tune the kernel bandwidth $\sigma$ . The data is segmented in nonoverlapping segments of 15 min. For each segment $i$ , the kernel matrix $\Omega_i$ is defined. All $\Omega_i$ are collected in $\Omega_C$ , for which the Shannon entropy $H(\Omega_C)$ is computed. Repeating this procedure for a range of $\sigma$ allows to select $\sigma$ that corresponds to the largest $H(\Omega_C)$ . . . . .	187
9.3	Features used to quantify the reduction in signal interaction strength: $S$ and $\Delta$ . . . . .	189

9.4	Signal interaction between MABP and EEG after administration of propofol at $t = 0$ . A reduction in interaction is observed among the different signal modalities after the administration of propofol, with a slow recovery to the reference level. . . . .	191
9.5	Changes in the physiological network, assessed using a graph model $G_T$ , for one neonate in the group of study (PMA 30 weeks, $1.0 \text{ mg kg}^{-1}$ ) at 10, 30, and 180 min after propofol administration.	192
9.6	The relation between features $S$ and $\Delta$ , computed from the $k_T(\text{MABP}, \text{EEG})$ interaction curves (Figure 9.4), and PMA and propofol dose. . . . .	192
9.7	Comparing the vertex degree values with the graph average degree after administration of propofol at $t = 0$ for all neonates ( $N = 22$ ) using $k_T$ . . . . .	193
10.1	The neonates were divided in five groups, corresponding to five different perioperative settings, based on clinical condition. . .	203
10.2	The connectivity of the neurocardiovascular graph was not affected by GA, BW, sex, the position of the liver, and the size of the hernia, but it was influenced by the clinical group and clinical time window. . . . .	208
10.3	Longitudinal overview of HR, MABP, $\text{SpO}_2$ , $\text{rScO}_2$ , EEG, graph connectivity, BR, CAR, and NVC. . . . .	210
10.4	The neurocardiovascular graph before, during and after cardiopulmonary resuscitation, followed by emergency VA-ECMO treatment.	214
10.5	The neurocardiovascular graph during surgery on VA-ECMO. A clot was developed in the arterial canula, shortly after the procedure ended, which was consequently removed by the surgeon.	215
11.1	Multiscale decomposition using the DWT. Left: the filter response becomes steeper with increasing wavelet index, approximating the ideal step response. Right: the number of decomposition levels decreases with increasing wavelet index. . . . .	229
11.2	Example of a multiscale decomposition, for one patient (propofol dataset). The median grid is shown for the entire recording of six hours. . . . .	230

11.3 A disadvantage of bivariate coupling measures is that we risk to detect spurious connectivities in a multivariate setting. Multivariate methods have an improved accuracy (no spurious connections), but also a larger complexity (more free parameters and longer computational time). . . . . 231

# List of Tables

2.1	Overview of brain monitoring techniques generally used in the NICU: cranial ultrasound (cUS), magnetic resonance imaging (MRI), transcranial Doppler ultrasound (TCD), functional MRI (fMRI), electroencephalography (EEG), and near-infrared spectroscopy (NIRS). . . . .	40
3.1	Thresholds used to define the physiological range of the signals under analysis. . . . .	61
4.1	Overview of the datasets used throughout this thesis: the propofol dataset, the congenital diaphragmatic hernia (CDH) dataset, esophageal atresia (EA) dataset and the postnatal dataset. . .	102
4.2	Propofol dataset demographics, including PMA, PNA, cUS findings, and propofol dose. . . . .	103
4.3	CDH dataset demographics, including GA, PNA, BW, sex, cUS findings, and Apgar scores. . . . .	105
4.4	EA dataset demographics, including GA, PNA, BW, and sex. No abnormalities were observed on cUS in any of the included neonates. . . . .	108
4.5	Neonatal dataset demographics, including GA, PNA, BW, length, head size, sex, and Apgar scores. . . . .	109
5.1	Patient demographics of the HRV study. Drug doses are presented as a mean over the intraoperative period (sevoflurane, midazolam, VIS) or as a sum of different boluses (fentanyl). . . . .	121

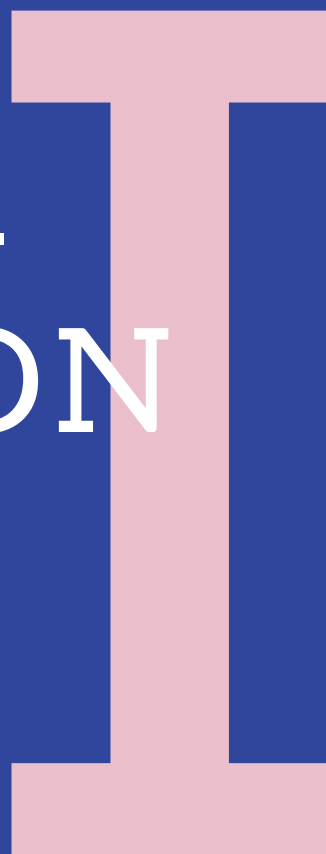
5.2	Significance of fixed effects in linear mixed effects analysis . . .	122
6.1	Patient demographics of sevoflurane versus midazolam group. .	135
7.1	Stratification of the original study group into two subgroups, based on the presence of brain abnormalities on a routine cUS.	154
8.1	Overview of patient demographics in the Graz dataset in the neonatal dataset: all eligible patients versus included patients. .	169
8.2	Overview of patient demographics in the neonatal dataset: cluster 1 versus cluster 2. . . . .	172
9.1	Stratification of the neonates into three age groups based on PMA: extremely preterm, very preterm and moderate to late preterm neonates. . . . .	183
10.1	Overview of the demographics for each of the five groups under study. . . . .	204
10.2	Overview of the drugs administered in each of the five groups under study. . . . .	205
10.3	Main findings for each of the five perioperative settings, based on the structure of the neurocardiovascular graph. . . . .	212



PAA

RT

# INTRO- DUCTION



introduction

01

# Introduction



## 1.1 Problem statement

Preterm birth is defined as a delivery before 37 completed weeks of gestation, which is the time period between conception and birth (Figure 1.1). Every year, an estimated 15 million babies are born preterm, which is more than 1 in 10 babies, and this number is rising in all countries around the world [43, 248]. In the European Union (EU), it is estimated that 500.000 babies are born preterm each year, in need for neonatal intensive care [441]. During the last decades, huge progress has been made to reduce the mortality of prematurely born infants [248]. The very premature neonates, born before 28 completed weeks of gestation, remain at risk for adverse health outcome and neurodevelopmental disability [3]. They represent up to 10 % of all preterm infants in the EU. Cerebral palsy, serious motor delays, cognitive impairments leading to learning deficits and increased behavioral problems (attention deficit hyperactivity disorder, autism) have been observed in very preterm infants [455, 266, 137, 451, 104, 429]. Emotional problems have also been reported with symptoms such as shyness, unassertiveness, social maladaptation and anxiety [11, 350, 383]. Another issue is visual development, which is highly compromised in neonates born prematurely [290]. These maladaptive outcomes have a severe effect on the children's quality of life and a huge economic impact on society: the economic cost of children's behavioral problems is 10 times the cost of a regular child [357]. Considering all of this, the focus of neonatal intensive care has shifted during the last decades from improving survival towards cot-side brain monitoring and neuroprotection of these vulnerable infants to improve their outcome and reduce neurodevelopmental disabilities [291].

Both the increasing number of preterm infants and the improved survival rates contribute to the increased prevalence of neonatal brain injury [459]. Preterm neonates are particularly susceptible to brain injury as the brain undergoes rapid development during the last trimester of pregnancy, which is the time period in which most preterm neonates are born. During this period, the brain significantly increases in volume, roughly triples in weight (from 100 grams at the end of the second trimester to almost 300 grams at term) [142], undergoes cortical folding (the formerly smooth surface smooth surface is becoming increasingly grooved and indented) and improves (functional) connectivity [108]. Due to the cortical folding, the surface area of the brain increases 30-fold in the last 16 weeks of pregnancy [16, 49]. During the third trimester, the brain is very sensitive to insults, mainly due to two reasons. First, the vascular bed is still immature, and therefore very fragile, making the brain sensitive to overperfusion [26]. When too much runs through the vascular bed, it is likely to rupture, which causes a bleeding. Second, brain cells don't have storage for the oxygen and nutrients they need to function [239]. The brain is therefore also very

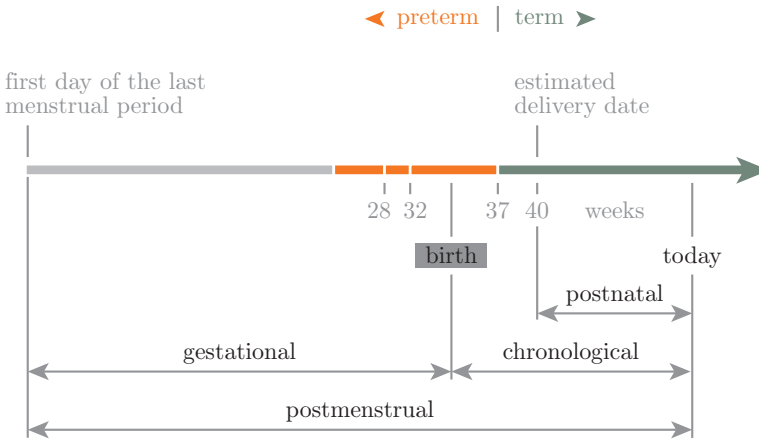


Figure 1.1: Preterm birth is defined as a delivery before 37 completed weeks of gestation. Gestational age (GA) (weeks) is used during pregnancy to describe how far along the pregnancy is (completed weeks). GA is defined as the number of weeks from the first day of the mother’s last menstrual cycle to the delivery. The chronological age or postnatal age (PNA) (days, weeks, months, years) is defined as the time elapsed from birth. The postmenstrual age (PMA) (weeks) is the sum of the GA and PNA. The corrected age (weeks, months) is defined as the chronological age reduced by the number of weeks born before 40 weeks of gestation.

sensitive to underperfusion. When there is not enough blood flowing to the brain, the brain cells don’t have the fuel to support their function, and might die as a result of that. Inadequate or highly fluctuating cerebral perfusion and oxygenation can result in brain injury [196] and can adversely affect brain development [8]. Therefore, close monitoring of the highly vulnerable preterm newborns, especially their brains, during the first critical weeks of life is of utmost importance.

Current methods for assessing the adequacy of cardiac output to support proper organ system are typically imprecise, difficult to perform, are not feasible for longitudinal monitoring, or lack specificity to cerebral circulation [423]. During the last decades, there is an increased interest in monitoring the regulation of cerebral blood flow (CBF) in the neonate. CBF regulation comprises various components, generally referred to as different regulation mechanisms [163]. Proper functioning of all of these regulation mechanisms is essential in order to

maintain CBF in the desired range to support brain function and avoid brain injury.

In literature, most studied focus on one of four regulation mechanisms. First, cerebral pressure autoregulation (CAR), a physiological mechanism which functions to maintain a more or less constant CBF in face of changes in perfusion pressure, was studied using a variety of linear measures including correlation [226, 227, 51], (wavelet) coherence [382, 242, 72, 8, 402] and transfer function analysis [423, 400, 61, 60]. Second, neurovascular coupling (NVC), which links transient neural activity to subsequent changes in CBF, was studied recently studied using (wavelet) coherence [67, 147] and linear transfer entropy [62]. Aside from these three studies, no other studies on background NVC are available in literature, most probably due to the larger technical complexity of NVC studies, which include an additional EEG processing step. Third, the baroreceptor reflex is the most important regulatory mechanism in the short term control of heart rate and blood pressure [19]. This reflex minimizes any variation in blood pressure by responses of both heart rate and arterial vascular tone [146] and can be assessed by computing the coupling between blood pressure and RR time series, derived from the ECG, using correlation analysis [146, 457, 456, 464, 37] and frequency domain methods, mainly in the low frequency range [96, 158, 168, 340, 18, 456, 147, 128]. Last, heart rate passivity was recently defined using the interaction between HR and NIRS-derived cerebral oxygenation as an additional index for cerebrovascular reactivity [262]. Preterm infants were observed to have a significantly better outcome when cerebral oxygenation remained independent of heart rate changes. Preterm infants were observed to have a significantly better outcome when cerebral oxygenation remained independent of heart rate changes. In general, failure in any one of these regulation mechanisms might result in an unstable CBF, generating a cycle of ischemia-reperfusion, which drives the mechanisms of preterm brain injury [423].

In order to monitor these regulation mechanisms, near-infrared spectroscopy (NIRS) and electroencephalography (EEG) can be used to measure cerebral oxygenation and the electrical activity of the brain, respectively. Both signals can be measured in a continuous, noninvasive way at the bedside, and have therefore found their way into the neonatal intensive care unit (NICU). In practice, NIRS can be used to monitor cerebral oxygenation during respiration, hypotension and during surgery to increase cerebral safety, and in the evolution of pathological conditions such as patent ductus arteriosus and hypoxic ischemic encephalopathy [104]. Continuous registration of the EEG (or its amplitude-integrated version) is the gold standard in the assessment of background activity, the diagnosis of (subclinical) seizure activity, and the evaluation of sleep-wake cycling [162, 161]. Combining NIRS and EEG at the bedside increases the

prognostic value of both modalities [104].

Physiological markers for various regulation mechanisms can be obtained by integrating multimodal signals in a pairwise fashion using coupling measures. In practice, most studies focus on one regulation mechanism, without taking into account the status of the other regulating components. In this dissertation, a model is proposed that allows to monitor various aspects of cerebral blood flow regulation at the same time. Formally, there were two goals for this thesis. Our first goal was to develop a new marker for neurovascular coupling, based on nonlinear interactions (Chapter 7). From a wider perspective, we want to show the viability of transfer entropy as a measure to capture individual CBF regulation mechanisms. The second goal of this thesis was to serve as a proof-of-concept for our signal interaction graph model capturing neurocardiovascular interactions. By applying the model in various clinical settings (Chapters 8, 9, 10), we test its behavior and explain it under various physiological conditions. This way, we illustrate the high potential of our model, which motivates further testing and large-scale validation.

Current clinical therapies have failed to fully prevent permanent brain injuries in neonates [336]. Early therapeutic intervention that supports and optimizes regulation of CBF, potentially based on the markers developed in this thesis, might help to improve neurological outcomes. In addition, precision medicine applied to neurocardiovascular monitoring could individualize neuroprotective treatments in critically ill neonates.

## 1.2 Outline of the thesis

This thesis is split up in five main parts (Figure 1.2). The first part is composed of three introductory chapters, which present the physiology and monitoring of the neonatal brain, the building blocks of the signal processing pipeline, and the datasets used throughout this thesis, respectively. The materials outlined in these chapters are necessary to understand the following chapters. The second part presents two studies based on univariate signal analysis, using heart rate variability analysis and descriptive statistics. The third part introduces a study based on bivariate signal analysis. The fourth part presents three studies based on multivariate signal analysis, in which we apply graph models to different datasets. The fifth part summarizes the main research conclusions and presents future directions for the methods introduced in this thesis. A more detailed description of each chapter can be found below.

I introduction	III bivariate analysis
01 introduction	07 transfer entropy measures neurovascular coupling
02 physiology and monitoring of the neonatal brain	IV multivariate analysis
03 signal processing pipeline	08 cardiovascular interactions during transitional period
04 datasets	09 neurocardiovascular graph during propofol
II univariate analysis	10 neurocardiovascular graph in perioperative period
05 heart rate variability during surgery	V conclusions
06 cerebral oxygenation and activity during surgery	11 conclusions and future research directions

Figure 1.2: This thesis is split up in five main parts: the introduction is followed by the univariate, bivariate, and multivariate analysis. At the end, the conclusive part describes the main conclusions and the future research directions.

### 1.2.1 Part I: Introduction

**Chapter 1** is the current chapter, introducing the problem statement and research objectives of this thesis. In addition, various national and international collaborations are presented, which were essential to derive the results described in this thesis.

**Chapter 2** provides an overview of the physiological background and monitoring techniques. First, the building blocks and the structural development of the brain are discussed. Next, the most commonly used neuroimaging and neuromonitoring techniques are described, with a special focus on NIRS and EEG. Then, we'll have a look at the regulation of CBF in the neonatal brain, and the most common pathologies that result from impaired regulation of CBF.

**Chapter 3** provides a comprehensive overview of the signal processing pipeline used in the remainder of the thesis. First, we'll discuss artifact detection and removal. Then, the univariate (spectral density, sample entropy, descriptive statistics), bivariate (various coupling measures) and multivariate (graph analysis, clustering) tools are described in detail, before arriving to the statistical analysis (hypothesis tests and regression models), which forms the end point of any analysis presented in this thesis.

**Chapter 4** discusses the datasets used in this thesis. First, the *propofol dataset* is described, measured at the University Hospitals Leuven, Belgium. Second, the *congenital diaphragmatic hernia* and the *esophageal atresia datasets* are presented, measured at the Sophia Children's Hospital, Rotterdam and the hospital Mannheim. Last, the *neonatal dataset* is described, measured at Medical University of Graz, Graz, Austria.

## 1.2.2 Part II: Univariate analysis

**Chapter 5** presents a study on heart rate variability during surgery. Sevoflurane-based anesthesia significantly suppressed the autonomic nervous system and the contribution of the sympathetic and parasympathetic branch decreased and increased, respectively, reflecting the desired effect of anesthesia, which is reducing stress.

**Chapter 6** studies cerebral oxygenation and activity in the perioperative period. Sevoflurane-based anesthesia resulted in increased cerebral oxygenation and decreased cerebral activity, suggesting adequate anesthesia. Midazolam-based anesthesia led to alarmingly low brain oxygenation values, below hypoxia threshold, and increased values of EEG power during the first 30 min of surgery, which might indicate conscious experience of pain.

## 1.2.3 Part III: Bivariate analysis

**Chapter 7** introduces a measure for neurovascular coupling based on nonlinear, nonparametric transfer entropy. Our results indicate that transfer entropy values computed using the nonlinear approach were able to discriminate between neonates with and without brain abnormalities, indicating a less functional neurovascular coupling in the former.

## 1.2.4 Part IV: Multivariate analysis

**Chapter 8** presents the first of three studies on multimodal interactions. In this study, we quantified signal interaction during immediate transition after birth. High correlation was already observed during the first minutes of life. Moreover, a data-driven clustering method unraveled an age-dependency in the correlation patterns.

**Chapter 9** studies the effect of propofol on neurocardiovascular coupling using graph analysis. Propofol was found to introduce a decrease in signal interaction up to 90 min after propofol administration. The clinical recovery phase was mainly determined by the EEG dynamics, which were observed to recover much slower compared to the other modalities. In addition, we found a more pronounced loss in cerebral-systemic interactions with increasing propofol dose.

**Chapter 10** presents the last study on neurocardiovascular coupling. Neurocardiovascular graphs provided new and crucial information about the effect of perioperative management on the (patho)physiology of surgical newborns, who are at risk for brain injury. The clinical condition of the patient, as well as the surgical and anaesthesiologic approach, was observed to affect the neonatal physiology and CBF regulation mechanisms at different levels.

## 1.2.5 Part V: Conclusion

**Chapter 11** summarizes the main findings of the research presented in this thesis. In addition, we'll have a look at future directions for the research outlined in this thesis.

## 1.3 Collaborations

The research outlined in this thesis was carried out in the BIOMED research group, part of STADIUS, center for dynamical systems, signal processing and data analytics, Department of Electrical Engineering (ESAT), KU Leuven, Belgium. This group is headed by Prof. Sabine Van Huffel, Prof. Alexander Bertrand and Prof. Maarten De Vos. My research wouldn't be possible, however, without various collaborations established during the project. These collaborations allowed access to new datasets, improved the algorithms and the practical implementation thereof, and provided extensive feedback on the

interpretation of the results. An overview of the different collaborations is presented below.

All of the research outlined in this thesis was conducted in strong collaboration with the Department of Neonatology, University Hospitals Leuven (Prof. Gunnar Naulaers, Prof. Katrien Jansen, Dr. Anneleen Dereymaeker, Dr. Liesbeth Thewissen, Dr. Anne Smits, Kate Carkeek, Jan Vervisch). The database used to develop the first version of our graph model (Chapter 9) and our marker for neurovascular coupling (Chapter 7) was recorded in Leuven by Dr. Liesbeth Thewissen and Dr. Anne Smits. In addition, all clinicians helped with the clinical interpretation of the results and gave important feedback during the biweekly neonatal meetings.

The idea of designing a model that allows to study various aspects of cerebral blood flow regulation at the same time – the main novelty of this thesis – resulted from numerous discussions with Prof. Alexander Caicedo, at the time he was still working in Leuven. In general, he provided essential suggestions and feedback during countless brainstorming sessions.

All aspects of the signal processing pipeline and the practical implementation thereof were thoroughly reviewed by numerous colleagues of the BIOMED group. We all presented our work numerous times a year to each other, which resulted in strong feedback that improved the quality of the work presented in this text. In particular, everyone working on neonatal monitoring (Amir Ansari, Mario Lavanga, Ofelie De Wel, Tim Hermans, Laura Smets) provided significant and important feedback.

The study of multimodal interactions during the transitional period presented in Chapter 8 is the result of a close collaboration with Prof. Gerhard Pichler, Dr. Christina Wolfsberger, and Prof. Berndt Urlesberger (Medical University of Graz, Austria).

The studies on heart rate variability (Chapter 5), cerebral oxygenation and brain activity (Chapter 6), and neurocardiovascular coupling (Chapter 10) in the (peri)operative period are a result of a close collaboration with Sophie Costerus (Sophia's Children Hospital, Rotterdam, The Netherlands). Furthermore, an important mention goes out to Prof. Dick Tibboel, Dr. Jurgen de Graaff, and Robert Flint, who all contributed significantly to the results presented in the corresponding chapters during our numerous meetings.

## **1.4 Conclusion**

This chapter introduced the problem statement and presented the main research objectives of the thesis. Afterwards, a chapter-by-chapter overview of the structure of this thesis was presented. Lastly, the collaborations that led to the results presented in this text were described.

introduction

02

# Physiology and monitoring of the neonatal brain

*partially based on:*

Hendriks, D., Smits, A., Lavanga, M., De Wel, O., Thewissen, L., Jansen, K., Caicedo, A., Van Huffel, S. and Naulaers, G. Measurement of Neurovascular Coupling in Neonates. *Frontiers in Physiology* 10 (2019), 65.



This chapter provides an extensive overview of the physiological background. First, we discuss the building blocks of the neonatal brain and explain how the brain can be monitored, with a focus on near-infrared spectroscopy and electroencephalography, the two signal modalities that form the basis of the work outlined in this thesis. After this, various components of cerebral blood flow regulation are described, and a graph model is introduced to study cerebral blood flow regulation at the bedside. Finally, we list the most common brain injuries resulting from improper regulation of cerebral blood flow.

## 2.1 The neonatal brain

### 2.1.1 Nervous system

The nervous system coordinates actions and sensory information by transmitting signals to and from different parts of the body. The nervous system of vertebrates consists of two parts (Figure 2.1): the central nervous system (CNS) and the peripheral nervous system (PNS).

**Central nervous system** The CNS is composed of white and gray matter. White matter mainly consists of axons, while gray matter mainly consists of neurons and unmyelinated fibers. Both tissue types contain various glial cells, which are the supporting cells of the brain. The CNS consists of two major structures (Figure 2.1): the brain and the spinal cord. The brain is the main functional, processing unit of the CNS. Anatomically, the brain consists of the brainstem (autonomic control of the body), cerebellum (*little brain*: sensory and motor information, including balance), diencephalon, and cerebrum (*endbrain*: emotion, memory, perception, motor functions, cognitive capabilities). The spinal cord consists of nerves that carry afferent sensory information to the brain and efferent motor signals to the peripheral effector organs (mainly muscles and glands).

**Peripheral nervous system** The PNS mainly consists of nerves, which are enclosed bundles of long fibers or axons, that connect the CNS to all other parts of the body, generally referred to as the *periphery*. In the PNS, there are two types of nerves: efferent motor nerves transmit signals from the brain to the periphery, while afferent sensory nerves transmit information from the periphery to the CNS. The motor pathways are further divided in two systems: the somatic and the autonomic system (ANS), that mediate voluntary and involuntary actions, respectively (Figure 2.1). The ANS consists of two branches:

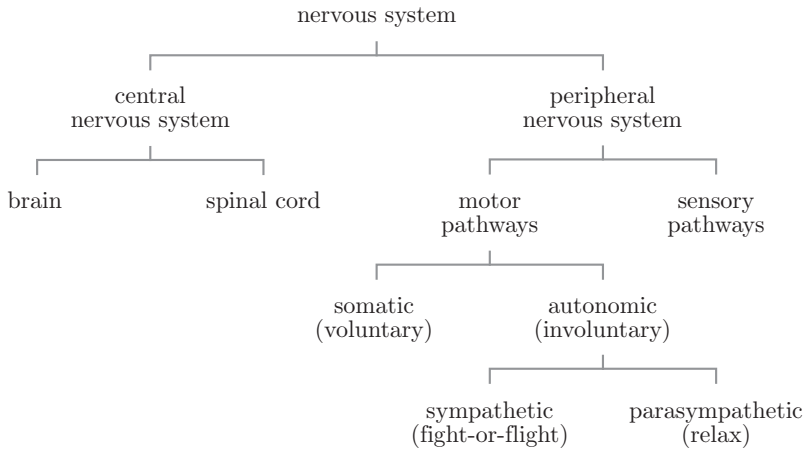


Figure 2.1: The nervous system of vertebrates consists of two parts: the central nervous system and the peripheral nervous system, which are further subdivided in various structures and systems.

the sympathetic branch is activated in case of emergency (*fight-or-flight*) to mobilize energy, while the parasympathetic branch predominates in quiet *rest and digest* conditions.

## 2.1.2 Building blocks of the brain

The brain is made up of different cell types, each with their own unique properties. The most common brain cells are neurons and glial cells. On average, the mature brain is composed of more than 100 billion neurons [295], and just as many – if not more – glial cells. Both cell types are essential for proper brain function.

**Neuron** Neurons are the information processing units of the brain. There are many different kinds of neurons that vary in their size and shape as well as in their function [385]. In general, a neuron is made up of four key parts: the cell body (soma), the dendrites, the axon, and the axon terminals (Figure 2.2). The dendrites are protrusions from the neuron that receive signals from other neurons. The cell body is the hub of the neuron that integrates all incoming signals by summing them together. The axon is a long fiber, along which

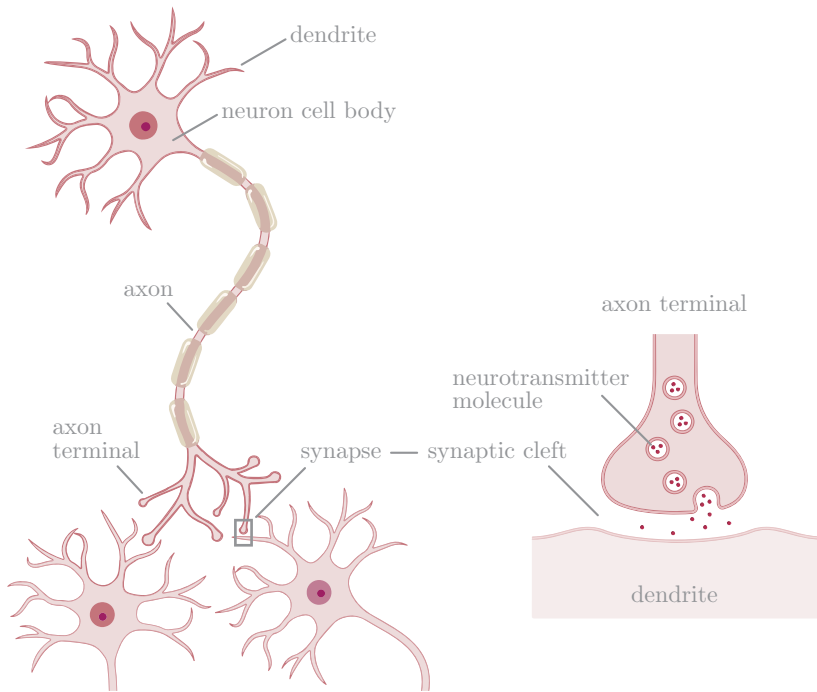


Figure 2.2: A neuron is made up of four key parts: the cell body, the dendrites, the axon, and the axon terminals. At the synapse, an action potential triggers the presynaptic neuron to release chemical neurotransmitters from its axon terminal, which consequently bind to the receptors of the target postsynaptic neuron.

electrical signals called *action potentials* are transmitted. Axons are covered in a fatty substance called myelin, which enhances the conduction velocity. At the synapse, an action potential will trigger the presynaptic neuron to release chemical neurotransmitters from its axon terminal, which will consequently bind to the receptors of the target postsynaptic neuron (Figure 2.2). During development, a vast amount of interconnections between neurons are made resulting in extensive, well-connected neural networks [385]. Each neuron can connect with up to 15,000 other neurons, summing up to a staggering amount of approximately  $10^{15}$  connections in the mature brain [286].

**Glial cell** Glial cells are non-neuronal cells; they don't produce electrical impulses, but communicate with each other and with neurons using chemical signals only (neurotransmitters and ions) [122]. Glial cells surround neurons and hold them in place. There are many types of glial cells in the brain; each type serves different functions [184]. In the CNS, glial cells include astrocytes, oligodendrocytes (myelin formation), ependymal cells (creation and secretion of cerebrospinal fluid), and microglia (immune defense). Astrocytes, which are the most abundant type of glial cell, link neurons to their blood supply while forming the blood-brain barrier. They regulate vasoconstriction and vasodilation, and they also take care of the external chemical environment of neurons by removing excess potassium ions, and by recycling neurotransmitters released during synaptic transmission. In the PNS, glial cells include Schwann cells (myelin formation) and satellite cells (regulate external chemical environment).

### 2.1.3 Brain development

The development of the brain starts shortly after conception and continues well into adolescence [170]. Four weeks after gestation, the neural plate forms, which is the foundation of the brain and the spinal cord. During development, the neural plate turns into the neural tube, from which the brain and the spinal cord develop.

In the first trimester, the brain grows millions of neurons, which connect across synapses to direct movement and growth. Special neural cells form and move throughout the embryo to kickstart nerve development. Neurons form their first synapses, allowing them to interact. In this stage, the brain makes up almost half of the weight of the fetus. In the second trimester, the nerves start to become covered with myelin. The brain stem, which controls heart rate (HR), breathing and blood pressure is almost entirely matured at the end of the second trimester. Brain development in the third trimester is marked by the rapid development of neurons in the brain and explosive growth: the brain almost triples in weight and size (Figure 2.3). The cerebrum is the fastest-growing part of the brain in the third trimester. The formerly smooth surface of the brain is becoming more and more grooved (cortical folding, gyrification), which results in a large increase in surface area. Rapid development of neurons and wiring translates in increased connectivity. By the time the baby is born, the brain resembles that of an adult brain, but continues to develop after birth and matures in response to the neonate's environment.

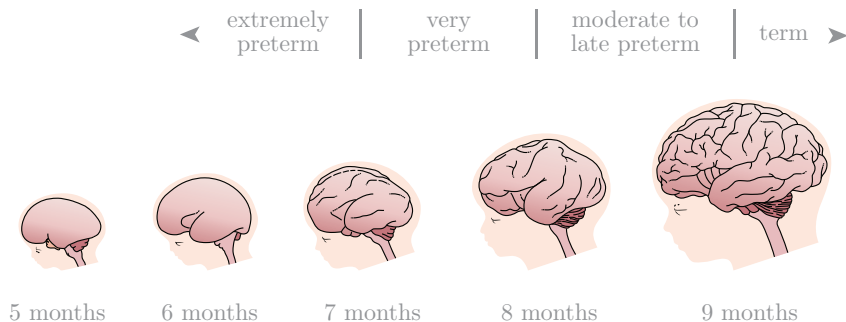


Figure 2.3: During the last trimester of pregnancy, the brain significantly increases in volume, roughly triples in weight (from 100 grams at the end of the second trimester to almost 300 grams at term), undergoes cortical folding (the formerly smooth surface smooth surface is becoming increasingly grooved and indented) and improves (functional) connectivity. Due to the cortical folding, the surface area of the brain increases 30-fold in the last 16 weeks of pregnancy. Adapted from [287].

## 2.2 Brain monitoring

Various techniques exist to monitor the neonatal brain. Each techniques is used in different settings, depending on the condition of the patient or the suspected injury.

### 2.2.1 Overview of neonatal brain monitoring

**Structural neuromonitoring** Structural neuromonitoring methods allow to assess the structure of the neonatal brain and detect structural lesions. The two most commonly used modalities in neonatal care are cranial ultrasound (cUS) and magnetic resonance imaging (MRI) (Table 2.1). In general, cUS is part of the routine neurological monitoring in the NICU and often serves as the initial diagnostic imaging modality due to its many favorable properties: it is safe, relatively low-cost, fast, and can be performed at the bedside [153, 291, 416]. cUS can be used to detect and track the evolution of peri- and intraventricular hemorrhages, hydrocephalus and periventricular leukomalacia (Section 2.4) [416]. MRI is often used as a complementary imaging technique to confirm the presence, exact location and extent of the lesions found on cUS [416], due to

its higher spatial resolution. Disadvantages include a high cost, the high level of acoustic noise, and the need for transportation and sedation of the neonate, making it only suitable for stable neonates [25].

**Functional neuromonitoring** Functional neuromonitoring methods allow to monitor brain function. The functional monitoring techniques can be stratified in *imaging* modalities and *signal* modalities.

Imaging modalities to study cerebral hemodynamics include transcranial Doppler ultrasound (TCD) and functional MRI (fMRI). Both modalities overlay a structural image with information on cerebral hemodynamics: blood flow velocity in case of TCD and blood flow in case of fMRI. TCD is an excellent modality to assess the anatomy of the cerebral vasculature of the newborn infant [257]. Abnormal flow patterns can be detected, which provide insight in the risk for brain injury and can play a role in determining the severity of brain damage [258, 89, 65]. Recently, the feasibility of TCD during surgery was demonstrated [84]. fMRI is based on the magnetic properties of hemoglobin and measures the blood oxygenation level dependent (BOLD) response, which reflects CBF in a volumetric cube of brain tissue [115, 139]. fMRI shares all of its disadvantages with MRI [25], limiting the use of fMRI mainly to asleep, stable neonates [114].

Signal modalities to study brain function include near-infrared spectroscopy (NIRS) and electroencephalography (EEG). These modalities are described in detail in the next two sections, as they form the basis for all of the research outlined in this thesis.

## 2.2.2 Near-infrared spectroscopy

NIRS is a noninvasive technology that can be used to measure the percentage of saturated hemoglobin in a target tissue. In the NICU, NIRS is mainly used to assess cerebral oxygenation on a bedside monitor in a continuous, noninvasive way [249, 397]. It has been widely adopted over the past two decades for research and is now increasingly being deployed for clinical use [64, 149, 410]. Other applications, such as measurement of other (superficial) organs such like the liver [353, 279, 417], the bowel [134, 384], the kidneys [384] and the peripheral circulation [437, 433, 316] are also possible, but they are not described here [133].

**Measurement** NIRS devices utilize light in the near-infrared band (wavelength between 650 and 900 nm) to which skin, bone, and connective tissue are mostly transparent. As the near-infrared light diffuses into the tissue, it interacts with

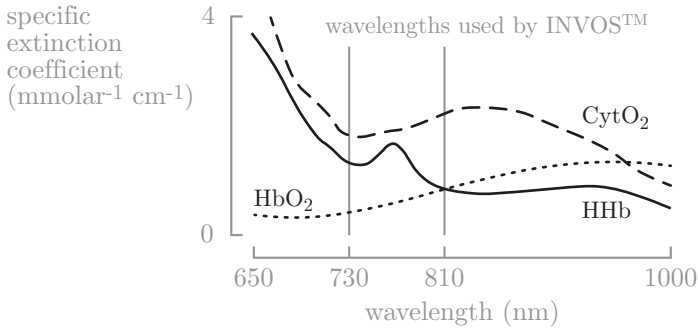


Figure 2.4: Absorption spectra for the three main chromophores that cause absorption in NIRS monitoring: cytochrome c oxidase (CytOx), oxyhemoglobin ( $\text{HbO}_2$ ) and deoxyhemoglobin (HHb). The INVOS<sup>TM</sup> monitor measures at two wavelengths: 730 nm and 810 nm (isosbestic point). Adapted from [98].

hemoglobin, the protein in red blood cells that carries oxygen. This interaction takes place in four ways: via absorption, reflection, scattering, and transmission. Although transmitted and absorbed light are lost and not returned to the sensor, a portion of the source light is reflected back to the sensor, and a smaller portion is scattered by motion, generally, blood flowing through arteries. Over the time frame of a typical NIRS recording, the structure of the monitored tissue remains constant: reflection, transmission, and scattering are assumed to be constant as well.

Therefore, the only variable optical factor is absorption, which changes based on the degree of oxygen saturation of the cerebral vasculature. There are three main chromophores that cause attenuation of the emitted light: oxyhemoglobin ( $\text{HbO}_2$ ), deoxyhemoglobin (HHb), and cytochrome c oxidase (CytOx).  $\text{HbO}_2$  represent hemoglobin that carries oxygen ( $\text{O}_2$ ), while HHb represent hemoglobin without  $\text{O}_2$  (the  $\text{O}_2$  has been given to the tissue). CytOx is the terminal enzyme in the mitochondrial respiratory chain and indicates the changes in cellular oxygenation [52]. Figure 2.4 shows the absorption spectra for CytOx,  $\text{HbO}_2$  and HHb in the infrared range. In biological tissue, the concentration of CytOx is less than 10% of the concentration of hemoglobin and its concentration changes very slowly (over days) [78]. Therefore, reliable *in vivo* measurements of CytOx are in practice difficult to obtain.

Unlike pulse oximetry, NIRS measurements are not pulse-synchronized and thus not limited to arterial hemoglobin sources [423]. Instead, the light interrogates

arterial, venous, and capillary beds, providing a regionalized composite measure. Given that only approximately 30% of blood is intra-arterial at any given time in most tissues, NIRS monitoring provides an approximate 30/70 arterial/venous-weighted estimate of oxygen saturation [435, 448], which closely parallels jugular venous oxygen saturation [176].

In general, NIRS relies on two physical principles: the differential absorption of near-infrared light and the modified Beer-Lambert law. Light of at least two distinct wavelengths is used, and the relative concentration of oxygenated and deoxygenated hemoglobin is consequently estimated using the modified Beer-Lambert law, thus providing an index of tissue oxygenation [390]. Several technologies for NIRS exist: continuous wave spectroscopy (CWS), spatially resolved spectroscopy (SRS), and time resolved spectroscopy (TRS) in the time and frequency domain. CWS is the most common technique, due to the inexpensive cost [68]. In this section, we describe CWS and SRS, since they are employed by the NIRS device (INVOS<sup>TM</sup>), which is the device used to measure cerebral oxygenation throughout this thesis.

**Beer-Lambert law** The Beer-Lambert law states that the attenuation of light in a nonscattering medium is proportional to the length of the path traveled in the medium and the concentration of the absorbing species (Figure 2.5):

$$A = \frac{I_0}{I} = \alpha \cdot C \cdot d \quad (2.1)$$

where  $A$  is the light attenuation,  $I_0$  is the incident (source) light intensity,  $I$  is the emergent light intensity,  $\alpha$  is the specific extinction coefficient of the absorbing compound (Figure 2.4),  $C$  is the concentration of the absorbing compound (e.g., HbO<sub>2</sub>, HHb, or CytOx) and  $d$  is the path length (distance between the points where the light enters and leaves the medium: the source-detector separation).

**Modified Beer-Lambert law** The Beer-Lambert law in Equation 2.1 is too simple to be used in practice. First, the law assumes a homogeneous, non-scattering medium. Biological tissues, however, are highly scattering media. Scattering increases the path length of the light, which in turn increases the probability of light absorption and loss of light (Figure 2.5) [34]. In addition, the tissue of interest is often surrounded by other tissues, which introduces yet another source of scattering [99]. Second, the head of the neonates is too big to allow the emitted light to be measured on the other side. Therefore, the optodes cannot be connected facing each other, but are rather placed next to each other (Figure 2.6). The distance between the electrodes is generally larger than 2 cm (acquire enough depth of of measurement) [120] and smaller than 5

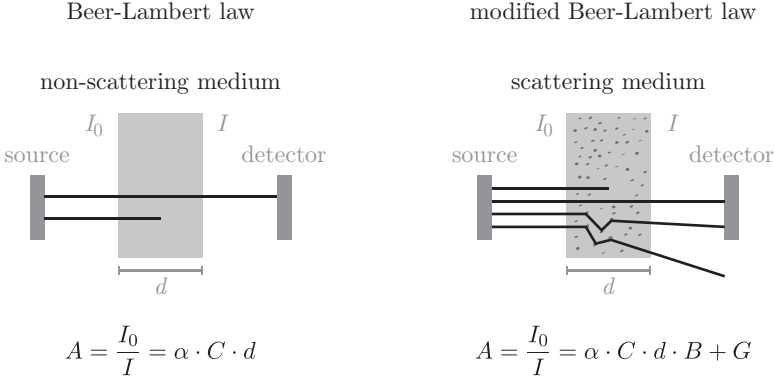


Figure 2.5: The Beer-Lambert law states that the attenuation of light in a nonscattering medium is proportional to the length of the path traveled in the medium and the concentration of the absorbing species. The modified Beer-Lambert law corrects for scattering.

cm (safe levels of light input) [445]. Due to the scattering, the light emitted by the source and captured in the detector follows a path inside the brain within a region that resembles a banana shape [47, 288]. Taking these effects into consideration, the Beer-Lambert law can be modified as follows:

$$A = \frac{I_0}{I} = \alpha \cdot C \cdot d \cdot B + G \quad (2.2)$$

where the differential path length factor (DPF)  $B$  is included to account for the extended path length between the source and the detector due to scattering, and  $G$  represents the losses due to scattering. In practice, DPF is estimated from time-of-flight measurements [99]. It represents a multiplicative correction factor. For example, a DPF of 4 means the mean path length of photons in the tissue is 4 times the source-detector separation). When measuring the oxygenation of the neonatal brain, the DPF is generally set to a constant values of 4.39 [110].

**Continuous wave spectroscopy** In CWS, a light source with constant intensity is used. Since CWS cannot estimate the actual path length ( $d \cdot B$ ) and the scattering properties of the tissue ( $G$ ), absolute values of concentration ( $\text{HbO}_2$ ,  $\text{HHb}$ ,  $\text{CytOx}$ ) can not be measured, only relative changes with respect to an initial baseline value [169]. By evaluating changes in Equation 2.2, and assuming

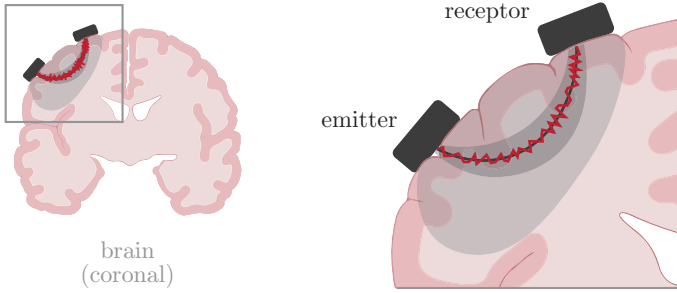


Figure 2.6: Propagation of near-infrared light in the brain: due to scattering, the light follows a path inside the brain within a region that resembles a banana shape.

$B$  and  $G$  constant, the scattering factor  $G$  can be eliminated. The equation for differential absorption becomes:

$$\Delta A = \Delta \left( \log \frac{I_0}{I} \right) = \alpha \cdot \Delta C \cdot d \cdot B \quad (2.3)$$

In general, measuring the concentration of  $m$  chromophores using  $n$  wavelengths corresponds to solving the following system:

$$\begin{bmatrix} \Delta A_1 \\ \Delta A_2 \\ \vdots \\ \Delta A_n \end{bmatrix} = \begin{bmatrix} \alpha_1(\lambda_1) & \alpha_2(\lambda_1) & \cdots & \alpha_m(\lambda_1) \\ \alpha_1(\lambda_2) & \alpha_2(\lambda_2) & & \alpha_m(\lambda_2) \\ \vdots & & \ddots & \vdots \\ \alpha_1(\lambda_n) & \alpha_2(\lambda_n) & \cdots & \alpha_m(\lambda_n) \end{bmatrix} \begin{bmatrix} \Delta C_1 \\ \Delta C_2 \\ \vdots \\ \Delta C_m \end{bmatrix} \cdot d \cdot B$$

where  $\alpha_m(\lambda_n)$  presents the specific extinction coefficient of chromophore  $m$ , measured at wavelength  $\lambda_n$ . When we want to measure the concentration of  $m = 2$  chromophores (e.g.,  $\text{HbO}_2$  and  $\text{HHb}$ ), the absorption needs to be measured at (at least)  $n = 2$  wavelengths, since the system doesn't have a solution for  $n < m$ . Including more wavelengths ( $n > m$ ) comes with two advantages. First, a robust estimate of the chromophore concentration can be obtained by solving the resulting overdetermined system. Second, a more detailed view on the absorption spectra (Figure 2.4) of the chromophores can be obtained.

**Spatially resolved spectroscopy** An improvement to the original one source-detector pair is SRS [390], where photons are measured at multiple spacings

from the source, improving the precision. In addition, the SRS system design enhances contribution of deeper tissues, while reducing the contribution of more superficial tissue like skin and adipose tissue to the NIRS signals [259].

SRS uses a solution of the continuous wave photon diffusion equation, which describes the propagation of photons in a highly scattering medium such as living tissue, to estimate the chromophore concentrations of interest [177]. The solution to this equation at large source-detector separation ( $\rho \gg 1/\sqrt{3\mu_a\mu'_s}$ ) is [390]:

$$\frac{\Delta A}{\Delta \rho} = \frac{\Delta \log(I_0/I)}{\Delta \rho} \approx \sqrt{3\mu_a\mu'_s} + \frac{2}{\rho} \quad (2.4)$$

where  $I_0$  denotes the intensity of the source,  $I$  the intensity of the back-scattered light,  $\rho$  the distance between the source and the detector,  $\mu_a$  the bulk absorption coefficient of the medium, and  $\mu'_s$  the reduced scattering coefficient of the medium (Figure 2.7). The scattering coefficient  $\mu'_s$  is modeled in function of the wavelength  $\lambda$  as  $\mu'_s(\lambda) = k(1 - h\lambda)$ , with  $k$  a factor of proportionality, and  $h$  the normalized slope of the scattering versus the wavelength. Substituting in Equations 2.4 gives:

$$k\mu_a(\lambda) = \frac{1}{3(1 - h\lambda)} \left( \frac{\Delta A}{\Delta \rho} - \frac{2}{\rho} \right)^2 \quad (2.5)$$

In practice, we are interested in the concentration of HbO<sub>2</sub> and HHb. To measure these concentrations, we need to measure the attenuation at two different wavelengths  $\lambda_1$  and  $\lambda_2$ :

$$\begin{bmatrix} k\text{HbO}_2 \\ k\text{HHb} \end{bmatrix} = \begin{bmatrix} \epsilon_{\text{HbO}_2}(\lambda_1) & \epsilon_{\text{HbO}_2}(\lambda_2) \\ \epsilon_{\text{HHb}}(\lambda_1) & \epsilon_{\text{HHb}}(\lambda_2) \end{bmatrix} \cdot \begin{bmatrix} k\mu_a(\lambda_1) \\ k\mu_a(\lambda_2) \end{bmatrix} \quad (2.6)$$

with  $\epsilon_{\text{HbO}_2}(\lambda)$  and  $\epsilon_{\text{HHb}}(\lambda)$  the measured extinction coefficient for HbO<sub>2</sub> and HHb at wavelength  $\lambda$ . From the relative quantities, the regional cerebral oxygen saturation (%) can be computed as follows:

$$\text{rScO}_2 = \frac{k\text{HbO}_2}{k\text{HbO}_2 + k\text{HHb}} \quad (2.7)$$

The regional cerebral oxygen saturation (rScO<sub>2</sub>, %) is an important quantity since it represents an absolute measure of tissue oxygenation [278, 393]. SRS assumes that the measurements in the different receptors are affected equally by the superficial tissue layers. Therefore, the influence of the superficial tissue layers on the measurements is canceled out [444].

The SRS device used in this thesis is the INVOS, commercialized by Somanetics. It uses two photodetectors located at 3 cm (measures scatter light) and 4 cm

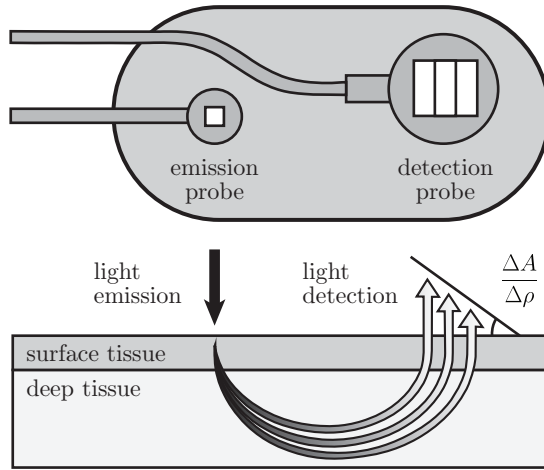


Figure 2.7: In spatially resolved spectroscopy (SRS), photons are measured at multiple spacings from the source, improving the precision. In addition, the SRS system design enhances contribution of deeper tissues, while reducing the contribution of more superficial tissue like skin and adipose tissue to the NIRS signals.

(primarily measures changes in  $\text{HbO}_2$  and HHb in deeper tissue) from the light source [276]. Other NIRS devices exist, but generate different parameters. A popular example is the NIRO device by Hamamatsu, which outputs a parameter called the tissue oxygenation index (TOI). A good correlation has been found between  $\text{rScO}_2$  and TOI, indicating that both variables measure the same underlying process [276].

**NIRS in the NICU** NIRS was first used for medical purposes by Jöbsis [185]. The first applications in neonatal brain monitoring were presented by Brazy et al. [52] and Delpy et al. [99]. After the introduction of SRS, the use of NIRS has become more popular [98, 390].

NIRS has been used to measure CBF, without [58, 112, 372, 141] and with the use of a dye (indocyanine green) [55, 219, 341], and to measure cerebral blood volume (CBV) [452, 33]. Good correlation has been observed when comparing measurements of NIRS-derived CBV and CBF [233, 339, 151]. NIRS has also been shown a good technology to measure jugular venous saturation, which is

the amount of oxygen left in the venous system after the brain has removed the oxygen that it needs [276, 438, 267, 364, 280]. NIRS can be used to detect patent ductus arteriosus (PDA) [229, 408] and reflects changes in intestinal blood flow [278].

Some authors have proposed that monitoring CBF is less important than monitoring oxygen consumption to detect brain hypoxia and ischemia (Section 2.4) [307, 308, 460]. Using NIRS technology, the balance between oxygen delivery and oxygen consumption can be defined as the fractional tissue oxygen extraction (FTOE) [280]:

$$\text{FTOE} = \frac{\text{SpO}_2 - \text{rScO}_2}{\text{SpO}_2} \quad (2.8)$$

Even though NIRS possesses a high potential for clinical use, it has been limited to research purposes, due to the sensitivity to motion artifacts [372], a poor reproducibility [233], the bias that results from optode position [410, 379, 381, 109], and lack of clinically normalized values [410, 308, 281, 230].

### 2.2.3 EEG

**Measurement** EEG provides a noninvasive measurement of the electrical activity of the cerebral cortex via electrodes attached to the scalp (Figure 2.8). The electrical activity comprises the postsynaptic potentials generated by large populations of similarly oriented active cortical pyramidal neurons close to the scalp electrode.

The conventional EEG measurement setup includes Ag/AgCl electrodes, whose positioning typically follows the 10-20 international system (Figure 2.9), which guarantees uniform and consistent monitoring of different brain regions. Each electrode is labeled with a letter (anatomical position: frontal (F), temporal (T), central (C), parietal (P), and occipital (O)) and a number (odd and even numbers for left and right hemisphere, respectively). EEG measures potential differences and can be monopolar (difference with common ground) or bipolar (difference between proximity electrodes). Typically, a reduced set of electrodes is used when measuring the EEG of newborns; generally a set of eight electrodes including Fp1, Fp2, C3, C4, T3, T4, O1, O2, and Cz. This is dictated by the necessity to reduce skin injuries and avoid the discomfort for the patient, as well as by the limited area due to the small head size.

At the end of the 1960s, the cerebral function monitor (CFM) was introduced with the aim of quickly scanning the brain function of adults at the intensive care unit (ICU) [253]. The CFM is also used in the NICU, and the version of

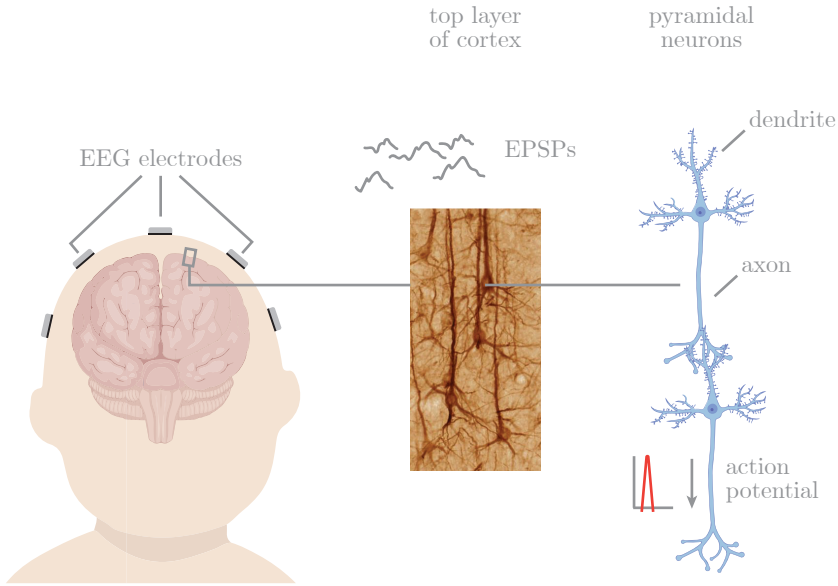


Figure 2.8: EEG provides a noninvasive measurement of the electrical activity of the cerebral cortex via electrodes attached to the scalp. The electrical activity comprises the postsynaptic potentials generated by large populations of similarly oriented active cortical pyramidal neurons close to the scalp electrode. Picture taken from [1].

EEG generated by the CFM is generally referred to as amplitude integrated EEG (aEEG). The aEEG is a highly processed form of conventional EEG, obtained after bandpass filtering from 2 to 15 Hz, a semi-logarithmic compression, rectification, smoothing, and time-compression. The aEEG has some advantages over conventional EEG: it needs fewer electrodes (only two to four) and is easier to interpret (less training required). Typically, the central electrodes (C3 and C4) and/or the parietal electrodes (P3 and P4) are used. An important disadvantage is the limited spatial coverage of aEEG, which increases the risk of missing important information [162, 161].

**Morphology** Not only the brain, but also the EEG of the newborn, especially the preterm newborn, is drastically different compared to that of an older child or adult. The appearance of the preterm EEG changes in parallel with the

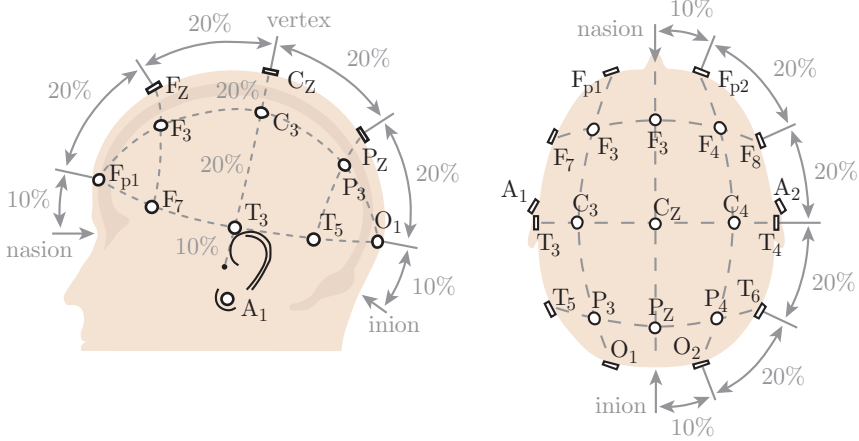


Figure 2.9: The international 10-20 montage of EEG guarantees uniform and consistent monitoring of different brain regions. The 10-20 refers to the distance between neighboring electrodes which equals 10% or 20% of the total distance from the nasion to the inion, which are respectively the suture that joins the nasal bone with the frontal bones and the occipital protuberance at the back of the skull.

physiological maturation of the CNS [232]. Changes in background continuity, interhemispheric synchrony, the appearance of specific waveforms and the organization of behavioural states can be observed [17, 427].

The *background pattern* gradually changes from a discontinuous pattern, which consists of bursts of high activity that alternate with periods of electrographic quiescence, towards a continuous trace with a relatively steady amplitude [243]. The length of the suppressed EEG segments can range from 60 seconds in the very young infant to less than 10 seconds in neonates at 36 weeks PMA [301]. The interburst intervals (IBI) grow in amplitude with increasing PMA, while the bursts decrease in amplitude, and increase in length and complexity [101].

The EEG *synchronization* at homologous regions of the two hemispheres, which provides information about the development of the corpus callosum and the formation of interhemispheric connections, changes from hypersynchrony until 30 weeks PMA over interhemispheric asynchrony to a synchronous signal after 36 weeks PMA [17, 301, 243].

*Specific waveforms* include delta brushes ( $\delta$ : 0.3–1.5 Hz) [440], temporal

sawtooth waves ( $\theta$  : 4–6 Hz) [232], frontal sharp transients ( $\delta$ : 1–3 Hz) [301] and anterior slow dysrhythmia, which all manifest at defined PMA, and can therefore be used to study maturation. A detailed discussion on EEG frequency bands is presented in Section 2.2.4. For a detailed discussion on these waveforms, we refer the reader to [17].

Differentiation of *sleep staging* is well established at around 30 weeks PMA [102, 70]. In preterm infants, only two main sleep stages, active sleep (or rapid eye movement (REM)) and quiet sleep (or non REM sleep (NREM)), and wakefulness can be distinguished [102, 232]. Around 36 weeks PMA, a more complex sleep state organization consisting of four sleep stages and wakefulness is established [102, 197, 232]. During maturation, the percentage of time spent asleep gradually decreases and is around 70% at term equivalent age [32].

**EEG in the NICU** While monitoring of physiological parameters such as the electrocardiogram (ECG), heart rate, blood pressure, oxygen saturation and temperature have long since be integrated into neonatal intensive care, continuous EEG monitoring to evaluate brain function is less common [404]. Interest in the neonatal brain has increased considerably during the last decades. This is in part due to better diagnostic methods in the acute and subacute stage. Similar to continuous monitoring of vital signs, bedside aEEG can help guide decision-making in real time for infants admitted to the NICU [395].

In neonatal intensive care, continuous registration of the EEG or aEEG is the gold standard in the assessment of background activity, the diagnosis of (subclinical) seizure activity, and the evaluation of sleep-wake cycling [70, 162, 161]. Monitoring of the EEG background continuity is an essential indicator to assess if the maturity of the infants is appropriate for a given gestational age (GA), and allows to detect dysmaturity [101]. The background continuity and depression can also be used to detect acute brain insults, such as periventricular hemorrhage (PVH) and periventricular leukomalacia (PVL) (Section 2.4), although acidosis, apneas and drugs can also play a role in EEG suppression. The EEG can provide real-time information of cerebral dysfunction, especially in case of lesions or systemic diseases [301]. Different sleep stages change the structure and appearance of the EEG. Therefore, the EEG can be used to do manual (expert) and automatic sleep staging in neonates [320, 95, 21].

## 2.2.4 Matching NIRS and EEG

Biomedical signals arise from a variety of sources, including movement, breathing, electrical activity of neurons (EEG) and optical absorption of light (NIRS),

among others [76]. Due to the different sources, biomedical time series are typically associated with different time scales of operation. An EEG signal changes rapidly due to the (de)synchronization of numerous neurons, while  $rScO_2$  changes very slowly: the hemodynamic effects that it captures work on a slow time scale. When one wants to compute the interaction between these signals (Section 3.4), it is important to define on which time scale the signals are interacting, and the signals have to be matched correspondingly. The brain-heart interaction takes place at a long time scale (low frequency activity), since  $rScO_2$  reflects the cardiovascular oscillations which develop in a timeframe of seconds. The speed of fluctuations of  $rScO_2$  is much lower compared to EEG oscillations, although  $rScO_2$  can contain faster frequency components, caused by cardiac pulsations. These faster frequency components are however not considered in this thesis.

In our analysis, matching the signal time scales corresponds to mapping the rapidly changing EEG with the much slower dynamics of the systemic signals, including HR, mean arterial blood pressure (MABP), arterial oxygen saturation ( $SpO_2$ ), and  $rScO_2$ . Figure 2.10 illustrates the difference in dynamics: the systemic signals have most of their power (Section 3.3.2) below 0.2 Hz (changes happen on a time scale of 5 seconds or longer), while most of the EEG power is contained within the frequency band from 0 to 4 Hz.

Multiple approaches exist to carry out the synchronization of the time scales. All of these approaches have one thing in common: we compress the EEG to a feature derived from it. Broadly three categories can be distinguished: methods based on the *continuity* of the EEG, methods based on the *spectral power* of the EEG, and methods based on *compression* of the EEG.

**Continuity** The EEG signals of premature neonates alternate between periods of high activity (bursts, or burst intervals) and periods of suppressed activity (interburst intervals), making its morphology discontinuous (Figure 2.11). This background pattern gradually changes to a continuous trace with relatively steady amplitude with increasing postmenstrual age (PMA), as mentioned before. The discontinuous morphology can be exploited in order to obtain surrogates for EEG activity in a similar time frame as the hemodynamic signals. First, the EEG needs to be segmented in burst and interburst intervals. This can be done manually, although this is an expensive, time-consuming procedure that requires input from an (multiple) expert(s). Alternatively, the EEG segmentation can be done in a fully automated way, using one of the algorithms that were developed for this purpose in the last few years [210, 292, 282]. Once the segmentation is available, various features can be defined in a sliding window to quantify the amplitude (power) and the duration (percentage of time) of the burst and

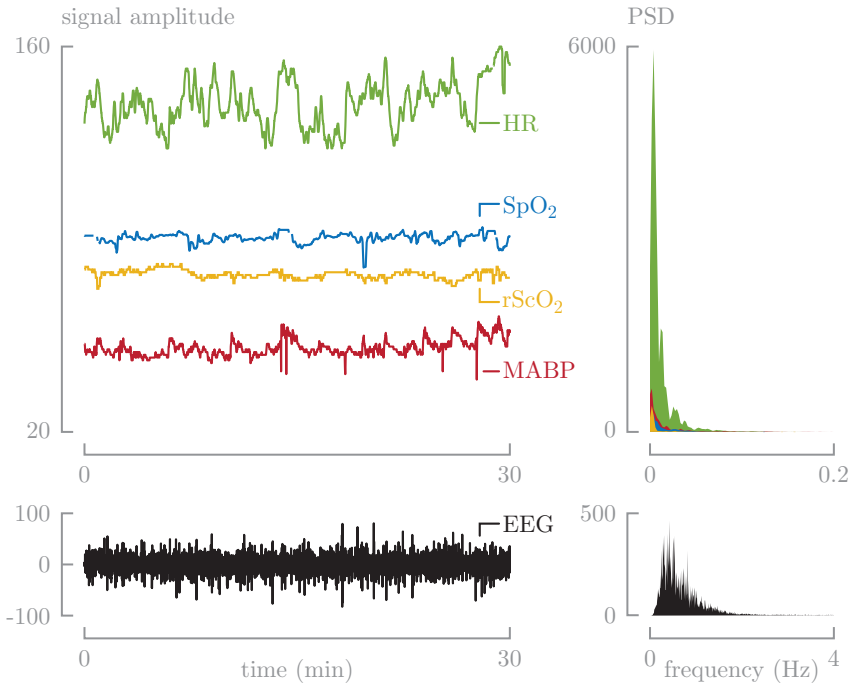


Figure 2.10: Biomedical time series are associated with different time scales of operation. The left panel depicts five signal modalities, HR (bpm), SpO<sub>2</sub> (%), rScO<sub>2</sub> (%), MABP (mmHg), and EEG ( $\mu$ V), in the time domain. The right panel shows the corresponding power spectral densities (PSD).

interburst intervals.

**Spectral content** One of the concepts that is frequently used to synchronize the EEG with the other time series is the notion of frequency, which gives an indication about the dynamics of a signal. Formally, the frequency content can be quantified using the power spectral density (PSD) or via a time-frequency representation. A formal definition of the PSD and various estimators is presented in Section 3.3.2. The extraction of the oscillatory components is not only useful to reduce the complexity of the system, but can also be used to describe the underlying physiology.

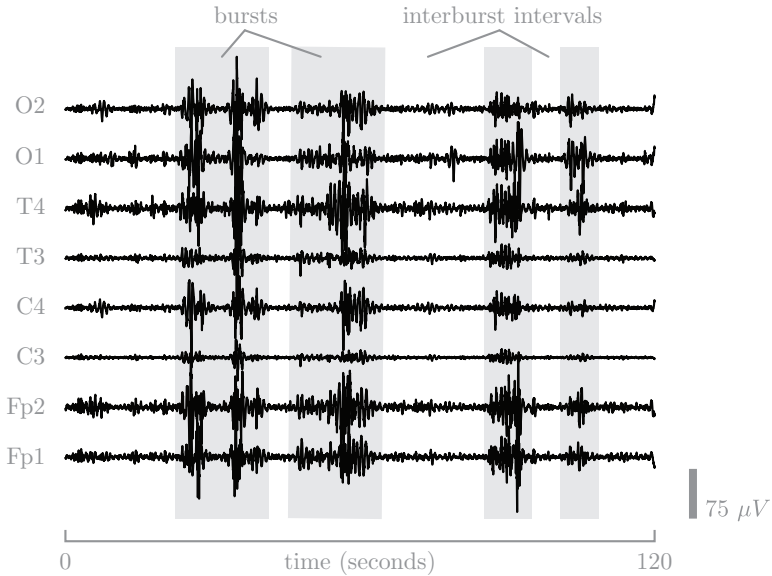


Figure 2.11: The EEG of premature neonates alternates between periods of high activity (bursts, or burst intervals, in gray) and periods of suppressed activity (interburst intervals), making its morphology discontinuous.

In practice, the EEG is often subdivided and analyzed in different frequency bands: the delta ( $\delta$ : 0.5–4 Hz), theta ( $\theta$ : 4–8 Hz), alpha ( $\alpha$ : 8–12 Hz), and beta ( $\beta$ : 12–30 Hz) frequency band (Figure 2.12). The delta band can be further divided into slow delta ( $\delta_1$ : 0.5–2 Hz) and fast delta ( $\delta_2$ : 2–4 Hz) [117]. In practice, delta oscillations are often of interest. According to Knyazev, delta oscillations belong to the *old brain*, which phylogenetically traces back to lizards [208]. During the development, the scalp electrical activity tends to be discontinuous and is centered around a frequency between 1 and 2 Hz, which defines the periodicity of the bursts in the cortical trace [17]. Delta oscillations regulate basic homeostatic needs, such as the blood flow circulation and normotension enforcement [243]. The slow-wave EEG is considered as the expression of the regulation of the brainstem (which is in charge of cerebral hemodynamics) or, at least, as a projection of the subcortical activity to the cortical areas.

Since the EEG is a non-stationary time series, a time-frequency analysis is typically preferred to describe the oscillations of the signal. In such an analysis,

the PSD is usually estimated in non-overlapping windows or with time-frequency approaches, such as the quadratic smoothed pseudo Wigner-Ville distribution [275, 234] and the continuous wavelet transform (CWT) [202, 121, 67] (Section 3.3.2). Once we have our time frequency representation of choice, two options exist to compress the power in a certain frequency band (Figure 2.12). The first method involves summing over the wavelet transform in predefined frequency intervals for each point in time (blue line in Figure 2.12). The second method is to instead follow the peak in the power spectrum for the given frequency interval in time (orange line in Figure 2.12), which is known as *ridge extraction* [97].

**Compression** A final method to match the EEG with the systemic signals and rScO<sub>2</sub> is by using the aEEG. This can be done in two ways. The first possibility is to take the aEEG directly from the CFM monitor, if available. The second possibility is to simulate aEEG from conventional EEG, by manually implementing a cascade of bandpass filtering (2–15 Hz), a semi-logarithmic compression, a rectification, a smoothing, and a time-compression step. The main difficulty of this approach is that none of the commercially available aEEG compression algorithms are published in literature. Therefore, it is hard to design a processing pipeline that outputs exactly the same result as the CFM monitor itself.

## 2.3 Regulation of cerebral blood flow

In the average adult human, the brain represents about 2% of the body weight. Remarkably, despite its relatively small size, the brain accounts for about 20% of the oxygen and, hence, calories consumed by the body [369]. Oxygen is needed to produce energy through the oxidative metabolism of glucose. This high rate of metabolism is remarkably constant despite widely varying mental and motoric activity [331]. Of this, it is estimated that neurons consume 75% to 80% of energy produced in the brain [175]. This energy is primarily utilized at the synapse with a large proportion spent in restoration of neuronal membrane potentials following depolarization [155]. Despite its great need for energy, the brain only has a very limited capacity to store oxygen, unlike many other organs of the human body. CBF thus needs to be sufficiently large, in order to avoid hypoxia (Section 2.4) (Figure 2.13) [336]. On the other hand, the vascular bed of the neonatal brain is still immature and sensitive to large changes in cerebral blood flow. Therefore, CBF can not be too high, otherwise it can rupture the fragile vascular bed [336]. It is clear that a tight temporal and regional control of CBF is of vital importance. The control of CBF is however highly

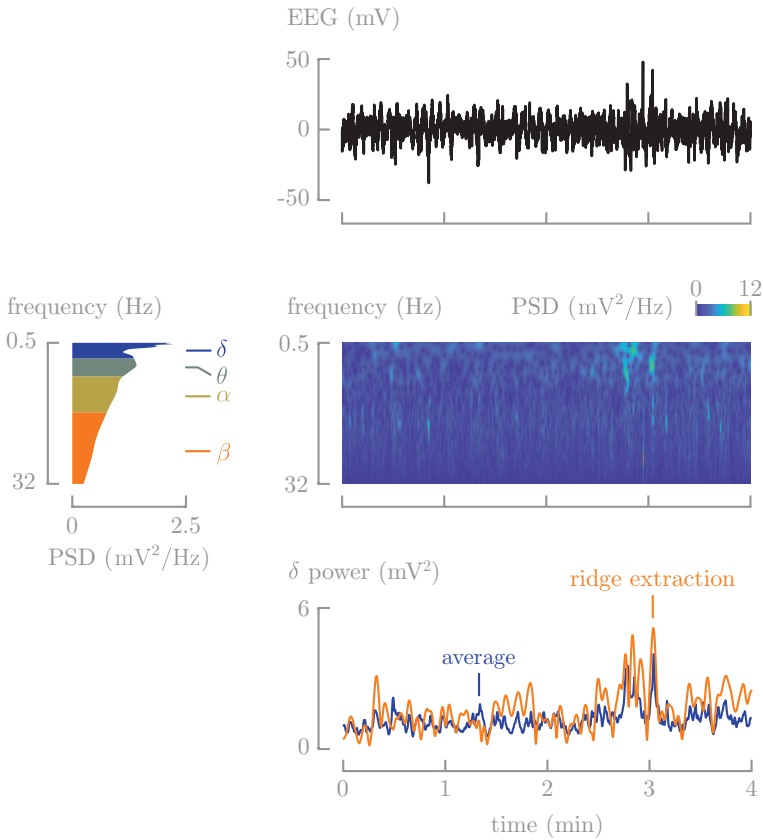


Figure 2.12: A four min long EEG segment (top) is translated into a two-dimensional time-frequency plot (middle right) using the CWT, which is further processed to obtain a time-average estimate of the PSD (middle left) and to obtain an estimate of the power in the  $\delta$  frequency band in time (bottom).

Table 2.1: Overview of brain monitoring techniques generally used in the NICU: cranial ultrasound (cUS), magnetic resonance imaging (MRI), transcranial Doppler ultrasound (TCD), functional MRI (fMRI), electroencephalography (EEG), and near-infrared spectroscopy (NIRS).

	structural			functional		
type	cUS	MRI	TCD	fMRI	EEG	NIRS
measurement	image	image	image	image	signal	signal
what	tissue	tissue	blood flow velocity	blood flow	electrical activity	venous oxygenation
area	entire brain	entire brain	entire brain	entire brain	surface of cortex	surface of cortex
resolution						
spatial (mm)	5	1-2	5	3	8 channels	1 channel
temporal (s)	0.01-0.02	0.1	0.01-0.02	1-2	0.004	1
instrument						
invasive	no	no	no	no	no	no
size	small	large	small	large	small	small
transport	yes	no	yes	no	yes	yes
cost	low	high	low	high	low	low

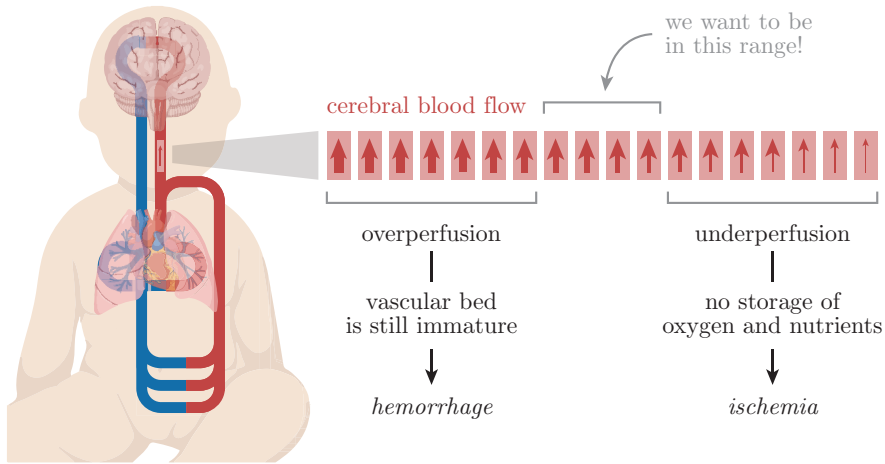


Figure 2.13: Cerebral blood flow is tightly regulated. Overperfusion (too much flowing through vascular bed) might lead to hemorrhage, while underperfusion (too little blood flowing to brain) might lead to ischemic damage.

complex, and only beginning to be elucidated. Recent studies have defined numerous key regulatory mechanisms, including but not limited to cerebral pressure autoregulation, neurovascular coupling, and baroreflex.

### 2.3.1 Cerebral autoregulation

In clinical practice, the relation between CBF, cerebral perfusion pressure (CPP), and cerebrovascular resistance (CVR) can be described using an analogy of Ohm's law as:

$$\text{CBF} = \frac{\text{CPP}}{\text{CVR}} = \frac{\text{MABP} - \text{ICP}}{\text{CVR}} \quad (2.9)$$

where CPP is defined as the difference between MABP and the intracranial pressure (ICP), which is mostly stable in neonates due to open cranial sutures and large fontanelles [399]. From Equation 2.9, it is clear that, in general, CBF is proportional to MABP. The human brain is however capable of keeping CBF more or less constant for changing perfusion pressures by changing cerebral vasoreactivity (CVR) during fluctuations in arterial blood pressure. The arterioles of the cerebral vascular bed constrict when pressure increases, and dilate when pressure drops. This phenomenon is generally referred to as cerebral

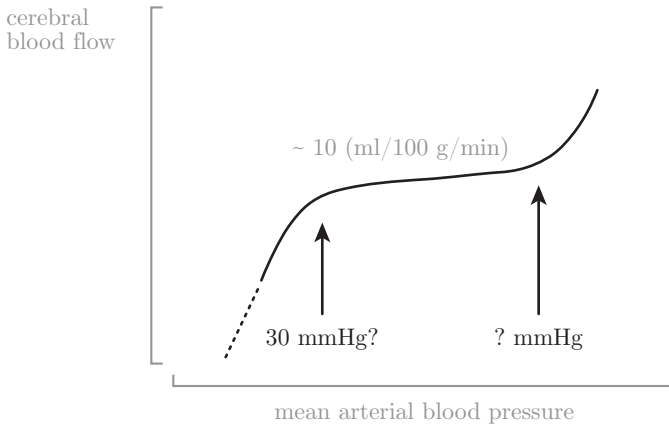


Figure 2.14: Schematic drawing of the relation between cerebral blood flow (CBF) and mean arterial blood pressure (MABP) in the preterm newborn during normal cerebral circulation. The flat portion (slope near zero) represents the autoregulatory plateau. Below the lower threshold, blood flow falls more than in proportion to pressure. The lower threshold is estimated at 30 mmHg or less. There are no good estimates of the upper threshold. Adapted from [148].

pressure autoregulation (CAR) or autoregulatory capacity [336]. The classic depiction of this regulation mechanism is a curve with stable CBF over a range of normal blood pressures and unstable CBF when the blood pressure falls outside of this range (Figure 2.14) [422]. Due to the multivariate and nonlinear nature of the underlying mechanisms involved in the regulation of CBF, the physiological pathways responsible for CAR are not yet fully understood [297, 250].

The introduction of TCD improved the time resolution of CBF measurements, which allowed to study the transient relations between changes in MABP and CBF using dynamical models (correlation, coherence, transfer function analysis) [238, 4]. Measurement of TCD are however highly affected by motion artifacts, which hinders their applicability in clinical practice [42]. NIRS presents an alternative for monitoring continuous tissue oxygenation [450, 410, 60]. Although NIRS does not measure CBF directly, several studies have shown that NIRS measurements are related to changes in CBF under constant cerebral oxygen consumption and constant arterial oxygen saturation [450].

Despite a large body of research in the last decades, CAR assessment is

currently not yet used in clinical practice as an online monitoring parameter. The main difficulties include a lack of a robust preprocessing algorithm, a lack of a gold standard and lack of standardization of the algorithms used in CA assessment [423].

### 2.3.2 Neurovascular coupling

Neurovascular coupling (NVC) refers to the regulation mechanism that links transient neural activity to the subsequent change in CBF. The first reports on this regulation mechanism date from more than 100 years ago [105]. NVC can be described on a macroscopic and a microscopic level. At the macroscopic level, the extremely high vascularization and tight regulation of CBF provides the brain with an adequate blood flow for a given metabolic demand. There is a close temporal and regional link between neuronal activity and CBF: brain regions with high activity receive an increased amount of blood flow.

At the microscopic level, the neurovascular unit is comprised of the vascular smooth muscle, the neuron and the astrocyte glial cell (Figure 2.15). Glutamate is released upon neuronal activation, which causes neurons and astrocytes to transmit signals in order to regulate CBF. Although it was assumed for a long time that these signals were only associated with a vasodilatory effect, recent studies show a more complex balance of vasodilation and vasoconstriction, in which both chemical and mechanical effects play an important role. Known chemical signals include prostaglandins, nitric oxide and adenosine, secreted by both neurons and astrocytes, which cause vasodilation of the smooth muscle cell. Astrocytes also secrete other vasodilators like potassium and epoxyeicosatrienoic acids and arachidonic acid, which is a vasoconstrictor. All these mediators have a direct impact on the smooth muscle of the arterioles and therefore control CBF in a direct way. In addition to these mechanisms present in the neurovascular unit, a second mechanism was recently described by which also pericytes around the capillaries cause vasodilation [172, 310].

**Spatiotemporal studies** In spatiotemporal studies, a standardized motor, visual, auditory, or cognitive task is given while the flow and/or activity in the brain is measured simultaneously [172]. The most widely used stimulus in adults is finger tapping, which is known to cause an increase in blood flow at the contralateral motor cortex [103]. In (preterm) neonates, spatiotemporal studies are inherently more difficult to perform. The majority of the spatiotemporal studies in neonates makes use of visual stimuli, which includes the projection of checkerboard patterns on LCD displays [231, 256], or flashing LEDs [193].

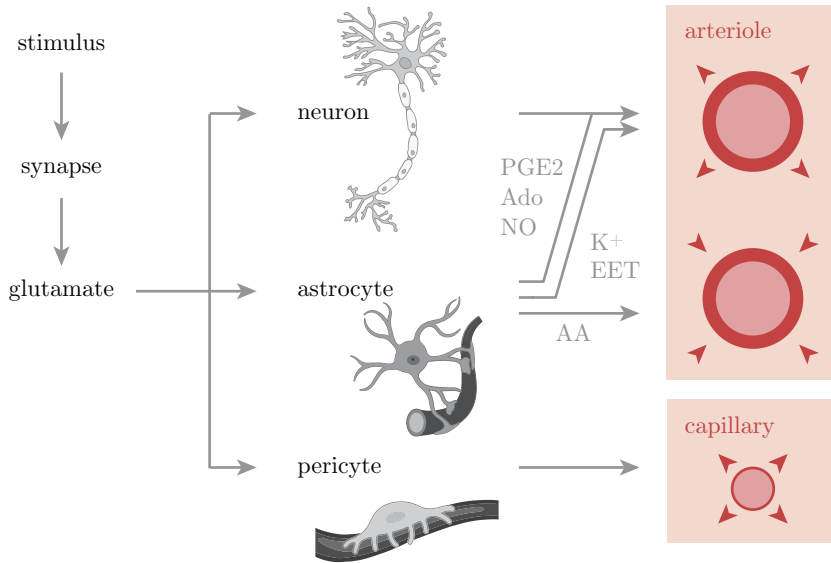


Figure 2.15: At the microscopic level, neurovascular coupling consists of neurons, astrocytes and pericytes that secrete various chemical signals causing vasodilation and vasoconstriction of arterioles and capillaries, which directly affects cerebral blood flow. The depicted chemical signals include prostaglandins (PGE2), nitric oxide (NO), adenosine (Ado), potassium ( $K^+$ ), epoxyeicosatrienoic acids (EET), and arachidonic acid (AA).

Less frequently used stimuli in preterm neonates include auditory [346, 462] and somatosensory stimuli [23, 22, 116].

The classical response to the stimulus described in adults is a sudden increase in CBF and cerebral oxygenation with a secondary, less pronounced decrease [159]. This type of response is typically called *functional hyperemia* [166], and is generally referred to as a *positive* response (Figure 2.16). A *negative* response occurs when the increase in blood flow to the brain is insufficient to meet the metabolic demand [166]. Since functional hyperemia is observed in hyperoxic, hypoglycemic and hyperglycemic states, it is clear that CBF increases are not simply triggered by local sensing of depleted nutrients [235, 324, 446]. The relative delay in the peak of increased blood flow indicates that neurons do not rely upon functional hyperemia to meet their initial needs for increased oxygen and glucose, since neuronal firing may have ended prior to measurable changes

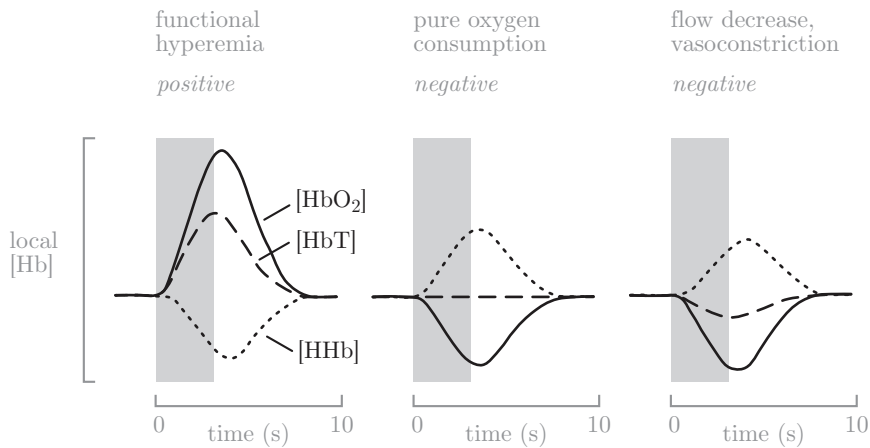


Figure 2.16: Left: functional hyperemia, characterized by an increase in  $[HbT]$  and  $[HbO_2]$ , and a decrease in  $[HHb]$  following the wash-in of oxygenated blood (positive response). Middle: only oxygen consumption in absence of functional hyperemia (negative response). Right: vasoconstriction or decrease in capillary volume (negative response). Adapted from [166].

in CBF [166].

Recent studies suggest that neurovascular coupling in neonates and preterm born infants can differ compared to adults, since many of the components involved in actuating and propagating the hemodynamic response are still in development, including perivascular cells such as astrocytes and pericytes [214]. Neural and vascular networks develop, expand and are then selectively pruned over the first year of life. In addition, the metabolic demands of the newborn brain are still evolving and are vastly different compared to the adult brain. Brain oxygenation increases during the first days of life, while cerebral oxygen extraction decreases [54]. In extremely preterm infants, there is no correlation between CBF and spontaneous changes in the cerebral metabolic rate of oxygen during the first 2 days after birth [201, 449]. Instead, changes in cerebral oxygen extraction rather than CBF meet changes in oxygen requirements arising from variations of the cerebral metabolic rate of oxygen. The vast differences in both neural and vascular network structure, as well as substantially different metabolic needs of the preterm brain are highly likely to affect early postnatal neurovascular coupling.

Using fMRI, numerous authors found a negative response in preterm infants

after stimulation [453, 160, 116, 48]. In addition, a systematic maturational trend in terms of a decreasing time-to-peak and an increasing positive peak amplitude were observed [22]. These findings suggest that in young infants the increase in cerebral oxygen consumption may be relatively greater than the corresponding increase in CBF during functional activation. The age-dependency of the neurovascular coupling was also confirmed in a rodent model, suggesting that the brain may be experiencing differences in energy supply and demand dynamics compared to the adult brain in the developmental period [213, 214].

Using fNIRS, the results and conclusions of the different studies are not unambiguous. Some authors described a normal hyperemic signal [231], some described an increase in brain deoxygenation [256], while others emphasized inter-patient differences [421]. In addition to the uncertainty regarding the sign of the hemodynamic response (positive versus negative) in neonates, more questions arise when we focus on specific pathologic conditions like bronchopulmonary dysplasia, congenital heart disease and pulmonary hypertension, where a lower oxygen saturation is present [345]. Furthermore, the effect of anesthetic and sedative drugs, which are frequently used in fMRI studies, needs to be investigated [123]. From a broader perspective, also the effect of other drugs, such as anti-epileptic drugs on NVC in neonates is not properly defined to date [356].

Studies both in animals and neonates do confirm the presence of a short hypoxic period after a stimulus in the brain of preterm infants [277, 214, 326], which is hypothesized to result in new angiogenesis and neurogenesis in the brain [215]. This hypothesis could explain the mechanisms of the positive effect of sensitive stimulation and the negative effect of overstimulation in newborns [214].

Despite the fact that the fMRI and fNIRS studies listed above aim to investigate neurovascular coupling, they actually only describe the hemodynamic changes observed in the brain after applying a stimulus. Precise studies on neurovascular coupling are based on concomitant measurements of brain hemodynamics and brain activity. This can be done by combining EEG measurements with fMRI measurements [273], with fNIRS measurements [365, 371] or with positron emission tomography (PET) measurements [189], although such studies are challenging from a technical point of view due to for example electrode heating [419] and the presence of numerous artifacts [130, 5]. Therefore, such studies are very scarce, especially in (preterm) neonates.

**General studies** Another approach is to assess NVC in *resting-state* conditions. The clinical goal is to develop a continuous measure for NVC which can be used in bedside monitoring, without explicitly evoking a potential as in spatiotemporal

studies. Naturally, EEG is the most common non-invasive method to assess the electrical activity of the brain, although it only measures cortical activity. NIRS or TCD can be used to measure CBF at the bedside in a non-invasive way; both are safe, cheap and easy to use, but TCD has the disadvantage of being investigator dependent. Therefore, general studies are usually based on EEG and NIRS recordings. Coupling can be defined using functional methods that take into account only the statistical correlations among time series, or effective methods that consider the directionality of the coupling as well (Section 3.4) [304, 126]. Although these studies investigate the interaction, they do not assess the concise nature of this interaction. The main difficulty to tackle in studies on multimodal integration is the fact that the different time series operate on different time scale, while simultaneously interacting with each other with a certain linear or nonlinear degree.

Using NIRS, a decrease in oxygenation was observed during bursts of EEG activity, followed by an important overflow (increase in cerebral oxygenation), suggesting a neurovascular signal that differs from the pattern commonly observed in adults [342]. During these bursts, increases in HR were also observed in another study [309]. This positive variation of HR was found to disappear over age with the emergence of a continuous EEG trace. An increase in oxygen extraction was found during increased electro-cerebral activity in preterm infants [396]. Significant differences were observed in presence of IVH: the cerebral vascular network was found to be unable to compensate for an increased metabolism resulting from neuronal activation when brain injury was present [246].

### 2.3.3 Other aspects of regulation

**Baroreflex** The baroreceptor reflex (short: baroreflex) is the most important regulatory mechanism in the short term control of heart rate and blood pressure [19]. This reflex minimizes any variation in blood pressure by responses of both heart rate and arterial vascular tone [146]. For example, an increase in blood pressure will be buffered by a decrease in both heart rate and peripheral vascular resistance. These responses of heart rate and vascular resistance are mediated by the parasympathetic and sympathetic system [146]. In practice, baroreflex sensitivity (BRS) is studied, which measures how much control the baroreflex has on the heart rate. Since vascular resistance is difficult to measure, BRS is typically assessed using the coupling of heart rate (RR intervals defined from ECG measurements) and blood pressure [19].

BR is present and functional from early fetal life [366, 454] and undergoes significant maturation *in utero* [366, 456]. After birth, control of blood pressure

undergoes further significant maturation as blood pressure declines over the first 3 months of infancy, then increases at 6 months of age [458, 456, 146]. Preterm birth appears to alter the normal maturational pattern, as hypotension is common in extremely preterm infants [128, 443]. Very low BRS values in very preterm infants might have clinical importance because a BR system is essential in the short term regulation of BP, and thus in avoiding hypotensive or hypertensive episodes [19].

The classical method of investigating BRS is based on the analysis of the changes in blood pressure and heart rate that are experimentally induced in a controlled fashion by either pharmacological or mechanical means [146]. These methods consider the slope of the (sigmoid-shaped) BP-RR interval relationship after administration of adrenaline (pressor response) or sodium nitroprusside (depressor response) [377, 211, 127]. These methods are not physiological, cannot be repeated many times over a short period, and are of limited use in neonates for medical ethical reasons [19]. BRS can also be assessed by explicitly computing the coupling between BP and RR time series. For this purpose, various techniques are available. Time domain methods generally consider the analysis the correlation [146, 457, 456, 464, 37]. Frequency domain methods are also used to assess BRS. They consider coherence, transfer function gain and phase, mainly in the low frequency range [96, 158, 168, 340, 18, 456, 147, 128].

**Heart rate passivity** Different variables can be sampled in cerebral and cardiovascular hemodynamics to assess cerebrovascular reactivity and autoregulation. Relying on blood pressure measurements alone to make informed clinical decisions ignores the complex circulatory control mechanisms that exist to optimize oxygen delivery to vital organs. Heart rate passivity (HRP) was recently defined using the interaction between HR and rScO<sub>2</sub> (measured using NIRS) as an additional index for cerebrovascular reactivity [262]. When rScO<sub>2</sub> remained independent of heart rate changes, a *weak* HRP, the preterm infants were observed to have a significantly better outcome.

### 2.3.4 Integrating CBF regulation using graphs

Let's say we want to study the various regulation mechanisms discussed above at the same time, in one model. We have CAR (coupling between MABP and rScO<sub>2</sub>), NVC (coupling between EEG and rScO<sub>2</sub>), baroreflex (coupling between HR and MABP), and HRP (coupling between HR and rScO<sub>2</sub>), which we all want to study in the same model. As one can easily see, to assess these regulation mechanisms, various signals are common. Therefore, it is straightforward to integrate all regulations mechanisms using a graph (Figure 2.17). The resulting

graph is often referred to as a *signal interaction graph*, in which the signals are on the nodes. The links between any pair of nodes depict the coupling between the corresponding signals. Following the specific choice of signals in our analysis (HR, MABP, SpO<sub>2</sub>, rScO<sub>2</sub>, and EEG), we refer to this model as the *neurocardiovascular graph*, as it presents the interaction between the brain and the cardiovascular system.

What to expect from the connectivity of this model? Since the neurocardiovascular graph captures regulation of CBF, some expectations regarding the magnitude and direction of coupling can be formulated (Figure 2.18). For the links corresponding to CAR and HRP, we expect a *weak*, non-significant coupling, as a large coupling would imply pathological conditions. Indeed, large coupling between MABP and rScO<sub>2</sub> implies impaired CAR and neonates with low HRP were observed to have a significantly better outcome. Directionality is expected from MABP and HR to rScO<sub>2</sub>, as both variables would contribute to changes in CBF. For the links corresponding to NVC and baroreflex, we expect a *large*, significant coupling, since both regulation mechanisms tightly link the corresponding signals. For NVC, directionality from EEG to rScO<sub>2</sub> is expected, as changes in brain activity trigger consequent changes in CBF.

The development and analysis of the neurocardiovascular graph is situated in the emerging field of *Network Physiology*, which aims to describe how the time series of multiple origins interact, either linearly or nonlinearly, at a specific scale, in a graph or lattice structure [35, 36].

## 2.4 Brain pathology

Among the most important brain pathologies, intraventricular hemorrhage (IVH) and periventricular leukomalacia (PVL) are of particular interest in this thesis, since their origin is related to fluctuations in the cerebral circulation.

### 2.4.1 Hypoxia

Hypoxia is a condition where the tissue is deprived of the necessary levels of oxygen. Hypoxic conditions can be counterbalanced physiologically by increasing CBF. If CBF is at its maximum, however, an increase in cerebral oxygen extraction (measured as an increase in FTOE), or a decrease in cerebral metabolism (measured as a decrease in EEG) might be observed in a secondary stage to neutralize the hypoxic conditions. Three classes of hypoxia are reported

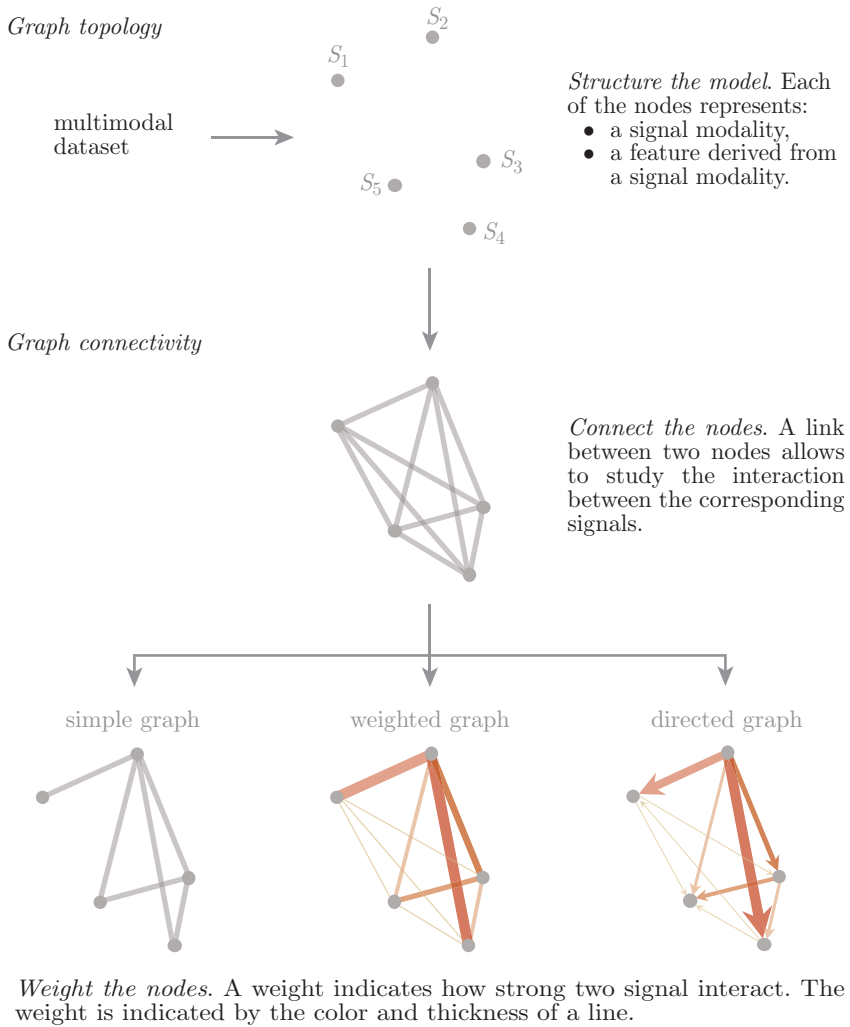


Figure 2.17: A multimodal dataset can be translated into various types of signal interaction graphs, including a simple graph (a link is present or not), a weighted graph (each link carries a certain weight) and a directed graph (each link carries a weight and has a direction).

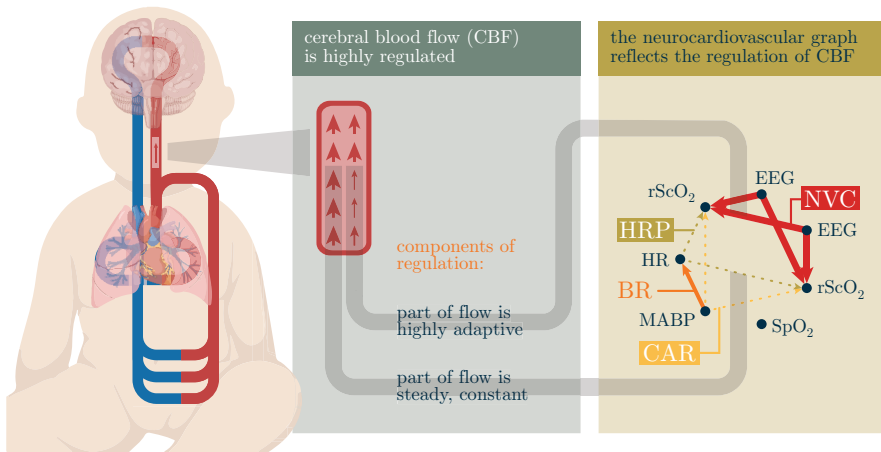


Figure 2.18: The neurocardiovascular graph allows to study various aspects of CBF regulation at the same time in one model. These regulation mechanisms include cerebral autoregulation (CAR), neurovascular coupling (NVC), heart rate passivity (HRP) and baroreflex (BR).

in literature: hypoxic hypoxia, anemic hypoxia and ischemic hypoxia (Figure 2.19).

Hypoxic hypoxia is caused by a reduction in arterial oxygen saturation, defined by a low amount of  $\text{HbO}_2$  with respect to  $\text{HbT}$ . Therefore, this condition can be monitored using  $\text{SpO}_2$ . A reduction in arterial oxygen saturation causes an unbalance in oxygen supply and demand in brain tissue. Therefore, the brain tries to compensate for this reduction in arterial oxygen saturation by increasing CBF [209, 187]. This can be done up to a certain upper limit, after which the brain is exposed to damage [138].

Anemic hypoxia is caused by a deficit in the concentration of hemoglobin, which is responsible for the transport of oxygen. As before, anemic hypoxia causes an unbalance in the oxygen supply and demand in brain tissue, which the brain will try to compensate for by increasing the CBF. When the upper limit is reached, the brain will again be exposed to damage [187, 165, 434].

Ischemic hypoxia is caused by a low CBF. In practice, CBF is regulated through numerous regulation mechanisms (Section 2.3). Impairment in each of these regulation mechanisms might cause ischemic hypoxia. To monitor ischemic hypoxia, one needs to measure CBF, which can be done using TCD, although the relation of Doppler indices in preterm infants with brain injury and outcome

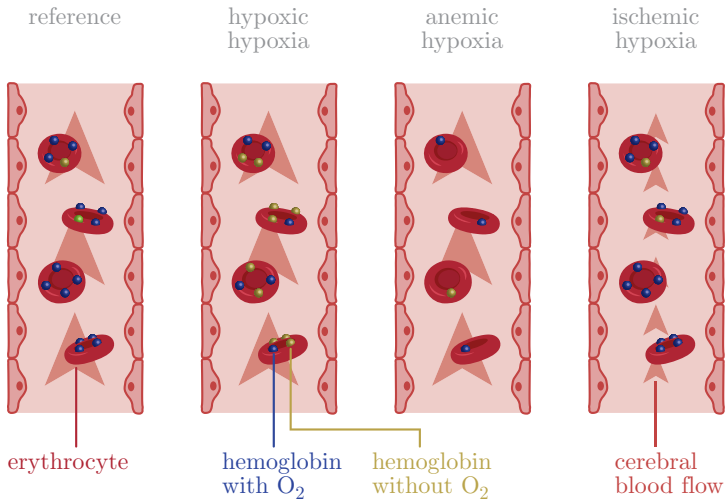


Figure 2.19: Three classes of hypoxia are reported in literature: hypoxic hypoxia, anemic hypoxia, and ischemic hypoxia. Red blood cells (erythrocytes) make up nearly half of the blood's volume (40 to 45 %). Every erythrocyte contains approximately 270 million hemoglobin molecules, which can bind oxygen ( $O_2$ ) [88].

remains controversial [65]. NIRS can be used to monitor oxygenation of cerebral tissue as an indirect measure of CBF (Section 2.2.2). In addition to both monitoring techniques, it is also possible to measure the status of the various regulation mechanisms. If the regulation mechanisms are properly functioning, it could potentially be assumed that CBF is within physiological limits.

## 2.4.2 Intraventricular hemorrhage

IVH is a major complication of prematurity and an important cause of brain injury in the newborn. Although the incidence has declined since the 1980s, IVH remains a significant problem, as improved survival of the extremely preterm infants has resulted in a greater number of survivors with this condition [194, 293]. Nowadays, the incidence of all grades of IVH in the extremely preterm population varies between 31 and 36% [45, 329, 386], while the incidence of severe IVH varies between 10 and 17% [45, 329, 391, 362, 386]. Approximately half of IVH occurs in the first 24 hours of life, and 80 to 90% within the first 72 hours of life [194].

IVH typically initiates in the periventricular germinal matrix, which is a richly vascularized collection of glial and neuronal precursor cells in the developing brain (Figure 2.20) [31]. IVH results from rupture of fragile capillaries in the germinal matrix [343]. When the hemorrhage in the germinal matrix is substantial, the ependyma, the lining of the ventricular system of the brain, breaks, which results in the cerebral ventricles filling up with blood. In neonatal care, the severity of IVH is typically graded from I to III with or without periventricular infarction, depending on its appearance on cUS (Figure 2.20) [218, 298, 428]. A severe IVH refers to grade III and any bleeding with periventricular infarction, both of which have a worse prognosis.

IVH has a detrimental effect on long-term neurodevelopmental outcome [227, 391], which is worse in case of severe IVH, but can not be neglected in mild IVH [269]. Numerous studies showed that severe IVH may lead to post-hemorrhagic ventricular dilatation, seizures, cerebral palsy, developmental delay, deafness, and blindness [194, 45]. In addition, neonates with severe IVH have increased mortality: around 20 % for grade III, and 90% for grade IV [45, 140].

Risk factors for the development of IVH include a low Apgar score, severe respiratory distress syndrome, hypoxia, hypercapnia [195, 154, 428]. Since IVH results from a rupture of fragile vessels in the germinal matrix, (large) fluctuations in cerebral blood flow are associated with the development of IVH [407, 306, 307]. In addition, factors influencing CBF like hypercarbia, hypotension, metabolic acidosis, and the use of inotropes have also been correlated with the development of IVH [86, 272, 411, 227, 306]. Analysis of CBF using NIRS has also shown that impaired cerebral autoregulation is highly correlated with the development of IVH [407, 306].

### 2.4.3 Periventricular leukomalacia

PVL is the most common ischemic injury in the cerebral white matter of a premature infant [430]. PVL is more common in premature infants than in term infants, with incidence rates of 39.6%, 27.4%, and 7.3% for infants born under 28, 32, and 37 weeks of gestation, respectively [344]. In Belgium, the overall incidence of PVL is estimated to be under 10%. This disease affects the immature white matter of the cerebral hemispheres and peaks at 24 to 32 gestational weeks and in those with a weight under 1500 grams [199].

PVL is caused by ischemic damage in the periventricular white matter adjacent to the external angles of the lateral ventricles [94, 367]. Morphologically, PVL is defined by two components (Figure 2.20): a *focal*, necrotic component in the periventricular white matter (*cysts*), and a *diffuse* component, characterized by reactive gliosis in the surrounding white matter [198] (Figure 2.20). PVL is

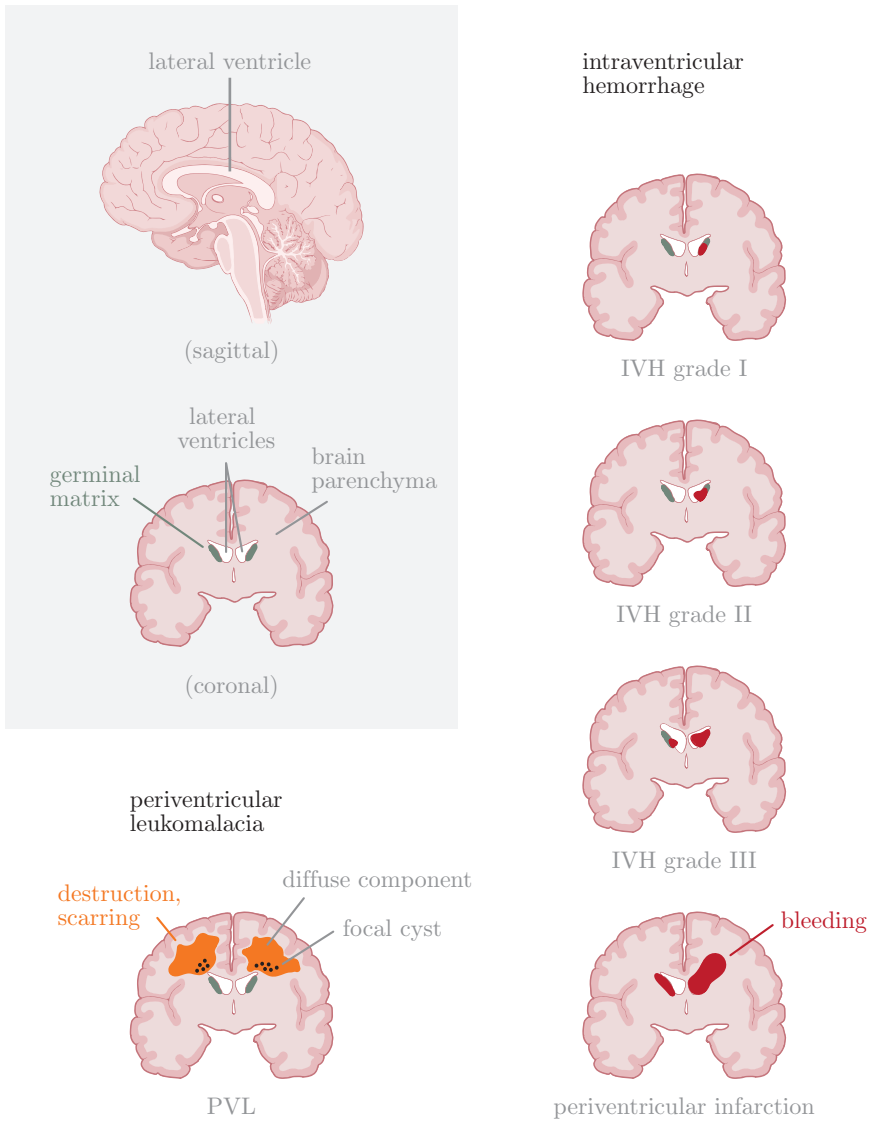


Figure 2.20: Bottom left: PVL is a brain injury characterized by damage to the white matter around the fluid-filled areas of the brain (ventricles). Right: IVH is a brain injury that includes a bleeding into the ventricles of the brain. The severity of the bleeding is graded from I to III, with or without periventricular infarction.

the leading cause of cerebral palsy, cognitive deficits, and visual disturbances in premature infants [100]. The traditional diagnostic hallmarks of PVL are periventricular echodensities or cysts detected by cUS. Using MRI, diffuse, non-cystic forms of PVL can also be detected [46].

In general, PVL results from inadequate brain perfusion. PVL developed in premature infants with extremely low blood flow to cerebral white matter, measured by means of PET [12]. Risk factors for the development of PVL include severe hypotension, marked hypocarbia, hypoplastic left heart syndrome, chorioamnionitis, patent ductus arteriosus with retrograde cerebral diastolic flow, and severe illness requiring extracorporeal membrane oxygenation (ECMO) [427].

## 2.5 Conclusion

Of all neonates, preterm neonates are particularly susceptible to brain injury as the brain undergoes rapid development during the last trimester of pregnancy. Inadequate or highly fluctuating cerebral perfusion and oxygenation can result in brain injury and can adversely affect brain development. Therefore, close monitoring of these vulnerable newborns, especially their brains, during the first weeks is of utmost importance. Early therapeutic intervention that supports and optimizes regulation of CBF might improve neurological outcomes. NIRS and EEG can be used to monitor cerebral oxygenation and the electrical activity of the brain, respectively. Physiological markers for various CBF regulation mechanisms can be obtained by integrating NIRS, EEG and systemic measurements in a pairwise fashion using coupling measures. The neurocardiovascular graph can be used to monitor various components of CBF regulation at the same time, in one visual model.

introduction

03

# Signal processing pipeline



This chapter provides an extensive overview of the mathematical background and computational tools used in this thesis. First, the general processing pipeline is introduced, since the processing pipeline shares numerous building blocks over the different studies presented in Chapter 5 onwards. Then, we'll have a look at the univariate (descriptive statistics, power spectral density, sample entropy), bivariate (pairwise coupling, surrogate data analysis) and multivariate tools (signal interaction graph, clustering), before finally arriving at the statistical analysis.

## 3.1 Data processing pipeline

One of the most common ways to obtain information about physiological systems is to study the features of the signal(s) recorded from them, using time series analysis techniques [131]. If one is only interested in the features of a single signal, a univariate analysis (Section 3.3) can perfectly carry out this task by itself. An increasing number of experiments are however being carried out in which several physiological signals are recorded simultaneously. In such a setting, the assessment of the interdependence between signals can give new insights into the functioning of the systems that produce them. Therefore, univariate analysis alone cannot accomplish such a task, as it is necessary to make use of a bivariate (Section 3.4) or a multivariate analysis (Section 3.5).

The data processing pipeline that is used in this thesis shares numerous building blocks over different studies. Figure 3.1 presents a schematic overview of the signal processing pipeline; the different blocks are discussed in the following sections.

## 3.2 Artifact removal

Biomedical signals are typically corrupted by different artifacts, due to the small amplitude of the measurements (scale of mV for ECG to  $\mu$ V for EEG). Artifact sources are related to physiological phenomena, electronic instrumentation, and environmental conditions. In general, artifacts can be divided into three distinct categories: missing values, out of range values, and motion artifacts [423]. The removal of the undesired disturbances in the signals is of utmost importance considering their impact on the remaining analysis [332]. In our analysis, long recordings are used, with a length ranging from hours to days (see Chapter 4). In such long recordings, numerous artifacts are typically present.

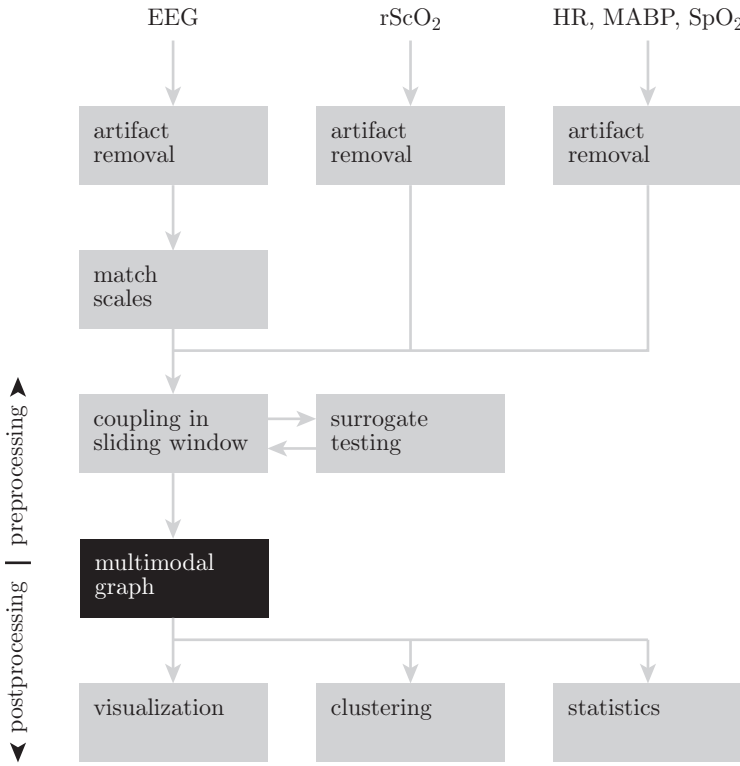


Figure 3.1: Schematic overview of the data processing pipeline used to compute the coupling between biomedical time series.

NIRS-derived  $rScO_2$  is mainly sensitive to motion artifacts, which typically present as rapid changes with respect to the overall slow dynamics of the  $rScO_2$  (Figure 2.10). Automated approaches to detect and correct for motion artifacts have been proposed, but typically require multiple channels [79] or the use accelerometers [368, 260]. These requirements hinder application of these algorithms in clinical practice. Univariate motion artifact detection methods do exist: these methods differentiate contaminated  $rScO_2$  segments from clean segments using features such as the moving standard deviation [351] or the wavelet transform [265].

Artifacts are omnipresent in neonatal EEG recordings, including but not limited to power line interference [17], electrode artifacts [223], artifacts resulting from

Table 3.1: Thresholds used to define the physiological range of the signals under analysis.

signal	unit	lower threshold	upper threshold
HR	(bpm)	0	500
MABP	(mmHg)	0	100
SpO <sub>2</sub>	(%)	0	100
rScO <sub>2</sub>	(%)	0	100
EEG	( $\mu$ V)	-	500

the use of high-frequency ventilators [223], and rocking or patting artifacts [243]. Physiological artifacts, such as muscular artifacts [70], ocular artifacts [17], cardiac artifacts [223], and respiratory artifacts, are typically also present in EEG recordings.

In the first step of the processing pipeline (Figure 3.1), artifacts are detected and removed. Note that we don't correct artifacts; we merely remove contaminated segments from the analysis. For this, we used two strategies. First, physiological boundaries were defined for each signal under study (Table 3.1). If the signal moved outside of these physiological boundaries, the corresponding signal segments were discarded. Second, motion artifacts were detected using the moving standard deviation in short windows. The moving standard deviation presents a straightforward method to detect if the signal changes more quickly than expected, which is often due to a motion artifact.

We defined an additional signal quality indicator for the EEG using the impedance signal, wherever available (propofol dataset, see Chapter 4). If the impedance exceeded 10 k $\Omega$ , the corresponding EEG data was removed, as such high impedance values indicate that the EEG electrodes haven't got good contact with the head. Therefore, the resulting EEG values can not be trusted. In addition, peaks were also located in the impedance signal, which were hypothesized to correspond to motion artifacts. These segments were also discarded from further analysis.

### 3.3 Univariate analysis

Throughout this text, a signal is denoted as  $x(k)$ , where we leave out the explicit temporal dependency ( $k$ ) when it is clear from the context. In the text, for example, we will mostly refer to a signal  $x$  instead of signal  $x(k)$ . A vector is denoted in lowercase and bold ( $\mathbf{x}$ ), while a matrix is denoted using capital

letters ( $X$ ). The size of a matrix is explicitly defined (rows  $\times$  columns), unless it is clear from the context. Signal length, sample size, and dataset sizes are denoted using lowercase  $n$ , while the size of a cohort of neonates is denoted using capital  $N$ .

### 3.3.1 Descriptive statistics

Descriptive statistics describe the distribution of a single variable including its central tendency (mean, median) and dispersion (standard deviation, variance, range, quartiles). Throughout this text, the mean and standard deviation are used to describe variables that are (approximately) normally distributed. The median and interquartile range (IQR) are used when the normality assumption doesn't hold, for example when the sample size is small.

The mean  $\bar{x}$  and variance  $s_x^2$  (square of the standard deviation  $s_x$ ) of a signal  $x(k)$ , with  $k = 1, \dots, n$ , are defined respectively as:

$$\bar{x} = \frac{1}{n} \sum_{k=1}^n x(k), \quad (3.1)$$

$$s_x^2 = \frac{1}{n} \sum_{k=1}^n (x(k) - \bar{x})^2. \quad (3.2)$$

The most commonly used definition of the median  $P_{50}$  and other percentiles  $P_i$  ( $0 < i \leq 100$ ) considers a list of  $n$  ordered values (least to greatest) and defines the smallest value in the list such that no more than  $i$  percent of the data is strictly less than that value and at least  $i$  percent of the data is less than or equal to that value (nearest-rank method). This is obtained by first calculating the ordinal rank  $r$ :

$$r = \left\lceil \frac{P}{100} \cdot n \right\rceil, \quad (3.3)$$

where  $\lceil \cdot \rceil$  is the ceiling operator (rounding to the next integer). The percentile  $P_i$  is then computed by taking the value from the ordered list that corresponds to the rank  $r$ . The IQR is defined as  $\text{IQR} = P_{75} - P_{25}$ .

### 3.3.2 Power spectral density

The PSD  $S_{xx}(f)$  measures how the power content of a time series  $x(k)$  is decomposed in different frequency components. Therefore, the PSD presents a

straightforward tool to study at which frequencies variations are strong and at which frequencies variations are weak. Various estimators exist for the PSD, including (but not limited to) the periodogram, the Welch method, and the CWT, which are all described in this section.

**Periodogram** The periodogram, here denoted as  $S_1(f)$  (the first estimate for the PSD), is defined for a signal  $x(k)$ ,  $k = 0, \dots, n - 1$  as [289]:

$$S_1(f) = \frac{1}{n} |X(f)|^2, \quad (3.4)$$

with

$$X(f) = \sum_{k=0}^{n-1} x(k) \exp(-j2\pi fk). \quad (3.5)$$

The periodogram is easy-to-compute and presents a good first estimate for the PSD, but it suffers from some problems: it is biased ( $E[S_1(f)] \neq 0$ ), not consistent (variance of the order of  $\sigma_x^2$ ), and suffers from spectral leakage and loss of resolution (due to the use of a rectangular window function) [332].

**Welch method** A common approach to reduce the variance (which may be interpreted as noise) of an estimate is to average over a number of statistically independent estimates. A number of periodograms, computed over multiple observations of a signal, can be averaged to obtain a better estimate of the PSD. Such statistically independent estimates can also be generated from a signal  $x(k)$  itself by dividing the data sequence into  $K$  segments of  $M$  samples each:

$$x_i(k) = x(k + (i - 1)M), \quad (3.6)$$

with  $1 \leq k \leq M$ ,  $1 \leq i \leq K$ . The Welch estimate, here denoted as  $S_2(f)$  (the second estimate for the PSD), is obtained by averaging modified periodograms as:

$$S_2(f) = \frac{1}{K} \sum_{i=1}^K S_{W_i}(f), \quad (3.7)$$

where

$$S_{W_i}(f) = \frac{1}{ME_w} \left| \sum_{k=0}^{M-1} x_i(k) w(k) \exp(-j2\pi fk) \right|^2, \quad (3.8)$$

with  $i = 1, 2, \dots, K$ .  $E_w$  is the average power of the window  $w(k)$ , defined as:

$$E_w = \frac{1}{M} \sum_{k=0}^{M-1} w^2(k). \quad (3.9)$$

The use of tapered windows provides the advantage that the ends of the given signal are reduced in amplitude. Therefore, discontinuities in the periodic version of the signal encountered in discrete Fourier transform (DFT) based procedures are reduced. In practice, a Hamming window of length  $n$  is used in all spectral estimates presented in this thesis. This window is defined as:

$$w(k) = 0.54 - 0.46 \cos\left(\frac{2\pi k}{n-1}\right). \quad (3.10)$$

The Welch estimates presents a more robust estimate of the PSD: the variance of the modified periodogram is inversely proportional to  $K$ , that is, the number of segments used.

**Continuous wavelet transform** A third estimate for the PSD is defined from the scalogram of the CWT of the signal as follows:

$$S_3(t, s) = |W_{xx}(t, s)|^2, \quad (3.11)$$

with

$$W_{xx}(t, s) = \int_{-\infty}^{+\infty} x(\tau) \psi^*\left(\frac{t-\tau}{s}\right) d\tau, \quad (3.12)$$

where  $\psi$  is the mother wavelet (usually, Morlet wavelet) and  $s$  is the scale of the wavelet transform. The lag  $\tau$  represents the shift in the time domain of the wavelet base  $\psi$ . In general,  $s \approx f^{-1}$ . In addition to frequency (or scale), this estimate of PSD provides a direct time-dependency, generally referred to as a time-frequency representation.

### 3.3.3 Approximate and sample entropy

The term *entropy* is used to assess the order or disorder of a system. In signal processing, entropy is adopted to measure the irregularity or unpredictability of a time series. A more regular time series is easier to predict and vice versa.

**Approximate entropy** Pincus et al. introduced approximate entropy (ApEn) as a statistic to robustly quantify the regularity of a time series [321, 322]. For a time series  $x(k), k = 1, \dots, n$ , a template vector of length  $m$  is defined as (Figure 3.2):

$$u^m(i) = \{x(i), x(i+1), x(i+2), \dots, x(i+m-1)\}, \quad (3.13)$$

and the distance function  $d(u^m(i), u^m(j))$  between two different ( $i \neq j$ ) template vectors is defined as the Chebyshev distance:

$$d(u^m(i), u^m(j)) = \max_k (|u^m(i+k) - u^m(j+k)|), \quad (3.14)$$

for  $k = 0, \dots, m-1$ . In theory, any distance function could be used, including the Euclidean distance. For a template vector  $u(i)$ , the probability that a segment  $u(j)$  is similar to the template vector can be computed as:

$$C_i^m(r) = \frac{\text{number of } u^m(j) \text{ that satisfy } d(u^m(i), u^m(j)) \leq r}{n - m + 1}, \quad (3.15)$$

where  $r$  is a predefined tolerance. Approximate entropy can consequently be defined as:

$$\text{ApEn}(m, r, n) = \phi^m(r) - \phi^{m+1}(r), \quad (3.16)$$

where:

$$\phi^m(r) = \frac{1}{n - m + 1} \sum_{i=1}^{n-m+1} \ln C_i^m(r). \quad (3.17)$$

Approximate entropy thus measures the likelihood that sequences of  $m$  consecutive points close to each other will still be close to each other when one extra data point is added to the sequence. A regular time series is characterized by a lower approximate entropy compared to an irregular, less predictable time series [81].

**Sample entropy** Richmann and Moorman proposed sample entropy (SampEn) as an improvement to approximate entropy [338]. Sample entropy is less sensitive to the length of the signal  $n$  and has a reduced bias compared to approximate entropy. Sample entropy is computed as:

$$\text{SampEn}(m, r) = -\log \frac{A}{B}, \quad (3.18)$$

where  $A$  is the number of template vector pairs having  $d(u^{m+1}(i), u^{m+1}(j)) < r$  and  $B$  is the number of template vector pairs having  $d(u^m(i), u^m(j)) < r$

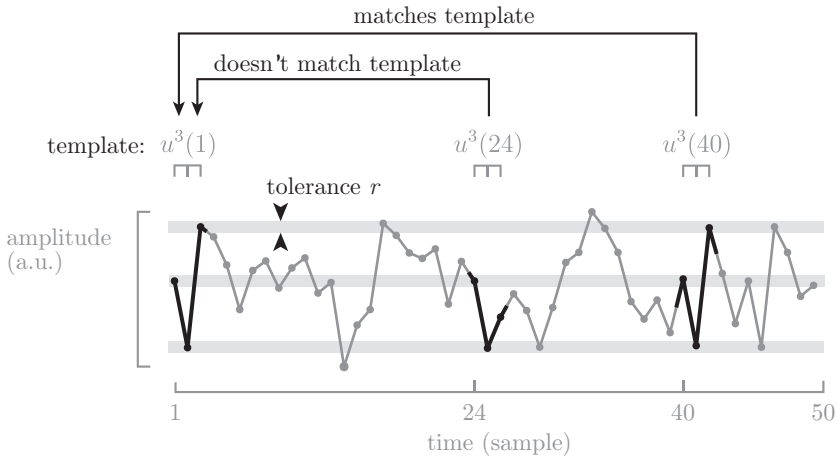


Figure 3.2: Sample entropy is based on the conditional probability that two sequences of length  $m$  matching at a tolerance  $r$  will still be matching for a length  $m + 1$ . Here, we present an example of template matching with length 3.

(Figure 3.2). The ratio  $A/B$  is the conditional probability that two sequences of length  $m$  matching a tolerance  $r$  will still be matching for length  $m + 1$ . The tolerance  $r$  is typically set as a percentage of the standard deviation of the original time series. This normalization prevents the result from being affected by the variance of the signal [81, 338]. It is clear from the definition that  $A$  will always have a values smaller or equal to  $B$ , making sample entropy zero or positive. Smaller sample entropy values indicate more self-similarity (easier to predict).

### 3.4 Bivariate analysis

In time series analysis, a common subject of interest is the coupling among the signals. Although biological systems can be very complex, it is possible to decompose their macroscopic behavior using various mathematical techniques (Figure 3.3). In general, these techniques fall apart in two categories: *functional* connectivity methods only consider the statistical correlations among the investigated signals; they only define the degree to which a given time series resembles another one. *Effective* connectivity methods also take into account

	linear	nonlinear
functional	<ul style="list-style-type: none"> <li>➤ correlation</li> <li>➤ coherence</li> <li>➤ wavelet coherence</li> </ul>	<ul style="list-style-type: none"> <li>➤ regression correlation</li> <li>➤ mutual information</li> <li>➤ RBF kernel function</li> </ul>
effective	<ul style="list-style-type: none"> <li>➤ transfer function</li> <li>➤ Granger causality</li> <li>➤ transfer entropy</li> </ul>	<ul style="list-style-type: none"> <li>➤ transfer entropy</li> </ul>

Figure 3.3: Schematic overview of coupling measures, which fall apart in two categories: functional (no directionality) and effective (directionality) measures. Both categories contain linear and nonlinear techniques.

directionality; they define the causal nature of the interaction. These methods define which signal causes changes in the other signal. In both categories, the techniques can be *linear* or *nonlinear*. A linear method is limited, as it can only capture interactions that are linear, proportional by nature. In the last few years, several nonlinear techniques have started to be used in biomedical time series analysis, mainly as a result of recent advances in information theory [216, 352] and in the study of the synchronization between chaotic systems [318, 44].

### 3.4.1 Linear correlation

Consider two signals  $x(k)$  and  $y(k)$ , sampled at  $k = 1, \dots, n$ . The sample correlation coefficient  $r_{xy}$  between these two signals is defined as:

$$r_{xy} = \frac{s_{xy}}{\sqrt{s_x^2 \cdot s_y^2}}, \tag{3.19}$$

with:

$$s_{xy} = \frac{1}{n} \sum_{i=1}^n (x(i) - \bar{x})(y(i) - \bar{y}), \quad (3.20)$$

with  $s_{xy}$  the covariance between  $x$  and  $y$ ,  $\bar{x}$  and  $\bar{y}$  the mean of  $x$  and  $y$ , respectively (Equation 3.1), and  $s_x^2$  and  $s_y^2$  the variance of  $x$  and  $y$ , respectively (Equation 3.2). The sample correlation coefficient is defined as the covariance between  $x$  and  $y$ , normalized using the variances  $s_x^2$  and  $s_y^2$ . Following normalization, it is bounded by  $-1$  (complete linear inverse correlation) and  $1$  (complete linear direct correlation). An inverse correlation is when signals have similar absolute values, but with opposite signs, while a direct correlation is when signals have similar values with the same sign. A sample correlation of  $0$  suggests a lack of linear interdependence.

In practice, the sample correlation coefficient is studied as a function of time delay  $\tau$ . For simplicity of computation, the signals are usually first normalized to have zero mean ( $\bar{x} = \bar{y} = 0$ ) and unit variance ( $s_x^2 = s_y^2 = 1$ ). In that case, the correlation coefficient can be defined as a function of time delay  $\tau$  as:

$$r_{xy}(\tau) = \frac{1}{n - \tau} \sum_{i=1}^{n-\tau} x(i + \tau)y(i). \quad (3.21)$$

Note that Equation 3.21 only holds for normalized signals with zero mean and unit variance, while Equation 3.19 is valid regardless of normalization. Usually, the correlation coefficient is studied as a function of time delay  $\tau$  and the largest value, together with the corresponding delay, is reported.

### 3.4.2 Regression correlation

The regression correlation is a nonparametric nonlinear regression coefficient, which describes the dependency of a signal  $x(k)$  on a signal  $y(k)$  with  $k = 1, \dots, n$  without directly specifying the type of relation between them [241, 317]. A linear relationship is assumed in the linear correlation framework. To determine the regression correlation, a scatter plot of  $y$  versus  $x$  is studied. In the original definition, a piecewise linear curve is fitted to the data [304]. In our analysis, we use a  $k$ -nearest neighbors regressor as nonlinear regressor. This nonparametric regressor approximates the association between the dependent and independent variables in an intuitive manner by averaging observations in the same neighborhood. In practice, the size of the neighborhood is defined by  $k$ , that is, the number of neighboring points considered. The value of  $k$  needs to be set by the user. In order to avoid overfitting, we determine  $k$  automatically

using 10-fold cross-validation (Figure 3.4). Once the regressor is determined, the nonlinear correlation coefficient between demeaned signals  $x$  and  $y$  is calculated as follows:

$$h_{y|x}^2 = \frac{\sum_{k=1}^n y(k)^2 - \sum_{k=1}^n (y(k) - f(x(k)))^2}{\sum_{k=1}^n y(k)^2}, \quad (3.22)$$

with  $f(x(k))$  is the nonlinear regressor evaluated at  $x(k)$ . The nonlinear correlation coefficient ranges from 0 ( $y$  is completely independent of  $x$ ) to 1 ( $y$  is fully determined by  $x$ ). The measure of association in the opposite direction  $h_{x|y}^2$  can be computed analogously. The difference between both measures:

$$\Delta h^2 = h_{x|y}^2 - h_{y|x}^2, \quad (3.23)$$

is referred to as the asymmetry of the nonlinear coupling. In a linear relationship,  $\Delta h^2 = 0$ , and the nonlinear correlation approximates the linear correlation. In a nonlinear relationship,  $\Delta h^2 \neq 0$ . The asymmetry  $\Delta h^2$  can therefore be interpreted as a measure for nonlinearity in a coupling pair.

### 3.4.3 RBF kernel function

Using the RBF kernel function, the similarity of the different signals is assessed in a possibly infinitely dimensional feature space, defined by the nonlinear map  $\phi$ . In practice, the similarity of two signals  $x$  and  $y$  is computed implicitly through use of the kernel trick as:

$$k_{xy} = \phi(x)^\top \phi(y) = \exp\left(-\frac{\|x - y\|_2^2}{2\sigma^2}\right), \quad (3.24)$$

where  $\sigma$  presents the kernel bandwidth. From the definition, it is clear that the RBF kernel similarity ranges from 0 to 1. The upper limit of one is only reached for identical signals ( $x = y$ ).

The kernel bandwidth  $\sigma$  defines the standard deviation, and thus the width of the Gaussian function. Intuitively, a large  $\sigma$  defines a Gaussian function with a large width. In that case, two signals can be considered similar, even if they are quite different (Figure 3.5). On the other hand, a small kernel bandwidth  $\sigma$  corresponds to a small standard deviation, meaning that two signals are only considered similar if they resemble each other closely. As one can easily see, the kernel bandwidth  $\sigma$  therefore has a profound influence on the resulting coupling values, and should therefore be chosen properly. The method that we designed for this tuning procedure is based on Shannon entropy (Equation 3.25) and is outlined in Chapter 9.

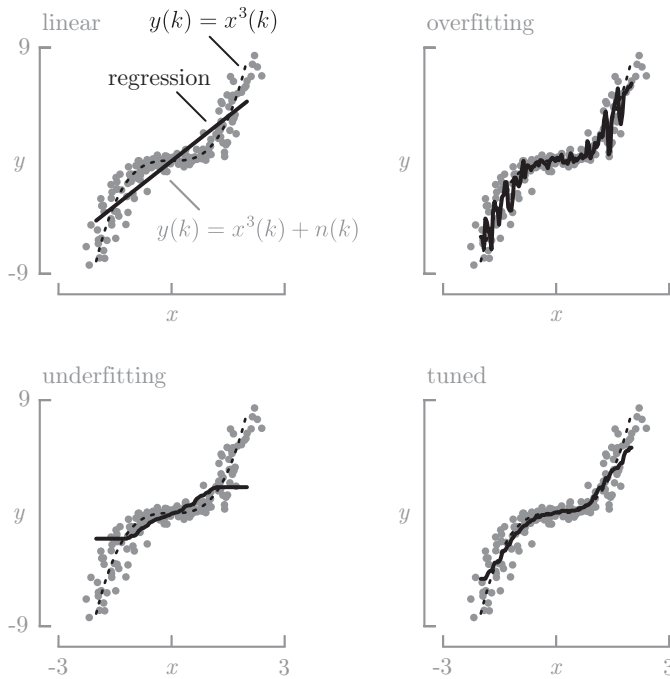


Figure 3.4: Illustration of linear and nonlinear regression on a toy example. The data was generated as  $y(k) = x^3(k) + n(k)$ , with  $n(k) \sim \mathcal{N}(0, 1)$  white noise. Linear OLS regression approximates the cubic relation using a line (top left). Three nonlinear  $k$ -nearest neighbors regressors are shown. If  $k$  is very small, the regressor is overfitting the data (top right). If  $k$  is very large, the regressor is underfitting the data (bottom left). In practice,  $k$  needs to be tuned (e.g., using cross-validation), which results in a tuned regressor (bottom right). The tuned regressor provides the best match with the underlying cubic relation in the data.

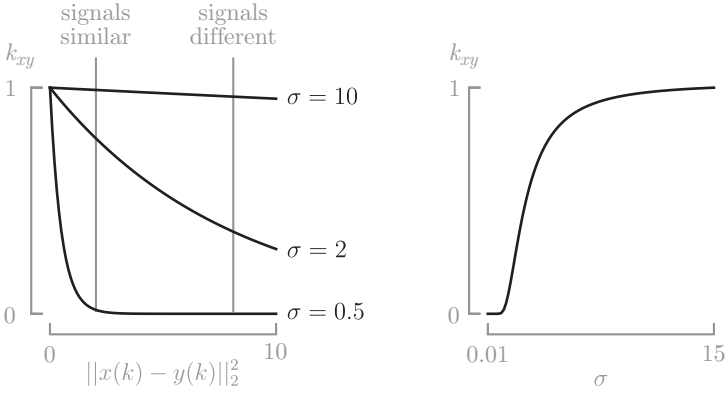


Figure 3.5: The kernel bandwidth  $\sigma$  has a profound influence on the coupling values obtained from the RBF kernel function (Equation 3.24). Left: a large  $\sigma$  might result in coupling near one for unrelated signals. Right: the effect of  $\sigma$  using two test signals with  $r_{xy} \approx 1$ : low  $\sigma$  results in coupling values near zero, while large  $\sigma$  results in coupling values near one.

### 3.4.4 Transfer entropy

**Entropy** The majority of methods available to compute coupling have a point in common: they all try to establish whether there is common information between the time series as a sign of their relationship. Therefore, it has become usual to investigate directly the existence of such relationship by means of information-theoretic tools. The basis of information theory was derived more than 60 years ago [363]. Central to this theory is the concept of *entropy*, defined as the average amount of bits necessary to encode the draws of a discrete variable  $X$  with  $m$  possible outcomes  $X_i$  with probability  $p_i$ <sup>1</sup>. The Shannon entropy of this set of probabilities is

$$H(X) = - \sum_{i=1}^m p_i \log p_i. \tag{3.25}$$

Entropy is positive and is measured in bits if the base of the logarithm is two. The outcomes of  $X$  can be partitioned into  $m$  bins and a first estimation for

<sup>1</sup>The discussion on entropy, mutual information and transfer entropy is outlined in terms of random variables, denoted with capital letters  $X$  and  $Y$ , instead of signals  $x$  and  $y$ . All of the discussed concepts and definitions however directly translate to bivariate signal analysis, by treating the signals as random processes.

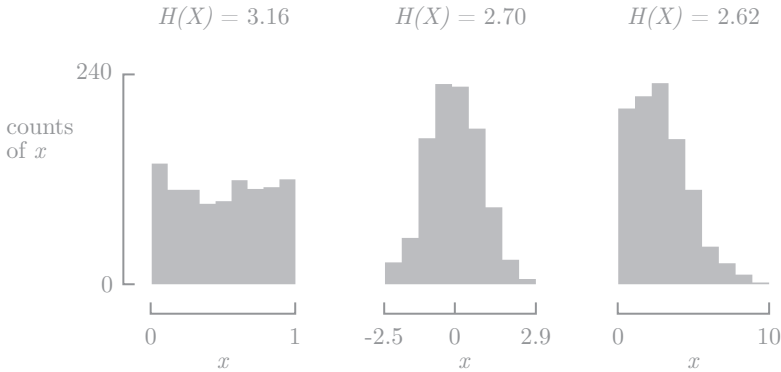


Figure 3.6: One thousand samples following a uniform distribution (left), a standard normal distribution (middle) and a Poisson distribution with  $\lambda = 3$  (right). The histograms and the corresponding probabilities are estimated using  $m = 10$  bins. The Shannon entropy  $H(X)$  (Equation 3.25) is included for each distribution. The distribution with the largest entropy (the uniform distribution) also has the largest uncertainty, since all possible states have approximately the same probability.

$p_i$  is given by the fraction of occurrences of  $X_i, i = 1, \dots, m$  after  $n$  outcomes. Roughly speaking, entropy can be regarded as a measure of the uncertainty of the outcome. A uniform distribution, in which all the states have the same probability, has the largest entropy, whereas a delta-type distribution will have minimum entropy (Figure 3.6).

**Mutual information** The concept of entropy can be extended from a univariate to the bivariate setting. Instead of considering one variable  $X$ , we now define the relationship between two variables  $X$  and  $Y$ . Mutual information (MI) quantifies the amount of common information in  $X$  and  $Y$  and is defined as

$$I(X; Y) = \sum p_{ij} \log \left( \frac{p_{ij}}{p_i p_j} \right), \quad (3.26)$$

where  $p_{ij}$  is the joint probability density function (PDF). MI tells us how much extra information one gets from one signal ( $X$ ) by knowing the outcomes of the other one ( $Y$ ). It is a symmetric measure ( $I(X; Y) = I(Y; X)$ ), and therefore it does not provide any information about the direction of the interaction.

**Transfer entropy** By incorporating dynamic structure in the index, the lack of asymmetry of MI can be resolved. Transfer entropy (TE) measures the amount of information transferred from one process (signal) to another. More specifically, TE from one variable  $X$  to another variable  $Y$  is the amount of uncertainty that is reduced in future values of  $Y$  by knowing the past values of  $X$ , given the past values of  $Y$ . Mathematically, if  $X$  and  $Y$  denote two random processes, TE from  $X$  to  $Y$  is defined as:

$$T_{X \rightarrow Y} = H(Y_n | Y_n^-) - H(Y_n | X_n^-, Y_n^-), \quad (3.27)$$

where  $Y_n$ ,  $Y_n^-$ ,  $X_n^-$  denote the signal  $Y$  at time  $n$ , the past of the signal  $Y$  and the past of the signal  $X$ , respectively, and  $H$  denotes the conditional Shannon entropy, defined as:

$$H(Y_n | Y_n^-) = - \sum_{i,j} p(y_i, \mathbf{y}_j^-) \log \left( \frac{p(y_i, \mathbf{y}_j^-)}{p(\mathbf{y}_j^-)} \right), \quad (3.28)$$

$$H(Y_n | X_n^-, Y_n^-) = - \sum_{i,j} p(y_i, \mathbf{x}_j^-, \mathbf{y}_j^-) \log \left( \frac{p(y_i, \mathbf{x}_j^-, \mathbf{y}_j^-)}{p(\mathbf{x}_j^-, \mathbf{y}_j^-)} \right), \quad (3.29)$$

with  $p(y_i, \mathbf{x}_j^-, \mathbf{y}_j^-)$  the probability that  $Y_n = y_i$ ,  $X_n^- = \mathbf{x}_j^-$ , and  $Y_n^- = \mathbf{y}_j^-$  (Equation 3.31).

**Normalized transfer entropy** A straightforward way to normalize TE is presented by:

$$T_{X \rightarrow Y}^n = \frac{H(Y_n | Y_n^-) - H(Y_n | X_n^-, Y_n^-)}{H(Y_n | Y_n^-)}, \quad (3.30)$$

following a procedure outlined in [144]. This measure can be interpreted as the fraction of uncertainty that is reduced in future values of  $Y$ , by knowing the past values of  $X$  give the past values of  $Y$ . The normalized TE is bounded between 0 (no coupling) and 1 (exact coupling).

**Embedding** In order to reconstruct the state space, and thus define the past of the signals under study, Takens delay uniform embedding can be used [394], defined as:

$$\mathbf{y}_k^- = [y_k, y_{k-\tau}, y_{k-2\tau}, \dots, y_{k-(d-1)\tau}] \quad (3.31)$$

This embedding procedure depends on two parameters: the dimension  $d$  and delay  $\tau$ . In theory, the dimension of the embedding  $d$  should be at least twice

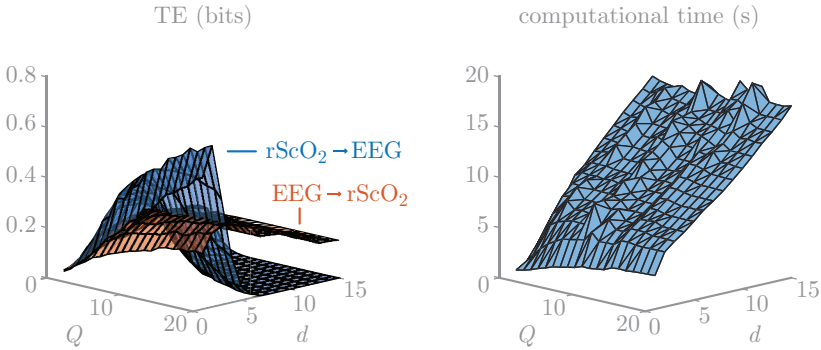


Figure 3.7: Effect of the number of quantization levels  $Q$  and the embedding dimension  $d$  on the resulting TE values (left) and computational time (right).

the order of the underlying system. In practice, however,  $d$  and  $\tau$  are generally unknown, and need to be chosen by the user. While there is an extensive literature on how to choose these parameters, the different methods proposed are far away from reaching any consensus [192]. A popular option is to take the delay embedding  $\tau$  as the autocorrelation decay time of the signal or the first minimum (if any) of the autoinformation. For the embedding dimension  $d$ , the Cao criterion offers an algorithm based on false neighbors computation [66]. However, alternatives for non-deterministic time-series are available [330].

The parameters  $d$  and  $\tau$  highly affect the outcome of the TE estimates. A low value of  $d$  can be insufficient to unfold the state space. A too large value of  $d$  makes the estimators less accurate given data length and significantly enlarges the computing time (Figure 3.7).

**Estimating probability density functions** Computation of TE corresponds to estimating the joint and marginal PDFs in Equation 3.28. For this task, we want to use estimators that are robust to moderate levels of noise and that are reliable on a very limited number of data samples in high-dimensional spaces [167, 217]. Parametric estimators can be used if the underlying distribution is known. In practice, however, underlying distributions are typically not known, and one has to reside to nonparametric estimators. A few popular non-parametric estimators are illustrated in Figure 3.9 and are described in the following paragraphs. These estimators have one thing in common: they are all associated by one or more

free parameters that need to be set properly, since these parameters highly influence the resulting PDF.

**Binning** Let's start with an example: assume we have a continuous variable  $X$  and we want to estimate the Shannon entropy. The easiest way to estimate the probabilities  $p_i$  consists in obtaining the histogram of  $X$  and taking  $p_i$  as the ratio between the number of samples in the  $i$ -th bin of the histogram of  $X$  and the total number of samples [304]. This procedure is commonly referred to as *binning*. To get accurate results, one should have a large number of samples and small bins [325]. In practice, the length of the data is always limited, making careful selection of a proper bin size very important (Figure 3.8). In time series analysis, data points are usually allocated to fixed, equally-spaced bins. This procedure corresponds to a discretization of the values in each variable using a predefined number quantization levels. Then, the probability is estimated as the relative frequency of visitation of the hypercubes in the multidimensional space spanned by the variables. Extension to uniform binning are estimators that use adaptive bin sizes, which are more robust but still suffer from systematic errors [124, 91]. In order to enhance robustness against outliers and sparse regions in the underlying distribution, the ranks can be used instead of the signal values (similar to most non-parametric statistical tests, Section 3.6.1).

**Kernel density estimation** In kernel density estimation (KDE), the PDF is estimated by summing individual distributions centered at each data point. The PDF is approximated using kernel functions to weight the distance from the reference point to any other point in the time series. Popular examples of kernels include the uniform (tophat) kernel, defined as:

$$k(x; h) = \frac{1}{2h}, \quad \text{for } |x| < h, \quad (3.32)$$

and Gaussian kernel defined in Equation 3.24 (Figure 3.9). Using the uniform kernel, the method counts the relative number of points having a distance less than  $h$  from the reference point, then averages across all points. The resulting PDF estimate is typically not smooth. In contrast, using the Gaussian kernel does results in a smooth estimate of the PDF.

**Nearest neighbors statistics**  $k$ -nearest neighbors statistics can also be used for nonparametric density estimation. Let  $X_1, \dots, X_n$  be our random sample, with  $X_i \in \mathbb{R}^d$ . For a given point  $x$ , we first rank every observation based on its distance to  $x$ . Let  $R_k(x)$  denote the distance from  $x$  to its  $k$ -th nearest neighbor point. For a given point  $x$ , the kNN density estimator estimates the

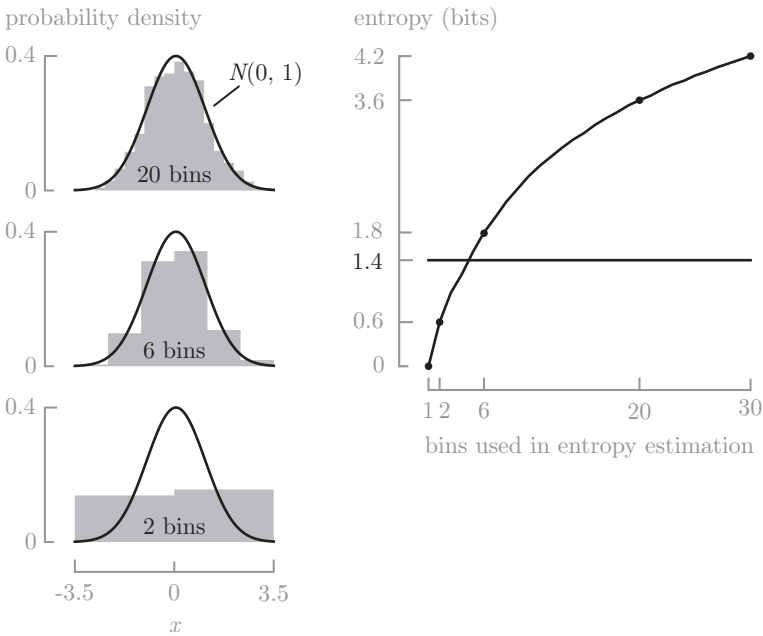


Figure 3.8: Robust estimation of Shannon entropy strongly depends on a proper choice of bin width. Consider a variable  $X \sim \mathcal{N}(0, 1)$  with 1000 samples. When the bin size is too low, we obtain an underestimation of  $H(X)$ . The extreme setting of using just one bin produces  $H(X) = 0$ . If the bin size is too high, we obtain an overestimation of transfer entropy. The upper limit is reached when the number of bins equals the number of samples, then:  $H(X) = \log(n)$  with  $n$  the number of samples of  $X$ . The horizontal line depicts the differential entropy of  $\mathcal{N}(0, 1)$  (1.4).

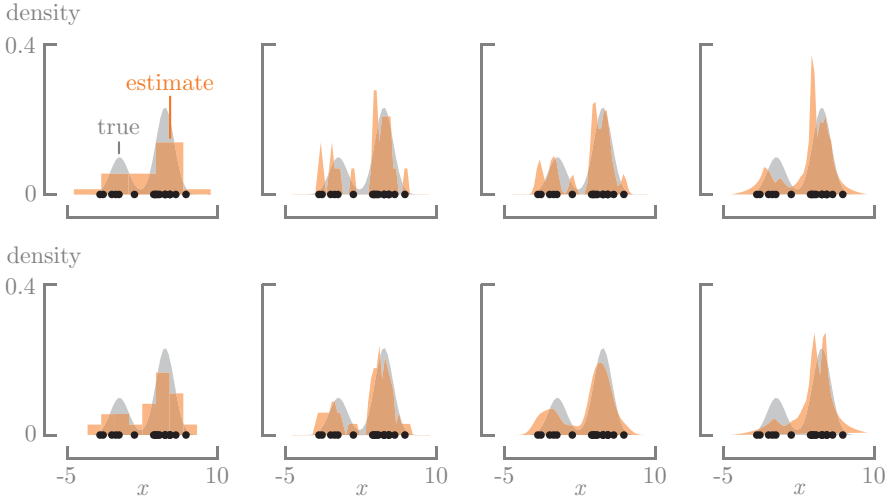


Figure 3.9: Illustration of various techniques to estimate the PDF from data. Twenty samples are generated using a weighted mixture of  $\mathcal{N}(0, 1)$  and  $\mathcal{N}(5, 1)$ , with weight 0.3 and 0.7, respectively. From these 20 samples, the PDF is estimated using binning (first column, top: 5 bins, bottom: 10 bins), KDE using a tophat kernel (Equation 3.32) (second column, top:  $h = 0.30$ , bottom:  $h = 0.70$ ) and a Gaussian kernel (Equation 3.24) (third column, top:  $\sigma = 0.3$ , bottom:  $\sigma = 0.7$ ), and nearest neighbors statistics (Equation 3.33) (last column, top:  $k = 4$ , bottom:  $k = 6$ ).

density by:

$$\hat{p}(x) = \frac{k}{n} \frac{1}{V_d \cdot R_k^d(x)}, \tag{3.33}$$

where  $V_d = \frac{\pi^{d/2}}{\Gamma(d/2+1)}$  is the volume of a unit  $d$ -dimensional ball and  $\Gamma(\cdot)$  is the Gamma function.

**Practical implementation** In the practical implementation of TE used in this text, the binning method is used to estimate the PDFs, since it is computationally much cheaper compared to the other methods, which typically require GPU processing in order to obtain estimates in a reasonable amount of time. Binning is also a convenient choice for us, since data of systemic variables (HR, MABP,

SpO<sub>2</sub>, rScO<sub>2</sub>) is typically already discretized (rounded). Only the EEG has to be binned, for which the number of bins was defined using Friedman-Diaconis rule as bin width =  $2 \cdot \text{IQR}(x) / \sqrt[3]{n}$ , with  $n$  the length of the signal. For a set of empirical measurements sampled from some PDF, the Freedman-Diaconis rule is designed roughly to minimize the integral of the squared difference between the histogram and the density of the theoretical probability distribution.

### 3.4.5 Surrogate analysis

The coupling values computed using one of the measures defined above may present values that do not reflect the existence of synchronization between time series. Instead, they may result from some feature of the individual signals (such as complexity, limited length, or non-stationarity) [38, 305, 327]. Thus, the estimated dependencies derived with the different coupling methods might be completely spurious. In order to check whether a coupling value is actually measuring synchronization, multivariate surrogate data can be constructed to test the hypothesis that the signals are independent [304]. Surrogates are data pairs that have no interdependences at all by design. We typically generate lots of such surrogate data pairs. This allows to quantify spurious connectivity, and correct for it. Four different methods to generate multivariate surrogates are described in this section. Figure 3.10 illustrates these different types of surrogates on a 1000 samples long segment of rScO<sub>2</sub> and EEG  $\delta$  power (0.5–4 Hz).

The first method generates two independent white noise sources. Since they are generated independently, we are certain that no interdependence exists between such data pair. This method is easy to implement, but has two main drawbacks: the amplitude distribution and the autocorrelation properties of the random noise sources do not correspond to the properties of the real data. The second method randomly shuffles the samples of both time series, thereby obtaining so called *time-shuffled surrogates*. The surrogate procedure has to be carried out independently for each time series, so that the cross-correlation is destroyed. Time-shuffled surrogates have the same amplitude distribution as the original data, while being completely independent from each other [296]. They do change the autocorrelation structure of the data, however. This is known to affect different synchronization indexes, especially when the time series present nonlinear structure [305, 304, 20]. By destroying the autocorrelation structure, the surrogates become very unlikely realizations of the real signals [236]. Multiple methods exist to generate surrogates with the same amplitude distribution of the original data and the same autocorrelation properties [304]. The simplest method consists in comparing the original version of one of the signals with temporally shifted versions of the other one [38, 217, 283, 325].

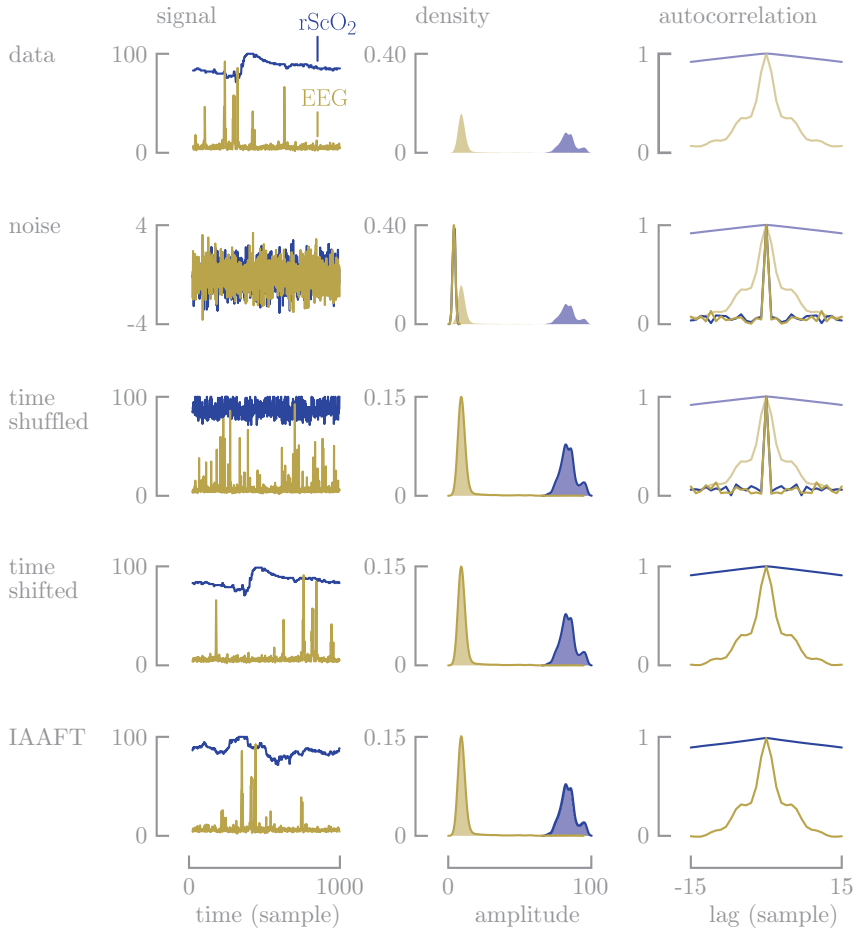


Figure 3.10: Different methods to generate surrogates: random noise sources, time-shuffled surrogates, time-shifted surrogates and surrogates generated using the IAAFT.

These surrogates are referred to as *time-shifted* surrogates. Another method is to use the iterative amplitude adjust Fourier transform (IAAFT). This method preserves the linear autocorrelation properties of the signals, while the phase of the signal is disrupted [352].

Surrogate analysis is needed to assess the robustness of coupling measures,

especially in large datasets where the risk of obtaining a coupling by chance is present. Generating surrogates is computationally (very) expensive, since it required re-estimation of the interdependence among many surrogate time series. In order to reduce the computational cost, it is possible to reduce the number of surrogates [143]. For a significance level  $\alpha$ ,  $N_{\text{surr}} = 1/\alpha - 1$  surrogates have to be generated (19 surrogates for  $\alpha = 0.05$ , 99 surrogates for  $\alpha = 0.01$ ). When we quantify the coupling between two signals  $x(k)$  and  $y(k)$ , the coupling between  $x(k)$  and  $N_{\text{surr}}$  surrogates of  $y(k)$  is estimated. The coupling is considered significant if and only if it is higher than the surrogate-based  $N_{\text{surr}}$  interaction intensities.

## 3.5 Multivariate analysis

### 3.5.1 Signal interaction graph

In most of the studies outlined in this thesis, the simultaneous interactions are assessed in a multimodal dataset. This corresponds to the computation of the coupling between all possible signal pairs using one of the techniques described in Section 3.4. Mathematically, this corresponds to the computation of a weighted graph [302]. Graphs can be used to describe a great variety of real-world situations, which explains the extensive use of these mathematical objects in many different fields. Despite the fact that graph theory was only recently introduced in the field of Network Physiology, it has been used extensively in studies on functional connectivity of the brain [119]. In these studies, the brain is modeled by a graph, which allows to study the interactions between or within different brain regions using EEG [157, 405, 224] or fMRI [432, 374, 132].

Using graphs has many advantages. First, graphs offer a straightforward methodology to deal with the quadratically increasing number of interaction pairs ( $n(n-1)/2$  for  $n$  signals) when adding signals to the analysis. Second, graphs allows for a clear and visual representation. Third, graphs allow to study clusters of signals in a straightforward way. This is especially useful when the interaction between different subsystems is of interest (e.g., the interaction between the cerebral system and the cardiovascular system), rather than the interaction between the signals themselves. Last, the behavior of the network as a whole can easily be studied, using the extensive methods on connectivity that are available in literature.

**Adjacency matrix** A weighted graph  $G$  consists of a nonempty finite set  $V$  of elements called vertices  $v_i$  (or nodes) and a finite set  $E$  of distinct unordered

pairs of distinct elements of  $V$  called edges  $w_{ij}$  (or links) [442]. Note that the edges of the graph are represented by their weights  $w_{ij}$ , which indicate the strength of the connections. The graph  $G$  is defined by its adjacency matrix  $A$ . The adjacency matrix  $A$  denotes the presence of edges between the vertices  $v_i$  of  $V$  and their corresponding weights. More precisely, the adjacency matrix  $A$  is constructed as

$$A_{ij} = \begin{cases} w_{ij} & , \text{ if there is an edge between } v_i \text{ and } v_j \\ 0 & , \text{ otherwise} \end{cases} . \quad (3.34)$$

**Vertex degree** The degree  $d_j$  associated with a vertex  $v_j$  of an undirected weighted graph with adjacency matrix  $A$ , is defined as the sum of all edges incident to  $v_j$ :

$$d_j = \sum_{i=1}^n w_{ij} = \sum_{i=1}^n A_{ij}, \quad (3.35)$$

where  $n$  is the number of vertices. Therefore, the degree  $d_j$  characterizes the connection strength of the vertex  $v_j$  with respect to the other vertices of the graph. In practice, the weights of the edges of a graph are often restricted to a predefined range, which is often normalized to  $w_{ij} \in [0, 1]$ . Considering normalized weights, the degree is bounded by 0 and  $n - 1$ . If  $d_j = 0$ , vertex  $v_j$  is called an isolated vertex, since it is not connected to any other vertex of the graph. A vertex degree  $d_j = n - 1$  indicates a dominating vertex  $v_j$ , connected to all other vertices of the graph with edge weight equal to 1.

**Average degree** The average degree  $\delta(G)$  of a graph  $G$  is defined as the mean value of all vertex degrees  $d_j$ :

$$\delta(G) = \frac{1}{n} \sum_{j=1}^n d_j, \quad (3.36)$$

and is a measure associated with the overall connectivity of the graph. Evidently, the bounds of are equal to those of the individual vertex degree  $d_j$ : a lower limit of 0, an upper limit of  $n - 1$ . Small values (close to 0) imply a weak connectivity, whereas high values (close to  $n - 1$ ) indicate a very strong connectivity of the graph.

### 3.5.2 Clustering

Clustering is an unsupervised technique to group objects in groups called clusters. The endpoint of the clustering procedure is a set of observations,

where each group of observations within a cluster is distinct from the other observations, and the objects within each group are broadly similar to each other. In practice, numerous clustering algorithms are available in literature, which can be stratified in four classes: methods based on connectivity, centroids, density, and Gaussian mixture models.

**Centroid-based** Centroid-based clustering is one of the most frequently used methods following its comparative simplicity. In this class, the most popular method is  $k$ -means clustering. Given a set of observations  $\{x_1, \dots, x_n \in \mathbb{R}^d\}$ , clustering algorithms aim to partition  $n$  observations into  $k \leq n$  sets  $S = \{S_1, \dots, S_k\}$ . First, an initial set of  $k$  centroids  $m_1^{(1)}, \dots, m_k^{(1)}$ , using Forgy (randomly choose  $k$  observations from the dataset as initial means) or random partition (randomly assign one of  $k$  cluster labels to each observation and consequently define initial mean centroids). Other initialization options exists, but are not discussed here. The  $k$ -means algorithm proceeds by alternating between two steps.

- *Assign* each observation to the cluster with the nearest centroid:

$$S_i^{(t)} = \{x_p : \|x_p - m_i^{(t)}\|^2 \leq \|x_p - m_j^{(t)}\|^2, \forall j, 1 \leq j \leq k\}. \quad (3.37)$$

- *Update* the centroids based on the obtained clustering:

$$m_i^{(t+1)} = \frac{1}{N_i^{(t)}} \sum_{x_j \in S_i^{(t)}} x_j, \quad (3.38)$$

where  $N_i^{(t)}$  is the number of observations in  $S_i^{(t)}$ .

The center of each cluster is recalculated in an iterative way until a certain stopping criterion is reached, most commonly, when the cluster centers converge.

**Connectivity-based** Clustering based on the computation of distances between the objects of the whole dataset is called connectivity-based or *hierarchical clustering*. These algorithms generally follow one of two strategies. Agglomerative clustering is a bottom-up approach: we start from distinct clusters and iteratively unite objects. Divisive clustering is a top-down approach: all points start in one cluster after which they are iteratively divided.

In order to define which clusters should be combined (agglomerative), or where a cluster should be split (divisive), a measure of similarity between the sets

of observations is required. First, a distance measure  $d(x_i, x_j)$  is defined as a measure of dissimilarity. The Euclidean distance, defined as:

$$d(x_i, x_j) = \|x_i - x_j\|_2 = \sqrt{\sum_k^d (x_{ik} - x_{jk})^2} \quad (3.39)$$

is most frequently used. Other options include (but are not limited to) the Manhattan distance, the maximum distance, and the Mahalanobis distance. Then, a linkage criterion is defined to determine the distance between sets of observations as a function of the pairwise distances between observations. For two clusters  $S_1$  and  $S_2$ , commonly used examples of linkage criteria include (but are not limited to) maximum, complete linkage:

$$\max\{d(x_i, x_j) : x_i \in S_1, x_j \in S_2\} \quad (3.40)$$

minimum, single linkage:

$$\min\{d(x_i, x_j) : x_i \in S_1, x_j \in S_2\} \quad (3.41)$$

and centroid linkage clustering:  $\|c_{S_1} - c_{S_2}\|$ , where  $c_{S_1}$  and  $c_{S_2}$  are the centroids of clusters  $S_1$  and  $S_2$ , respectively.

Connectivity-based algorithms yield a dendrogram of the data that presents the structure of the information rather than its distinct separation on clusters.

**Silhouette scores** Assume the data  $\{x_1, \dots, x_n \in \mathbb{R}^d\}$  have been clustered into  $k$  clusters  $S = \{S_1, \dots, S_k\}$  using any of the techniques described above. For each datapoint  $x_i \in S_k$ , let

$$a(x_i) = \frac{1}{|S_k| - 1} \sum_{x_j \in S_k} d(x_i, x_j), \quad (3.42)$$

be the mean distance between  $x_i$  and all other points in the same cluster  $S_k$ , where  $|S_k|$  is the number of data points belonging to  $S_k$ . The measure  $a(x_i)$  indicates how well a datapoint  $x_i$  is assigned to its cluster  $S_k$  (the smaller the value, the better the assignment). For each datapoint  $x_i$ , we define an additional measure  $b(x_i)$  as:

$$b(x_i) = \min_{k \neq i} \frac{1}{|S_k|} \sum_{x_j \in S_k} d(x_i, x_j), \quad (3.43)$$

as the smallest mean distance of  $x_i$  to all points in any other cluster of which  $x_i$  is not a member. The cluster with the smallest mean dissimilarity is often

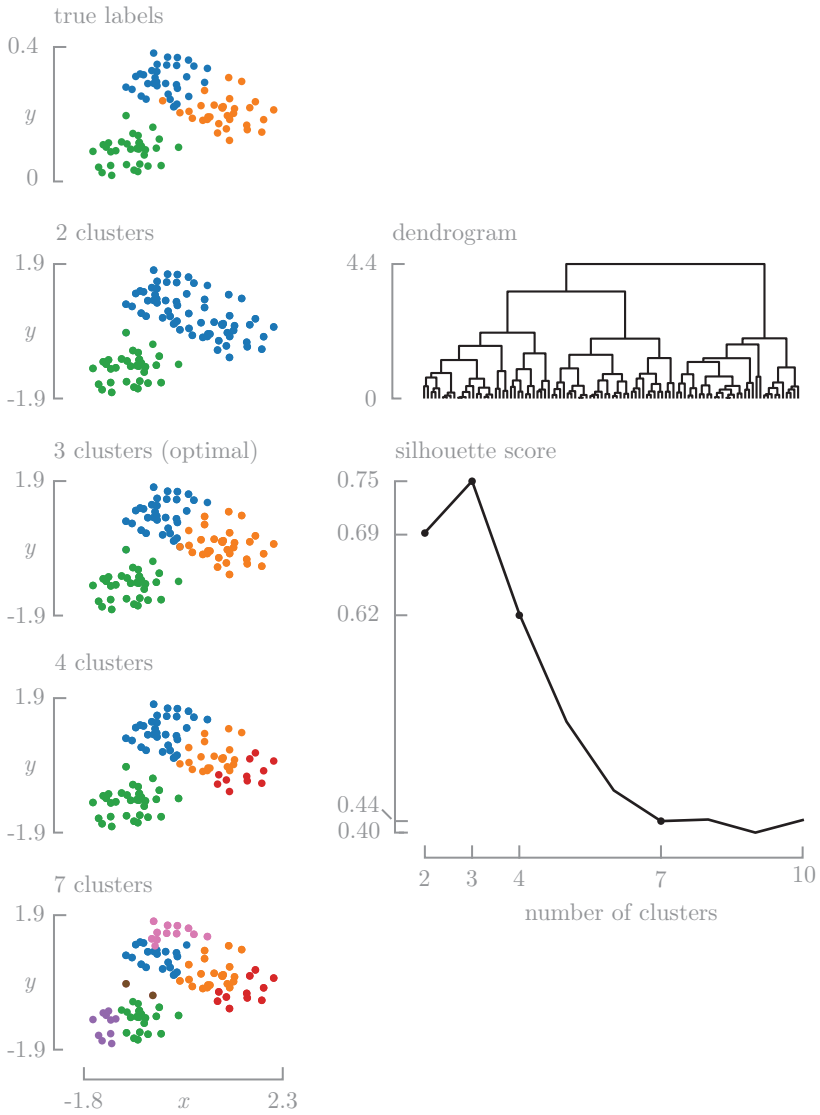


Figure 3.11: Hierarchical clustering using different numbers of clusters, illustrated on toy data of 100 samples generated from isotropic Gaussian blobs with three centers. Since the data was generated from three centers, optimal clustering is reached for three clusters (Silhouette score of 0.75).

referred to as the neighboring cluster of  $x_i$ , since this cluster presents the next best fit for point  $x_i$ . Finally, we define the Silhouette score of a point  $x_i \in S_k$  as:

$$s(x_i) = \frac{b(x_i) - a(x_i)}{\max(a(x_i), b(x_i))}, \quad (3.44)$$

and  $s(x_i) = 0$  if  $|S_k| = 1$ . From its definition, it is clear that the Silhouette score is lower bounded by  $-1$  (data point shows better match with neighboring cluster) and upper bounded by  $1$  (data point shows great match to its own cluster). A Silhouette score of zero indicates that the data point is on the border of two natural clusters. The mean of the Silhouette scores over all points in a clusters measures how tightly grouped all points in that cluster are. The mean of the Silhouette scores over the entire datasets measures how well the data have been clustered.

## 3.6 Statistics

In this section, all of the tools that are used for statistical analysis of the data are presented. These tools fall apart in two categories: statistical hypothesis tests, and regression analysis.

### 3.6.1 Statistical hypothesis tests

A common task in research is to compare two populations or groups. Statistical hypothesis tests can be used for this purpose. As the name suggests, these tests typically assume a null hypothesis of no relationship or no difference between the groups. Then, they determine whether the observed data fall outside of the range of values predicted by the null hypothesis. In practice, this is done using a test statistic, which is a number that describes how much the relationship between the variables in the test differs from the null hypothesis. The value of the test statistic is ultimately translated in a  $p$  value, which describes how likely it is that the null hypothesis is true. A  $p$  value smaller than  $0.05$  is typically chosen to reject the null hypothesis.

In this section, we'll have a look at various hypothesis tests used throughout this thesis (Figure 3.12). First, the  $t$ -test, a parametric test assuming normality is described. The datasets used in this thesis are often of limited size. Comparing statistics between different groups therefore corresponds to comparing groups with small sample sizes. Therefore, an underlying normal distribution can typically not be assumed and we have to resort to *nonparametric* tests, such as

the Wilcoxon rank sum test, the Wilcoxon signed-rank test, the Fisher exact test, the permutation test, and the likelihood-ratio test.

***t*-test** The independent samples *t*-test can be used to determine if the means of two sets of data are significantly different from each other. For exactness, the *t*-test requires that the means from the two populations being compared follow normal distributions. Under weak assumptions, by the central limit theorem, sample means of moderately large samples are often well-approximated by a normal distribution even if the data itself are not normally distributed.

A general definition of the test statistic *t* (Welch's *t*-test), which accounts for unequal sample sizes ( $N_1 \neq N_2$ ) and unequal variances ( $s_{x_1} > 2s_{x_2}$  or  $s_{x_2} > 2s_{x_1}$ ), is defined as:

$$t = \frac{\bar{x}_1 - \bar{x}_2}{s_{\bar{\Delta}}}, \quad (3.45)$$

where

$$s_{\bar{\Delta}} = \sqrt{\frac{s_{x_1}^2}{N_1} + \frac{s_{x_2}^2}{N_2}}. \quad (3.46)$$

Here,  $s_{x_i}^2$  is an unbiased estimator of the variance of each sample *i*. For use in significance testing, the distribution of the test statistic *t* is approximated as a Student's *t*-distribution, with degrees of freedom *k* equal to

$$k = \frac{(s_{x_1}^2/N_1 + s_{x_2}^2/N_2)^2}{(s_{x_1}^2/N_1)^2/(N_1 - 1) + (s_{x_2}^2/N_2)^2/(N_2 - 1)}. \quad (3.47)$$

**Wilcoxon rank sum test** The Wilcoxon rank sum test (also called the Mann-Whitney *U* test) is a nonparametric alternative to the two-sample *t*-test for the comparison of continuous variables between two independent (unpaired) groups. The test is based solely on the order in which the observations from the two samples fall.

Say we have  $N_A$  and  $N_B$  samples from two populations *A* and *B*, respectively. We wish to test the null hypothesis  $H_0$  that the distribution of measurements in *A* is the same as in *B*:

$$H_0 : A = B. \quad (3.48)$$

The rank sum test detects if there are location shifts of the mean and formulates the alternative hypothesis  $H_1$  as  $H_1 : A < B$ ,  $H_1 : A > B$ , or  $H_1 : A \neq B$ .



The Wilcoxon rank sum test is based upon ranking the  $N_A + N_B$  observations of the combined sample. A rank can be assigned to each of the observations: the smallest observation has rank 1 and the largest observation has rank  $N_A + N_B$ . The Wilcoxon rank sum test statistic is the sum of the ranks for the observations in one of the samples: let's say the observations in  $A$ . This sum is denoted as  $w_A$  and the corresponding random variable as  $W_A$ .

If  $H_0$  is true, we expect random ranking in the combined samples, which translates to  $w_a \approx w_B$ . If  $H_1 : A > B$  ( $H_1 : A < B$ ) is true, we expect  $w_A$  to be unusually large (small) according to the distribution of rank sums when  $H_0$  is true. For  $H_1 : A \neq B$ , a rank sum that is either too big or too small provides evidence against  $H_0$ .

When one performs a Wilcoxon rank sum test, tables are required to find  $p$  values. These tables are supplemented with a normal distribution approximation in the presence of larger samples. Then, we can treat the distribution of  $W_A \sim \mathcal{N}(\mu_A, \sigma_A)$ , with:

$$\mu_A = \frac{N_A(N_A + N_B + 1)}{2}, \quad (3.49)$$

$$\sigma_A = \sqrt{\frac{N_A N_B (N_A + N_B + 1)}{12}}. \quad (3.50)$$

If we denote probability as  $\text{pr}(\cdot)$ , we can write more precisely:

$$\text{pr}(W_A \geq w_A) \approx \text{pr}(Z \geq z), \quad (3.51)$$

with

$$z = \frac{w_A - \mu_A}{\sigma_A}, \quad (3.52)$$

and  $Z \sim \mathcal{N}(0, 1)$ . In practice, the normal distribution approximation can be used for sample sizes  $N_A, N_B > 10$ .

The Wilcoxon test is valid for data from any distribution (normal or not) and is much less sensitive to outliers than the two-sample  $t$ -test. When the assumptions to the two-sample  $t$  test hold, the Wilcoxon test is somewhat less likely to detect a location shift than the two-sample  $t$ -test. However, the losses in this regard are usually quite small [111]. The Mann-Whitney  $U$  test is essentially identical to the Wilcoxon test, even though it uses a different test statistic.

**Wilcoxon signed-rank test** The Wilcoxon signed-rank test is a nonparametric test used to compare two related samples, matched samples, or repeated

measurements on a single sample to assess whether their population mean ranks differ. Therefore, this test is a paired difference test. It can be used as an alternative to the paired  $t$ -test when the distribution of the difference between two samples' means cannot be assumed to be normally distributed.

Comparable to the Wilcoxon rank sum test, this test involves ranking. Say we have  $N$  samples  $A_1$  and  $A_2$  from a population  $A$ , samples at two different times. Now, the differences  $|a_{2i} - a_{1i}| \neq 0$  are ranked as  $R_i$ . The smallest difference gets rank 1, while the largest difference gets rank  $N_r$ , which is the reduced sample size of the non-zero differences.

The test statistic is consequently defined as the sum of the signed ranks:

$$W = \sum_{i=1}^{N_r} \text{sgn}(a_{2i} - a_{1i}) \cdot R_i, \quad (3.53)$$

where  $\text{sgn}$  denotes the sign function. Under null hypothesis  $H_0$ ,  $W$  follows a specific distribution with no simple expression. As for the Wilcoxon rank sum test,  $W$  can be compared to a critical value from a reference table for small sample sizes. As  $N_r$  increases,  $W \sim \mathcal{N}(0, \sigma_W)$ , with:

$$\sigma_W = \sqrt{\frac{N_r(N_r + 1)(2N_r + 1)}{6}}. \quad (3.54)$$

Again,

$$\text{pr}(W \geq w) \approx \text{pr}(Z \geq z), \quad (3.55)$$

with  $z = w/\sigma_W$  and  $Z \sim \mathcal{N}(0, 1)$ . As before,  $\text{pr}(\cdot)$  denotes probability. In practice, the normal distribution approximation can be used for sample sizes  $N_r > 20$ .

**Fisher exact test** Fisher's exact test is a statistical significance test used to determine if there are nonrandom associations between two categorical variables. In practice, this test is used in the analysis of contingency tables when the sample sizes are small, although the test is valid for all sample sizes. For this discussion, let's assume a  $2 \times 2$  contingency table:

		A = 0	A = 1		total		
B = 0		$N_{00}$	$N_{01}$		$N_{00} + N_{01}$		
B = 1		$N_{10}$	$N_{11}$		$N_{10} + N_{11}$		(3.56)
total		$N_{00} + N_{10}$	$N_{01} + N_{11}$		N		

with  $N = N_{00} + N_{01} + N_{10} + N_{11}$  is the total number of elements. In this table, we study two dichotomous variables  $A$  and  $B$ , and  $N_{ij}$  elements fall in the category  $A = i$  and  $B = j$ . In a practical setting, the row or column counts are fixed (or chosen). In that case, the entire table is determined by one of the cell counts (e.g.,  $N_{00}$ ), and this number follows a hypergeometric distribution under the null hypothesis that the relative proportions of one variable (e.g.,  $A$ ) are independent of the second variable (e.g.,  $B$ ).

**Permutation test** A permutation test is a type of test in which the distribution of the test statistic under the null hypothesis is obtained by calculating all possible values of the test statistic under all possible rearrangements of the observed data points.

To illustrate the idea behind the permutation test, say we have two random variables  $X_A$  ( $n_A$  samples with mean  $\bar{x}_A$ ) and  $X_B$  ( $n_B$  samples with mean  $\bar{x}_B$ ) from two populations  $A$  and  $B$ , respectively (Figure 3.13). Now, we want to know whether these samples come from the same distribution. The permutation test can be used to determine whether the observed difference between the sample means is large enough to reject the null hypothesis  $H_0$  that the data drawn from  $A$  comes from the same distribution as the data drawn from  $B$ .

First, the observed value of the test statistic is defined as  $T_{\text{obs}} = \bar{x}_A - \bar{x}_B$ . Next, the observations of groups  $A$  and  $B$  are pooled, and the difference in sample means is calculated for every possible way of dividing the pooled variables into two groups of size  $n_A$  and  $n_B$ . Note that this corresponds to a permutation of the group labels  $A$  and  $B$ : there are  $(n_A + n_B)! / (n_A! \cdot n_B!)$  possibilities to do this. The set of calculated differences is the exact distribution of possible differences (for this sample) under the null hypothesis that group labels are randomly assigned. The one-sided (two-sided)  $p$  value of the test statistic is calculated as the proportion of sampled permutations where the (absolute) difference in means was greater than or equal to  $T_{\text{obs}}$  ( $|T_{\text{obs}}|$ ).

Permutation tests exist for any test statistic, regardless of whether or not its distribution is known, but might be computationally expensive. In practice, it can happen that there are too many possible orderings of the data to allow complete enumeration in a convenient manner. When we want to compare two groups of size 20, we have to look at roughly 138 billion options. In such case, it is possible to use Monte Carlo sampling, which takes a small (relative to the total number of permutations) random sample of the possible replicates.

**Likelihood-ratio test** In regression analysis (following section), we are often interested to know whether a predictor variable significantly contributes to a

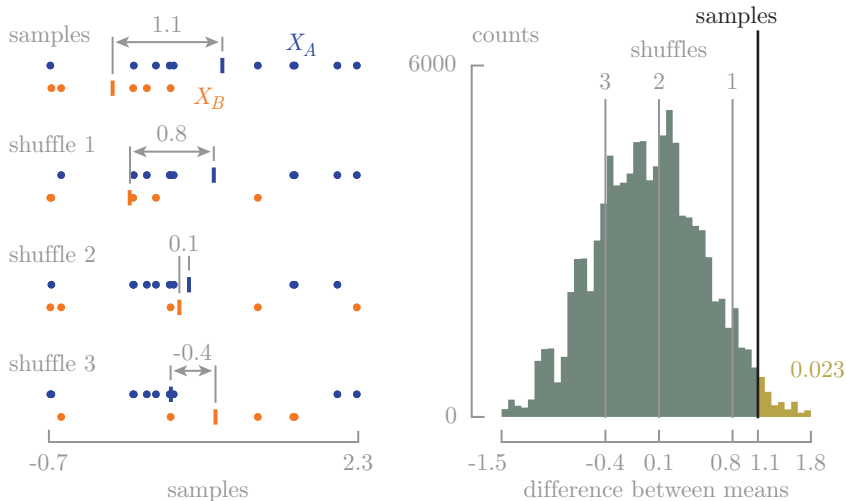


Figure 3.13: Graphical illustration of the permutation test. Data generated: 15 samples from  $A \sim \mathcal{N}(1, 1)$ , 5 samples from  $B \sim \mathcal{N}(0, 1)$ . Monte Carlo sampling using  $10^5$  shuffles, of which three shuffles are presented on the left. The permutation test gives  $p = 0.023$ , while the Wilcoxon rank sum test indicates  $p = 0.05$ .

regression model. In order to formally test this, we quantify the difference among nested models, because of one the models can be said to be nested within the other. The likelihood-ratio (LR) test is performed by estimating two models and comparing the fit of one model to the fit of the other. Removing predictor variables from a model will almost always make the model fit less well, that is, the model will have a lower log likelihood. The LR test compares the log likelihoods of the two models. If this difference is statistically significant, then the less restrictive model (the one with more variables) is said to fit the data significantly better than the more restrictive model. If one has the log likelihoods from the models, the LR test is fairly easy to calculate. The LR test statistic is defined as:

$$LR = -2 \ln \left( \frac{L(m_1)}{L(m_2)} \right) = 2(\ln(L(m_2)) - \ln(L(m_1))) \quad (3.57)$$

with  $L(m_i)$  the likelihood of model  $m_i$ . Note that, in the definition above,  $m_1$  denotes the more restrictive model, while  $m_2$  denotes the less restrictive model.

The resulting test statistic is  $\chi^2$ -squared distributed with the degrees of freedom  $k$  equal to the number of variables that are constrained.

### 3.6.2 Regression

**Ordinary least squares regression** Ordinary least-squares (OLS) (multiple) linear regression is the most commonly used model to examine the relationship between an output (dependent variable) and one or more inputs (independent variables) [333]. The most generic case refers to the multiple regression where the dependent variable  $y$  and its variance are explained by a set of  $p$  dependent variables:

$$y_i = \beta_0 + \beta_1 x_{i1} + \beta_2 x_{i2} + \cdots + \beta_p x_{ip} + \epsilon_i, \quad (3.58)$$

for each  $i = 1, \dots, n$ , where  $y_i$  is the dependent variable,  $x_{ip}$  is the  $p$ -th explanatory variable,  $\beta_0$  is the  $y$ -intercept (constant term),  $\beta_p$  is the slope for the  $p$ -th explanatory variable and  $\epsilon_i$  is the model's error term. This can be written more compactly in matrix notation as:

$$\mathbf{y} = X\boldsymbol{\beta} + \boldsymbol{\epsilon}, \quad (3.59)$$

with

$$\mathbf{y} = \begin{bmatrix} y_1 \\ y_2 \\ \vdots \\ y_n \end{bmatrix}, \quad X = \begin{bmatrix} 1 & x_{11} & \cdots & x_{1p} \\ 1 & x_{21} & \cdots & x_{2p} \\ \vdots & \vdots & \ddots & \vdots \\ 1 & x_{n1} & \cdots & x_{np} \end{bmatrix}, \quad \boldsymbol{\beta} = \begin{bmatrix} \beta_0 \\ \beta_1 \\ \vdots \\ \beta_p \end{bmatrix}, \quad \boldsymbol{\epsilon} = \begin{bmatrix} \epsilon_1 \\ \epsilon_2 \\ \vdots \\ \epsilon_n \end{bmatrix}.$$

The OLS model minimizes the sum of squared residuals, and leads to a closed-form expression for the estimated value of the unknown parameter vector  $\boldsymbol{\beta}$ :

$$\boldsymbol{\beta} = (X^\top X)^{-1}(X^\top \mathbf{y}) = X^\dagger \mathbf{y}, \quad (3.60)$$

where  $X^\dagger$  is called the Moore-Penrose pseudoinverse of  $X$ . Once  $\boldsymbol{\beta}$  is determined, the model estimate is given by:

$$\hat{\mathbf{y}} = X\boldsymbol{\beta}. \quad (3.61)$$

The OLS regression model defined in Equation 3.58 is based on four assumptions (Figure 3.14). First, the relationship between the regressor and the response is linear in the coefficients. Second, the distribution of the error terms is normal:  $\epsilon \sim \mathcal{N}(0, \sigma_\epsilon^2)$ . Third, the variance of the error terms ( $\sigma_\epsilon^2$ ) is constant for each value of  $x$  (homoscedasticity). Last, successive residuals should not be correlated (independence of the error terms).

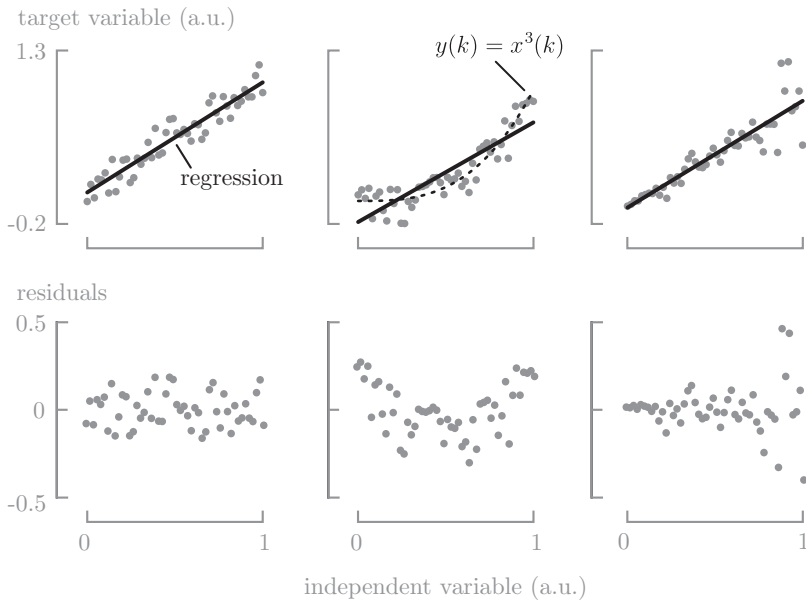


Figure 3.14: The OLS regression model is based on four assumptions: linearity in the coefficients, normality of the error terms, homoscedasticity, and independence of the error terms. Left: regression in which all four assumptions are satisfied. In the residuals plot, no clear pattern can be observed. Middle: the relation between  $y$  and  $x$  is nonlinear. The residuals show a clear parabolic trend. Right: data with heteroscedastic noise ( $\sigma_\epsilon^2$  ranges from 0–0.2 from left to right). The residuals grow in amplitude when  $x$  grows.

The most common performance (goodness of fit) metric for linear regression is the coefficient of determination  $R^2$ , which quantifies the proportion of the variation in the dependent variable that is predicted from the independent variable(s) (Figure 3.15). Formally,  $R^2$  is defined as:

$$R^2 = \frac{SS_{\text{reg}}}{SS_{\text{tot}}} = 1 - \frac{SS_{\text{res}}}{SS_{\text{tot}}}, \quad (3.62)$$

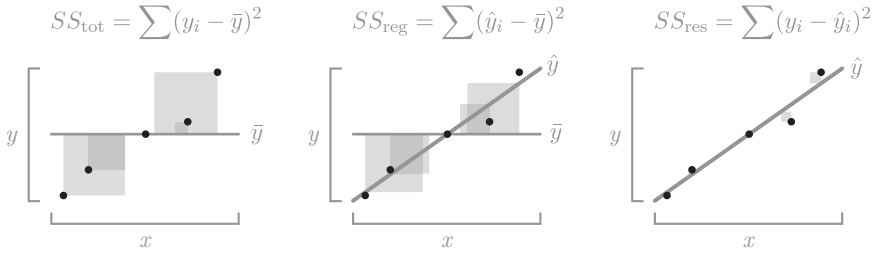


Figure 3.15: Visual representation of the coefficient of determination, which can be defined using the total sum of squares (left), the explained sum of squares (middle), and the residual sum of squares (right).

with

$$SS_{\text{res}} = \sum \epsilon_i^2 = \sum (y_i - \hat{y}_i)^2, \quad (3.63)$$

$$SS_{\text{reg}} = \sum (\hat{y}_i - \bar{y})^2, \quad (3.64)$$

$$SS_{\text{tot}} = \sum (y_i - \bar{y})^2. \quad (3.65)$$

In the best case, the modeled values exactly match the observed values. Then,  $SS_{\text{res}} = 0$  and  $R^2 = 1$ . A baseline model, which predicts the mean  $\bar{y}$  will have a  $R^2 = 0$ . The coefficient of determination can also turn negative, for models that have worse predictions than the baseline model.

The coefficient of partial determination can be defined as the proportion of variation that cannot be explained in a reduced model, but can be explained by the predictors specified in a full(er) model. Assume we have two predictor  $x_i$  and  $x_j$ . For the corresponding multiple regression model, we wish to know what percent of the variation not explained by  $x_i$  is explained by  $x_j$ . In other words: given  $x_i$ , what additional percent of the variation can be explained by  $x_j$ ? Note that here the full model includes both predictors  $x_i$  and  $x_j$ , while the reduced model only includes  $x_i$ .

The coefficient of partial determination  $R_{j|i}^2$  can be defined as:

$$R_{j|i}^2 = \frac{SS_{\text{reg}}(x_j|x_i)}{SS_{\text{res}}(x_i)}, \quad (3.66)$$

$$= \frac{SS_{\text{reg}}(x_i, x_j) - SS_{\text{reg}}(x_i)}{SS_{\text{res}}(x_i)}, \quad (3.67)$$

$$= \frac{SS_{\text{res}}(x_i) - SS_{\text{res}}(x_i, x_j)}{SS_{\text{res}}(x_i)}. \quad (3.68)$$

Then, this coefficient gives us the proportion of variation explained by  $x_j$  that cannot be explained by  $x_i$ .

**Generalized least squares regression** The generalized least squares (GLS) estimator of the coefficients of a linear regression is a generalization of the OLS estimator that is used when the Gauss-Markov theorem (which dictates homoscedasticity and absence of serial correlation) is violated. In such situations, the GLS estimator is the best linear unbiased estimator.

The linear regression is

$$\mathbf{y} = X\boldsymbol{\beta} + \boldsymbol{\epsilon}, \quad (3.69)$$

where  $\mathbf{y}$  is a  $n \times 1$  vector of output ( $n$  is the sample size),  $X$  is a  $n \times (p + 1)$  matrix of regressors ( $p$  is the number of regressors),  $\boldsymbol{\beta}$  is a  $(p + 1) \times 1$  vector of regression coefficients to be estimated, and  $\boldsymbol{\epsilon}$  is a  $n \times 1$  vector of error terms. We assume that  $X$  has full rank,  $E[\boldsymbol{\epsilon}|X] = 0$ , and  $\text{Var}[\boldsymbol{\epsilon}|X] = V$ , where  $V$  is a  $n \times n$  symmetric positive definite matrix. We allow for heteroscedasticity (the errors can have different variances) and correlation (the covariances between errors can be different from zero) by allowing  $V$  to be a symmetric positive definite matrix, and thus not restricting it to  $V = \sigma^2 I$  (as in OLS), with  $I$  the identity matrix. When the covariance matrix  $V$  is diagonal (the error terms are uncorrelated), the GLS estimator is called a weighted least squares estimator.

Since  $V$  is a symmetric, positive semidefinite matrix, there exists an invertible matrix  $\Sigma$ , such that:

$$V = \Sigma \Sigma^\top. \quad (3.70)$$

If we multiply the regression equation by  $\Sigma^{-1}$ , we obtain:

$$\Sigma^{-1}\mathbf{y} = \Sigma^{-1}X\boldsymbol{\beta} + \Sigma^{-1}\boldsymbol{\epsilon}. \quad (3.71)$$

Define:

$$\tilde{\mathbf{y}} = \Sigma^{-1}\mathbf{y}, \quad \tilde{X} = \Sigma^{-1}X, \quad \tilde{\boldsymbol{\epsilon}} = \Sigma^{-1}\boldsymbol{\epsilon}, \quad (3.72)$$

so that the transformed regression equation can be written as:

$$\tilde{\mathbf{y}} = \tilde{X}\boldsymbol{\beta} + \tilde{\boldsymbol{\epsilon}}. \quad (3.73)$$

Then:

$$\hat{\boldsymbol{\beta}}_{\text{GLS}} = (\tilde{X}^{\top}\tilde{X})^{-1}\tilde{X}^{\top}\tilde{\mathbf{y}}, \quad (3.74)$$

$$= (X^{\top}V^{-1}X)^{-1}X^{\top}V^{-1}\mathbf{y}. \quad (3.75)$$

The GLS estimator is thus defined as the OLS estimator of the coefficients of the transformed regression equation (Equation 3.73).

**Linear mixed effects regression** Equation 3.58 is based on numerous assumptions. The first assumption is the independence of the input variable (collinearity, homoscedasticity). Although the different values should be drawn randomly from the underlying data distribution, this is generally not the case if the data comes from patients recorded at different time points.

The core of mixed models is that they incorporate fixed and random effects. A fixed effect is a parameter that does not vary, while random effects are parameters that are themselves random variables. This is really the same as in linear regression, where we assume the data are random variables and the parameters are fixed effects. Now, the data are random variables, and the parameters are random variables (at one level), but fixed at the highest level (for example, we still assume some overall population mean,  $\mu$ ). The linear mixed model (LME) is defined as:

$$\mathbf{y} = X\boldsymbol{\beta} + Z\mathbf{u} + \boldsymbol{\epsilon}, \quad (3.76)$$

where  $\mathbf{y}$ ,  $X$ ,  $\boldsymbol{\beta}$  and  $\boldsymbol{\epsilon}$  are defined as before.  $Z$  is the  $n \times qJ$  design matrix for the  $q$  random effects and  $J$  groups.  $\mathbf{u}$  is a  $qJ \times 1$  vector of  $q$  random effects (the random complement to the fixed  $\boldsymbol{\beta}$ ) for  $J$  groups.

Is we estimated it,  $\mathbf{u}$  would be a column vector, similar to  $\boldsymbol{\beta}$ . However, in classical statistics, we do not actually estimate  $\mathbf{u}$ . Instead, we nearly always assume that:

$$\mathbf{u} \sim \mathcal{N}(\mathbf{0}, G), \quad (3.77)$$

with  $G$  the variance-covariance matrix of the random effects. Random effect complements are thus modeled as deviations from the fixed effect, with zero

mean: random effects are deviations around  $\beta$ . Random effects can be a random intercept and/or a random slope. If the model contains a random intercept only,  $G$  is a  $1 \times 1$  matrix which contains the variance of the random intercept. If the model contains a random intercept and a random slope:

$$G = \begin{bmatrix} \sigma_{\text{int}}^2 & \sigma_{\text{int,slope}}^2 \\ \sigma_{\text{int,slope}}^2 & \sigma_{\text{slope}}^2 \end{bmatrix}. \quad (3.78)$$

Note that  $G$  is a square, symmetric, positive semidefinite matrix. Assuming the random effects are independent,  $G$  reduces to:

$$G = \begin{bmatrix} \sigma_{\text{int}}^2 & 0 \\ 0 & \sigma_{\text{slope}}^2 \end{bmatrix}. \quad (3.79)$$

The final element in equation 3.76 is the variance-covariance matrix of the residuals,  $\epsilon$ , which is most commonly defined as:

$$R = I\sigma_{\epsilon}^2, \quad (3.80)$$

where  $I$  is the identity matrix and  $\sigma_{\epsilon}^2$  the residual variance. This structure assumes a homogeneous residual variance for all (conditional) observations and that they are (conditionally) independent. Other structures can be assumed such as compound symmetry or autoregressive. The final model depends on the distribution assumed, but is generally of the form:

$$(\mathbf{y}|\beta; \mathbf{u} = u) \sim \mathcal{N}(X\beta + Z\mathbf{u}, R). \quad (3.81)$$

### 3.7 Conclusion

The signal processing pipeline used in this thesis consists of three main blocks. First, artifacts are removed, which are typically present in long recordings ranging from hours to days. Second, the time scale of the EEG is matched to the slower dynamics of the other signals under study (HR, MABP, SpO<sub>2</sub>, rScO<sub>2</sub>). Third, the coupling between the time series is defined in a pairwise fashion, using linear (correlation) and nonlinear (regression correlation, RBF kernel function, TE) coupling measures. The significance of the coupling is ensured using surrogate data analysis. After these processing steps, the resulting model and features derived thereof are visualized, or further processed using clustering techniques. The endpoint of every analysis outlined in this thesis is a statistical analysis, which can be based on statistical hypothesis tests or regression models, depending on the research question(s) at hand.

introduction

04

# Datasets



In the following chapters, we study the behavior of a newly designed physiological marker for NVC (Chapter 7) on the one hand, and the (neuro)cardiovascular graph on the other hand (Chapters 8, 9, 10) in different clinical settings. The datasets that correspond to these different clinical settings are introduced in this chapter. Table 4.1 presents a general overview.

## 4.1 Propofol dataset

The *propofol* dataset was collected as part of a study on propofol dose selection [375]. All subjects were recruited at the NICU of the University Hospitals Leuven, Leuven, Belgium. The trial was registered on ClinicalTrials.gov as NCT01621373. Ethical approval was provided by the ethical committee at the University Hospitals Leuven, Leuven, Belgium and informed consent from parents was obtained.

In the original study, 50 neonates were included. Due to incomplete data and overly noisy channels found in 28 neonates, only 22 of the 50 neonates are included in the signal processing studies outlined in this thesis. These neonates were all sedated using propofol as part of an INSURE (intubation, surfactant, and extubation) procedure. The neonates are characterized by a median (IQR) PMA of 30 (28.25–30) weeks, a median (IQR) postnatal age (PNA) of 1 (1–1) days, and a median (IQR) propofol dose (Diprivan 1%; AstraZeneca, Brussels, Belgium) of 1 (1–1.5) mg kg<sup>-1</sup> (Table 4.2). More information about the clinical characteristics of the subjects can be found in the original paper describing the dataset [375].

The systemic variables (HR (bpm), MABP (mmHg), and SpO<sub>2</sub> (%)) were measured with IntelliVue MP70 (Philips, Eindhoven, The Netherlands) with a Nellcor pulse oximeter. These variables were recorded continuously with a sampling frequency of 1 Hz (Rugloop; Demed, Temse, Belgium). All 22 neonates had an arterial line, which enabled an invasive measurement of MABP. NIRS was used to measure rScO<sub>2</sub> (%) noninvasively with INVOS 5100 using a cerebral neonatal OxyAlert NIRS sensor (Covidian, Mansfield, Massachusetts). As for the systemic variables, the sampling frequency for rScO<sub>2</sub> is equal to 1 Hz. Cerebral functioning was assessed using a one-channel EEG ( $\mu$ V). The EEG was measured between C3 and C4 (Figure 2.9) at a sampling frequency of 100 Hz (Olympic Cerebral Function Monitor 6000, Natus).

The multimodal dataset used in this study consists of concomitant measurements

Table 4.1: Overview of the datasets used throughout this thesis: the propofol dataset, the congenital diaphragmatic hernia (CDH) dataset, esophageal atresia (EA) dataset and the postnatal dataset.

$N$	location	GA (weeks)	PNA (days)	parameters	description
Propofol dataset					
22	Leuven	25-38	1-19	HR, ABP, SpO <sub>2</sub> , rScO <sub>2</sub> , EEG	Neonates undergoing INSURE. Data is recorded from the moment of propofol administration up to 12 hours after.
CDH dataset					
44	Rotterdam, Mannheim	35-41	2-12	HR, ABP, SpO <sub>2</sub> , rScO <sub>2</sub> , EEG, tcCO <sub>2</sub> , T <sup>o</sup> , drug list	Neonates with a congenital diaphragmatic hernia undergoing surgery to repair the defect. Data is recorded over multiple days in the perioperative period.
EA dataset					
27	Rotterdam	32-40	1-5	HR, ABP, SpO <sub>2</sub> , rScO <sub>2</sub> , EEG	Neonates with an esophageal atresia undergoing surgery to repair the defect. Data is recorded over multiple days in the perioperative period.
Postnatal dataset					
106	Graz	31-40	0	HR, SpO <sub>2</sub> , rScO <sub>2</sub>	Measurements of vital signs immediately after birth: measurements start after less than a minute.

Table 4.2: Propofol dataset demographics, including PMA, PNA, cUS findings, and propofol dose.

	$N$	$P_{25}$	$P_{50}$	$P_{75}$
PMA (weeks)	22	28.25	30	30
PNA (days)	22	1	1	1
cranial ultrasound				
inhomogeneous echodensities	6			
IVH, grade I or II	3			
propofol ( $\text{mg kg}^{-1}$ )	22	1	1	1.5

of five signal modalities (HR, MABP,  $\text{SpO}_2$ ,  $\text{rScO}_2$ , EEG), recorded from 5 min before propofol administration up to 10 hours after. For each neonate, a six hour long segment of multimodal data was considered in the analysis, with the start aligned at the moment of propofol administration. This length was defined based on the shortest recording found in the dataset to provide uniformity.

Using a six hour window allows to study the effect of propofol and the recovery period. Propofol is a three-compartment drug, characterized by a short  $\alpha$  and  $\beta$  (median estimates of 1 and 13 min, respectively) and a long  $\gamma$  half-life (median estimate of 350 min) [113, 9]. The pharmacodynamic effects are primarily associated with the first ( $\alpha$ ) and second ( $\beta$ ) exponential half-life, which indicates that the effect of propofol at the end of the analysis window is minimal [375, 418, 136]. Therefore, the analysis window is divided in two parts: the first three hours are used to study the response to propofol, while the last three hours are used as a reference. Figure 4.1 presents an example of a six hour long segment of multimodal data for one neonate from the group of study.

## 4.2 Congenital diaphragmatic hernia dataset

The *congenital diaphragmatic hernia* (CDH) dataset was collected in a multicenter, observational, prospective study on perioperative neuromonitoring in neonates with CDH undergoing surgery in one of two tertiary pediatric expertise centers: the Erasmus MC Sophia Children’s Hospital, Rotterdam, The Netherlands, and the Mannheim University Hospital, Mannheim, Germany. The neonates were managed according to the revised 2016 CDH-EURO consortium guidelines [222]. The trial was registered as NL6972. Ethical approval was provided by the Medical Ethics Committee at the Erasmus University Medical

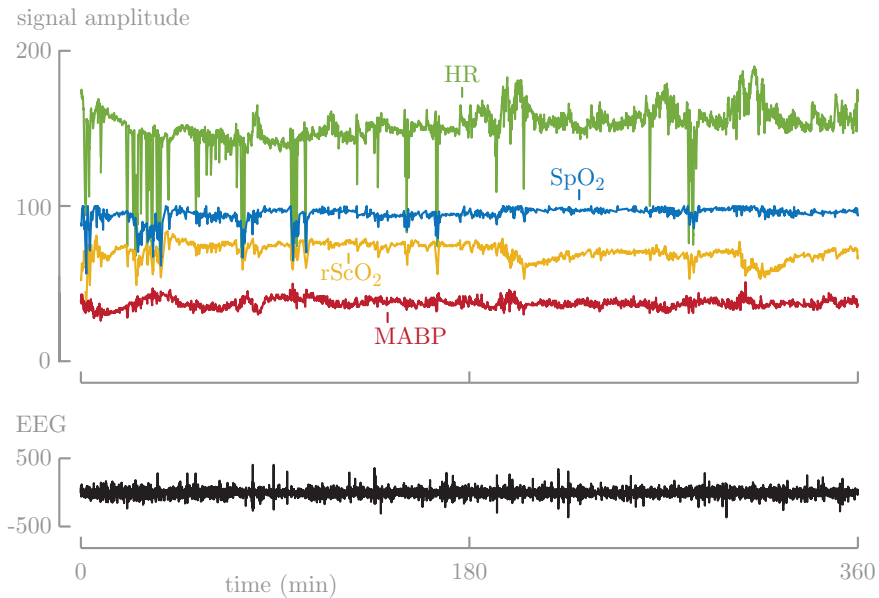


Figure 4.1: A six hour long segment of multimodal data for one patient (PMA: 27 weeks, PNA: 2 days) in the propofol dataset (raw data, as received), including HR (bpm), SpO<sub>2</sub> (%), rScO<sub>2</sub> (%), MABP (mmHg), and EEG ( $\mu$ V).

Center, Rotterdam, The Netherlands. Informed consents from both parents was obtained.

CDH neonates were eligible for inclusion between July 2018 and July 2020 if scheduled to receive surgical treatment within the first 28 days of life, regardless of the type of surgery (open or minimal access). Exclusion criteria were a major cardiac or chromosomal anomaly, or a syndrome associated with altered cerebral perfusion or major neurodevelopmental impairment. During this period, 44 neonates were included. The neonates are characterized by a median (IQR) GA of 38+1 (37+2–38+3), a median (IQR) PNA of 4 (3–6) days, and a median (IQR) birth weight (BW) of 3000 (2493–3285) grams (Table 4.3). 25 of the included neonates are male, 19 are female.

In the perioperative period, seven signals (five modalities) were measured simultaneously. HR (bpm), MABP (mmHg), using an indwelling arterial catheter, and SpO<sub>2</sub> (%) were measured at 1 Hz (Primus, Draeger, Luebeck, Germany). Two frontal rScO<sub>2</sub> (%) channels, measured using NIRS, were

Table 4.3: CDH dataset demographics, including GA, PNA, BW, sex, cUS findings, and Apgar scores.

	<i>N</i>	<i>P</i> <sub>25</sub>	<i>P</i> <sub>50</sub>	<i>P</i> <sub>75</sub>
GA (weeks)	44	37+2	38+1	38+3
PNA (days)	44	3	4	6
BW (days)	44	2493	3000	3285
sex				
male	25			
female	19			
cranial ultrasound				
choroid plexus cyst	1			
IVH, grade II	1			
IVH, grade III	1			
periventricular echodensities	1			
enlarged ventricles	2			
Apgar				
1	36	5	7	7
5	37	7	8	8
10	35	7	8	9

recorded at 1 Hz (neonatal sensor, INVOS 5100C, Covidien, Boulder, Colorado, United States). Two EEG channels, left (C3–P3) and right (C4–P4) (Figure 2.9), were measured at 256 Hz (BrainRT, OSG, Rumst, Belgium). Measurements started the day before surgery and continued until 24 hours postoperatively. The ECG was recorded at 200 Hz during surgery (Primus, Draeger, Luebeck, Germany).

Perioperative management, including physiological parameters and pharmacologic therapy, was recorded in the electronic patient data management system (HiX, Chipsoft BV, Amsterdam, the Netherlands). In Rotterdam, the Shell+ RT software Suite of the BrainRT was reprogrammed for real-time data extraction. In Mannheim, AnStat software (Carepoint, Ede, the Netherlands) was used for real-time data extraction. Both software extracted data in the same manner. The vasoactive inotropic scores (VIS), which reflect the need and grade of vasoactive/inotropic pharmaceutical intervention were computed manually. This score presents the necessity of cardiovascular support [129]. On the days before and after the day of surgery, each patient received a cranial ultrasound, performed by an experienced paediatric radiologist or neonatologist, to screen for intracranial abnormalities and brain injury.

Patients were operated in the operating room (OR) if transport was possible, and at the NICU if transport to the OR was impossible due to cardiorespiratory instability, or if the clinicians preferred to perform surgery in the NICU. In the OR, anesthesia was based on continuous administration of inhaled sevoflurane with bolus of fentanyl and rocuronium, performed by a pediatric anesthesiologist. Patients operated at the OR underwent thoracoscopic surgery if they were hemodynamically stable and if the liver was not herniated. In the NICU, anesthesia was based on continuous midazolam, continuous fentanyl, bolus fentanyl and continuous vecuronium, guided by a neonatologist or pediatric intensivist. Neonates on VA-ECMO were operated in the PICU and received continuous midazolam and morphine with a bolus of fentanyl and rocuronium, guided by a pediatric intensivist.

### 4.3 Esophageal atresia dataset

The *esophageal atresia* (EA) dataset was collected in a multicenter, observational, prospective study on perioperative neuromonitoring in neonates with EA undergoing surgery in the Erasmus MC Sophia Children's Hospital, Rotterdam, The Netherlands. EA patients were treated according to the protocol of the Dutch Consortium Esophageal Atresia. The trial was registered as NL6972. Ethical approval was provided by the Medical Ethics Committee at the Erasmus University Medical Center, Rotterdam, The Netherlands. Informed consents from both parents was obtained.

EA neonates were eligible for inclusion between July 2018 and July 2020 if scheduled to receive surgical treatment within the first 28 days of life, regardless of the type of surgery (open or minimal access). Neonates were excluded when major cardiac or chromosomal anomalies, syndromes associated with altered cerebral perfusion, or syndromes associated with major neurodevelopmental impairment were present or if the patient needed extracorporeal membrane oxygenation treatment. During this period, 27 neonates were included. The neonates are characterized by a median (IQR) GA of 38+4 (36–40), a median (IQR) PNA of 2 (1–3) days, and a median (IQR) BW of 2900 (2080–3183) grams (Table 4.4). 11 of the included neonates are male, 16 are female.

In the perioperative period, seven signals (five modalities) were measured simultaneously. HR (bpm), MABP (mmHg), using an indwelling arterial catheter, and SpO<sub>2</sub> (%) were measured at 1 Hz (Primus, Draeger, Luebeck, Germany). Two frontal rScO<sub>2</sub> (%) channels, measured using NIRS, were recorded at 1 Hz (neonatal sensor, INVOS 5100C, Covidien, Boulder, Colorado, United States). Two EEG channels, left (C3–P3) and right (C4–P4)

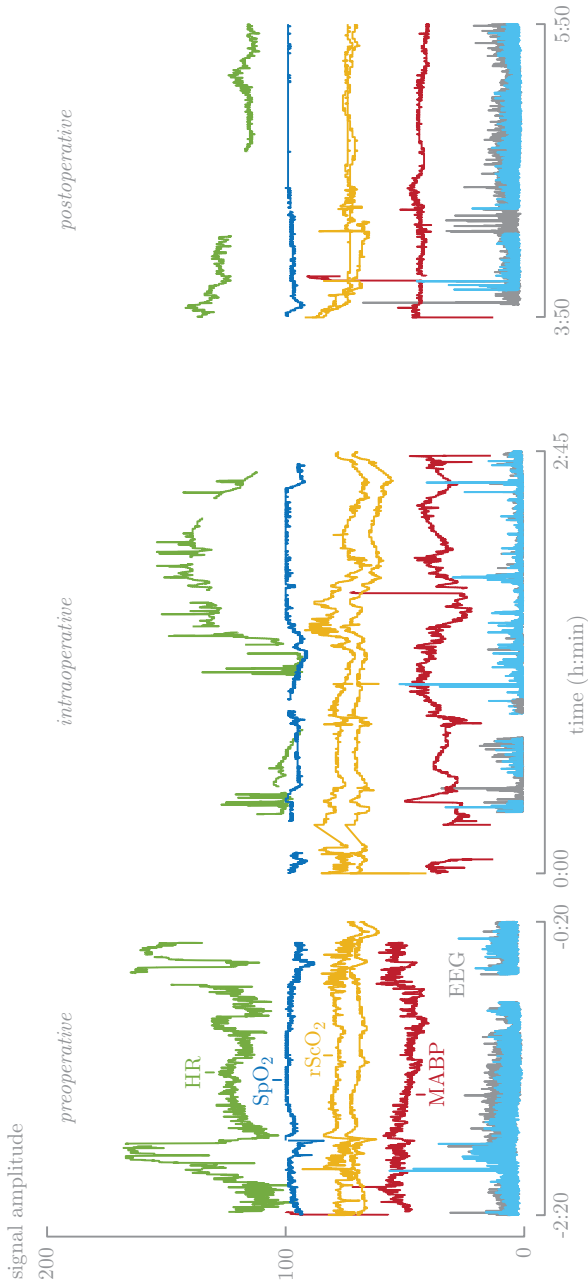


Figure 4.2: A seven hour long segment of multimodal data for one patient (GA: 38 weeks, PNA: 2 days, BW: 3500 grams, liver up, Boston C, open surgery at OR, measured in Rotterdam) in the CDH dataset (processed), including HR (bpm), SpO<sub>2</sub> (%), rScO<sub>2</sub> (%), MABP (mmHg), and EEG  $\delta$  power ( $\mu V^2$ ). Approximately 14 and 24 hours of data were measured before and after surgery, respectively, but only 2 hours are shown.

Table 4.4: EA dataset demographics, including GA, PNA, BW, and sex. No abnormalities were observed on cUS in any of the included neonates.

	$N$	$P_{25}$	$P_{50}$	$P_{75}$
GA (weeks)	27	36	38+4	40
PNA (days)	27	1	2	3
BW (days)	27	2080	2900	3183
sex				
male	11			
female	16			

(Figure 2.9), were measured at 256 Hz (Rotterdam: BrainRT, OSG, Rumst, Belgium. Mannheim: Braintrend, Fritz Stephan GMBH, Gackenbach, Germany). Measurements started the day before surgery and continued until 24 hours postoperatively. The ECG was recorded at 200 Hz during surgery (Primus, Draeger, Luebeck, Germany).

Perioperative management, including physiological parameters and pharmacologic therapy, was recorded in the electronic patient data management system (HiX, Chipsoft BV, Amsterdam, the Netherlands). The VIS were computed manually. On the days before and after the day of surgery, each patient received a cranial ultrasound, performed by an experienced paediatric radiologist or neonatologist, to screen for intracranial abnormalities and brain injury.

## 4.4 Neonatal dataset

The neonatal dataset was collected for a post-hoc analysis of data obtained from a prospective observational study, conducted at a tertiary center, the Division of Neonatology, Department of Pediatrics and Adolescent Medicine, Medical University of Graz. This study was approved by the Regional Committee on Biomedical Research Ethics (EC number 27-465 ex 14/15). Written informed consent was obtained before the birth of the infant.

Term and preterm infants, delivered by Caesarean section with decision to conduct full life support, were included in the prospective observational study. Infants with severe cardio-circulatory, pulmonary, or cerebral congenital malformation were excluded. Antepartum medical history and birth history were collected. For the post-hoc analysis, 106 neonates included in 2018 were considered as representative for the target population. The neonates are characterized by a median (IQR) GA of 38+3 (25+6–39) weeks, a median

Table 4.5: Neonatal dataset demographics, including GA, PNA, BW, length, head size, sex, and Apgar scores.

	$N$	$P_{25}$	$P_{50}$	$P_{75}$
GA (weeks)	106	35+6	38+3	39
PNA (days)	106	0	0	0
BW (days)	106	2326	2960	3360
length (cm)	106	46	49	51
head (cm)	106	33	34	35
sex				
male	57			
female	49			
Apgar				
1	106	9	9	10
5	106	9	10	10
10	106	9	10	10

(IQR) PNA of 0 (0–0) days, and a median (IQR) BW of 2960 (2326–3360) grams. 57 of the included neonates are male, 49 are female. Birth time was defined when the neonate was fully delivered. Cord clamping was routinely performed more than 30 seconds delayed. Afterwards, the neonates were placed in supine position on the resuscitation desk under an overhead heater. The neonates were dried and wrapped into warmed towels. The immediate postnatal transition care was according to the latest European Resuscitation Guidelines (**LIT**).

Three signals were measured during the first 15 min of life. Immediately after birth a NIRS sensor was fixed on the left fronto-parietal side using a modified CPAP cap or an elastic bandage. NIRS measurements were performed using the INVOS Cerebral/Somatic Oximeter Monitor (Medtronic, Minneapolis, MN, U.S.A.) with a neonatal transducer. Measurements of SpO<sub>2</sub> and HR were performed using pulse oximetry at the right hand or wrist with the IntelliVue MP30 Monitor (Philips, Amsterdam, The Netherlands). Measurements were performed during the first 15 minutes after birth. All variables were stored in a multichannel system *alpha-trace digital MM* (BEST Medical Systems, Vienna, Austria) at a sampling frequency of 1 Hz. The fractional tissue oxygen extraction (FTOE) was computed as an additional parameter from the rScO<sub>2</sub> and SpO<sub>2</sub> as defined in Equation 2.8.

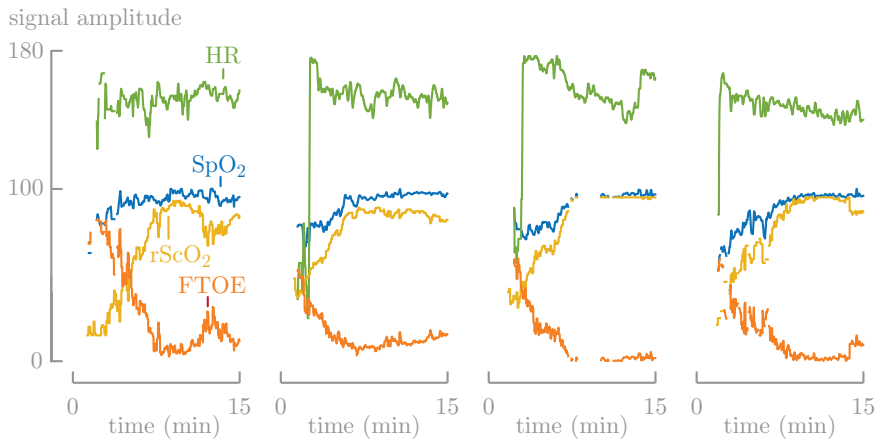


Figure 4.3: A 15 min long segment of multimodal data for four patients (GA: 37+2, 39, 34+1, 38+5 weeks from left to right, respectively) in the neonatal dataset (raw data, as received), including HR (bpm), SpO<sub>2</sub> (%), rScO<sub>2</sub> (%) and FTOE (%).

## 4.5 Conclusion

This chapter introduced four clinical settings, which are used in the following chapters to validate our proposed methodology. The propofol dataset is composed of neonates undergoing INSURE, measured over a period of six hours after propofol administration. The CDH and EA datasets include neonates undergoing non-cardiac-major surgery in the first days of life, measured over multiple days in the perioperative period. The neonatal dataset presents 15 min long measurements of vital signs during immediate transition after birth.



PA

RT

# UNI- VARIATE ANALYSIS



univariate analysis

05

# Heart rate variability during non-cardiac-major surgery

*based on:*

Hendrikx, D.\*, Costerus, S.\*, Van Huffel, S., de Graaff, J., Wijnen, R., Caicedo, A., Tibboel, D., Naulaers, G. Heart rate variability during non-cardiac-major surgery. Submitted (2021).

(\*: joint first author)



In awake neonates, a suppressed HRV is associated with adverse outcome, while during anesthesia, a lowered HRV indicates adequate anesthesia and analgesia. It remains unknown whether induced decreased HRV due to anesthetics is related to adverse outcome, since triggers for postoperative brain injury are still largely unknown. In this chapter, we investigate HRV in the transition from awake to anesthesia, and we relate various HRV metrics to diagnosis, demographics and medication.

## 5.1 Introduction

The surgical newborn is at risk for brain injury, since fluctuations in perioperative cerebral perfusion could trigger the development of brain injury [387]. CBF is regulated by vasomotor, chemical, metabolic, and neurogenic mechanisms, of which the ANS is an important factor. Anesthesia, surgery, and critical illness lead to a varied degree of physiological stress that alters the ANS. In adults, most anesthetics interfere with sympathetic neural activity and cardiovascular control [284]. In contrast to adults, the effect of sedatives and anesthetics on the neonatal ANS is still unknown.

The ANS is the regulatory system that controls most of the organ systems and homeostatic mechanisms [436, 270]. In general, the ANS consists of two components: the sympathetic (SNS) and the parasympathetic nervous system (PNS). The SNS prepares the body for the so-called *Fight-or-flight* response by increasing cardiac output and blood flow. The PNS is responsible for relaxation and moderating control over the active sympathetic system [436, 270]. Heart rate is controlled by an interplay between the SNS and PNS. Neonates have a higher heart rate which is related to cardiac-linked SNS predominance and decreased vagal tone [373]. The contribution of the PNS increases with PNA [415, 212]. Hence, the development of the cardiac autonomic innervation is not complete after birth [373]. To date, the understanding of ANS maturation in healthy term neonates is still limited [225].

The functional state of the ANS can be studied using heart rate variability (HRV) analysis, derived from the ECG [392], in which one evaluates the sympathovagal balance at the cardiac sinoatrial level by analyzing the fluctuations of the RR interval between consecutive sinus heartbeats. This reflects the dynamic interactions that exist between the heart and the ANS [240]. Large HRV is associated with being healthy, while reduced HRV is associated with a compromised cardiovascular system [2, 183, 413, 204], hypoxic-ischemic encephalopathy (HIE) [252], IVH [252], infection and sepsis [150] in preterm neonates. In addition, HRV provides information about the cardiac chronotropic

regulation and adaption postnatally [212], since the maturation of the ANS is accompanied by increasing HRV and a pronounced increase of parasympathetic activity [240]. Neonates present an immature cardiovascular control and ANS, which manifests with an extremely low vagal tone at rest, reflected by a very high heart rate. The immaturity manifests itself also as a weaker blood-pressure control and chemoregulation and a reduced baroreflex sensitivity.

A combination of time-domain, frequency-domain and nonlinear HRV metrics to capture all aspects of the ANS. Frequency-domain analysis allows to decompose the ANS into the sympathetic and parasympathetic branch [361]. One often computes the absolute and relative power in the low frequency (LF) and the high frequency (HF) bands and the LF/HF ratio. For interpretation, the relative power of LF and HF represent the the sympathetic and parasympathetic branch of the ANS, respectively, and LF/HF represents the sympathovagal balance. Numerous studies confirm that the weak parasympathetic tone is accompanied by a predominant LF tone [92, 75]. The heart rate evolves while the brain and the ANS mature: the cardiac frequency decreases, the HRV increases. A third component that can be derived from the spectral analysis is the very low frequency (VLF) band, which was recently found to be fundamental to health [225]. In non-anesthetized neonates, a decrease in VLF was found to be more strongly associated with all-cause mortality than LF and HF [225, 360].

During surgery, one of the most used anesthetics in the neonatal intensive care is sevoflurane. Sevoflurane is known to induce deep sleep in the neonate, characterized by a significant decrease in cerebral activity [85]. So far, the functional state of the ANS of the sick neonate has not been studied during surgery-induced deep sleep. In children, the autonomic balance was observed to shift during deep sleep, with more pronounced influences of the PNS [425]. In healthy term neonates, the sleep state was observed to affect various HRV parameters: in quiet sleep, HRV was lower and the contribution of the PNS branch increased [106].

The aim of this chapter was to quantify the effect of sevoflurane anesthesia on HRV in neonates undergoing major non-cardiac surgery.

## 5.2 Dataset

This study focused on neonates with EA and CDH, which are two major non-cardiac anomalies that require surgical repair within the first days of life. Details on the structure of the dataset and recording was presented in Section 4.2 (CDH) and 4.3 (EA).

Surgery was performed in the operating room (OR) and anesthesia was sevoflurane based (end expired concentration between 1% and 3%), with bolus fentanyl (induction:  $1\text{--}5 \mu\text{g kg}^{-1}$ ) and rocuronium ( $0.5\text{--}1.0 \text{ mg kg}^{-1}$ ), performed by a pediatric anesthesiologist. Repeated administration of analgesia was based on clinical evaluation. CDH neonates received continuous midazolam preoperatively, while EA neonates did not (Table 5.1).

## 5.3 Methods

**Tachogram** The tachogram was derived in four steps (Figure 5.1). First, the ECG was segmented into non-overlapping epochs of 5 minutes [360]. Second, the epoch signal quality was quantified to detect flatline and overly noisy epochs [264]. Only artifact-free epochs were considered for further analysis. If no clean epochs were found, the patient was completely discarded from the analysis. Third, R peaks were detected and located [263]. Last, various HRV metrics were computed, directly from the resulting RR time series (time-domain metrics) or after linear interpolation and resampling at 8 Hz (frequency-domain and nonlinear metrics) [181].

**HRV metrics** The *time-domain metrics* included the mean and the standard deviation (SDNN), which measures the variability of all frequency components, since the variance is equal to the total power of the spectral analysis. Both time-domain metrics are expressed in milliseconds (ms).

The sympathovagal activity was assessed using different *frequency bands* via the CWT (Section 3.3.2): the VLF (0–0.08 Hz), LF (0.08–0.2 Hz) and HF (0.2–3 Hz) bands [247, 92]. The CWT spectrogram was compressed by summing over frequencies and taking the median in each 5-min epoch. Computation of VLF, LF and HF power was done in absolute ( $\text{ms}^2$ ) and normalized units (n.u.):

$$\text{LF (n.u.)} = \frac{\text{LF}}{\text{LF} + \text{HF}} \quad (5.1)$$

$$\text{HF (n.u.)} = \frac{\text{HF}}{\text{LF} + \text{HF}} \quad (5.2)$$

The representation in normalized units emphasizes the controlled and balanced behavior of the two branches of the ANS and minimizes the effect of changes in total power. Finally, LF/HF was computed to define the autonomic balance.

*Nonlinear measurements* define the unpredictability of a time series, which results from the complexity of the HRV regulation mechanisms. In order to

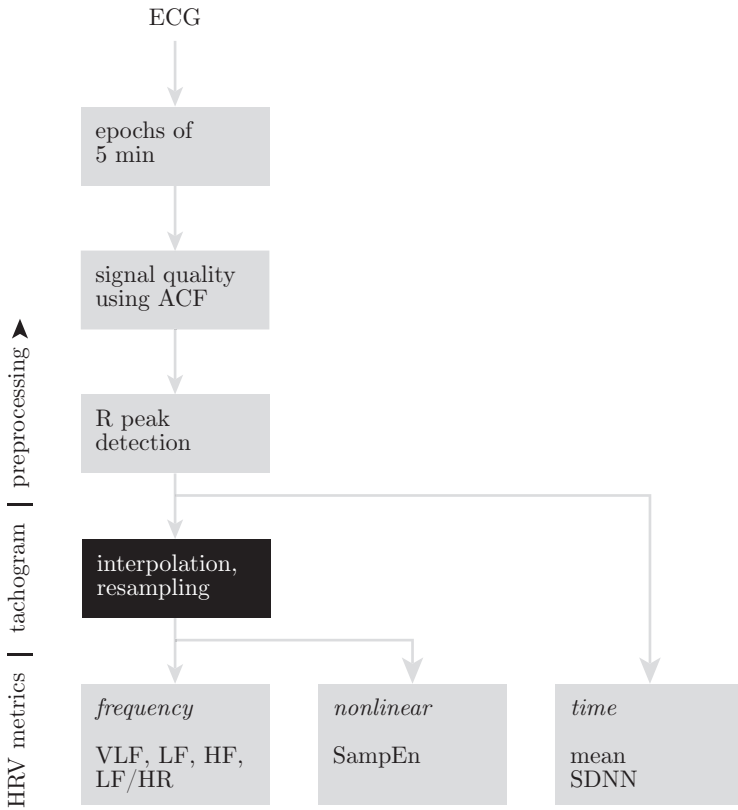


Figure 5.1: Data processing pipeline used to translate ECG to tachogram to various time-domain, frequency-domain and nonlinear HRV metrics.

Table 5.1: Patient demographics of the HRV study. Drug doses are presented as a mean over the intraoperative period (sevoflurane, midazolam, VIS) or as a sum of different boluses (fentanyl).

<i>demographics</i>		
sex		male: 12, female: 14
GA	(weeks)	38+3 (36+3–40+1)
PNA	(days)	2 (2–3)
BW	(g)	2985 (2280–3230)
<i>diagnosis</i>		EA: 12, CDH: 14
<i>surgery</i>		
type		open: 8, conversion: 8, thoracoscopy: 10
duration	(hh:mm)	01:48 (01:15–02:34)
<i>medication</i>		
sevoflurane	(end-expired, %)	1.7 (1.3–2.0)
midazolam	$\mu\text{g kg}^{-1} \text{h}^{-1}$	57 (0–103.8)
fentanyl	$\mu\text{g kg}^{-1}$	3.5 (0–8.8)
VIS		7.3 (4.5–12.6)

quantify complexity, sample entropy was used, following its robustness on short time series [221, 237].

**Statistical analysis** Data are presented as median (IQR). The temporal analysis of the HRV metrics was done using the Wilcoxon signed-rank test (Section 3.6.1), due to the small sample size, which impedes the assumption of normality. The HRV metrics were analyzed using LME models (Section 3.6.2), for which the significance of the fixed effects was assessed using the LR test (Section 3.6.1). Significance was defined as  $\alpha = 0.05$ .

## 5.4 Results

**Demographics** Thirty-three patients were eligible for inclusion. One patient was removed because of overly noisy data and six patients were removed because of flatline data. The patient demographics of the resulting 26 patients were collected in Table 5.1.

Table 5.2: Statistical significance of fixed effects in LME analysis. Sex, PNA, BW, intraoperative midazolam and fentanyl dose were removed as explanatory variables from the model, as they did not contribute significantly to any of the models. The remaining fixed effects included diagnosis, surgery type, GA, end-expired sevoflurane concentration and VIS, for which the  $p$  values are listed in this table.

	diagnosis	surgery	GA	sevoflu- rane	VIS
<i>time domain</i>					
mean (ms)	.52	.72	.08	.006	< .001
SDNN (ms)	.006	.15	.46	.77	.83
<i>frequency domain</i>					
VLF (ms <sup>2</sup> )	.06	.06	.019	.41	.039
LF (ms <sup>2</sup> )	.19	.12	.036	.26	.24
LF (n.u.)	.81	.21	.06	.26	.49
HF (ms <sup>2</sup> )	< .001	.006	.87	.004	.14
HF (n.u.)	.81	.21	.06	.46	.49
LF/HF	.78	.27	.034	.55	.36
<i>nonlinear</i>					
SampEn	.67	.91	.71	.005	.046

**Baseline** For seven neonates, data was available in the period they were still awake before surgery started (Figure 5.2). In all other neonates, the ECG recording was only started after the start of anesthesia. Over the transition from awake to anesthesia, we observed a significant decrease in SDNN ( $p = .047$ ), in absolute power in the VLF ( $p = .016$ ), LF ( $p = .031$ ) and HF ( $p = .047$ ) frequency band, in LF/HF ( $p = .031$ ) and in relative power in the LF band ( $p = .031$ ). The relative power in the HF frequency band increased significantly ( $p = .031$ ). The mean RR and the sample entropy did not show a significant trend.

**Linear mixed-effects model** For each of the nine HRV metrics, a LME model was fitted. Sex, PNA, BW, intraoperative midazolam and fentanyl dose were removed as explanatory variables from the model, as they did not contribute significantly to any of the models, as assessed by the LR test. The remaining fixed effects included diagnosis (EA or CDH), surgery type (thoracoscopy, conversion or open), GA, end-expired sevoflurane concentration and VIS, for which the  $p$  values are presented in Table 5.2.

The diagnosis was observed to influence both SDNN ( $p = .006$ ) and the absolute

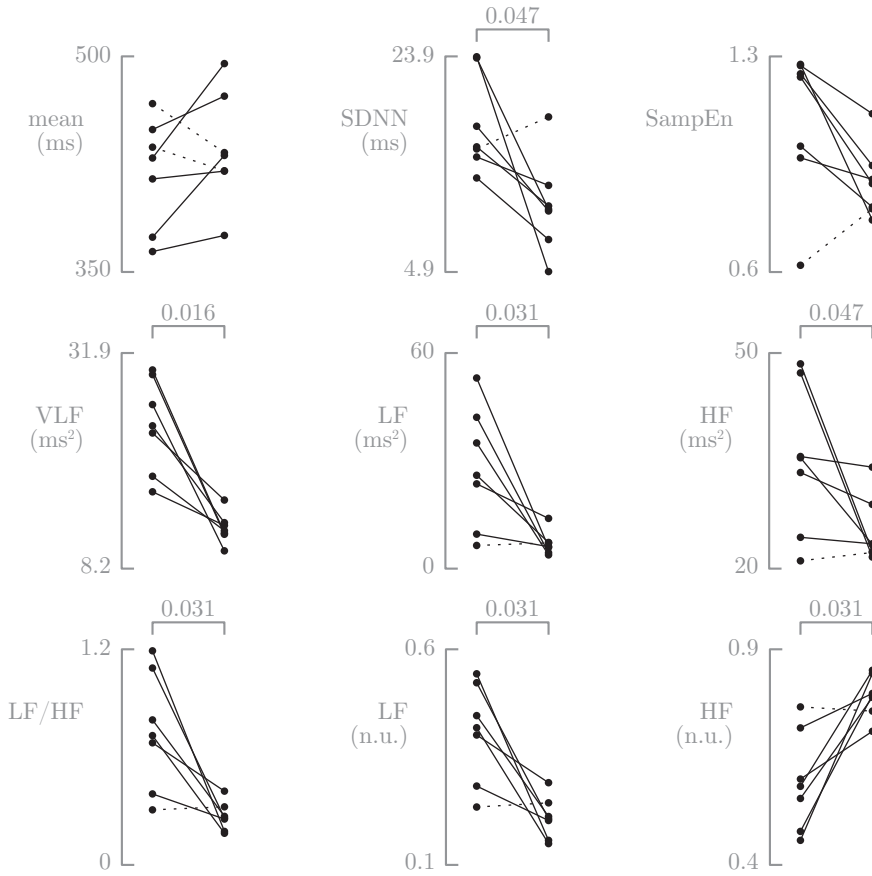


Figure 5.2: HRV metrics in a cohort with baseline data (seven neonates) changed significantly when transitioning from awake to sevoflurane-based anesthesia. The majority trend (increase or decrease) is indicated by solid lines.

power in the HF band ( $p < .001$ ). Both parameters were larger for CDH compared to EA. The type of surgery impacted the absolute power in the HF band ( $p = .006$ ), which increased from conversion to open to thoracoscopic surgery. Changes in GA were associated with changes in absolute power in the VLF ( $p = .019$ ) and LF band ( $p = .036$ ), as well as the LF/HF ratio ( $p = .034$ ) (Figure 5.3). All three parameters decreased with increasing GA. The end-expired sevoflurane concentration was observed to alter the mean RR interval ( $p = .006$ ), the absolute power in the HF band ( $p = .004$ ) and the sample entropy ( $p = .005$ ) (Figure 5.4). All three parameters decreased with increasing sevoflurane concentration. The VIS impacted the mean RR interval ( $p < .001$ ), the absolute power in the VLF band ( $p = .039$ ) and the sample entropy ( $p = .046$ ) (Figure 5.5), which all decreased with increasing VIS.

## 5.5 Discussion

**Baseline** In seven patients, the ECG included baseline epochs, measured before sevoflurane administration, which showed that the HRV metrics drastically changed when the neonate underwent anesthesia (Figure 5.2). Despite the small subcohort size, the trends were clear and statistically significant. Furthermore, these trends are in line with a study in healthy newborns [106] and numerous studies in adults [245]. Three observations could be made, based on the data. First, in the transition from awake to anesthesia, we observed a decrease in total HRV, indicated by the decrease in SDNN and the decrease in absolute VLF, LF and HF power. The values recorded during surgery were lower compared to reference neonatal HRV metrics reported in literature [225]. In awake neonates, a lowered HRV might point towards a compromised cardiovascular system [2, 183, 413, 204]. During anesthesia, a lowered HRV might be used as an indicator for adequate analgesia and anesthesia, since anesthesia aims to blunt the natural stress response of the surgical trauma, which translates into a reduction in HRV [361]. It is hard to take apart these two effects in our data (a lowered HRV following a comprised cardiovascular system or adequate anesthesia) as literature about HRV in anesthetized neonates is lacking. The decrease in HF might result from an altered respiration following the transition from spontaneous breathing to mechanical ventilation at a fixed rate. Since the HF band includes the respiratory sinus arrhythmia, it could change following a change in respiration pattern. Second, no clear trends were observed in mean HR (mean RR interval) nor in complexity (sample entropy). The amplitude of the HR signal doesn't change significantly, but its dynamics change vastly under anesthesia. Third, a shift in autonomic balance was observed in the transition from awake to anesthesia: LF/HF decreased and relative power in the LF and HF band decreased and increased, respectively, indicating that the

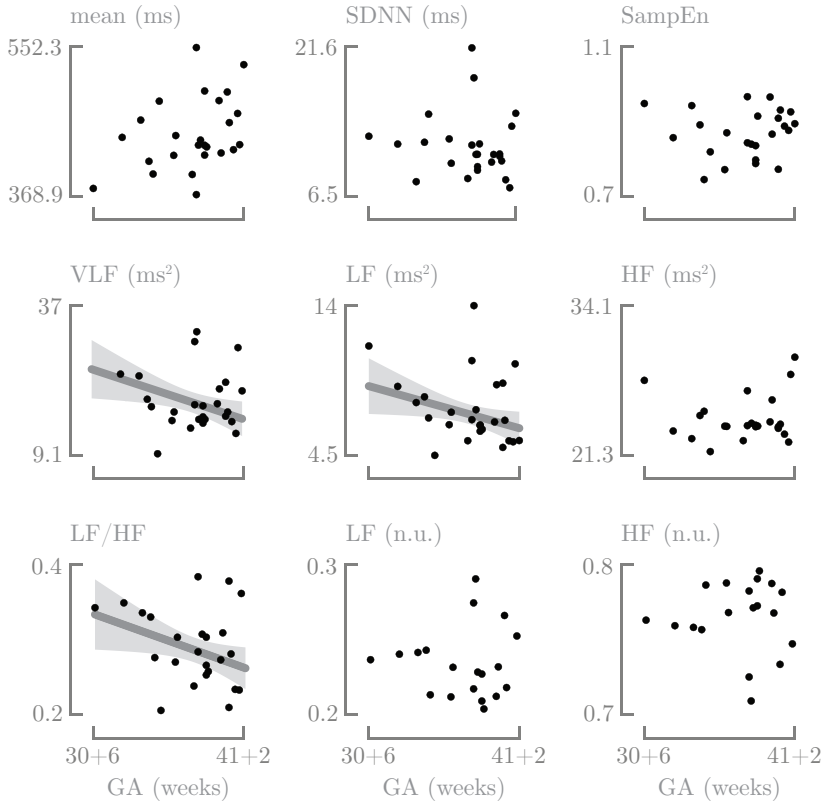


Figure 5.3: GA age significantly alters absolute power in the VLF and LF band, as well as the LF/HF ratio. The dots present the patient means. The LME model was fitted on all data.

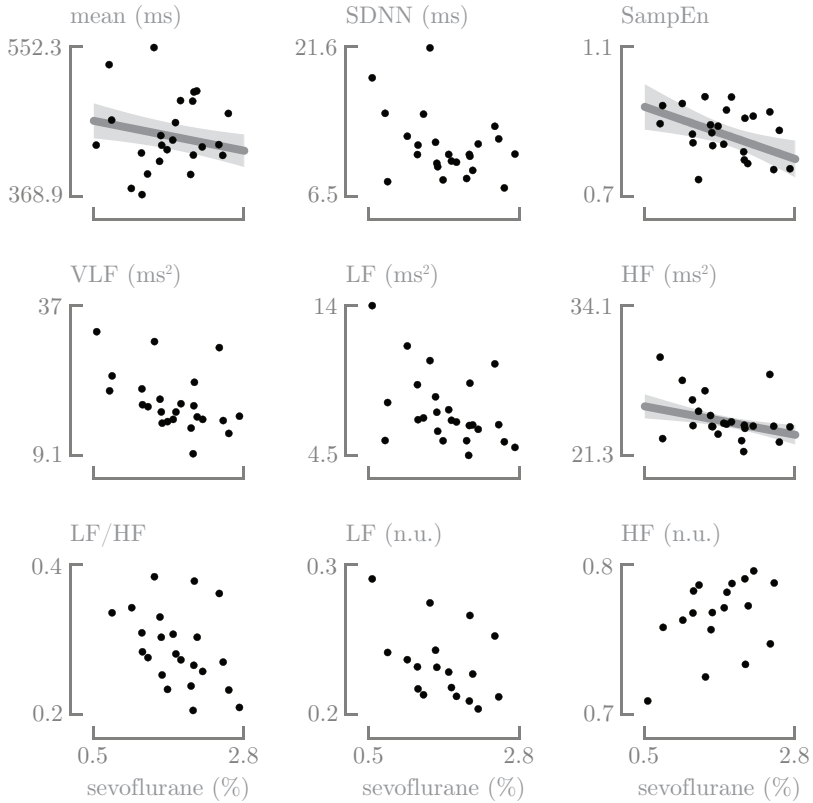


Figure 5.4: End expired sevoflurane concentration (%) significantly alters the mean RR interval, the sample entropy, and the absolute power in the HF band. The dots present the patient means. The LME model was fitted on all data.

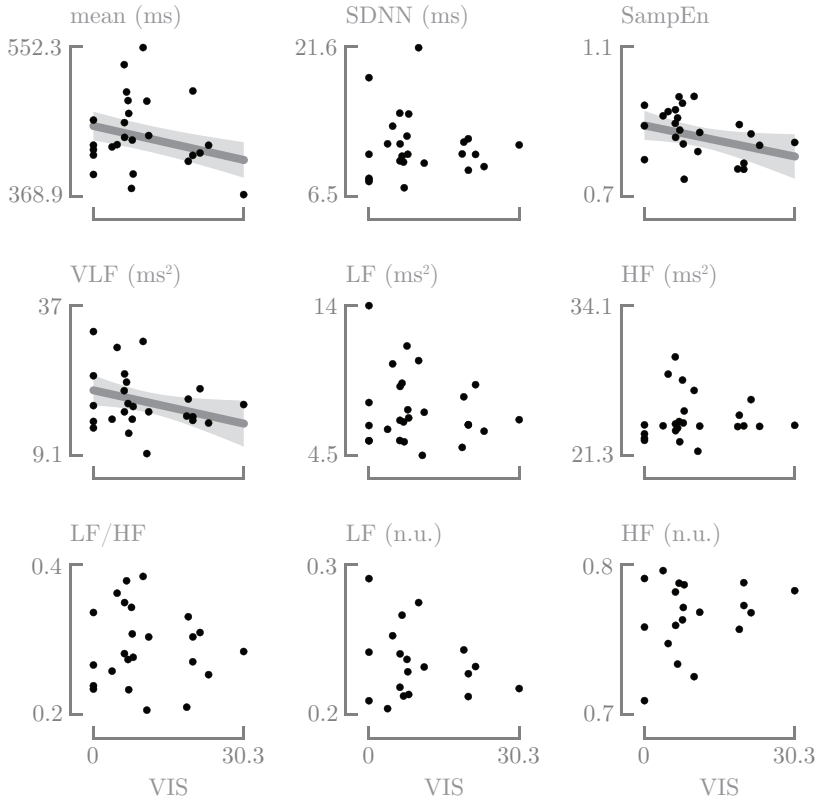


Figure 5.5: VIS significantly alters the mean RR interval, the sample entropy, and the absolute power in the VLF band. The dots present the patient means. The LME model was fitted on all data.

contribution of the sympathetic branch reduces, while the contribution of the parasympathetic branch increases. This reflects the desired effect of anesthesia, which is to reduce stress.

**Diagnosis** We observed a significantly lower SDNN and power in the HF band for the EA group compared to the CDH group (Table 5.2). SDNN measures total HRV, since it measures the combined power of all frequency components. The difference in SDNN reflects the difference in absolute power in the HF band, since the absolute power in the VLF and LF band were comparable among the groups. Since HF correlates with PNS, this could suggest that the PNS is already more mature in the CDH group compared to the EA group.

**Maturation** Postnatal adaption and maturation of the ANS have a significant effect on the HRV parameters. The vagal tone increases with increasing GA, but the development of the LF and VLF is faster than the vagal increase [75, 87]. This is confirmed by our data, which showed a decreased power in the VLF and the LF band and a shift in autonomic balance with increasing GA (Figure 5.3). A good maturation of the ANS requires at least a GA of 37 weeks [125]. In addition, the ANS continues to develop in the first weeks postnatally. Therefore, we initially included PNA as a confounder in our models, but we observed no significant effect of PNA. The PNS reaches maturity within a few days after birth, while the SNS reaches maturity by early infancy. In this period, the ANS is vulnerable to adverse environmental and physiologic influences [271].

**Surgery** Absolute power in the HF frequency band increased from conversion to open to thoracoscopic surgery. Minimally invasive surgery is generally recognized as an improvement in the field of surgery, due to benefits including a shorter operating and recovery time, minimizing stress and pain due to smaller incisions, and even improving mortality [83, 82]. Our results seem to confirm a smaller stress response in the neonates on thoracoscopic repair, as indicated by the increased power in the HF band, which correlates with the parasympathetic branch of the ANS.

**Medication** We studied various administered drugs to explain the differences in HRV metrics: sevoflurane, midazolam, fentanyl and the combined action of vasoactive and inotropic medication (VIS). The anesthetic effect of sevoflurane is predominantly mediated by the  $\alpha 1$ -subunit of the GABA<sub>A</sub> receptor [186, 182]. We observed a decrease in mean RR interval (a higher HR), in absolute power in the HF band and in sample entropy with increasing end-expired sevoflurane

concentration (Figure 5.4). Sevoflurane mediates a decrease in myocardial contractility and MABP, which can be compensated for by an increase in HR [300]. Midazolam is a short-acting benzodiazepine which acts by binding to the benzodiazepine receptor at the intersection between  $\alpha$  and  $\gamma$  subunits of the GABA<sub>A</sub> receptor in the CNS [347, 285]. Midazolam was administered in 6 of the patients, but did not have an effect on HRV. Fentanyl was administered in all of the patients and also didn't affect the HRV. VIS reflects the grade of vasoactive and inotropic pharmaceutical intervention and quantifies the necessity for cardiovascular support. Increasing VIS was associated with a decrease in mean RR interval (increase in HR), a decrease in absolute power in the VLF band and a decrease in sample entropy (Figure 5.5), which could be explained by association between the VLF band and hormonal regulation. The administration of vasoactive or inotropic medication causes an increase in stress hormone levels affecting the hormonal regulation, which is reflected by a decrease in VLF.

## 5.6 Conclusion

Sevoflurane-based anesthesia didn't affect HR, but significantly suppressed the ANS, as indicated by a decrease in all HRV metrics, except entropy. In addition, the contribution of the sympathetic and parasympathetic branch decreased and increased, respectively, reflecting the desired effect of anesthesia, which is to reduce stress. The type of congenital anomaly, GA, the administered sevoflurane concentration as well as the vasoactive and inotropic medication affected the HRV in neonates intraoperatively. In awake neonates, a suppressed HRV is associated with adverse outcome. During anesthesia, a lowered HRV indicates adequate anesthesia and analgesia. It remains unknown whether induced decreased HRV due to anesthetics is related to adverse outcome since triggers for postoperative brain injury are still largely unknown.

univariate analysis

06

# Cerebral oxygenation and activity during surgical repair of neonates with congenital diaphragmatic hernia

*based on:*

Hendrikx, D.\*, Costerus, S.\*, IJsselmuiden, J., Zahn, K., Perez-Ortiz, A., Van Huffel, S., Flint, R., Caicedo, A., Wijnen, R., Wessel, L., de Graaff, J., Tibboel, D. and Naulaers, G. Cerebral oxygenation and activity during surgical repair of neonates with congenital diaphragmatic hernia: a comparative analysis. Accepted for publication in *Frontiers in Pediatrics* (2021).

(\*: joint first author)



Neonatal brain monitoring is increasingly used due to reports of brain injury perioperatively. Little is known about the effect of sedatives and anesthetics on cerebral oxygenation and activity. In this chapter, we study these effects in the perioperative period in a cohort of neonates with a CDH using a univariate analysis, based on signal amplitude and power in different EEG bands.

## 6.1 Introduction

Clinicians are increasingly monitoring the neonatal brain during high-risk neonatal surgery, due to the increased number of neonates who develop brain injury perioperatively and the subsequent impaired neurodevelopmental outcome [244, 388, 228, 387]. Multimodal brain monitoring is needed to monitor the interplay between cerebral oxygenation and activity [85]. NIRS presents a continuous, non-invasive measurement of brain oxygenation ( $rScO_2$ ), with reference values between 55 and 85% for awake neonates [104]. Baseline  $rScO_2$  can however vary as a result of sensor placement [381, 200], sensor type [206, 207], and the measurement device [205, 7]. Furthermore, FTOE can be used to analyze cerebral oxygen consumption [280]. Intraoperative use of NIRS has been explored, but no coherent results have been reported in non-cardiac neonatal surgery [85] and NIRS-guided treatment guidelines are only available in pediatric cardiac surgery [13].

The activity of the neonatal brain can be quantified using EEG, which measures the overall electrical activity of the cortical pyramidal neurons [243]. Consequently, EEG has a great sensitivity of showing changes in neural functioning [57]. The power of the EEG can be computed in different frequency bands. Delta oscillations ( $\delta$ : 0.5–4 Hz) dominate the neonatal EEG and regulate basic homeostatic needs [208], and can be further divided into slow delta ( $\delta_1$ : 0.5–2 Hz) and fast delta ( $\delta_2$ : 2–4 Hz). Noxious-evoked EEG activity can be studied by analyzing gamma oscillations ( $\gamma$ : 32–100 Hz) over the contralateral somatosensory cortex and by analyzing the fast delta band ( $\delta_2$ ) [117]. Strong increases in gamma  $\gamma$  oscillations and increased energy in the fast delta  $\delta_2$  frequency band was shown to reflect nociceptive pain in neonates following heel lance [117].

To date, little is known about the effect of anesthetic approaches on cerebral oxygenation [85, 80]. In this study, neonates with a CDH, treated according to a standardized international guideline [378], received two different anesthetic approaches intraoperatively: a sedative-agent (midazolam) versus an anesthetic-agent (sevoflurane), both supplemented with analgesia and muscle relaxation.

The aim of this study was to determine the effects of both approaches on cerebral oxygenation and cerebral activity in the perioperative period.

## 6.2 Dataset

This study focused on neonates with CDH, a major non-cardiac anomaly that requires surgical repair within the first days of life. Details on the structure of this datasets and the recording equipment were presented in Section 4.2.

The neonates enrolled in this study were stratified in two groups (Table 6.1). In Rotterdam, surgery was performed in the OR and anesthesia was sevoflurane-based (end expired concentration between 1% to 2%), with bolus fentanyl (induction  $1\text{--}5 \mu\text{g kg}^{-1}$ ) and rocuronium ( $0.5\text{--}1 \text{mg kg}^{-1}$ ), performed by a pediatric anesthesiologist. In Mannheim, surgery was performed at the NICU, and anesthesia was based on continuous midazolam ( $70\text{--}100 \mu\text{g kg}^{-1} \text{h}^{-1}$ ), fentanyl ( $2\text{--}5 \mu\text{g kg}^{-1} \text{h}^{-1}$ ) and vecuronium ( $0.1\text{--}0.3 \text{mg kg}^{-1}$ ), and bolus fentanyl ( $2\text{--}10 \mu\text{g kg}^{-1}$ ), performed by a neonatologist. Repeated administration of analgesia was based on clinical evaluation. Clinicians were blinded for EEG, but not for rScO<sub>2</sub>.

## 6.3 Methods

**Signal processing pipeline** Artifacts were removed from all input signals, based on a predefined physiological range (Section 3.2). Then, EEG power was extracted in three frequency bands:  $\delta_1$ ,  $\delta_2$  and  $\gamma$  using the CWT (Section 3.3.2), and FTOE was defined from SpO<sub>2</sub> and rScO<sub>2</sub> (Equation 2.8).

After these preprocessing steps, the signals were compressed to their mean in four data windows: the preoperative window (Pr: six to three hours before the start of surgery), the intraoperative window (In: entire surgical procedure), and two postoperative windows (Po3: three to six hours and Po15: 15 to 18 hours after the end of surgery). These data windows were used to balance the data and to remove transitional effects, such as artifacts of transport, artifacts of care, the effect of intraoperative administered medication.

**Correlations** Three correlations were studied to determine their effect on our results. First, the correlation between VIS and rScO<sub>2</sub>, FTOE was studied to clarify possible effects of cerebral vasoconstriction. Second, the correlation between the dose of the anesthetic drug and rScO<sub>2</sub>, EEG was defined to quantify

Table 6.1: Patient demographics of sevoflurane versus midazolam group.

	sevoflurane group	midazolam group	<i>p</i>
<i>N</i>	20	17	
male	11 (55%)	10 (59%)	.821
GA (weeks)	38+1 (36+5–38+5)	37+6 (34+5–38+1)	.111
PNA (days)	3 (2–4)	6 (3–12)	.008
BW (kg)	3.0 (2.7–3.3)	2.8 (1.9–3.1)	.070
Apgar 5 min	8 (8–9)	8 (7–8)	.478
o/e LHR	50 (41–58)	40 (33–54)	.337
left-sized defect	17 (85%)	11 (65%)	.977
liver-up	5 (25%)	12 (71%)	.005
hernia size (A–D)	6A, 8B, 5C, 1D	1A, 9B, 6C, 1D	.185
scheduled for			
thoracoscopy	8 (40%)	4 (23%)	.026
laparotomy	12 (60%)	13 (77%)	.026
conversion	8 (40%)	0 (0%)	.002
surgery duration (min)	95 (70–125)	182 (114–203)	.000
patch	12 (60%)	15 (88%)	.056
mechanical ventilation			
before	17 (85%)	17 (100%)	.101
VA-ECMO			
before	0 (0%)	5 (29%)	.022
during	0 (0%)	0 (0%)	1.00
rocuronium (mg kg <sup>-1</sup> )	0.8 (0.6–1.0)	-	
vecuronium			
induction (mg kg <sup>-1</sup> )	-	0.2 (0.15–0.21)	
during (mg kg <sup>-1</sup> h <sup>-1</sup> )	-	0.09 (0.05–0.10)	
fentanyl			
induction (μg kg <sup>-1</sup> )	2.3 (1.7–2.9)	5 (4–7)	.000
during (μg kg <sup>-1</sup> )	6.2 (4.1–11.5)	10 (7–17)	.119
during (μg kg <sup>-1</sup> h <sup>-1</sup> )	-	4 (3–5)	
sevoflurane (%)	1.5 (1.1–1.9)	-	
midazolam			
before (μg kg <sup>-1</sup> h <sup>-1</sup> )	47 (0–92)	40 (30–50)	.735
induction (μg kg <sup>-1</sup> )	1 (5%)	10 (59%)	.000
during (μg kg <sup>-1</sup> h <sup>-1</sup> )	47 (0–67)	100 (68–100)	.003
after (μg kg <sup>-1</sup> h <sup>-1</sup> )	39 (26–99)	50 (20–50)	.647
VIS			
before	0 (0–5)	17 (10–25)	.000
during	9 (5–17)	17 (12–35)	.010
after	2 (0–11)	17 (10–28)	.001

changes in cerebral oxygenation and activity related to the dose of the anesthetic drug. Third, the correlation between cerebral oxygenation and cerebral activity was investigated to study whether the assumption of reduced cerebral activity resulting in increased  $rScO_2$  holds true in this study.

**Statistical analysis** Data are presented as median (IQR). The  $t$ -test was used for the comparison of the patient demographics (Section 3.6.1). A GLS regression model (3.6.2) was used to test the differences between anesthesia based on sevoflurane versus midazolam on cerebral oxygenation in the perioperative period. The GLS model showed a better fit for the compared to a LME model, based on the Akaike information criterion (AIC) [50]. Post hoc comparisons were based on analysis of marginal means with Tukey's correction for multiple comparisons. All statistical computations were carried out in R [398]. Significance was defined as  $\alpha < 0.05$ .

## 6.4 Results

**Demographics** Informed consent was obtained in 49 neonates, of which 37 neonates could be analyzed: 20 neonates in the sevoflurane group, 17 neonates in the midazolam group. In the midazolam group, 5 neonates received VA-ECMO treatment until one day before surgery. In the sevoflurane group, eight patients who underwent thoracoscopic surgery were converted to an open approach because of the need for a patch. Both groups were comparable with regards to demographics (Table 6.1), except for a lower amount of herniated livers (25% vs. 71%,  $p = .005$ ), a lower VIS preoperatively (0 (0–5) vs. 17 (10–25),  $p < .001$ ), a lower PNA on the day of surgery (3 (2–4) days vs. 6 (3–12) days,  $p = .008$ ), more thoracoscopic surgery (40% vs. 23%,  $p = .026$ ), and a shorter surgery duration (95 (70–125) min vs. 182 (114–203) min,  $p < .001$ ) in the sevoflurane group compared to the midazolam group.

**Anesthesia** Preoperatively, in the sevoflurane group, five neonates were not sedated while on mechanical ventilation, two neonates received continuous administration of morphine, seven neonates received continuous administration of midazolam and six neonates received continuous administration of both midazolam and morphine (Figure 6.1). In the midazolam group, all neonates received continuous midazolam, supplemented with continuous administration of fentanyl and were intubated multiple days before surgery. The patients in the sevoflurane group that were intubated and sedated before start of surgery received comparable dosages of midazolam (47 (0–92)  $\mu\text{g kg}^{-1} \text{h}^{-1}$  and 40 (30–

50)  $\mu\text{g kg}^{-1} \text{h}^{-1}$ ,  $p = .735$ , respectively, Table 6.1) compared to the midazolam group.

Intraoperatively, the end expired sevoflurane concentration was 1.5% (1.1–1.9). The time between the start of administration of sevoflurane and start of the surgical procedure was 66 (45–76.6) min. In six neonates, the preoperative continuous midazolam administration was continued intraoperatively and in two neonates the preoperative continuous morphine administration was continued intraoperatively during sevoflurane anesthesia (Figure 6.1). Three neonates received a bolus of propofol (2.9, 3.7 and 7.3 mg  $\text{kg}^{-1}$  for endotracheal intubation).

In the midazolam group, the midazolam dosage was 100 (68–100)  $\mu\text{g kg}^{-1} \text{h}^{-1}$ . The time between the administration of midazolam and the start of the surgical procedure was 21 (1–30) min. The midazolam dosage in the sevoflurane group of those in whom the midazolam was continued from pediatric intensive care unit (PICU) ( $N = 6$ ) was significantly lower (47 (0–67)  $\mu\text{g kg}^{-1} \text{h}^{-1}$ ,  $p = .003$ ) compared to the midazolam group (Table 6.1). The fentanyl bolus dosage during the induction of anesthesia was lower in the sevoflurane group compared to the midazolam group (2 (2–3)  $\mu\text{g kg}^{-1}$  vs. 5 (4–7)  $\mu\text{g kg}^{-1}$ ,  $p < .001$ ), although the cumulative fentanyl bolus dosages that were administered intraoperatively did not differ (10 (7–17)  $\mu\text{g kg}^{-1}$  vs. 6 (4–12)  $\mu\text{g kg}^{-1}$ ,  $p = .119$ ). Yet, the midazolam group received additional continuous administration of fentanyl (4 (3–5)  $\mu\text{g kg}^{-1} \text{h}^{-1}$ ), whereas the sevoflurane group did not.

Postoperatively, the midazolam dosages did not differ significantly between the sevoflurane (39 (26–99)  $\mu\text{g kg}^{-1} \text{h}^{-1}$ ) and the midazolam group (48 (20–50)  $\mu\text{g kg}^{-1} \text{h}^{-1}$ ) (Table 6.1).

**Vital parameters** Preoperatively, HR was significantly lower in the sevoflurane group (137 (126–141) bpm) compared to the midazolam group (142 (138–152) bpm) (Figure 1A, appendix 3). MABP did not differ, although the VIS was significantly lower in the sevoflurane group (0 (0–5)) than in the midazolam group (17 (10–25)). Intraoperatively, HR and MABP significantly dropped in sevoflurane group (HR: 138 (132–156) bpm, MABP: 44 (42–48) mmHg) compared to the midazolam group (HR: 162 (153–171) bpm, MABP: 55 (50–60) mmHg). Intraoperatively, the VIS score was again significantly lower in the sevoflurane group (9 (5–17)) than in the midazolam group (17 (12–35)). Three to six hours postoperatively, HR remained significantly lower in the sevoflurane group (127 (120–135) bpm) compared to the midazolam group (141 (139–148) bpm). VIS was still significantly lower in the sevoflurane group (2 (0–11)) compared to the midazolam group (17 (10–28)). Fifteen to 18 hours postoperatively, HR remained significantly lower in the sevoflurane group

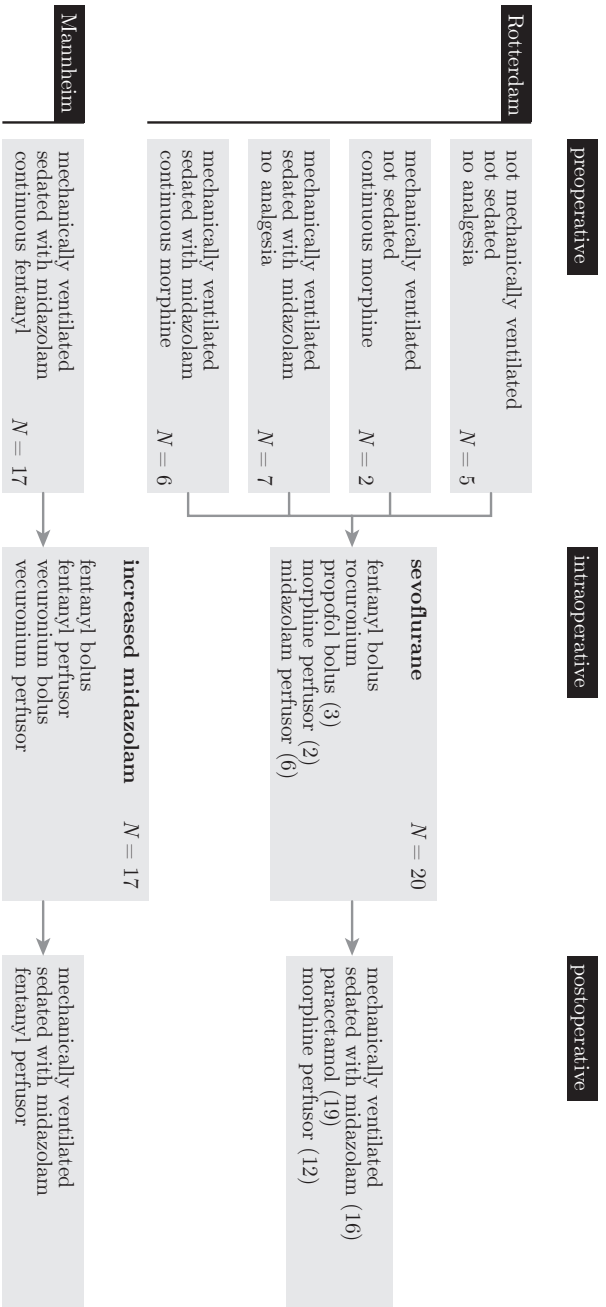


Figure 6.1: Overview of the medication administered to the neonates before, during and after surgery.

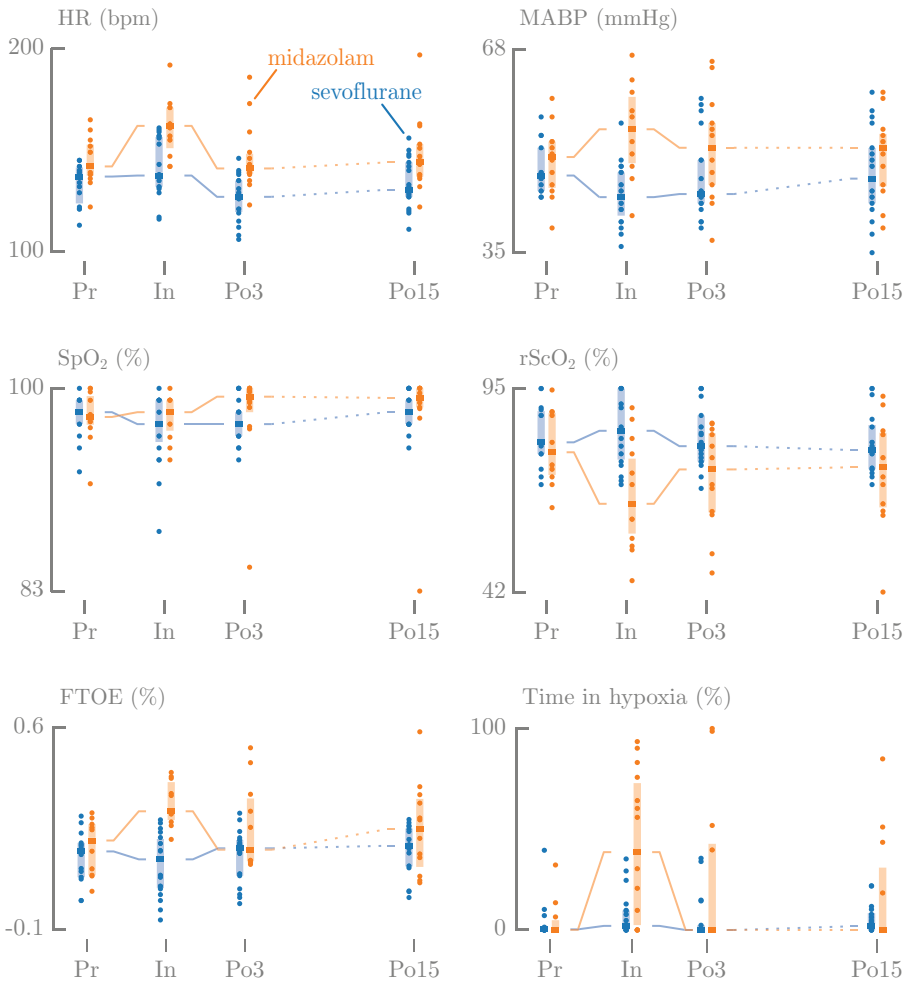


Figure 6.2: Longitudinal overview of the perioperative changes in HR, MABP, SpO<sub>2</sub>, rScO<sub>2</sub>, FTOE, time in hypoxia, EEG slow delta ( $\delta_1$ ), EEG fast delta ( $\delta_2$ ), and EEG gamma ( $\gamma$ ).

(131(127–135) bpm) compared to the midazolam group (144 (137–153) bpm). SpO<sub>2</sub> and partial pressure of carbon dioxide (P<sub>a</sub>CO<sub>2</sub>) did not differ between the group perioperatively.

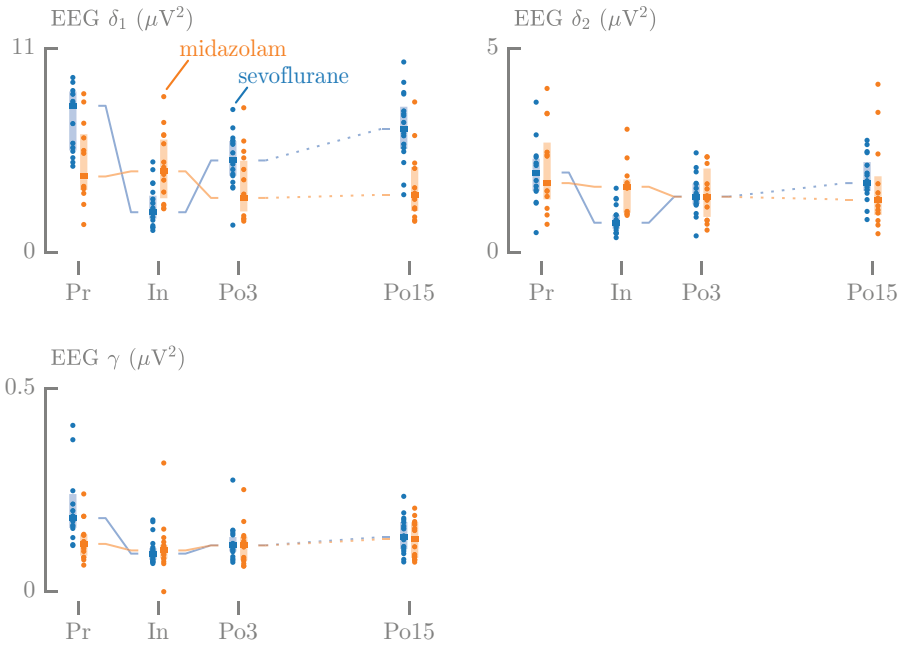


Figure 6.2 (cont.): Longitudinal overview of the perioperative changes in HR, MABP, SpO<sub>2</sub>, rScO<sub>2</sub>, FTOE, time in hypoxia, EEG slow delta ( $\delta_1$ ), EEG fast delta ( $\delta_2$ ), and EEG gamma ( $\gamma$ ).

**Cerebral oxygenation** Preoperatively, rScO<sub>2</sub>, FTOE and the time in cerebral hypoxia did not differ significantly between the groups (Figure 6.2). Intraoperatively, the rScO<sub>2</sub> values were significantly higher in the sevoflurane group (84% (77–95)) compared to the midazolam group (65% (59–76),  $p < .001$ ). The opposite was true for FTOE, which was lower in the sevoflurane group (14% (5–21)) compared to the midazolam group (31% (29–40),  $p < .001$ ). The time in hypoxia was significantly shorter in the sevoflurane group (2% (0.4–9.6)) compared to the midazolam group (38.6% (4.9–70),  $p = .023$ ). Three until six hours and fifteen until eighteen hours postoperatively, rScO<sub>2</sub>, FTOE and the time in cerebral hypoxia did not differ between the groups.

**Cerebral activity** Preoperatively, the power in the EEG slow delta  $\delta_1$  and gamma  $\gamma$  frequency bands was significantly higher in the sevoflurane group ( $\delta_1$ : 7.9 (5.5–8.6)  $\mu V^2$ ,  $\gamma$ : 0.19 (0.16–0.28)  $\mu V^2$ ) compared to the midazolam group ( $\delta_1$ : 4.1 (3.4–6.2)  $\mu V^2$ ,  $p = .009$ ,  $\gamma$ : 0.12 (0.09–0.14)  $\mu V^2$ ,  $p = .002$ ). No

difference between both groups was observed for the fast delta  $\delta_2$  band (2.0 (1.5–2.3)  $\mu\text{V}^2$  vs. 1.7 (1.4–2.5)  $\mu\text{V}^2$ ) (Figure 6.2).

Intraoperatively,  $\delta_1$ ,  $\delta_2$  and  $\gamma$  power decreased in the sevoflurane group and remained low during the entire intraoperative period. In the midazolam group, a 3-fold increase of  $\delta_2$  power was observed in the first 30 min of the surgical procedure, which a subsequent decrease thereafter (Figure 6.3). A comparable pattern was observed for the  $\gamma$  frequency band, which was characterized by a 5-fold increase with a subsequent decrease to baseline. The intraoperative median values of slow delta  $\delta_1$  and fast delta  $\delta_2$  power decreased significantly in the sevoflurane group ( $\delta_1$ : 2.2 (1.9–3.0)  $\mu\text{V}^2$ ,  $\delta_2$ : 0.73 (0.59–0.91)  $\mu\text{V}^2$ ) compared to the midazolam group ( $\delta_1$ : 4.4 (3.1–6.0)  $\mu\text{V}^2$ ,  $p < .001$ ,  $\delta_2$ : 1.6 (1.0–1.7)  $\mu\text{V}^2$ ,  $p = < .001$ ). No overall differences were observed for the  $\gamma$  frequency band (0.09 (0.08–0.10)  $\mu\text{V}^2$  vs. 0.10 (0.01–0.11)  $\mu\text{V}^2$ ). During surgery, a higher maximal end expired sevoflurane concentration was not associated with a lower cerebral activity (Figure 6.4). In contrast, a higher maximum midazolam dose was associated with lower cerebral activity ( $p = .023$ ) (Figure 6.4). The neonates who received a bolus of propofol for intubation had an EEG delta power (2.15 - 2.16  $\mu\text{V}^2$ ) that was comparable to the other neonates in the sevoflurane group.

Three until six hours postoperatively,  $\delta_1$ ,  $\delta_2$  and  $\gamma$  power increased again in the sevoflurane group ( $\delta_1$ : 5.0 (4.2–6.0)  $\mu\text{V}^2$ ,  $\delta_2$ : 1.4 (1.2–1.7)  $\mu\text{V}^2$ ,  $\gamma$ : 0.11 (0.10–0.13)  $\mu\text{V}^2$ ), decreased in the midazolam group ( $\delta_1$ : 2.9 (2.4–4.8)  $\mu\text{V}^2$ ,  $\delta_2$ : 1.36 (0.95–1.93)  $\mu\text{V}^2$ ,  $\gamma$ : 0.11 (0.08–0.13)  $\mu\text{V}^2$ ) compared to the intraoperative period. Fifteen until 18 hours postoperatively, the power in the EEG  $\delta_1$ ,  $\delta_2$  and  $\gamma$  frequency bands further increased in the sevoflurane group ( $\delta_1$ : 6.7 (5.6–7.6)  $\mu\text{V}^2$ ,  $\delta_2$ : 1.7 (1.5–2.4)  $\mu\text{V}^2$ ,  $\gamma$ : 0.14 (0.10–0.17)  $\mu\text{V}^2$ ), increased in the midazolam group ( $\delta_1$ : 3.1 (2.4–4.8)  $\mu\text{V}^2$ ,  $\delta_2$ : 1.31 (0.98–2.23)  $\mu\text{V}^2$ ,  $\gamma$ : 0.13 (0.08–0.17)  $\mu\text{V}^2$ ) compared to the intraoperative period.

**Correlations** Preoperative, no correlation between rScO<sub>2</sub> or FTOE and cerebral activity was observed (Figure 6.5).

Intraoperatively, a significantly ( $p = 0.01$ ) positive correlation between rScO<sub>2</sub> and cerebral activity in the midazolam group was found (Figure 6.5). In contrast, there was no correlation between FTOE and cerebral activity. A higher maximum dose of midazolam was associated with a significant decrease in rScO<sub>2</sub> and EEG  $\delta_1$  power (Figure 6.4). The same trends were observed for the maximum end expired sevoflurane concentration, although these trends were not significant. In the sevoflurane group, rScO<sub>2</sub> negatively correlated with VIS ( $R^2 = 0.23$ ,  $p = .004$ ) and FTOE positively correlated with VIS ( $R^2 = 0.21$ ,  $p = .04$ ) (Figure 6.6). These correlations were not found in the midazolam group.

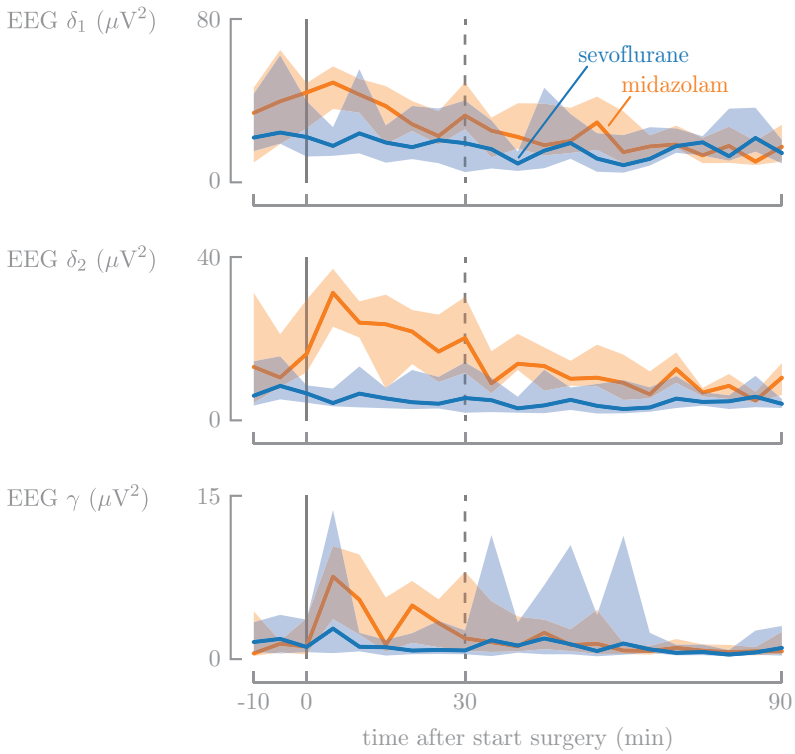


Figure 6.3: In the sevoflurane group,  $\delta_1$ ,  $\delta_2$  and  $\gamma$  power decreased during surgery and remained low over the entire intraoperative period. In the midazolam group, a 3-fold and 5-fold increase of  $\delta_2$  and  $\gamma$  power were observed in the first 30 min of the surgical procedure, with a subsequent decrease thereafter.

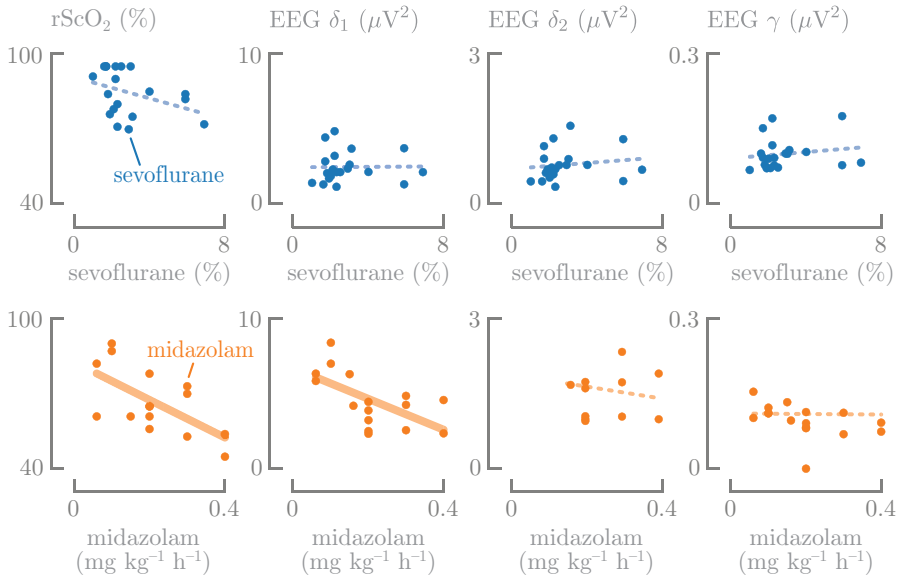


Figure 6.4: A higher maximum dose of midazolam was associated with a significant decrease in rScO<sub>2</sub> and EEG  $\delta_1$  power during surgery. The same trends were observed for the maximum end expired sevoflurane concentration, although these trends were not significant.

Postoperatively, rScO<sub>2</sub> was negatively correlated with VIS ( $R^2 = 0.35$ ,  $p = .001$ ) and FTOE positively correlated with VIS ( $R^2 = 0.32$ ,  $p = .001$ ) in the sevoflurane group, and not in the midazolam group (Figure 6.6).

## 6.5 Discussion

In this analysis, we describe the effects of two different anesthetic approaches on cerebral oxygenation and activity in CDH neonates perioperatively. Surgery with sevoflurane-based anesthesia resulted in stable cerebral oxygenation, decreased oxygen consumption and decreased cerebral activity. Furthermore, the EEG power ( $\delta_2$ ,  $\gamma$ ) did not indicate conscious awareness of pain stimuli during surgery. Surgery with midazolam-based anesthesia resulted in low rScO<sub>2</sub>, increased cerebral oxygen consumption and increased cerebral activity during the first 30 min of the surgical procedure. In this group, increases in power in the fast

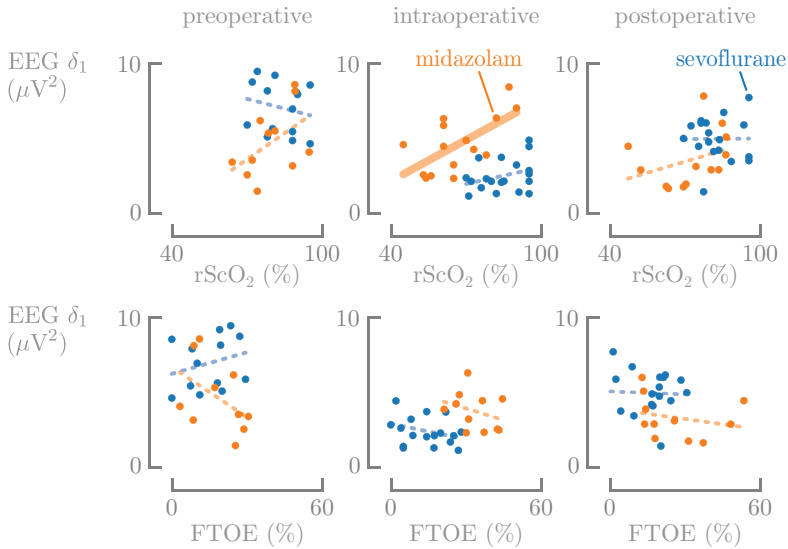


Figure 6.5: Intraoperatively, rScO<sub>2</sub> significantly correlated with cerebral activity in the midazolam group ( $R^2 = 0.41$ ,  $p = 0.01$ ).

delta and gamma frequency band indicated conscious perception of pain during surgery.

**Cerebral oxygenation** Intraoperatively, rScO<sub>2</sub> values were observed to be significantly higher in the sevoflurane group compared to the midazolam group, which reached alarmingly low rScO<sub>2</sub> values (Figure 6.2). In the sevoflurane group, brain activity decreased significantly intraoperatively, which resulted in stable rScO<sub>2</sub> and lowered FTOE, despite a reduction in MABP (Figure 6.2). These results are in line with a study in children between 0 and 2 years [337]. In the midazolam group, the changes in EEG power were accompanied by a decrease in rScO<sub>2</sub> and an increase in FTOE, despite an increase in HR and MABP (Figure 6.2). P<sub>a</sub>CO<sub>2</sub>, as well as vasoactive and inotropic medication affect vascular resistance and subsequently cerebral perfusion [255, 148]. In both groups, P<sub>a</sub>CO<sub>2</sub> levels were comparable, stable and within clinical range. In the sevoflurane group, increased VIS was associated with lower rScO<sub>2</sub> values and higher FTOE during and after surgery. Hemodynamic support, mostly with norepinephrine, was highest in the midazolam group (Table 10.1) without

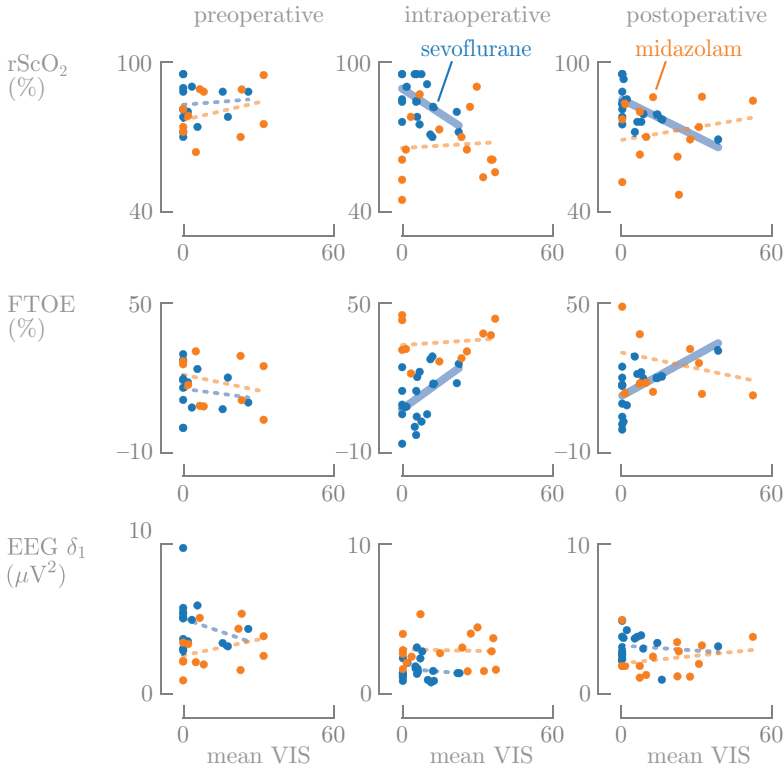


Figure 6.6: In the sevoflurane group, rScO<sub>2</sub> negatively correlated with VIS ( $R^2 = 0.23$ ,  $p = .04$ ) and FTOE positively correlated with VIS ( $R^2 = 0.21$ ,  $p = .04$ ) during surgery. The same correlations were found after surgery for rScO<sub>2</sub> ( $R^2 = 0.35$ ,  $p = .01$ ) and FTOE ( $R^2 = 0.32$ ,  $p = .001$ ).

affecting  $r\text{ScO}_2$  or FTOE. A recent study signals that norepinephrine elevates MABP, while, paradoxically, reducing cerebral perfusion in adults [401].

**Cerebral activity** The power in the  $\delta_1$ ,  $\delta_2$  and  $\gamma$  frequency band decreased significantly during sevoflurane administration, independently of the maximum end expired sevoflurane concentration (Figure 6.4). Overall, EEG power didn't decrease during midazolam-based anesthesia, but an increase in maximum midazolam dose was found to be associated with a decrease in activity. The median time between bolus administration or increased perfusor dose of midazolam and the start of surgical procedure was 21 min. During the first 30 min of surgery, a threefold increase in fast delta power and a fivefold increase in gamma power were observed, suggesting that nociceptive stimuli were registered by the brain (Figure 6.3) [117]. After 30 min, the power in the different bands stabilized to lower baseline values. This might suggest that the increased dose of midazolam, administered before the start of the surgical procedure, requires 21 plus 30 min to reach a new steady state concentration, since higher dosages of midazolam lowered EEG power (Figure 6.4). Alternatively, one could argue that surgery started too soon after administering midazolam and analgesia, since cerebral activity only decreased after 30 min. A loading dose helps to induce the anesthetic effect quicker, although this was given in 59% of the neonates in the midazolam group.

**Pharmacological approaches** A recent study showed that higher sevoflurane doses significantly correlated with more suppressed background patterns [389]. This correlation was not observed in our study, but this could be due to the relatively small range in sevoflurane concentrations that were administered (Figure 6.4). Patients in the midazolam group received midazolam preoperatively for multiple days and had a median midazolam dosage of  $0.1 \text{ mg kg}^{-1} \text{ h}^{-1}$  intraoperatively. This is substantially higher than the dosing advice of  $0.06 \text{ mg kg}^{-1} \text{ h}^{-1}$  for sedation with midazolam in neonates with a GA above 32 weeks, although this was already questioned by our research group [426]. A steady-state concentration is reached 24 hours after start of continuous administration. The elimination half-life of midazolam is approximately six hours in the first week of life in full-term neonates [59], although the severity of disease and inflammation may also affect the elimination of midazolam in critically ill neonates [294]. A recent Cochrane review concluded that midazolam was an effective sedative in neonates [285], although transient cerebral hypoperfusion was observed after a bolus of midazolam, as well as significant higher rates of adverse neurological events in neonates treated with midazolam compared to morphine [156, 414]. In this study, neonates in the midazolam group all received continuous administration of fentanyl. Single use of fentanyl dosages of

50 to 100  $\mu\text{g kg}^{-1}$  is a commonly used anesthetic approach during congenital cardiac surgery or if the neonate has limited hemodynamic reserve [152]. A randomized trial in 1987 already proved the additional value of fentanyl in the stress response of neonates intraoperatively [15]. Another study compared the effect of fentanyl with fentanyl plus midazolam on stress response during neonatal cardiac surgery, and concluded that intraoperative administration of fentanyl plus midazolam did not reduce stress response compared fentanyl alone [152]. This suggests that high doses of fentanyl might be a better anesthetic approach than midazolam with lower dosages of fentanyl.

**Strengths and limitations** Strengths: both centers have long-lasting experience treating high-risk CDH patients and have acted as *founding fathers* for well-established international guidelines. Neither treatment modalities, nor composition of the treatment teams changed during the study period. In addition, both centers used validated pain assessment instruments (Comfort-B) as pharmacodynamic endpoint to evaluate and treat pain. Limitations: exposure to medication was compared based on dosages instead of its plasma concentrations. Neonates in the midazolam group were more critically ill (more liver-up, a higher VIS, a longer duration of surgery, Table 10.1) than neonates in the sevoflurane group. In addition, this is a center comparison study and not a randomized controlled trial.

## 6.6 Conclusion

In this chapter, we compared two anesthetic approaches for CDH surgery, which showed that sevoflurane-based anesthesia resulted in increased cerebral oxygenation and decreased cerebral activity, suggesting adequate anesthesia. In contrast, midazolam-based anesthesia in neonates with a more severe CDH (more liver-up, a higher VIS, a longer duration of surgery) led to alarmingly low  $\text{rScO}_2$  values, below hypoxia threshold, and increased values of EEG power during the first 30 min of surgery, which might indicate the conscious experience of pain. Following these limitations of midazolam, we argue that current perioperative medication strategies with midazolam and analgesia might not be sufficient for perioperative anesthesia. These results stimulate the integration of population-pharmacokinetic models in combination with multimodal neuromonitoring to reach evidence-based perioperative pharmacotherapy in these vulnerable patients.

PA

RT



# BIVARIATE ANALYSIS

bivariate analysis

07

# Nonparametric transfer entropy as a measure for neurovascular coupling

*based on:*

Hendrikx, D., Thewissen, L., Smits, A., Naulaers, G., Allegaert, K., Van Huffel, S. and Caicedo A. Nonlinear Transfer Entropy to Assess the Neurovascular Coupling in Premature Neonates. *Advances in Experimental Medicine and Biology* 1232 (2020), 11–17.



In the adult brain, it is well known that increases in local neural activity trigger changes in regional blood flow and, thus, changes in cerebral energy metabolism, through the NVC regulation mechanism. It is not yet clear to what extent this mechanism is present in the premature brain. In this chapter, we explore the use of TE in order to compute the nonlinear coupling between changes in brain function, assessed by means of EEG, and changes in brain oxygenation, assessed by means of NIRS. The resulting TE values serve as a marker for NVC, and are contrasted between two groups: one with and one without brain abnormalities.

## 7.1 Introduction

In the adult brain, increases in local neural activity trigger increases in regional blood flow, and thus changes in regional cerebral energy metabolism. This regulation mechanism, that couples neural activity and hemodynamics, is generally referred to as NVC. In practice, brain oxygenation levels can be assessed by means of NIRS, while brain function can be measured by means of EEG. In the neonatal brain, however, the presence and extent of the NVC is still unclear. Some neonatal fMRI and NIRS studies have reported adult-like NVC [23, 231], while other studies in both humans and rodent models have reported differences in hemodynamic responses in the early postnatal brain compared to adults [213, 463].

In this chapter, we use nonlinear and nonparametric TE to compute the coupling between NIRS-derived rScO<sub>2</sub> and EEG; we use this measure to assess the NVC in the premature brain. TE allows to quantify the directionality of information transfer between NIRS and EEG signals. In a previous study, we measured the coupling between rScO<sub>2</sub> and EEG using a linear model to compute TE [62]. The results indicated that changes in brain oxygenation were likely to precede changes in amplitude of EEG activity, indicating a NVC response that differs from the response commonly observed in adults. In this context, however, it is important to mention that the coupling between neuronal activity and brain hemodynamics incorporates nonlinear effects, indicating that a nonlinear measure (such as the nonlinear TE presented in this chapter) might be more appropriate for NVC quantification [246].

Finally, we compare the NVC in a cohort of neonates that underwent sedation with propofol. We evaluated the prognostic value of TE in order to detect neonates that presented small brain hemorrhages.

Table 7.1: Stratification of the original study group into two subgroups, based on the presence of brain abnormalities on a routine cUS.

	no brain injury	brain injury	<i>p</i>
PMA (weeks)	30 (29–30.5)	29.5 (28.25–30)	0.5471
PNA (days)	1 (1–1)	1 (1–1.75)	0.1247
propofol dose (mg kg <sup>-1</sup> )	1 (1–1.50)	1 (0.625–1.75)	0.6285

## 7.2 Dataset

This study focuses on neonates that received propofol as a sedative in the clinical setting of endotracheal intubation. Details of the structure of this dataset and the recording equipment was presented in Section 4.1.

The number of patients in the propofol dataset was reduced from 22 to 21, after visual inspection learned that the EEG of one neonate was highly corrupted by noise and could not be used. After exclusion, the study group consisted of 21 premature neonates, stratified into two groups based on the presence of brain abnormalities, observed on routine cUS (Tabel 7.1). Both groups were comparable with respect to demographics; the PMA was 30 (29–30.5) weeks vs. 29.5 (28.25–30) weeks and the PNA was 1 (1–1) days vs. 1 (1–1.75) days for the group without and with brain injury, respectively. Both groups also received a comparable dose of propofol: 1 (1–1.50) vs. 1 (0.625–1.75) mg kg<sup>-1</sup>.

## 7.3 Methods

**Signal processing pipeline** The EEG signal was preprocessed in order to remove bad electrode contact artifacts (impedance exceeding 10 k $\Omega$ ) and motion artifacts, observed as peaks in the EEG impedance. Due to the different temporal characteristics of the rScO<sub>2</sub> and EEG signal, we used the running root mean squared (RMS) of the EEG, which is a continuous estimate of EEG power. More specifically, the RMS value was computed using a window length of 5 seconds and an overlap of 4 seconds, producing a new value every second. The window length of 5 seconds was defined in order to assess EEG delta activity.

In the present analysis, the TE is estimated by binning the original time series, which allows to estimate the PDFs required to compute the TE. This approach is very general, since no model is assumed for the data. Therefore, this approach also takes into account nonlinear interactions. Moreover, uniform embedding

with dimension  $L = 10$  was used to capture the past of the signals. TE was implemented in MATLAB using the ITS toolbox, developed by Luca Faes. We used surrogate data to assess the significance of the TE values, obtained by randomly shuffling the original signals (*time-shuffled surrogates*, Section 3.4.5). Since the TE is a non-symmetric measure, two different thresholds of significance were defined. The TE curves were computed using a window of 15 min with an overlap of 10 min, producing a new value every 5 min.

**Features** Two features were computed from the resulting TE curves to quantify the effect of propofol on the TE curves: the minimal value  $M$  and the maximal deviation  $\Delta$  from baseline (Figure 7.1). These feature values were computed in the first 3 hours of the analysis window. Baseline level was defined as the median value of the last 3 hours of the analysis window. Since propofol is considered to be washed out after 3 hours, we assume that the baseline level presents an indication for the background, reference NVC.

**Statistical analysis** Data are presented as median (IQR). The difference in demographics and features between both groups was assessed using the Wilcoxon rank sum test (Section 3.6.1), due to the small sample size, which impedes normality assumption. Significance was defined as  $\alpha = 0.05$ .

## 7.4 Results

In Figure 7.2, the median TE curves are presented for the cohort of neonates with and without brain injury. The significance of the TE values was defined by a randomly shuffling of the data (Monte Carlo simulation), which lead to two significance threshold  $T_{rScO_2 \rightarrow EEG}^*$  and  $T_{EEG \rightarrow rScO_2}^*$  depicted in Figure 7.2. The Wilcoxon rank-sum test indicated that  $T_{EEG \rightarrow rScO_2}^*$  is significantly larger than  $T_{rScO_2 \rightarrow EEG}$  ( $p < 0.001$ ).

Figure 7.2 shows a comparison between the group of neonates without and with brain injuries based on the features  $M$  and  $\Delta$ . In addition, the baseline level is also compared between the two groups. Resulting  $p$  values were equal to 0.259, 0.845 and 0.039 for features  $M$ ,  $\Delta$  and the baseline, respectively, which indicates that the response to propofol is comparable in both groups (features  $M$  and  $\Delta$ ), while background NVC (baseline) might be lower in neonates with brain injury.

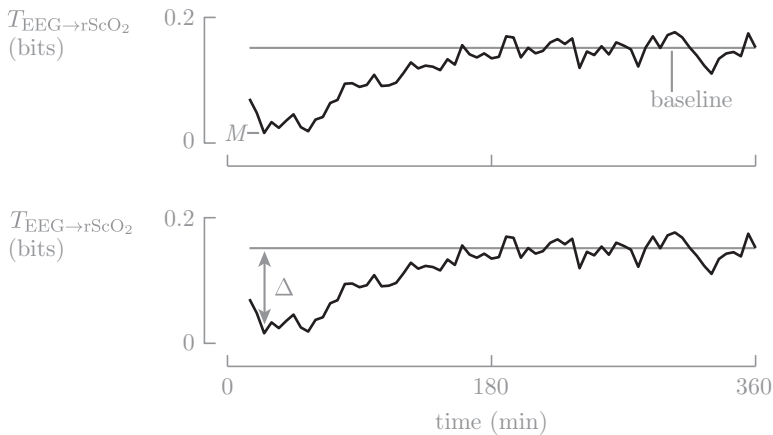


Figure 7.1: Two features were computed from the TE curves to quantify the effect of propofol: the minimal value  $M$  and the maximal deviation  $\Delta$  from baseline, which was defined as the median value of the last 3 hours of the analysis window.

## 7.5 Discussion

In this study, we found that the transfer of information, quantified by means of TE, is larger in the direction from EEG to  $rScO_2$  than from  $rScO_2$  to EEG. This indicates that changes in EEG amplitude are likely to precede changes in  $rScO_2$ . In other words: changes in brain function trigger changes in brain hemodynamics and metabolism, which is in agreement with the NVC of the adult brain. It is however important to note that the transfer of information  $rScO_2$  to EEG is not zero, indicating a flow of information also in this direction. This might be caused by the feedback mechanisms that are in charge of the regulation of brain metabolism, that is, the delivery of nutrients and oxygen to meet the metabolic demand.

In a previous study, we measured the coupling between  $rScO_2$  and EEG using a linear model to compute TE [62]. The results indicated that changes in brain oxygenation were likely to precede changes in amplitude of EEG activity. This contradicts the results we obtained in the present study. The non-parametric approach to compute TE, used in this study, estimates all the transfer of information from one process to another, including the linear and non-linear

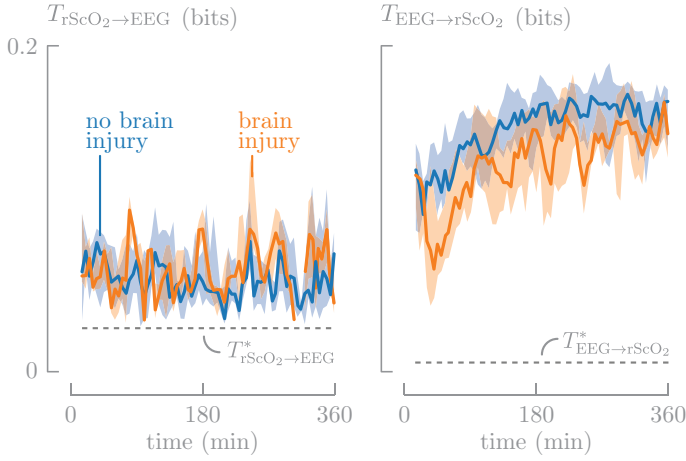


Figure 7.2: TE curves after administration of propofol at  $t = 0$ ;  $T_{rScO_2 \rightarrow EEG}$  (left) and  $T_{EEG \rightarrow rScO_2}$  (right). The solid line denotes the median, the shaded area the IQR. The dashed lines ( $T_{rScO_2 \rightarrow EEG}^*$  and  $T_{EEG \rightarrow rScO_2}^*$ ) indicate the significance levels ( $\alpha = 0.05$ ) for the TE values, obtained by surrogate data analysis.

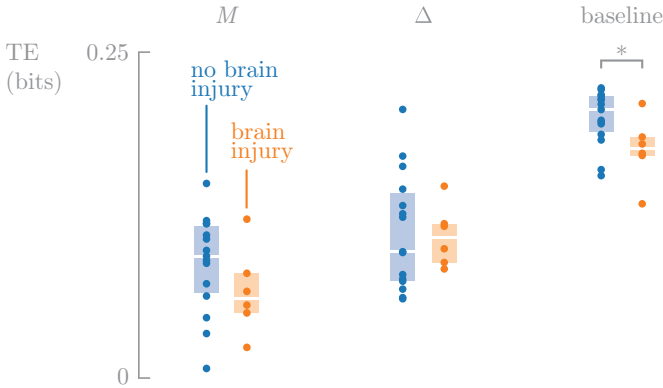


Figure 7.3: Comparison of feature and baseline values between the normal and abnormal neonates;  $M$ ,  $\Delta$ , and baseline indicate the minimal value, the maximal deviation from baseline and baseline values, respectively.

part. Taking this into account, and the results presented in [62], we can conclude that the linear model for TE is not able to model the nonlinear processes involved in NVC which, once taken into account, determine a different directionality in the flow of information. In addition, the nonlinear TE is able to capture the effect of propofol in the NVC, which was not observed using the linear model. These results indicate that it is possible that there are two different mechanisms affecting NVC, one acting on its linear part, and another one explained more by a non-linear process.

In Figure 7.2, lowered values of EEG to rScO<sub>2</sub> coupling are observed, which consequently increase to a steady baseline value in all patients in the study group. Propofol induces a reversible state of diminished responsiveness behaviorally similar to quiet sleep, which is characterized by a more discontinuous EEG and is associated with lower FTOE values. This indicates lower brain oxygen consumption, which could explain the reduced EEG to rScO<sub>2</sub> interaction. Based on visual inspection of Figure 7.2, it appears that the reduction in EEG to rScO<sub>2</sub> coupling is more severe for the cohort of neonates with brain abnormalities. A more concise study, based on the feature values of  $M$  and  $\Delta$ , presented in Figure 7.3, indicates that there is no significant difference in response between the neonates with and without brain injury. Remarkably, the rScO<sub>2</sub> to EEG coupling is not influenced by propofol.

The TE baseline values, presented in Figure 7.3, were observed to be significantly lower in the cohort of neonates with brain injury. From a signal processing point of view, a lower TE indicates a less functional NVC. Thus, the cerebral vascular network in the neonates with brain injury might be less able to compensate for increased metabolism resulting from neuronal activation. These results are in agreement with a study from Mahmoudzadeh et al., who observed a less functional NVC in preterm neonates with IVH compared to a control group [246]. In addition, Chalak et al. also observed a significantly lower NVC in newborns with neonatal encephalopathy (NE) compared to a healthy control group, assessed by means of wavelet coherence [67], which indicates that brain injury might alter CBF regulation mechanisms such as NVC.

## 7.6 Conclusion

The results obtained in this chapter are in agreement with literature and point out that brain abnormalities might alter NVC, and that this alteration in NVC can be captured using signal processing techniques combining NIRS-derived rScO<sub>2</sub> and EEG measurements. Therefore, we have shown that the nonlinear TE could be used as a physiological marker to guide therapeutic decision-making

or predict neurological outcome. However, further studies are needed in order to validate this methodology in a larger cohort of neonates, using different clinical models.

P A

R T



MULTI-  
VARIATE  
ANALYSIS

multivariate analysis



# Coupling between regional oxygen saturation of the brain and vital signs during immediate transition after birth

*based on:*

Hendrikx, D., Caicedo, A., Van Huffel, S., Naulaers, G., Wolfsberger, C., Urlesberger, B., and Pichler, G. Coupling between regional oxygen saturation of the brain and vital signs during immediate transition after birth. Submitted to *Neonatology* (2021).



In the first study on multivariate signal analysis, we focus on the coupling between the regional cerebral oxygen saturation of the brain and the vital signs during immediate transition after birth. The transition from fetus to neonate is a critical time of physiological adaptation, which requires complex physiological changes that must occur in a relatively short period of time. The fetus must move from reliance on the maternal heart, lungs, metabolic and thermal systems to being able to self-sufficiently deliver oxygenated blood to the tissues and regulate various body processes. While most term infants achieve physiological homeostasis without difficulty, careful assessment during this period of adaptation is required to ensure that the infant makes the transition smoothly and without compromise. Prompt recognition of those infants who present with signs of serious illness enables caregivers to initiate treatment aimed at minimizing the effects of such illness.

## 8.1 Introduction

Major cardio-pulmonary changes occur when extra-uterine respiration and circulation are established during the immediate postnatal transition period [312, 315]. To monitor the immediate transitional period, pulse oximetry and ECG are routinely used, which measure arterial oxygen saturation ( $\text{SpO}_2$ ) and heart rate (HR) [93, 191, 328]. In addition, there is currently a growing interest to monitor the regional cerebral tissue oxygenation ( $\text{rScO}_2$ ) and the regional cerebral tissue fractional oxygen extraction (FTOE) during the immediate transition using NIRS [69, 355, 29, 28, 409, 314, 354, 27, 447]. The brain is one of the most vulnerable organs and needs adequate perfusion and oxygen delivery to maintain cerebral tissue oxygenation and activity [311, 313]. Cerebral hypoxia-ischemia might cause perinatal cerebral injury including IVH or PVL [335, 334], which may lead to subsequent neurodevelopmental morbidity [335, 203, 220, 180]. Baik et al. [27] described that preterm neonates with a GA under 32 weeks who developed an IVH already show lower  $\text{rScO}_2$  values during immediate postnatal transition. Cerebral hyper-oxygenation might cause cell damage within the cerebral white matter in preterm infants [135, 380].

$\text{rScO}_2$  is measured in the arterial, capillary, and venous compartment of the tissue and depends on oxygen delivery to the brain and oxygen consumption by the brain. Oxygen delivery depends on the hemoglobin content of the blood, the  $\text{SpO}_2$  and CBF, which in turn depends on cardiac output (CO) and vascular resistance. In neonates, CO is mainly determined by HR, since the ability to increase stroke volume is limited [40]. The balance between oxygen delivery and consumption in the brain can be studied using FTOE [280]. An

increase in FTOE might indicate a reduction in oxygen delivery with a constant consumption, or a consumption of oxygen that exceeds the oxygen delivery.

Studies on the correlation between HR and SpO<sub>2</sub>, and rScO<sub>2</sub> and FTOE are scarce and not unambiguous [261]. In an observational analysis of cerebral NIRS, both rScO<sub>2</sub> and FTOE correlated with HR and SpO<sub>2</sub> in neonates of 32 to 40 weeks of gestation during the first six postnatal hours, whereby the immediate transitional period was not included [403]. In another observational study, no correlation was observed between rScO<sub>2</sub> and SpO<sub>2</sub> in clinically stable preterm infants admitted to the NICU after the immediate transitional period [174]. The correlation between HR and rScO<sub>2</sub> has also been analyzed in neonates, expressed as the so-called tissue oxygenation heart rate reactivity index (TOHRx) [262]. Higher TOHRx values were observed in preterm neonates before developing an IVH [73], which are therefore considered predictive for detecting developing morbidities [262]. Mitra et al. described better outcome in preterm neonates if rScO<sub>2</sub> remained independent of changes in HR [262]. Zanelli et al. described that preterm neonates who developed an IVH showed higher mean HR with lower blood pressure and mean SpO<sub>2</sub> [461]. However, data describing any correlation between HR, SpO<sub>2</sub>, rScO<sub>2</sub> and FTOE during the immediate transition after birth is currently not available.

Therefore, the primary aim of the present study was to perform correlation analyses between HR, SpO<sub>2</sub>, rScO<sub>2</sub> and FTOE during immediate transition after birth in term and preterm neonates to gain more insight into the concise nature of these interactions. Our primary hypothesis was that both HR and SpO<sub>2</sub> are coupled to rScO<sub>2</sub> and FTOE.

## 8.2 Dataset

This study focuses on neonates monitored during immediate transition after birth. Details on the structure of this dataset and the recording equipment was presented in Section 4.4.

## 8.3 Methods

**Signal processing pipeline** The starting point of the analysis was 15 minutes of multimodal data (Figure 8.1). Data of the first two minutes after delivery were excluded since they were characterized by a large amount of missing data, due to the transport of the neonates to the resuscitation desk and the time required to apply the sensors. After exclusion of the first two minutes, the

analysis was done in a sliding window (length of 3 minutes, overlap of 2 minutes), which resulted in 11 sliding windows, time stamped from minute 5 to minute 15.

The signals under study are known to change vastly in the first few minutes and stabilize in the transitional period [312]. To minimize the effect of these large amplitude changes on the coupling values, linear detrending was performed in the sliding window. After detrending, the coupling between any pair of signals was computed using linear and regression (nonlinear) correlation analysis. The linear correlation defines the relationship between two signals using a line, while the nonlinear correlation accounts for nonlinear relationships. In the nonlinear correlation framework, the strength and asymmetry (amount of nonlinearity) were defined. The significance of all correlation values was assessed using surrogate data [352], and non-significant values were set to 0. If the original signals contained missing values in the sliding window, no correlation values were computed. If more than 25% of the correlation values were missing, the patient was excluded from the analysis.

**Clustering** After the correlation analysis, a clustering step was performed to group patients with similar correlation curves. Hierarchical clustering was used with complete linkage clustering, in which the Euclidean distance was used to quantify similarity. Silhouette scores were computed to calculate the goodness of fit of the clustering procedure. The Silhouette scores indicate how similar a set of curves is to its own cluster compared to the other clusters, with values from  $-1$  (clusters assigned in the wrong way) to  $1$  (clusters can be clearly distinguished). These scores were used to determine the optimal number of clusters, and to determine the between-cluster discriminatory power of the individual correlation curves.

**Statistical analysis** After clustering, the demographic data of the groups/clusters were de-blinded. Comparison of continuous parameters was done using the Wilcoxon rank sum test. Comparison of counts was done using the Fisher's exact counts. Significance was defined as  $\alpha = 0.05$ . Data are presented as median (IQR).

## 8.4 Results

Data of 106 neonates were eligible for the present post-hoc analysis. Due to missing data, 58 neonates were excluded, and 48 neonates were included.

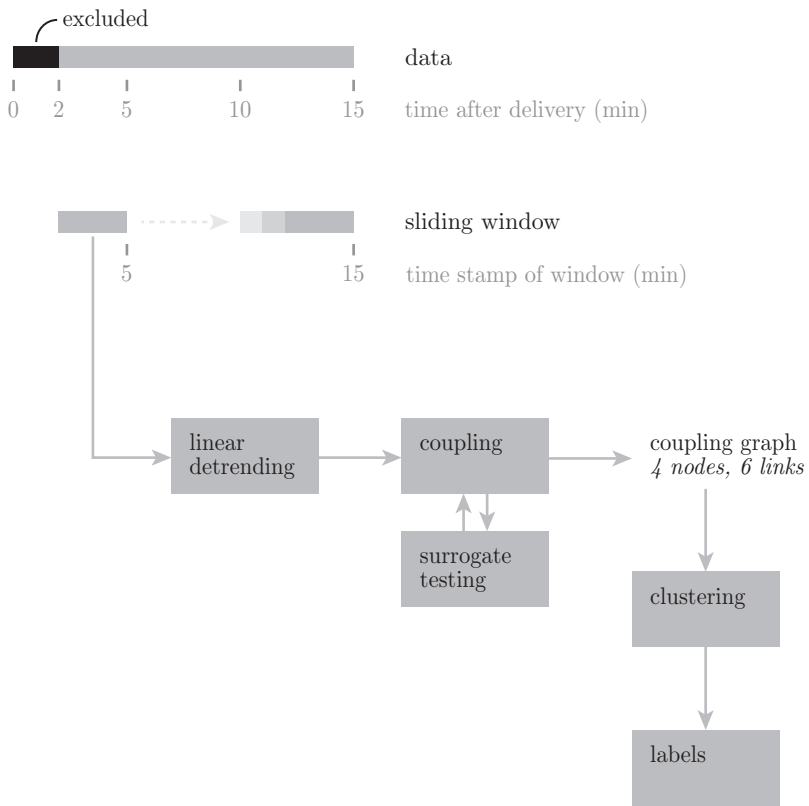


Figure 8.1: The signal processing pipeline used to study neonates during immediate transitional after birth.

Table 8.1: Overview of the patient demographics in the neonatal dataset: all eligible neonates (left) versus the included neonates (right).

	<i>included (N = 48)</i>				<i>excluded (N = 58)</i>				<i>p</i>
	<i>N</i>	<i>P</i> <sub>25</sub>	<i>P</i> <sub>50</sub>	<i>P</i> <sub>75</sub>	<i>N</i>	<i>P</i> <sub>25</sub>	<i>P</i> <sub>50</sub>	<i>P</i> <sub>75</sub>	
GA (weeks)	48	37	38.7	39.1	58	34.3	38	39	–
BW (g)	47	2600	3140	3424	58	1980	2898	3185	.042
length (mm)	46	47	50	51	53	45	48	51	–
head (mm)	46	34	34	35	53	31.5	34	35	–
sex									
male	23				34				–
female	25				41				–
HR (bpm)	48	88	93	95	58	85	91	93	.013
SpO <sub>2</sub> (%)	48	142	151	157	52	140	154	162	–
rScO <sub>2</sub> (%)	48	68	75	79	58	68	79	86	.026
FTOE (%)	48	15	20	25	58	8	12	20	.001
Apgar									
1	48	9	9	9	58	8	9	9	–
5	48	10	10	10	58	9	10	10	–
10	48	10	10	10	58	10	10	10	–
pH of the umbilical cord									
arterial	47	7.30	7.31	7.34	51	7.29	7.32	7.34	–
venous	40	7.36	7.38	7.4	52	7.36	7.38	7.40	–
blood pressure 15 min after birth (mmHg)									
systolic	46	55	63	73	53	57	62	68	–
diastolic	46	29	35	41	53	29	36	45	–
mean	46	38.5	44	50.5	53	39	45	52	–
temperature 15 min after birth (C°)									
peripheral	10	37	37.4	37.58	19	37.1	37.2	37.45	–
rectal	47	36.95	37.1	37.3	57	36.8	37.1	37.3	–
respiratory support									
oxygen	4				14				.036
CPAP	8				20				.047
PPV	0				7				.014
intubation	0				0				–

The included and excluded neonates were comparable with respect to patient demographics, except for a slightly lowered birth weight and more frequent use of supplemental oxygen in the excluded neonates (Table 8.1).

The cluster Silhouette score reached a maximum value for two clusters, indicating that the data could best be separated in two clusters: cluster 1 ( $N = 39$ ) and cluster 2 ( $N = 9$ ) (Figure 8.2). The Silhouette scores for the correlation curves

indicated that the differentiation between the clusters was highest for  $\text{SpO}_2$ – $\text{rScO}_2$  (linear: 0.47, nonlinear: 0.48) and  $\text{SpO}_2$ –FTOE (linear: 0.56) (Figure 8.3). For  $\text{HR}$ – $\text{rScO}_2$ , the Silhouette scores also confirm a differentiation between cluster 1 and cluster 2, mainly for the nonlinear correlation (0.40).

Figure 8.2 presents the linear and nonlinear correlation curves for both clusters.  $\text{SpO}_2$  had linear and nonlinear correlations with  $\text{rScO}_2$  and FTOE, whereby the correlations with  $\text{rScO}_2$  were more pronounced in cluster 2. The linear correlation of  $\text{SpO}_2$  with FTOE was also different between the clusters, being positive in cluster 1 and variable in cluster 2.  $\text{HR}$ – $\text{rScO}_2$  and  $\text{HR}$ –FTOE demonstrated a nonlinear correlation in both clusters, again being more pronounced in cluster 2, whereby linear correlations were mainly absent. As expected, the most pronounced linear and non-linear correlations were observed between  $\text{rScO}_2$  and FTOE in both clusters.

Figure 8.4 presents the asymmetry of the nonlinear correlation, which was highest for all coupling pairs with HR, without difference between the clusters, indicating strong nonlinearity in the coupling with HR. The asymmetry of the nonlinear correlation  $\text{SpO}_2$ – $\text{rScO}_2$  demonstrated higher levels for cluster 1 compared to cluster 2, indicating a higher nonlinearity in the coupling in cluster 1.

After de-blinding the demographic data revealed that the neonates in cluster 2 were significantly younger (mainly preterm) compared to the neonates in cluster 1 (mainly term) (Table 8.2). In addition, the neonates in cluster 2 had a lower birth weight and were smaller, which is considered to be a reflection of the GA difference between both clusters. All other demographic parameters were not different between the two clusters.

In cluster 1, one neonate presented with lips, jaw, and cleft palate. Other than that, the neonates in cluster 1 did not suffer from respiratory distress, cerebral injuries, or heart problems. In cluster 2, two neonates had idiopathic respiratory distress syndrome (IRDS) and one neonate a patent ductus arteriosus (PDA). No cerebral injuries were present among the neonates in cluster 2.

## 8.5 Discussion

The present study demonstrated for the first time that in addition to  $\text{SpO}_2$ , also HR has a nonlinear correlation with  $\text{rScO}_2$  and FTOE in term and preterm neonates during immediate transition after birth. In addition, we were able to demonstrate by clustering that the coupling of  $\text{SpO}_2$  and HR with cerebral oxygenation was more pronounced in neonates with a lower GA. Furthermore,

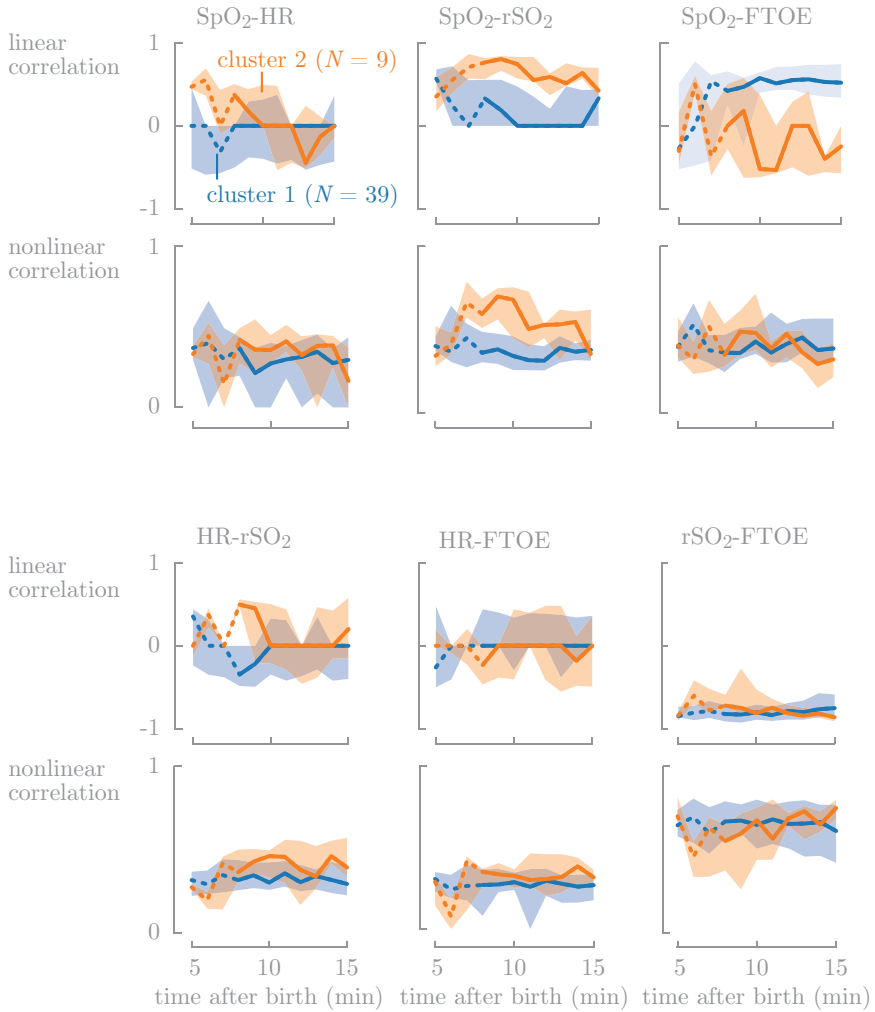


Figure 8.2: Linear and nonlinear correlation curves for both clusters. The main differentiation between both clusters can be observed in the  $\text{SpO}_2\text{-rSO}_2$  and the  $\text{SpO}_2\text{-FTOE}$  curves. The data is presented as median (line) and IQR (shaded area).

Table 8.2: Overview of the patient demographics in the neonatal dataset: cluster 1 (left) versus cluster 2 (right).

	<i>cluster 1 (N = 39)</i>				<i>cluster 2 (N = 9)</i>				<i>p</i>
	<i>N</i>	<i>P</i> <sub>25</sub>	<i>P</i> <sub>50</sub>	<i>P</i> <sub>75</sub>	<i>N</i>	<i>P</i> <sub>25</sub>	<i>P</i> <sub>50</sub>	<i>P</i> <sub>75</sub>	
GA (weeks)	39	37.6	38.9	39.3	9	35.3	35.6	38.2	.002
BW (g)	39	2812	3190	3475	8	1883	2440	2983	.028
length (mm)	38	49	50	51	8	44.8	46	49	.026
head (mm)	38	34	34.5	35	8	30.6	33.3	34.6	.044
sex									
male	17				6				–
female	22				3				–
HR (bpm)	39	89	93	96	9	85	91	92	.038
SpO <sub>2</sub> (%)	39	144	151	158	9	141	152	155	–
rScO <sub>2</sub> (%)	39	69	76	78	9	65	73	81	–
FTOE (%)	48	15	20	25	58	8	12	20	.001
Apgar									
1	39	9	9	9	9	8	9	9	–
5	39	10	10	10	9	9	10	10	–
10	39	10	10	10	9	10	10	10	–
pH of the umbilical cord									
arterial	38	7.29	7.31	7.34	9	7.30	7.30	7.32	–
venous	34	7.36	7.38	7.39	6	7.34	7.38	7.41	–
blood pressure 15 min after birth (mmHg)									
systolic	37	57	65	73	9	52	59	62	–
diastolic	37	29	35	42	9	30	32	35	–
mean	35	41.5	45	51	8	37.25	39.5	42.25	–
temperature 15 min after birth (C°)									
peripheral	10	37	37.4	37.58	0				–
rectal	38	37	37.1	37.3	9	36.8	37.1	37.2	–
respiratory support									
oxygen	2				2				–
CPAP	5				3				–
PPV	0				0				–
intubation	0				0				–

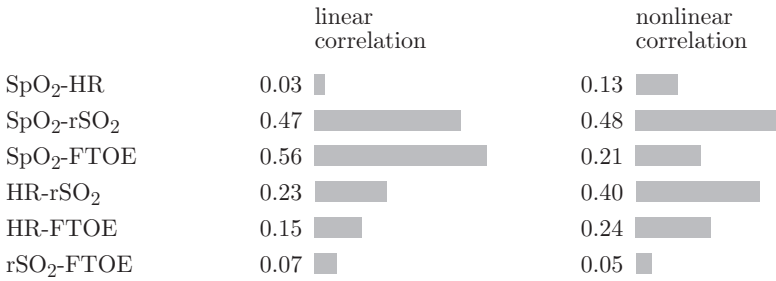


Figure 8.3: The Silhouette scores indicate that the main difference in coupling curves between the two clusters is observed for the linear and non nonlinear correlation SpO<sub>2</sub>-rScO<sub>2</sub> (0.47 and 0.48, respectively), and the linear correlation SpO<sub>2</sub>-FTOE (0.56).

the nature of the SpO<sub>2</sub>-rScO<sub>2</sub> coupling was observed to change with age: the magnitude decreases and becomes more nonlinear as age increases.

SpO<sub>2</sub> can be assumed to be the main contributor to rScO<sub>2</sub> since oxygen delivery is directly dependent on saturation of the delivered hemoglobin to the brain. To date, most studies on cerebral oxygenation during the immediate transition period measuring both SpO<sub>2</sub> and rScO<sub>2</sub> demonstrated a similar but not equal behavior [28, 312]. Therefore, rScO<sub>2</sub> and SpO<sub>2</sub> are expected to be coupled, even during the immediate transition period, which is now confirmed by our results. Furthermore, our results suggest that the coupling between rScO<sub>2</sub> and SpO<sub>2</sub> might be age dependent: as GA increases, the SpO<sub>2</sub>-rScO<sub>2</sub> coupling reduces in amplitude and becomes more nonlinear (Figures 8.2 and 8.4). Hunter et al. found no SpO<sub>2</sub>-rScO<sub>2</sub> correlation in preterm neonates, which seems to be contradicting to our results in more preterm neonates but is in accordance with our findings in more term neonates. The difference between our study and the study of Hunter et al. is the time point of measurement suggesting that the behavior of SpO<sub>2</sub>-rScO<sub>2</sub> coupling is in addition to GA also dependent on PNA being more pronounced during immediate transition. A further difference between the two studies is that the neonates in the study of Hunter et al. had an overall lower GA than the neonates in the present study.

The coupling between HR and rScO<sub>2</sub> was comparable in both groups, although slightly elevated in the cluster with the younger neonates. This coupling was characterized by a linear part that was approximately zero, but a significant nonlinear part, suggesting that HR changes might be reflected in rScO<sub>2</sub>, only

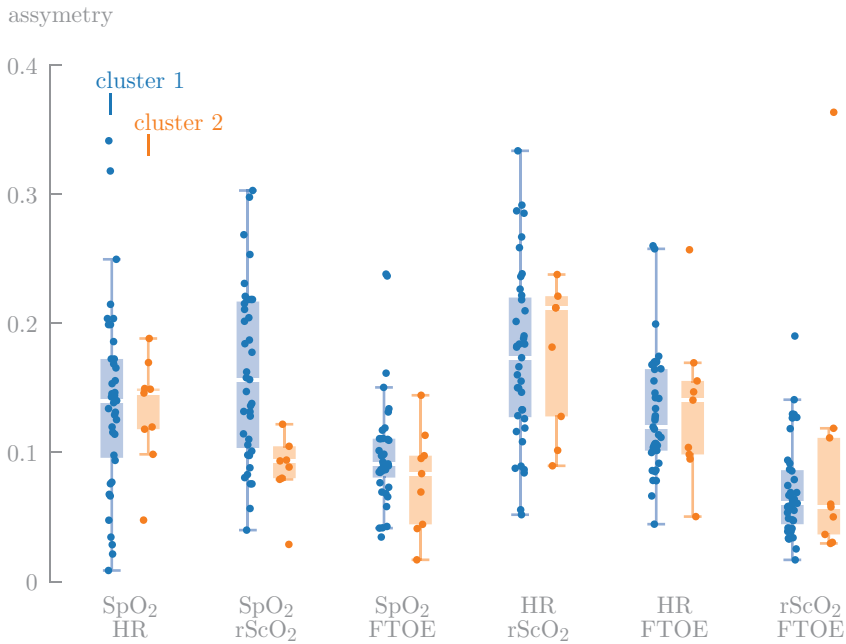


Figure 8.4: Asymmetry of the nonlinear correlation coefficient measures the degree of nonlinearity. The asymmetry was highest for coupling pairs involving HR. A significant between-cluster difference was observed for the SpO<sub>2</sub>-rScO<sub>2</sub> coupling.

in a nonlinear way. The linear correlation between HR and rScO<sub>2</sub> was recently described by Mitra et al. as TOHRx [262]. In their study, they analyzed preterm infants at a median age of two days and found that heart rate has a key influence on cerebral haemodynamics in preterm infants, suggesting also a diagnostic value in identifying impaired cerebrovascular reactivity. In addition, a maturational effect was described: the linear correlation decreased with increasing GA. Their findings on extremely low gestational age preterm neonates are in accordance with our findings in moderate to late preterm and term neonates with no linear correlation between HR and rScO<sub>2</sub> or FTOE considering the decrease of this linear correlation with increasing GA. However, our data suggest a persisting nonlinear correlation with increasing GA.

In another study, it has been demonstrated that HR has a significant impact on cerebral oxygenation during immediate transition after birth when bradycardia

occurs in combination with the additional presence of hypoxemia [53]. This study also suggests some coupling of HR and cerebral oxygenation that is in accordance with the present finding of nonlinear correlations. In the present study, none of the neonates had severe hypoxia or bradycardia, therefore a separate analysis of these neonates was not performed.

HR and stroke volume together define CO. Therefore, the present study supports the influence of CO on cerebral oxygenation by having an impact of cerebral perfusion. Correlations between  $rScO_2$  and CO in extremely preterm infants in the first 72 hours of life have already been described [179]. In contrast, Baik et al. [30] described 15 minutes after birth that CO measured non-invasively was not correlated with cerebral oxygenation. At the first sight, the latter study seems to contradict our findings. However, Baik et al. only performed linear correlations, which were also not observed in the present study concerning HR. Nonlinear correlations of CO and cerebral oxygenation are not available to date, making a comparison between the study by Baik et al. and the present study not feasible.

To find patterns in the data, hierarchical clustering was applied to the coupling curves. This way, a data-driven interpretation of the patterns in the curves was obtained. After being completely blinded for the demographics during the clustering step the demographic data were received after the final clustering was established. This way of analysis is a unique approach. In a traditional analysis, the data is usually divided in various groups at the start of the analysis, based on some defined (demographic) characteristic like gestational age, after which the groups are compared. In this analysis, we took all data together, and divided the data only at the end of the analysis in an automatic way using a data-driven approach. This way, the data are grouped based on the characteristics comprised in the data, instead of based on clinical (demographic) data. Finally, a difference in gestational age was detected, which suggests a maturational effect.

The main strengths of the present study were two-fold. First, the approach of de-blinding of the demographic data after clustering revealed a difference in gestational age. Second, both linear and nonlinear correlations were analyzed in the immediate transition after birth. A limitation might be the low number of neonates included in cluster 2, whereby independently of the sample size the results are consistent.

## 8.6 Conclusion

In addition to SpO<sub>2</sub>, also HR demonstrated a nonlinear correlation with rScO<sub>2</sub> and FTOE in term and preterm neonates during immediate transition after birth. In addition, the coupling of SpO<sub>2</sub> and HR with cerebral oxygenation was more pronounced in neonates with a lower GA. Furthermore, the present study showed that the SpO<sub>2</sub>–rScO<sub>2</sub> coupling decreases and becomes more nonlinear as GA increases. These findings suggest a benefit of cerebral oxygenation monitoring during immediate transition, and support the necessity of monitoring SpO<sub>2</sub> and HR, since both influence cerebral oxygenation. Taking all these parameters, which are tightly linked during the immediate transition, into account might help to understand the processes during adaptation better and improve support in neonates in need of resuscitation.



multivariate analysis

09

# The neurocardiovascular graph reflects propofol dynamics

*based on:*

Hendrikx, D., Thewissen, L., Smits, A., Naulaers, G., Allegaert, K., Van Huffel, S. and Caicedo, A. Using Graph Theory to Assess the Interaction Between Cerebral Function, Brain Hemodynamics and Systemic Variables in Premature Infants. *Complexity 2018* (2018), 6504039.



Graphs can be used to describe a great variety of real-world situations and have therefore been used extensively in different fields. In this chapter, we used graphs for the first time to study the interaction between cerebral function, brain hemodynamics, and systemic variables in premature neonates. For this, we used a clinical setting of propofol administration for endotracheal intubation (INSURE). The structure of the neurocardiovascular graph, and the change thereof following propofol administration was studied.

## 9.1 Introduction

A graph is a structure that can be used to represent the relation between different objects. In this context, a graph can be thought of as a diagram which consists of a set of points, where some or all of them are joined by lines. Formally, the points of the graph are referred to as *vertices* or *nodes*, whereas the lines between them are called *edges* or *links*. In general, graphs can be used to describe a great variety of real world situations [178]. Think, for example, of a social network, where people are represented by nodes and the edges between the nodes are used to indicate friendship. Another example is a geographic network of cities, with an edge between two cities indicating a direct connection through a highway. In addition to the presence (or lack) of an edge connecting two nodes, extra measurements can be associated with the edges. These measurements are formally referred to as *edge weights*. In a social network, edge weights could be used to denote the strength of the friendship (acquaintances, close friends, ...), whereas in a geographic network, the weights can indicate the physical distance or the amount of traffic typically encountered on each road. Mathematically, this type of diagram corresponds to a weighted graph.

In this chapter, weighted graphs are used to study the interaction of cerebral function, brain hemodynamics, and systemic variables in premature neonates. Multiple studies are available in the literature on the pairwise interactions between some of these variables. Caicedo et al. analyzed the relation between MABP and rScO<sub>2</sub>, measured by means of NIRS [61]. The coupling between these two variables, defined using a transfer function approach, was found to be a measure for CAR. Semenova et al. examined the relation between MABP and EEG [358]. The authors documented that preterm infants with a high clinical risk index for babies (CRIB) score were found to be associated with a higher nonlinear coupling between EEG activity and MABP, quantified by means of MI. Tataranno et al. examined the relation between rScO<sub>2</sub> and EEG and found that increased oxygen extraction was related to spontaneous activity transients observed in the EEG [396]. In contrast to the studies mentioned above, we

aim to analyze the interaction between cerebral and systemic variables using an extended multimodal approach, integrating three systemic variables (HR, MABP, and SpO<sub>2</sub>), rScO<sub>2</sub>, and EEG.

This study is situated within the interdisciplinary field of Network Physiology, which analyses how diverse physiologic systems dynamically interact and collectively behave to produce distinct physiologic states and functions [35]. Moreover, the use of graphs enables a graphical representation of the interaction between the different physiological systems in time. This study shows for the first time a comprehensive model of different physiological processes comprising CAR, NVC or baroreflex, working at the same moment in time. In literature, most studies focus on these processes individually without taking into account the influence of the other processes. With the graph approach outlined in this chapter, we try to show the different processes, their interaction and the importance of the individual processes at each moment in time. To the best of our knowledge, this is a totally new mindset and way of showing the physiological interaction between cerebral function, brain hemodynamics and systemic variables in newborn neonates.

The interaction between the different variables is studied using premedication by means of propofol as a model. Propofol (2,6 di-isopropylphenol) is a short-acting anesthetic: it has a rapid onset of action and is generally short in duration. In neonates, however, it is documented that clinical recovery takes time [375]. In clinical practice, propofol is administered to the neonates as a single intravenous (IV) bolus. Practices on propofol dosing, particularly in highly vulnerable premature neonates, are not standardized and vary between different NICUs. Multiple studies, however, indicate that propofol dose values of 2 to 2.5 mg kg<sup>-1</sup> should be used as preintubation medication in premature neonates [299, 370, 303, 136].

Propofol administration is frequently associated with a decrease in MABP in neonates [439, 375, 418, 299, 370, 303], children [420] and adults [74, 274, 171]. Propofol distributes into the CNS and fat tissue immediately after IV dosing, which explains the rapid onset of this anesthetic drug. In a secondary phase, propofol is redistributed into the circulation, which leads to vasodilation. Combined with the blunted reflex tachycardia, this can result in hypotension [370]. Therefore, a decrease in MABP is observed up to one hour after administration of propofol in neonates [418]. Premedicating neonates with propofol generally causes a modest and short-lasting decrease in HR, SpO<sub>2</sub> and rScO<sub>2</sub>, as opposed to the longer lasting and more pronounced decrease in MABP [418, 303, 136, 173]. In addition, the discontinuity pattern of the EEG is also influenced by propofol, which induces a reversible state of diminished responsiveness behaviorally similar to quiet (NREM) sleep [359]. During quiet sleep, the EEG of premature neonates shows a spontaneous, physiological

Table 9.1: Stratification of the neonates into three age groups based on PMA: extremely preterm, very preterm and moderate to late preterm neonates.

	extremely preterm < 28 weeks	very preterm 28–31 6/7 weeks	moderate to late preterm 32–36 6/7 weeks
# patients	5	13	4
PNA (days)			
median	1	1	1
range	1–2	1–2	1–3
dose (mg kg <sup>-1</sup> )			
median	1.0	1.0	2.75
range	0.5–1.5	0.5–2.5	1.0–4.5

discontinuity of electrical activity, characterized by higher amplitude, lower frequency EEG rhythms (tracé alternant, TA) [56, 342]. This phenomenon is generally referred to as burst-suppression, which corresponds to an increase in IBI duration [6, 71]. Moreover, a larger IBI duration is associated with smaller FTOE values, which indicate lower brain energy consumption [63].

## 9.2 Dataset

This study focuses on neonates that received propofol as a sedative in the setting of endotracheal intubation. Details on the structure of this dataset and the recording equipment was presented in Section 4.1.

The study group consisted of 22 neonates, which were stratified into three groups, based on PMA, which is a major covariate of propofol clearance in the absence of variability in PNA [10] (Table 9.1). These groups are referred to as *extremely preterm* (<28 weeks PMA), *very preterm* (28–31 6/7 weeks PMA), and *moderate to late preterm* (32–36 6/7 weeks PMA) [248]. The neonates in these three groups had a PNA of 1 (1–2) days, 1 (1–2) days, and 1 (1–3) days, respectively. The propofol dose administered to these neonates was 1 (0.5–1.5) mg kg<sup>-1</sup>, 1 (0.5–2.5) mg kg<sup>-1</sup>, and 2.75 (1–4.5) mg kg<sup>-1</sup>, respectively. The dataset used in the present analysis was collected with the aim to find the median effective dose (ED50) of propofol for sedation. Therefore, lower values of starting propofol dose were used, and older neonates were sedated using higher doses of propofol compared to the youngest neonates.

## 9.3 Methods

**Signal processing pipeline** The signal processing pipeline that is used in this study was introduced in Chapter 3 and is depicted in Figure 3.1. First, artifact removal was done. EEG segments with impedance values exceeding  $10\text{ k}\Omega$  were removed from the raw EEG [243]. In addition, movement artifacts identified as rapid changes in the impedance measurement were detected and also removed from the raw EEG.

Second, due to the different temporal characteristics between the EEG and all other signal modalities, the EEG signals are processed in order to obtain surrogates for brain activity in a similar time frame as the other measured signals. The EEG signal is segmented in burst and IBI segments using an in-house algorithm based on the line length [210]. The RMS value and the duration in time for burst and IBIs in overlapping windows of two min are used as a surrogate for EEG. The running window is shifted in one second, producing a new score every second. In this way, the sampling frequency of the surrogate measures for EEG has the same sampling frequency as the other signal modalities. In total, five features are computed from the discontinuous neonatal EEG: running RMS values of the original EEG, BIs, and IBIs and running duration values of the BIs and IBIs. In this paper, we only report the results using the running IBI duration, since this is a very robust measure for EEG activity, and thus cerebral metabolism, as validated by our group in a previous study [210]. In addition, this measure is highly interpretable. It is important to note, however, that the other EEG features give similar results, since the different feature values are highly related. An example of the five EEG features is presented in Figure 9.1.

Third, the pairwise interaction between the multimodal signals is quantified. In this chapter, we compute the pairwise coupling using two similarity measures. Therefore, we generate two graph models for each neonate. Both coupling measures are based on the RBF kernel function, which is a nonlinear similarity measure. The first measure uses the input signals in the RBF kernel, and is defined for two signals  $x(k)$  and  $y(k)$  as:

$$k_T(x(k), y(k)) = \phi(x(k))^\top \phi(y(k)) = \exp\left(-\frac{\|x(k) - y(k)\|_2^2}{2\sigma^2}\right). \quad (9.1)$$

The subscript  $T$  indicates that time domain signals are used in the kernel. The similarity  $k_T$  is bounded by 0 (absence of common interactions) and 1 (exact common interactions). Consequently, it highly depends on signal amplitudes and can be affected by delays between the signals. A graph model computed using the similarity measure  $k_T$  is denoted as  $G_T$ . The second similarity measure

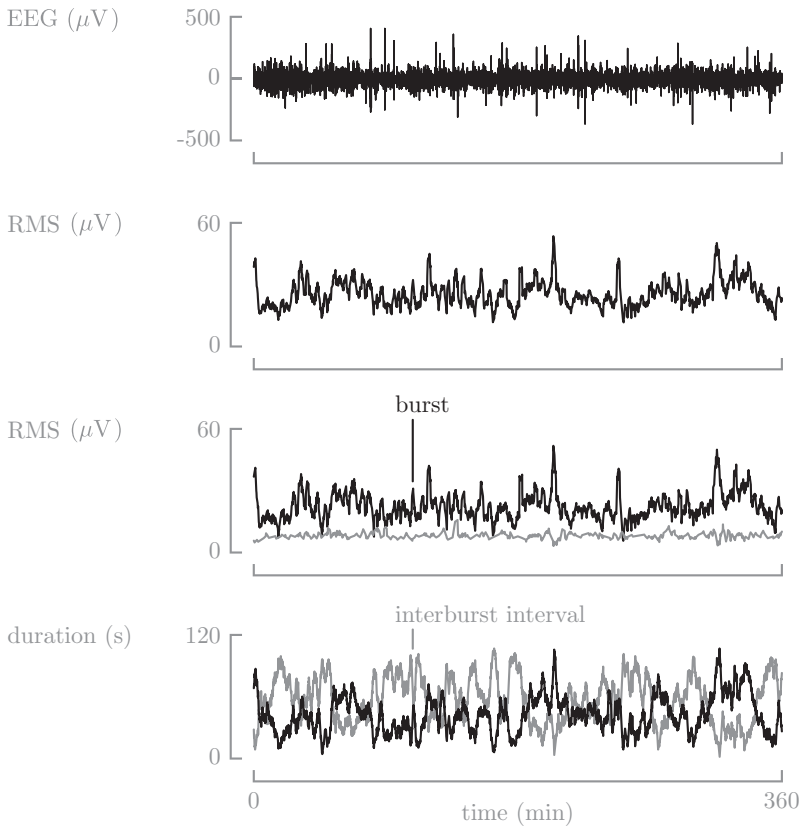


Figure 9.1: Illustration of the features computed from the EEG signal. The top row illustrates a 6 hour long segment of EEG for one neonate in the group of study (PMA 27 weeks,  $0.5 \text{ mg kg}^{-1}$ ). The second row illustrates the running RMS value, while the third and last row illustrate the running RMS and running duration values for bursts and IBIs, respectively.

uses the PSD of the signals in the RBF kernel. Thus, the time input data is transformed to the frequency domain, before computing the RBF kernel function. Mathematically, this similarity measure  $k_F$  is defined as:

$$k_F(\mathcal{F}(x(k)), \mathcal{F}(y(k))) = \exp\left(-\frac{\|\mathcal{F}(x(k)) - \mathcal{F}(y(k))\|_2^2}{2\sigma^2}\right), \quad (9.2)$$

where  $\mathcal{F}(x(k))$  and  $\mathcal{F}(y(k))$  represent the PSD of  $x(k)$  and  $y(k)$ , respectively. The subscript  $F$  indicates that frequency domain signals are used in the kernel. The PSD is computed using Welch's method using overlapping subwindows of 5 min in order to reduce the noise in the PSD estimate (maximal overlap) (Section 3.3.2). Note that the kernel presented in Equation 9.2 is a valid positive definite kernel, since the input data is transformed before application of the kernel function. As before, the similarity defined by  $k_F$  is bounded by 0 and 1. The transformation to the frequency domain allows to include time-delayed signal interactions and interactions of opposite sign, in contrast to  $k_T$  which only takes into account instantaneous amplitude interactions. In physiological systems, it is possible that if one signal increases (decreases), another signal decreases (increases) to maintain homeostasis and that this interaction is not instantaneous but delayed. A graph computed using the similarity measure  $k_F$  is denoted as  $G_F$ .

**Kernel tuning** In order to compute the similarity measure, the bandwidth  $\sigma$  of the RBF kernel should be tuned, i.e. optimized to avoid kernel overfitting and underfitting. In the present analysis, the similarity measures  $k_T$  and  $k_F$  both depend on this parameter  $\sigma$ ; the optimization procedure is the same for both similarity measures. Therefore, it is outlined in terms of  $k$ , which represents the two similarity measures. The strategy used to select the kernel bandwidth for the present analysis considers the kernel matrix  $\Omega$ , defined as  $\Omega_{ij} = k(x_i, x_j)$ ,  $i, j = 1, \dots, n$ . The kernel bandwidth  $\sigma$  is tuned by maximizing the Shannon entropy of the kernel matrix  $\Omega$ , defined as:

$$H(\Omega) = -\sum_k p_k \log_2 p_k, \quad (9.3)$$

where  $p_k$  is equal to the probability of seeing the  $k$ th possible element of the matrix  $\Omega$ . The entropy is thus determined by estimation of the PDF of the matrix  $\Omega$ . By maximizing the Shannon entropy we try to obtain a uniform distribution of the values in the kernel matrix, and therefore we try to avoid both overfitting and underfitting.

The kernel bandwidth is tuned for each neonate individually. The following optimization problem is used to define the tuned bandwidth  $\sigma_{\text{opt}}$  (Figure 9.2):

$$\sigma_{\text{opt}} = \max_{\sigma} H(\Omega_C), \quad (9.4)$$

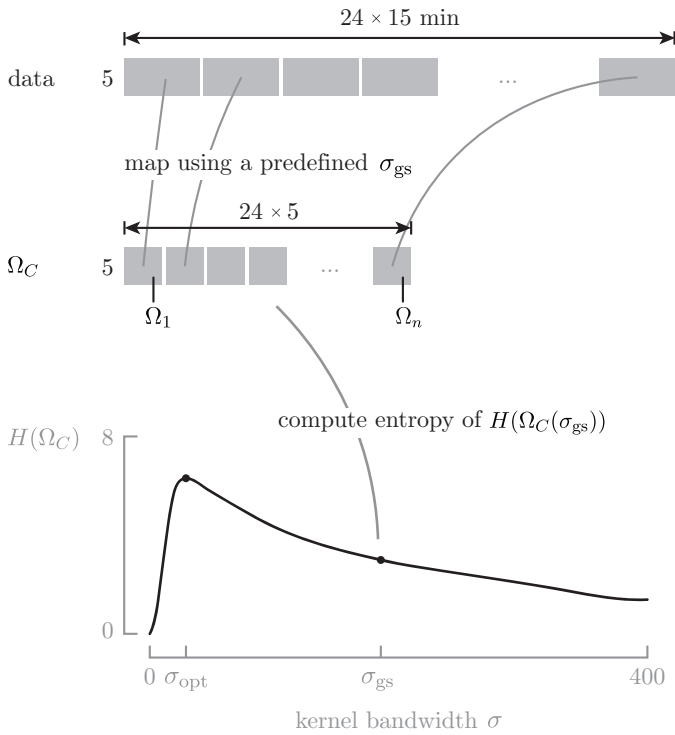


Figure 9.2: Method used to tune the kernel bandwidth  $\sigma$ . The data is segmented in nonoverlapping segments of 15 min. For each segment  $i$ , the kernel matrix  $\Omega_i$  is defined. All  $\Omega_i$  are collected in  $\Omega_C$ , for which the Shannon entropy  $H(\Omega_C)$  is computed. Repeating this procedure for a range of  $\sigma$  allows to select  $\sigma$  that corresponds to the largest  $H(\Omega_C)$ .

with

$$\Omega_C = [\Omega_1 \ \Omega_2 \ \dots \ \Omega_n], \quad (9.5)$$

where  $\Omega_C$  is a collection of kernel matrices, computed from all the signal segments recorded per neonate. Thus, a collection of kernel matrices is computed from the 6 hours long data segment instead of only one kernel matrix in the optimization procedure. If we would consider only one kernel matrix per neonate, it would only contain 25 entries, since the kernel matrix is a  $5 \times 5$  matrix. Clearly, this is not enough data to estimate a robust PDF. Therefore, to solve this problem, we assume that the graph model does not change and that it is situated in the same nonlinear subspace throughout the 6 hours long analysis window. This assumption indicates that the  $\sigma_{\text{opt}}$  should be uniform throughout the analysis window and that  $\sigma_{\text{opt}}$  can be computed using  $\Omega_C$ .

Figure 9.2 illustrates the optimization procedure in a schematic way. The original data segment of 6 hours was segmented into non-overlapping segments of 15 minutes. Thus,  $n = 24$  signal segments of 15 minutes were defined. For each of these segments  $i$ , the kernel matrix  $\Omega_i$  was computed and all these kernel matrices  $\Omega_i$  were concatenated as indicated in equation 9.5. The use of a collection of kernel matrices allows to estimate the PDF, and consequently, the Shannon entropy. Therefore,  $H(\Omega_C)$  is characterized by one global maximum. For the group of study, median (range) values of  $\sigma_{\text{opt}}$  are 27 (26 – 29) and 94 (86 – 113) for  $k_T$  and  $k_F$ , respectively.

**Interaction strength features** In order to quantify the strength of the changes in signal interaction, two features are computed from the interaction curves: the normalized area  $S$  between the interaction curve and reference level; and the maximal deviation  $\Delta$  from reference level (Figure 9.3). Both feature values are computed in a time frame from 0 to 90 min after propofol administration. Reference levels are defined as the median value of an interaction curve in a time frame from 180 to 360 min after propofol administration, as mentioned before. Normalization of  $S$  is done by dividing the area by the length of the time interval. so that  $S$  and  $\Delta$  are bounded by 0 (no deviation from reference level) and 1 (very strong deviation from reference level).

**Statistical analysis** Data are presented as mean (IQR). The relation between the features  $S$  and  $\Delta$  and PMA and propofol dose is studied using OLS regression (Section 3.6.1). The coefficient of determination  $R_i^2$  is used to indicate the goodness of fit of the linear model (subscript  $i$  denotes the predictor variable  $i$ ). In addition, the coefficient of partial determination  $R_{i|j}^2$  was computed to account for the effect of both predictor variables at the same time. The

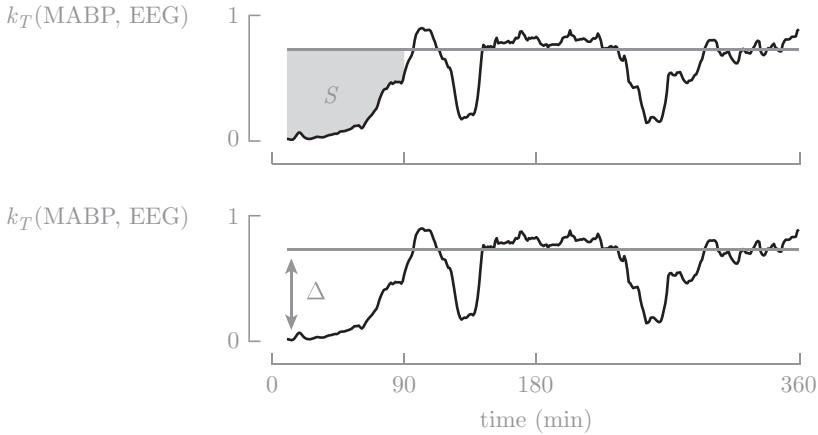


Figure 9.3: Features used to quantify the reduction in signal interaction strength:  $S$  (top) and  $\Delta$  (bottom). The feature values are illustrated for one neonate in the group of study (PMA 30 weeks,  $2.5 \text{ mg kg}^{-1}$ ). Feature values  $S$  and  $\Delta$  are computed from 0 to 90 min, while the reference level is defined as the median value of the interaction curve from 180 to 360 min.

significance of the coefficient of (partial) determination was assessed using the Monte Carlo permutation test with  $10^5$  repetitions. Significance was defined as  $\alpha = 0.05$ .

## 9.4 Results

**Interaction MABP and EEG** Figure 9.4 illustrates the interaction curves of MABP and EEG (running IBI duration) after administration of propofol, computed using  $k_T$  (Equation 9.1). A pronounced loss in interaction was observed, followed by a gradual increase to a reference level, which was reached 90 min after propofol administration. This loss in interaction was present among all of the signal modalities of the multimodal dataset, as illustrated by the temporal overview of the graph structure in Figure 9.5.

Figure 9.6 presents the relation between features the ( $S$  and  $\Delta$ ) and PMA and propofol dose. The coefficient of determination was equal to  $R_A^2 = 0.09$  and  $R_D^2 = 0.53$  for feature  $S$ , and  $R_A^2 = 0.17$  and  $R_D^2 = 0.30$  for feature  $\Delta$

(subscripts  $A$  and  $D$  are used to denote PMA and dose, respectively). Since PMA and dose were correlated ( $r_{AD} = 0.45$ ), we also computed the coefficient of partial determination, which was equal to  $R_{A|D}^2 = 0.002$  and  $R_{D|A}^2 = 0.49$  for feature  $S$ ; and  $R_{A|D}^2 = 0.05$  and  $R_{D|A}^2 = 0.20$  for feature  $\Delta$ . PMA and dose were not collinear using a linear model, as assessed using the variance inflatable factor (VIF), which was equal to  $VIF = 1.2572$ . In general, a VIF close to 1 indicates the lack of collinearity.

**Overall interactions** Propofol-induced loss of interaction among the signals was associated with a drop in average degree  $\delta(G_T)$  (Figure 9.7). The drop in average graph degree can also be observed in Figure 9.5, which illustrates the structure of the graph for one neonate in the group of study at different time instances. The average degree was highly determined by the MABP vertex degree ( $d_{\text{MABP}}$ ) during the first 30 min after propofol administration (Figure 9.7), in graphs computed using both  $k_T$  as well as  $k_F$ . From 30 min onwards, the increase of  $\delta(G_T)$  was mainly influenced by  $d_{\text{EEG}}$ , which was found to have lower values compared to all other modalities in this time frame. As before, this effect can be observed in graphs computed using  $k_T$  and  $k_F$ , although it was less pronounced for graphs computed the latter similarity measure. The corresponding results from  $k_T$  and  $k_F$  might indicate that time-delayed or interactions of opposite sign were not present in our dataset, or that the influence of those interactions was not relevant, probably due to the length of the analysis window (15 min).

## 9.5 Discussion

In the present analysis, we study how different physiologic systems dynamically interact and collectively behave after IV propofol bolus administration in preterm neonates. These physiologic systems are presented by the different signal modalities under study, and we focus on the interaction between the brain and the cardiovascular system. This study can therefore be situated in the interdisciplinary field of Network Physiology [35].

Our data indicates that propofol causes a change in the dynamical interactions between the different signals up to 90 min after propofol administration. The strength of this effect was observed to be mainly determined by propofol dose, rather than the differences in PMA. In addition, the recovery phase was observed to be mainly determined by EEG dynamics, due to a much slower recovery to reference level compared to the other signal modalities.

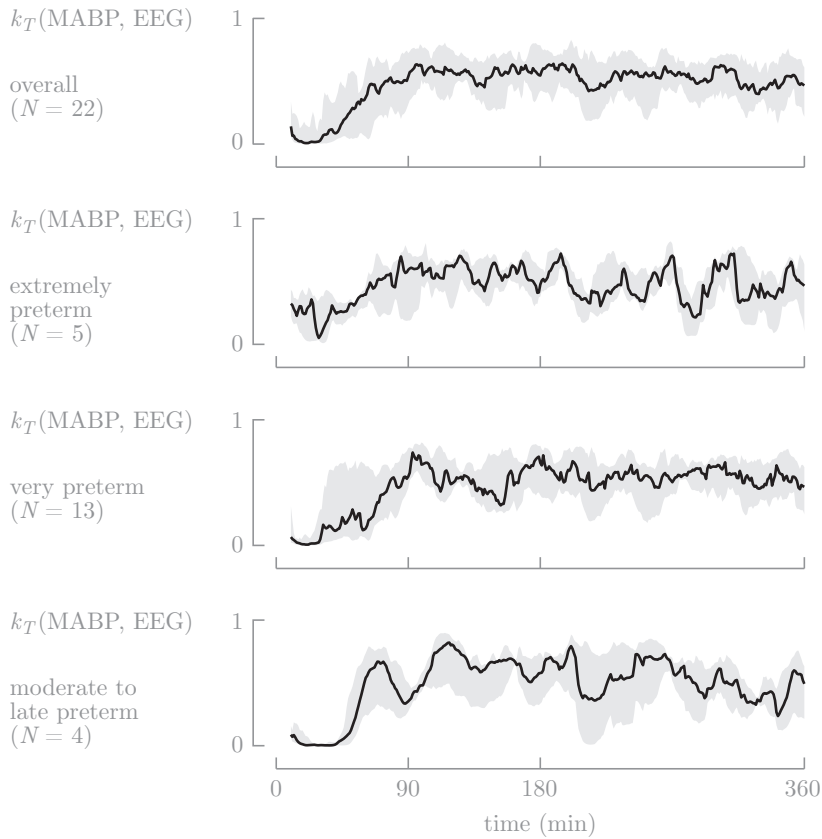


Figure 9.4: Signal interaction between MABP and EEG after administration of propofol at  $t = 0$ . A reduction in interaction is observed among the different signal modalities after the administration of propofol, with a slow recovery to the reference level. The black line and gray shaded area present the median and IQR, respectively.

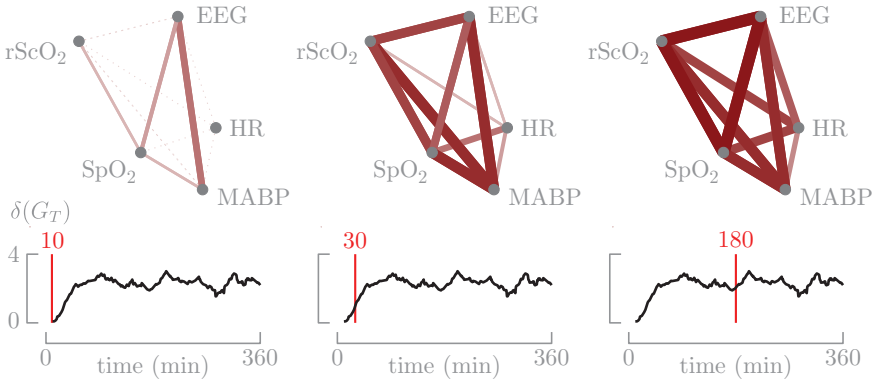


Figure 9.5: Changes in the physiological network, assessed using a graph model  $G_T$ , for one neonate in the group of study (PMA 30 weeks,  $1.0 \text{ mg kg}^{-1}$ ) at 10 (left), 30 (middle), and 180 (right) min after propofol administration. Under each graph, the average graph degree  $\delta(G_T)$  is presented, which measures the average connection strength of the graph edges. From left to right, the edge weights increase, which translates in an increased  $\delta(G_T)$ .

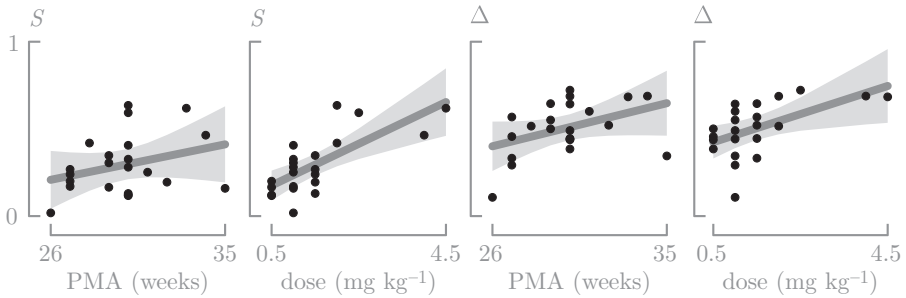


Figure 9.6: The relation between features  $S$  and  $\Delta$ , computed from the  $k_T(\text{MABP}, \text{EEG})$  interaction curves (Figure 9.4), and PMA and propofol dose. The data points and the OLS fit are depicted in black and gray, respectively. The shaded area indicates the 95-percentage confidence bounds on the OLS fit.

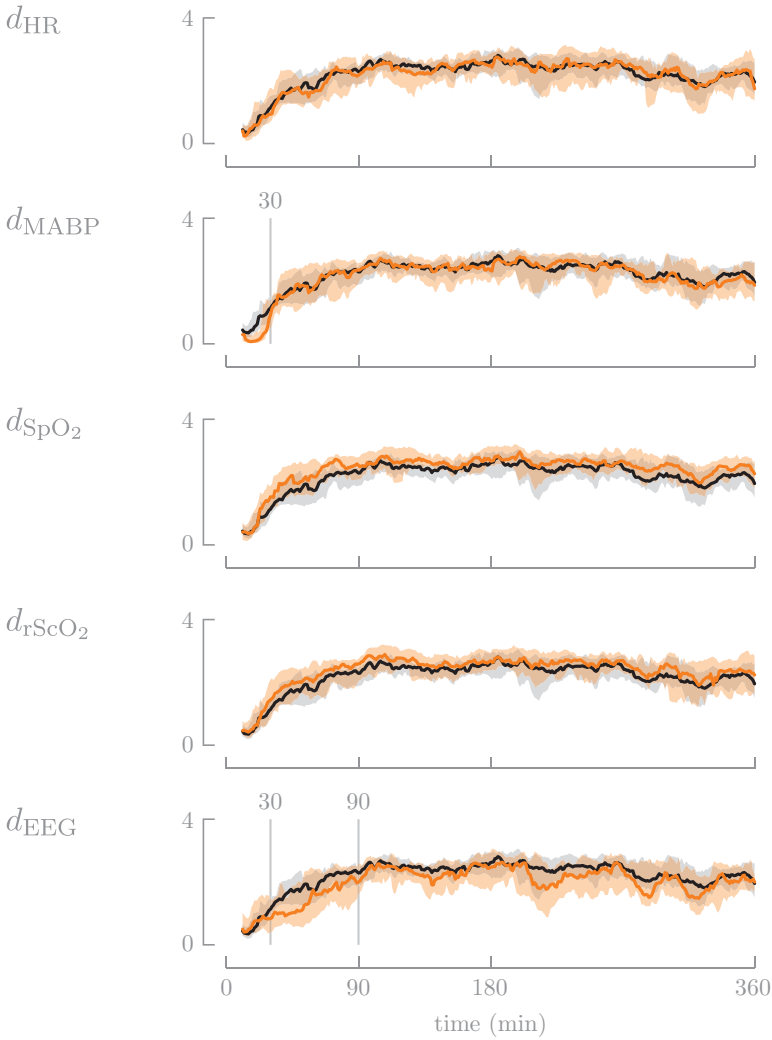


Figure 9.7: Comparing the vertex degree values (orange) with the graph average degree (black) after administration of propofol at  $t = 0$  for all neonates ( $N = 22$ ) using  $k_T$ .  $d_{MABP}$  highly determines the signal interaction pattern during the first 30 min, while  $d_{EEG}$  highly influences the signal interaction pattern from 30 min to 90 min after propofol administration. After 90 min, the neonates are recovered from propofol, as indicated by the steady reference levels observed after 90 min.

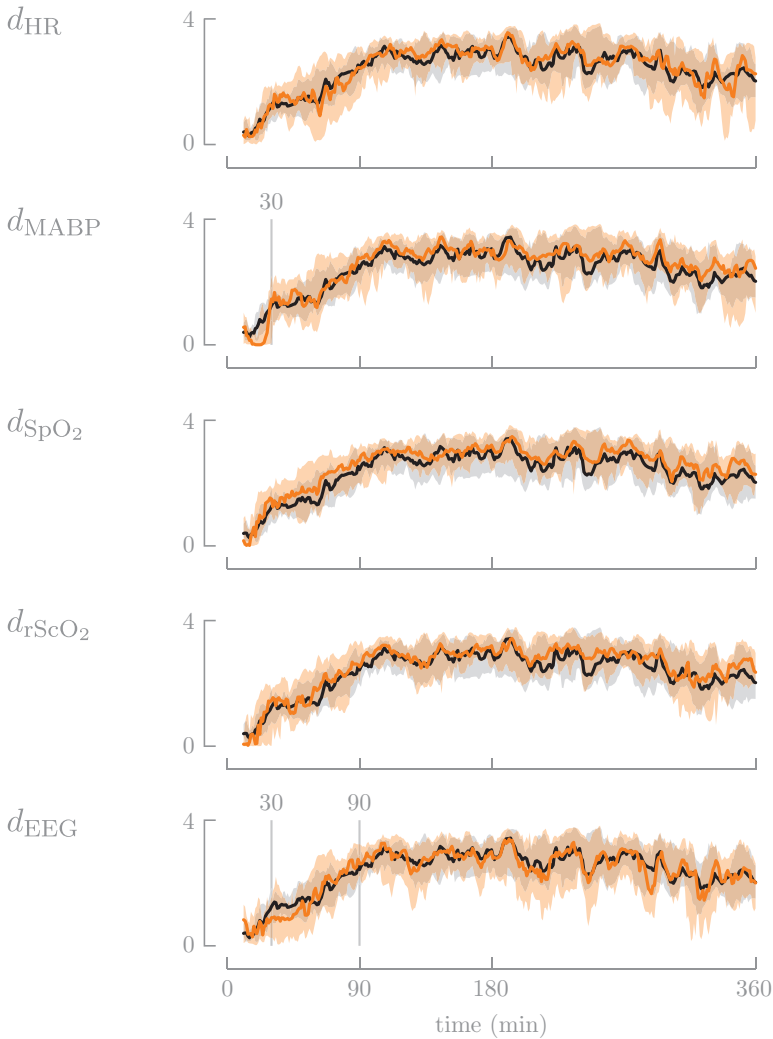


Figure 9.7 (cont.): Comparing the vertex degree values (orange) with the graph average degree (black) after administration of propofol at  $t = 0$  for all neonates ( $N = 22$ ) using  $k_F$ .  $d_{MABP}$  highly determines the signal interaction pattern during the first 30 min, while  $d_{EEG}$  highly influences the signal interaction pattern from 30 min to 90 min after propofol administration. After 90 min, the neonates are recovered from propofol, as indicated by the steady reference levels observed after 90 min.

**Interaction MABP and EEG** Sedation of neonates using propofol induced a reduction in the interaction between MABP and EEG (Figure 9.4), with only a slow, gradual increase back to reference level. The most pronounced decrease in interaction pattern was observed for the oldest neonates in the group of study (moderate to late preterm group): a strong loss of interaction was observed during the first 60 min after propofol administration, followed by a brisk increase back to baseline (Figure 9.4). This pattern clearly differs from the younger neonates (extremely to very preterm group), which were characterized by a less pronounced reduction in interaction and a more gradual increase back to reference levels.

Two possible indicators for the observed difference in signal interaction patterns are proposed. First, we could argue that the difference in coupling curves is a result of age. Morphologically, the continuity of neonatal EEG changes with age; the oldest neonates are characterized by a much more continuous EEG pattern (tracé continue) compared to the younger neonates (tracé discontinu) [101]. A more continuous EEG could result in a more pronounced increase in IBI duration after propofol, potentially explaining the more pronounced loss in signal interaction observed among the oldest neonates in the group of study. Second, we could argue that the difference in coupling curves is a result of a difference in propofol dosing. In this study, higher doses were administered to older neonates (Table 9.1). In literature, a higher incidence of hypotension was reported with increasing dose of propofol [370]. Evidently, a more pronounced impact on MABP can be responsible for a stronger loss in signal interaction.

Since PMA and propofol dose were correlated ( $r_{AD} = 0.45$ ), the influence of each factor on the resulting signal interaction pattern was assessed using features  $S$  and  $\Delta$  (Figure 9.6). From this analysis, it is clear that the influence of PMA on the feature values was minimal, especially when taking into account the effect of the dose, as indicated by the coefficients of partial determination. This suggests that the interaction between MABP and EEG presented in Figure 9.4 was mainly influenced by propofol dose, rather than a difference in age.

**Overall interactions** The phase of sedation using propofol is characterized by a markedly different network structure compared to the reference phase, indicating a clear association between network topology and physiologic function. This is illustrated in Figure 9.5: after 10 min, the graph is weakly connected indicating a highly reduced overall signal interaction as opposed to the strongly connected graph observed 3 hours after propofol administration.

The MABP was observed to be the main contributor to the reduction in signal interaction during the first 30 min after propofol administration (Figure 9.7). During this time frame, MABP strongly influenced the strength of the overall

interaction pattern, since its vertex degree was lower compared to the average graph degree. This effect can be explained as an amplitude effect, since propofol administration is associated with a pronounced decrease in MABP, which can last up to one hour after propofol administration [370, 439, 375, 418]. The physiologic response of the other signal modalities is affected by propofol to a lesser extent compared to MABP. This is only part of the explanation, however, since the propofol-induced loss in signal interaction was also observed when using  $k_F$  as a similarity measure (Figure 9.7), indicating that the dynamics of MABP also decouple in addition to just its amplitude.

For 30 to 90 min after propofol administration, the degree of the EEG signal was considerably lower compared to the degree of the other modalities (Figure 9.7). In this time frame, the EEG was the only signal with a degree below the average degree, indicating a slow recovery of EEG dynamics with respect to the other modalities. Thus, MABP dynamics recover faster (generally recovered 30 min after propofol administration) compared to EEG dynamics (recovery takes up to 90 min after propofol administration). From a signal processing point of view, this might indicate the safety of propofol, since MABP could adapt to the needs of brain metabolism, once the EEG signal is recovered. It is important to note, however, that the neonates included in the present analysis were all sedated using propofol as part of an INSURE procedure. Surfactant also causes a significant decrease in EEG activity, which can last up to 24 hours after surfactant administration [412]. The extent of this effect is however not clear at this point, since no control group without surfactant was available to compare with.

From 90 min after propofol administration on, the vertex and average degree curves were characterized by stable reference levels (Figure 9.7), indicating that the signal interaction pattern is restored from the effect of propofol.

## 9.6 Conclusions

In this chapter, we have shown that graph theory can be used to assess changes in signal interaction and that the resulting graphs can be used to study the difference between distinct physiologic states.

For our propofol case study, we derived that the overall signal interaction pattern after propofol administration was highly influenced by both MABP and EEG. MABP dynamics were observed to recover first, followed by a much slower recovery of the EEG signal, meaning that MABP dynamics are recovered while EEG metabolism is still down. When EEG dynamics finally recover, MABP can adapt to supply new needs of the brain in order to sustain its function.

Overall, the extent of loss in coupling observed after propofol administration was found to be determined only by propofol dose, not by age. Propofol was found to affect signal dynamics with an overall recovery time of around 90 min, after which the interaction curves reached steady baseline with a high degree of signal interaction.

multivariate analysis

10

# Neurocardiovascular coupling; revealing insight in perioperative physiology

*based on:*

Hendrikx, D.\*, Costerus, S.\*, Caicedo, A., Zahn, K., Perez-Ortiz, A., Van Huffel, S., de Graaff, J., Wijnen, R., Wessel, L., Tibboel, D. and Naulaers, G. Neurocardiovascular coupling; revealing insight in perioperative neonatal physiology. Accepted for publication in *European Journal of Anaesthesiology* (2021).

(\*: joint first author)



This chapter presents the second study in which we used graph theory explicitly to study the interaction between cerebral function, brain hemodynamics, and systemic variables in neonates. In this study, we used a different clinical setting to validate our proposed methodology: neonates with CDH undergoing surgery in the first days of life. Five different types of perioperative management were compared; we assessed the effect of each of them on the neurocardiovascular graph.

## 10.1 Introduction

Despite state-of-the-art perioperative monitoring, the outcome after non-cardiac neonatal surgery can be complicated by significant acute and long-term sequelae [268]. Structured analysis revealed a high incidence of brain injury on MRI after non-cardiac neonatal surgery: 75% in preterm, 48% in full term [387]. Furthermore, interdisciplinary follow-up studies showed delayed neurodevelopment after neonatal surgery [388, 228, 90, 349]. To date, the effect of perioperative management on the neonatal brain is largely unknown [387]. Triggers for perioperative brain injury could be revealed by studying changes in the neonatal physiology perioperatively. To this end, a new direction in neuromonitoring is needed which includes neuromonitoring combined with computational models.

An overview of the coordinated interaction between the brain and the cardiovascular and cardiopulmonary systems can be created by extending standard monitoring with measurements of cerebral tissue oxygenation (rScO<sub>2</sub>) and cerebral activity (EEG) [163]. Such an overview provides insight in the regulation of CBF, including various regulation mechanisms such as NVC, CAR, cerebral oxygen balance, and HRP [336, 376, 310, 262]. Impairment in regulation might result in inadequate brain perfusion, which in turn might cause HIE [67], IVH [246], and PVL [431].

An advanced computational approach is needed to capture the status of the CBF regulation mechanisms, since numerous multimodal signals need to be included [163]. To achieve this, we used a previously designed model based on signal interaction graphs [164, 35]. We applied the signal interaction graph framework perioperatively to neonates diagnosed with CDH. Neonates with CDH show pulmonary hypoplasia and abnormal morphology of the pulmonary vasculature, resulting in severe respiratory insufficiency and an increased risk of developing persistent pulmonary hypertension (PPHN). A larger diaphragmatic defect leads to more severe pulmonary hypoplasia, and neonates with a (partial)

intrathoracic liver are more prone to develop PPHN. VA-ECMO treatment is imperative when therapy-resistant PPHN occurs [378].

In this study, the neonates were stratified in various groups based on different types of perioperative management. The aim of this study was to determine whether the signal interaction graph, referred to as neurocardiovascular graph, provided clinically relevant information about the neonatal pathophysiology and the CBF regulation mechanisms perioperatively.

## 10.2 Dataset

This study focused on neonates with CDH, a major non-cardiac anomaly that requires surgical repair within the first days of life. Details on the structure of this dataset and the recording equipment were presented in Section 4.2.

The neonates enrolled in this study were divided in five groups (Tables 10.1 and 10.2), corresponding to five different perioperative settings: thoracoscopic surgery in the OR, conversion from thoracoscopy to laparotomy in the OR, laparotomy in the OR, laparotomy in the NICU and laparotomy in the PICU during VA-ECMO. The subjects were stratified into these groups based on clinical condition (Figure 10.1). Thoracoscopic surgery in the OR was preferred if the neonate was cardiopulmonary stable and did not have a herniated liver. Laparotomy in the OR was done if the patient was cardiopulmonary stable, but had a herniated liver. Surgery was performed in the ICU if the patient was not cardiopulmonary stable. Reasons for conversion from thoracoscopy to laparotomy were the need for a patch in case of a large diaphragmatic hernia, or a ventilation problem (hypoxia or hypercapnia). Preoperatively, the data of the thoracoscopic repair and conversion groups were merged, as they included the most clinically stable patients with similar demographics (Table 10.1).

## 10.3 Methods

**Signal processing pipeline** The signal processing pipeline that is used in this study was introduced in Chapter 3 and is depicted in Figure 3.1. After acquisition, the signals were first preprocessed to remove artifacts. This procedure consisted of filtering the EEG (0.5–32 Hz), removing amplitudes outside of the physiologic range, defined as negative values and saturation values above 100, and detecting motion artifacts, defined as epochs in which the moving standard deviation exceeded 3. Then, the temporal scale of the EEG

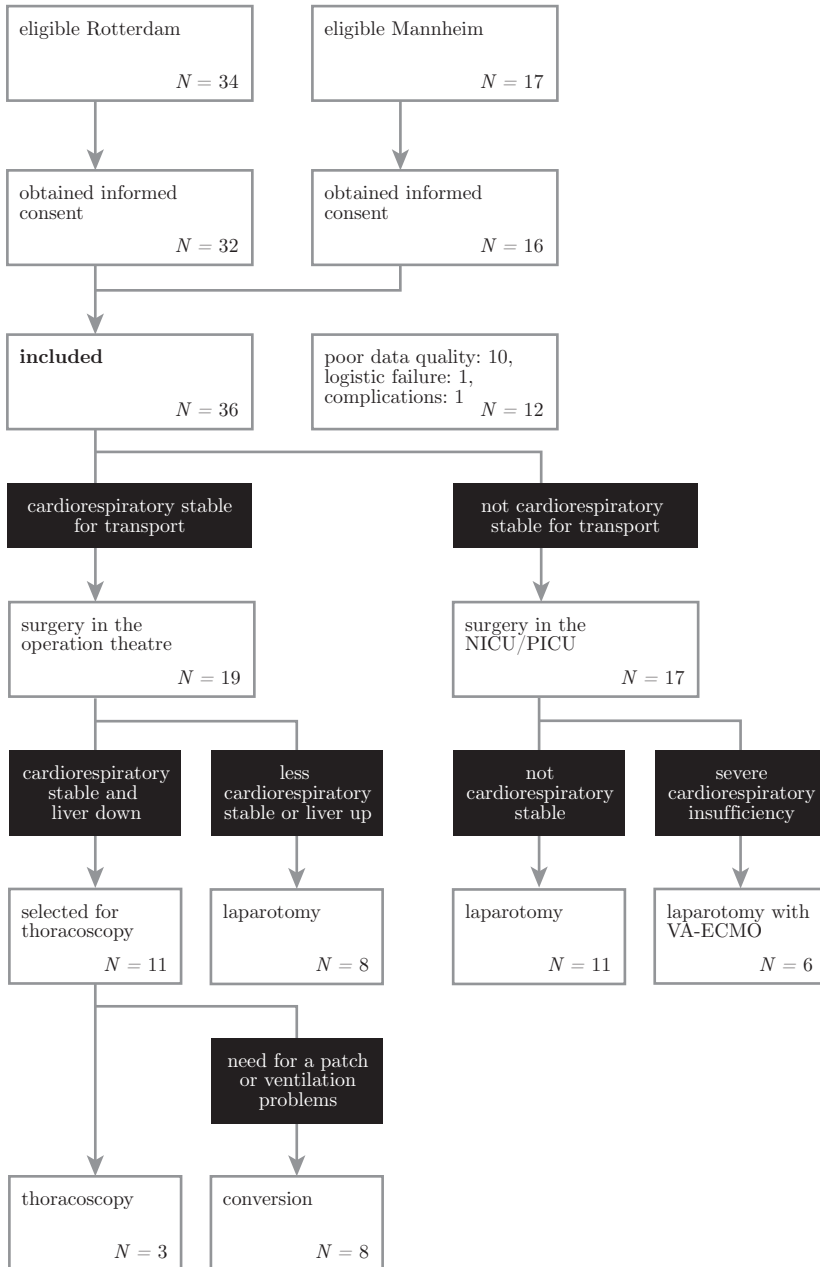


Figure 10.1: The neonates were divided in five groups, corresponding to five different perioperative settings, based on clinical condition.

Table 10.1: Overview of the demographics for each of the five groups under study.

	thoracoscopy	operation theater conversion	laparotomy	laparotomy	NICU	PICU
number	3	8	8		11	6
GA (weeks)	40+4 (30+6-40.6)	38+2 (35-40+1)	38+1 (36+3-41)		37+6 (33+2-38+2)	38+1 (36+6-41+6)
PNA (days)	3 (3-4)	4 (2-5)	3.5 (2-4)		6 (4-11)	7.5 (6-9)
BW (kg)	3.2 (2.9 - 3.2)	3.0 (2.0 - 3.5)	3.1 (2.3 - 3.5)		2.8 (1.7 - 3.1)	3.1 (2.5 - 3.5)
antenatal diagnosed	1 (33%)	6 (75%)	7 (88%)		7 (64%)	1 (17%)
Apgar 5 min	9 (9-10)	8 (8-8)	8 (5-8)		8 (7-8)	6 (4-8)
<i>o/e</i> LHR	41	51 (34 - 75)	44 (36 - 74)		40 (32-44)	39 (27 - 57)
mechanical ventilation	2 (67%)	2 (25%)	8 (100%)		11 (100%)	6 (100%)
left-sized defect	3 (100%)	8 (100%)	5 (63%)		9 (82%)	1 (17%)
liver-upt	0 (0%)	0 (0%)	5 (63%)		8 (73%)	5 (83%)
defect size (A, B, C, D)	2A, 1B	2A, 3B, 2C, 1D	2A, 3B, 3C	1A, 4B, 5C, 1D		2B, 1C, 3D
surgery duration (min)	118 (42-128)	120.1 (85-170)	72 (61-124)	155 (105-202)		101 (81-120)
patch	0 (0%)	5 (63%)	8 (100%)	10 (91%)		6 (100%)
P <sub>a</sub> CO <sub>2</sub> (kPa)	6.9 (6.6-7.2)	6.1 (5.3-7.7)	5.9 (5.3-7.4)	5.0 (4.7-6.2)		5.5, 7.8
died	0 (0%)	0 (0%)	1 (13%)	0 (0%)		1 (17%)

Table 10.2: Overview of the drugs administered in each of the five groups under study.

	thoracoscopy		operation theater		NICU		PICU	
			conversion	laparotomy	laparotomy	laparotomy	ECMO	
rocuronium								
during ( $\text{mg kg}^{-1}$ )	0.74 (0.65-0.74)	1.0 (0.6-1.0)	0.62 (0.57-0.82)	1.0 (1.0-1.0)	1.0 (1.0-1.0)	1.0 (1.0-1.0)	1.0 (1.0-1.0)	
vecuronium								
induction ( $\text{mg kg}^{-1}$ )	-	-	-	-	0.1 (0.07-0.1)	-	-	
during ( $\text{mg kg}^{-1} \text{h}^{-1}$ )	-	-	-	-	0.2 (0.18-0.21)	-	-	
fentanyl								
induction ( $\mu\text{g kg}^{-1}$ )	1.3 (0.9-1.3)	2.5 (1.7-2.9)	2.1 (1.9-3.0)	5.0 (4.0-7.0)	4.0 (3.1-4.0)			
during ( $\mu\text{g kg}^{-1}$ )	5.6 (4.5-5.7)	6.3 (5.0-16.5)	6.3 (4.0-8.7)	11.0 (7.0-16.0)	11.3 (3.4-25)			
during ( $\mu\text{g kg}^{-1} \text{h}^{-1}$ )	-	-	-	4.5 (3.0-5.0)	-			
morphine								
during ( $\mu\text{g kg}^{-1} \text{h}^{-1}$ )	-	-	-	-	13.7 (8.4 - 18.6)			
sevoflurane								
during (MAC expired %)	1.0 (1.0-1.9)	1.7 (1.0-2.5)	1.5 (1.1 - 2.4)	-	-			
midazolam								
before ( $\mu\text{g kg}^{-1} \text{h}^{-1}$ )	84 (50-200)	0 (0-133)	42 (0-133)	40 (30-50)	140 (60-257)			
induction ( $\mu\text{g kg}^{-1}$ )	0 (0%)	0 (0%)	1 (13%)	10 (91%)	4 (67%)			
during ( $\mu\text{g kg}^{-1} \text{h}^{-1}$ )	67 (50-179)	0 (0-125)	42 (0-133)	100 (75-100)	134 (75-257)			
after ( $\mu\text{g kg}^{-1} \text{h}^{-1}$ )	67 (25-125)	90 (0-133)	34 (0-133)	50 (20-50)	131 (50-257)			
VIS								
before	4.1 (0-26)	0 (0-16)	8 (0-32)	17 (8-23)	20 (5-61.5)			
during	8.5 (5-18.5)	12.3 (5-28)	7.5 (0-47)	17 (12-32)	7.3 (5-25)			
after	1.7 (0-9)	1.8 (0-39)	1.5 (0-30)	14 (7-27)	9.5 (5-35)			

was matched with the hemodynamic signals using a running estimate of the power in the  $\delta$  frequency band (0.5–4 Hz) [41].

Signal interaction graphs were computed in a sliding window of 15 min, which was found to be the minimal length required to estimate signal interaction in a robust way. In each window, the signal interaction was assessed between every pair of signals, which corresponds to the computation of a signal interaction graph. TE, a nonlinear, effective coupling measure was used, implemented in MATLAB using binning (Freedman-Diaconis rule on EEG) and nonuniform embedding using the ITS toolbox, developed by Luca Faes [118]. Finally, the TE values were normalized as 0 (no coupling) to 1 (perfect coupling) following a procedure outlined in [144].

To balance data and remove transitional effects, such as artifacts of transport and care and the effect of intraoperatively administered medication, the neurocardiovascular graphs were computed in five time windows: the preoperative window (6 to 3 hours before surgery), the entire surgical period, and three postoperative windows: 3 to 6 hours, 9 to 12 hours, and 15 to 18 hours after surgery, respectively. In each window, the graphs were compressed using the temporal mean.

**Statistical analysis** Data are presented as median (IQR). LME models were used to assess differences in the neurocardiovascular graph connectivity, per group over time. Post hoc analysis was done using estimated marginal means with Tukey's correction for multiple comparisons. All statistical computations were carried out in R [398]. Significance was defined as  $\alpha = 0.05$ .

## 10.4 Results

**Patient characteristics** Forty-eight neonates were enrolled in the study, of which 11 neonates were excluded following the absence of multiple signals due to data transfer and storage problems. One neonate was excluded due to cardiopulmonary resuscitation intraoperatively, leaving 36 patients included (Figure 10.1).

**Graphs** The connectivity of the neurocardiovascular graph was not affected by GA, BW, sex, the position of the liver, and the size of the diaphragmatic hernia, but it was influenced by the clinical group and clinical time window (both  $p < .001$ ).

**Thoracoscopic repair group** Neonates selected for thoracoscopic repair had the largest connectivity of 0.33 (0.26–0.37) preoperatively (Figures 10.2 and 10.3). During surgery, the connectivity of the neurocardiovascular graph dropped, reaching values of as low as 0.12 (0.08–0.15) ( $p < .001$ ), which increased again to 0.24 (0.23–0.33) ( $p < .001$ ), 0.26 (0.25–0.36) and 0.32 (0.32–0.32) postoperatively. Preoperatively and postoperatively, there was intact and strong interaction between the vital parameters and a functioning BR, CAR and NVC (Table 10.3). During surgery, CAR remained intact, while both BR and NVC disappeared.

**Conversion group** During surgery, graph connectivity slightly decreased to 0.31 (0.24–0.34) (Figures 10.2 and 10.3). After surgery, connectivity further decreased to 0.27 (0.23–0.31) ( $p < .001$ ), after which it increased again to 0.33 (0.26–0.34) and 0.32 (0.30–0.34) ( $p = .014$ ). The interaction between the vital parameters dropped intraoperatively, after which it steadily increased postoperatively (Table 10.3). CAR and NVC remained intact over the perioperative period. BR dropped intraoperatively, but restored again after surgery.

**Open repair OR group** In the open repair OR group, the connectivity was 0.28 (0.20–0.36) preoperatively, then slightly dropped to 0.25 (0.12–0.28) ( $p < .001$ ) intraoperatively, and increased again to 0.25 (0.15–0.31) ( $p = .037$ ), 0.27 (0.12–0.30), and 0.30 (0.18–0.32) postoperatively (Figures 10.2 and 10.3). The interaction among the vital parameters was strong preoperatively, dropped intraoperatively, and reached baseline values again postoperatively (Table 10.3). CAR remained intact over the perioperative period. The same holds true for BR and NVC, although they were associated with slightly lowered values during surgery.

**Open repair NICU group** The graph connectivity remained stable for neonates on open surgery in the NICU, reaching values of 0.30 (0.23–0.34), 0.34 (0.26–0.38), 0.26 (0.22–0.33), 0.32 (0.24–0.37), and 0.28 (0.27–0.36) for the five consecutive time windows, respectively (Figures 10.2 and 10.3). Interaction among the vital parameters, including BR, was absent over the entire perioperative period (Table 10.3). CAR was intact over the perioperative period. NVC was characterized by the largest values compared with all other groups, over all time windows.

**ECMO group** Neonates on VA-ECMO had the lowest connectivity before surgery of 0.27 (0.23–0.30). The connectivity increased to 0.34 (0.28–0.41) during surgery. Postoperatively, the connectivity was 0.30 (0.30–0.32), 0.21

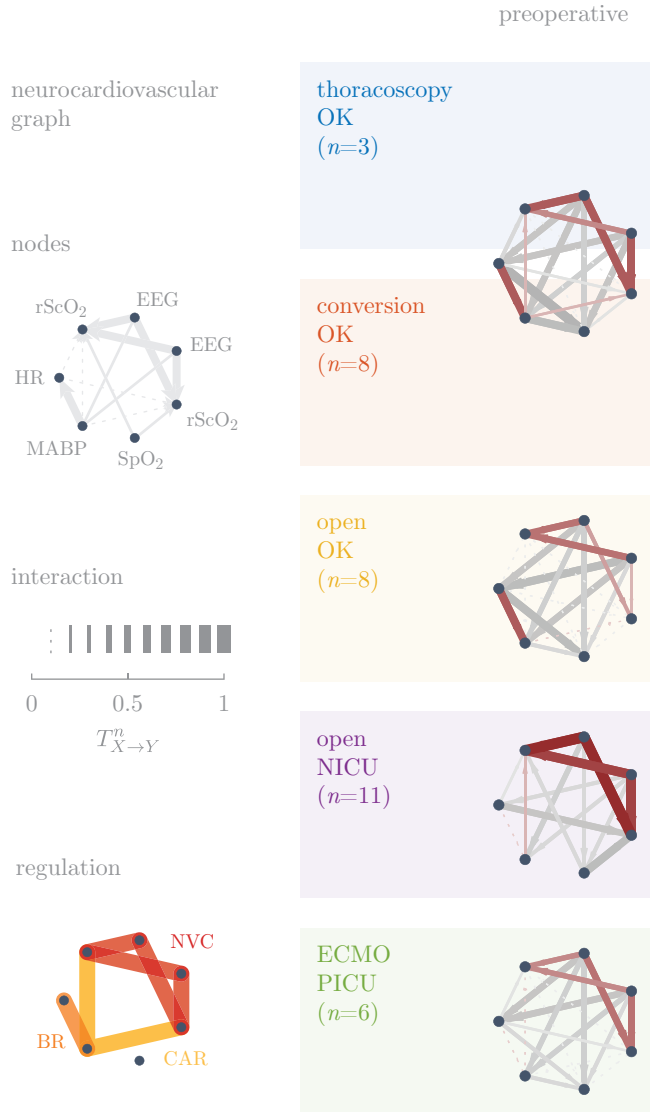


Figure 10.2: The connectivity of the neurocardiovascular graph was not affected by GA, BW, sex, the position of the liver, and the size of the hernia, but it was influenced by the clinical group (rows) and clinical time window (columns). Graphs are presented as a median over all patients in a group. The regulation mechanisms are highlighted in (shades of) red, while all other graph connections are presented in gray.

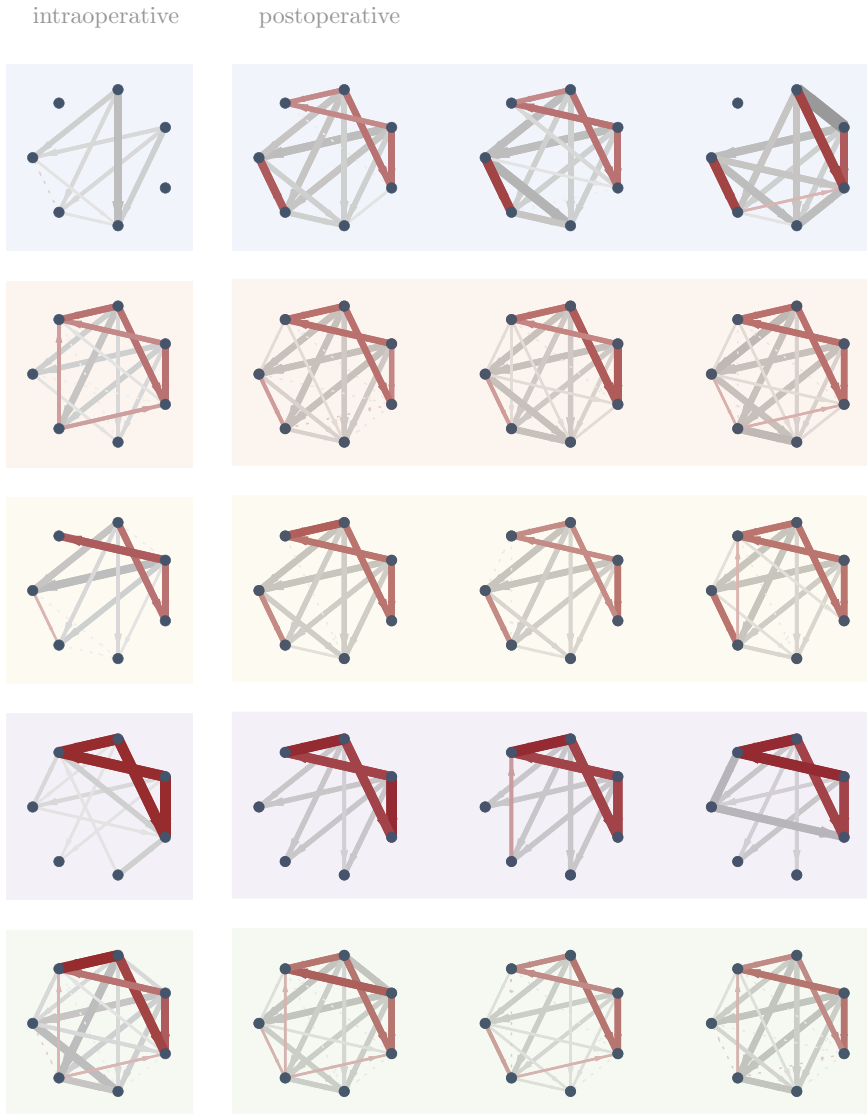


Figure 10.2 (cont.): The connectivity of the neurocardiovascular graph was not affected by GA, BW, sex, the position of the liver, and the size of the hernia, but it was influenced by the clinical group (rows) and clinical time window (columns). Graphs are presented as a median over all patients in a group. The regulation mechanisms are highlighted in (shades of) red, while all other graph connections are presented in gray.

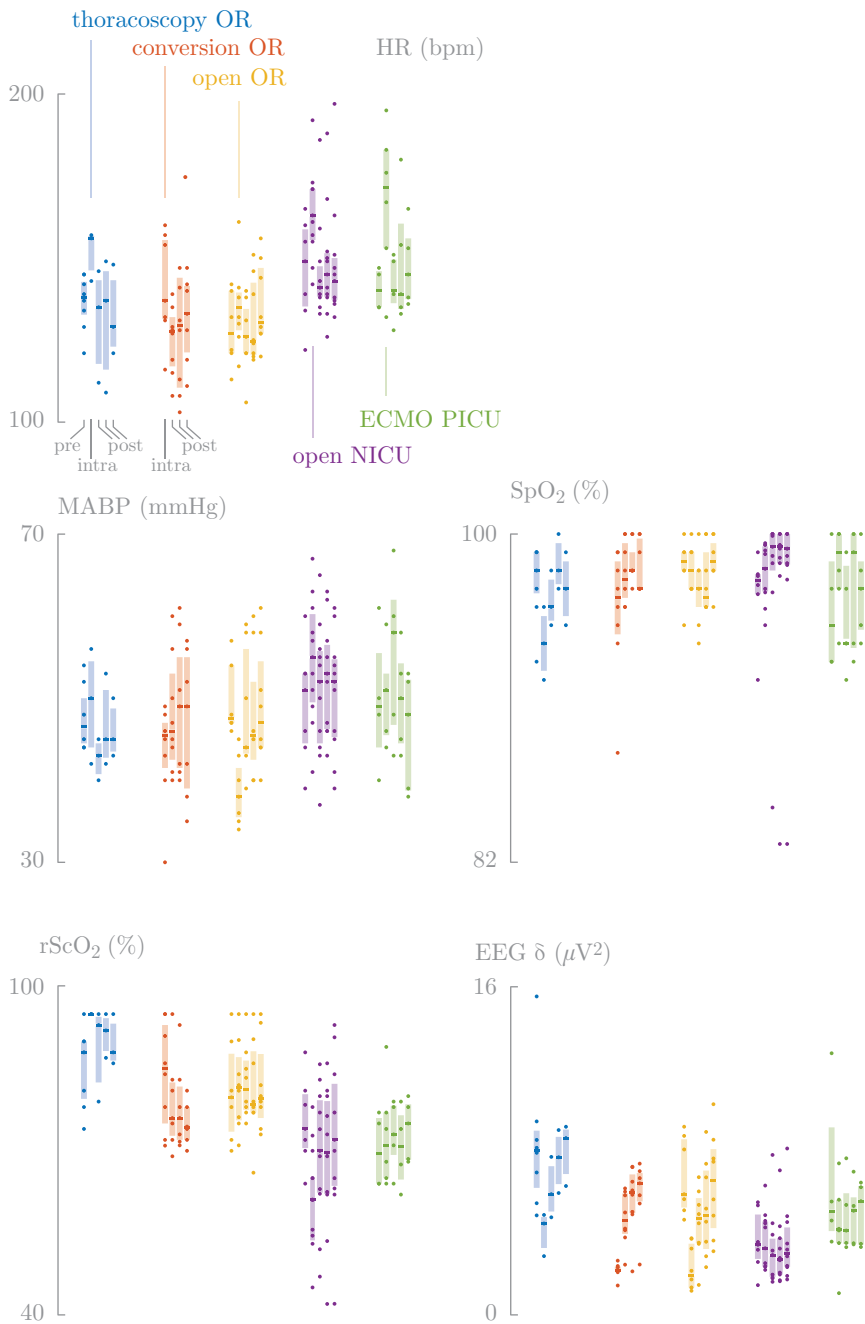


Figure 10.3: Longitudinal overview of HR, MABP, SpO<sub>2</sub>, rScO<sub>2</sub>, EEG, graph connectivity, BR, CAR, and NVC. Each dot represents a patient mean in the corresponding time window.

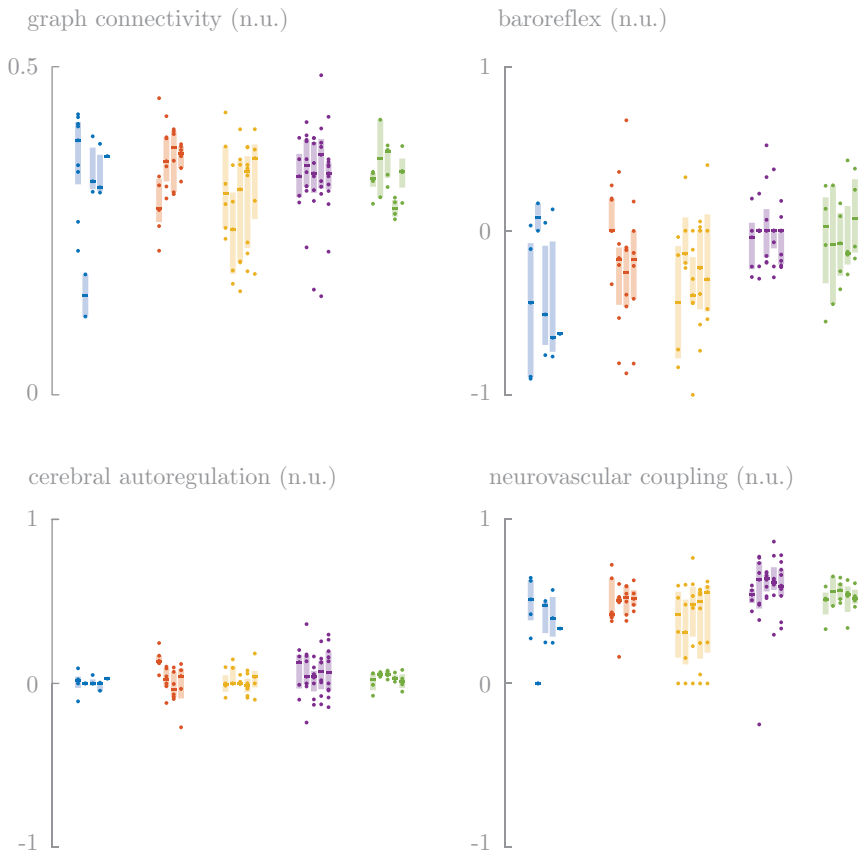


Figure 10.3 (cont.): Longitudinal overview of HR, MABP, SpO<sub>2</sub>, rScO<sub>2</sub>, EEG, graph connectivity, BR, CAR, and NVC. Each dot represents a patient mean in the corresponding time window.

Table 10.3: Main findings for each of the five perioperative settings, based on the structure of the neurocardiovascular graph.

	surgical approach	anesthetic approach	BR	CAR	NVC	main results
OR	thoracoscopy	sevoflurane	−	+	−	largest reduction in connectivity
	conversion	sevoflurane	−	−	+	larger connectivity compared with the open repair OR
	laparotomy	sevoflurane	+	+	+	all regulation mechanisms intact
ICU	laparotomy	midazolam	−	+	+	largest observed values of NVC
	laparotomy VA-ECMO	midazolam	−	+	+	high interaction vital parameters

(0.20–0.23) ( $p < .001$ ) and 0.28 (0.26–0.31) ( $p < .001$ ). Strong interaction among the vital parameters, intact CAR, and NVC was observed throughout the perioperative period (Table 10.3). CAR values only increased slightly intraoperatively, and in the first hours after surgery. BR was absent, especially in the preoperative period, as well as in the postoperative windows of 9 to 12 hours and 15 to 18 hours after surgery.

**Events** One patient needed cardiopulmonary resuscitation (CPR) intraoperatively which was followed by emergency VA-ECMO treatment (Figure 10.4). This patient was not part of the five clinical groups described above, but was treated as a special case instead, since surgery was done on ECMO in the OR (this combination doesn't fit any of the perioperative settings described above). Three to two and a half hours before CPR, the overall graph connectivity was large. Interactions among vital parameters, BR, CAR and NVC were observed to be intact and functioning. Over time, the graph connectivity gradually dropped together with the consistent decrease in  $\text{SpO}_2$  and  $\text{rScO}_2$ , and NVC and BR disappeared. Regarding graph structure, two observations could be made. First, 1.5 hours before CPR the coupling strength (the outdegree of the node) of HR decreased. Second, EEG coupling switched direction after CPR. After the start of VA-ECMO, the network built up connectivity again. First, BR returned followed by NVC and increased interaction among the vital parameters. After a half to one hour, EEG starts directing the network again, moving to the baseline graph structure displayed in Figure 2.18. One day postoperatively,

cUS showed an intraparenchymal hemorrhage in the left hemisphere and a hemorrhage in the right lateral ventricle.

Another patient, who underwent surgery during VA-ECMO developed a clot in the arterial canula shortly after the surgical procedure ended, which was consequently removed by the surgeon (Figure 10.5). This patient was part of the ECMO group described above. After 23 days, a supratentorial (occipital) and infratentorial subdural hemorrhage in the right hemisphere was observed on MRI. Looking at the structure of the neurocardiovascular graph, three observations can be made. First, in the 30 min leading up to the formation of the clot, a very high EEG to HR coupling was observed in combination with a pronounced drop in HR amplitude. Second, in the 60 min after clot formation, both CAR and HRP increased. Third, after removal of the clot, the connectivity of the neurocardiovascular graph steadily increased, characterized by a very strong directed EEG to MABP coupling.

**Correlations** During sevoflurane anesthesia, increased sevoflurane concentration correlated with increased BR ( $R^2 = 0.34$ ) and decreased HRP ( $R^2 = 0.32$ ); increased fentanyl dose correlated with increased HRP ( $R^2 = 0.60$ ), increased CAR ( $R^2 = 0.41$ ) and decreased EEG to MABP coupling ( $R^2 = 0.42$ ); and increased partial pressure of  $\text{CO}_2$  ( $\text{PaCO}_2$ ) correlated with increased HRP ( $R^2 = 0.33$ ).

During midazolam sedation, increased midazolam dosage correlated with increased CAR ( $R^2 = 0.47$ ) and increased interaction between MABP and the two EEG signals ( $R^2 = 0.39$  for the left channel, and  $R^2 = 0.34$  for the right channel); and increased fentanyl dosage correlated with increased MABP to EEG coupling ( $R^2 = 0.33$  for the left channel and  $R^2 = 0.37$  for the right channel).

Increased  $\text{PaCO}_2$  correlated with decreased BR during both sevoflurane and midazolam anesthesia.

## 10.5 Discussion

Both the anesthesiological and the surgical approach highly influenced the connectivity of the neurocardiovascular graph (Figure 10.2). Despite the small sample size and the novelty of the applied methodology, some observations can be made, which will have to be validated in future studies. The largest reduction in connectivity was observed during thoracoscopic surgery, which included an absence of BR and NVC (Table 10.3). This was striking, as neonates

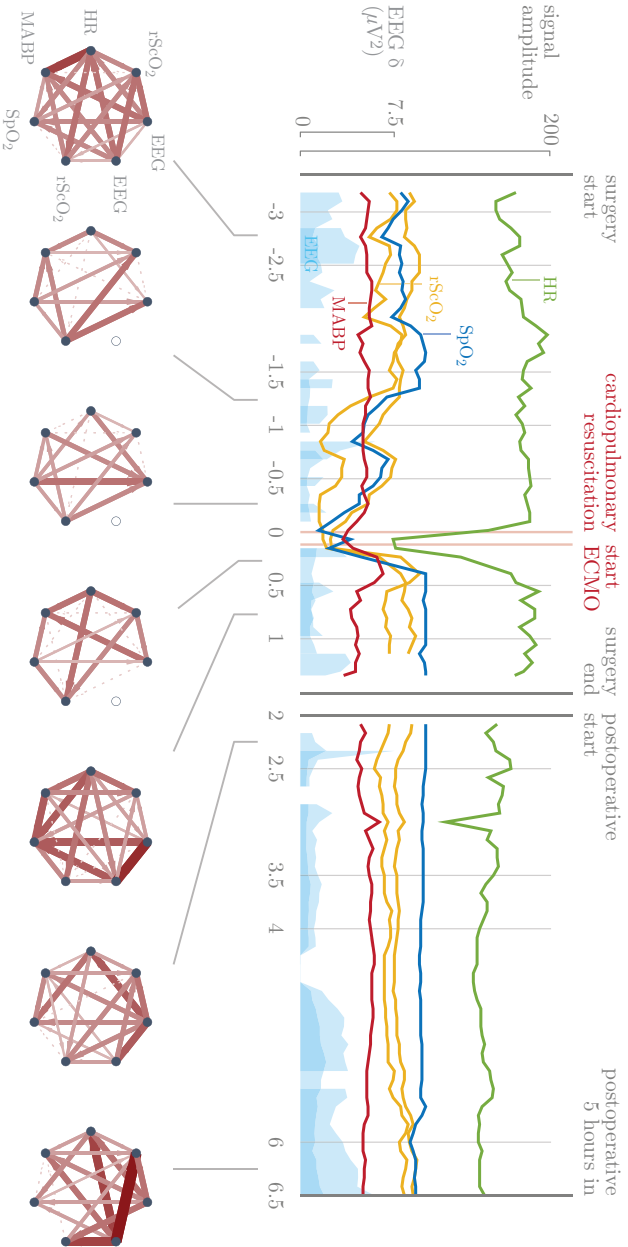


Figure 10.4: The neurocardiovascular graph before, during and after cardiopulmonary resuscitation, followed by emergency VA-ECMO treatment. The signals and graphs are presented as a median in 5 and 30 min windows, respectively. If a node is not displayed, the signal was not available in the corresponding time window, and thus, no interaction values could be computed.

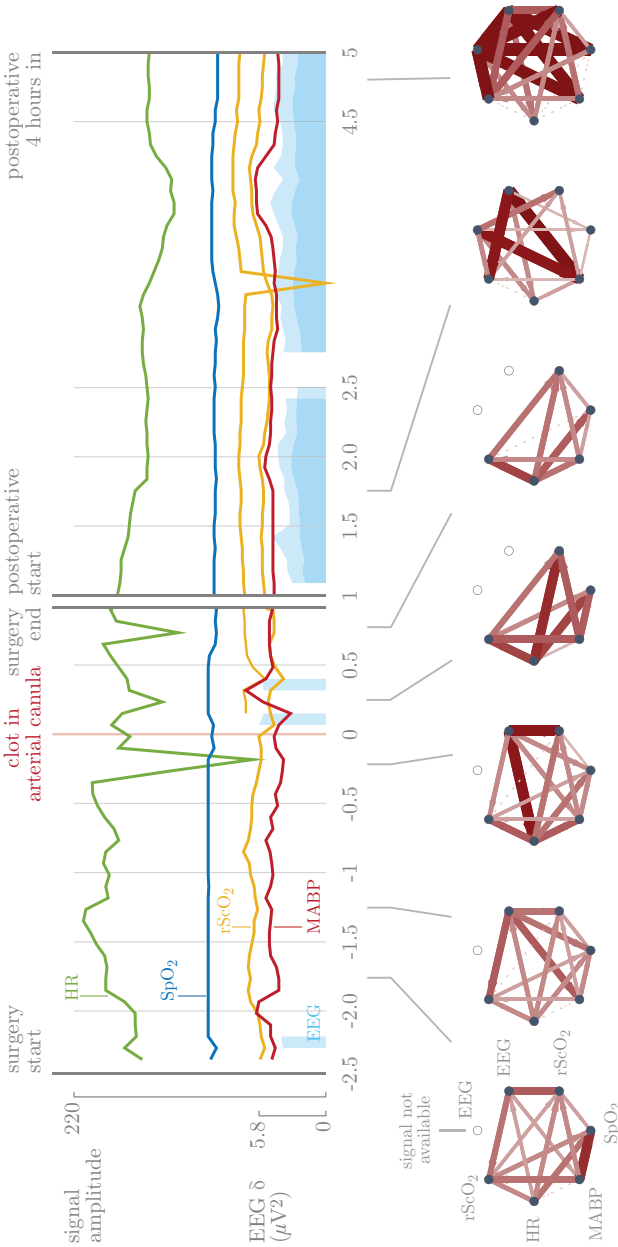


Figure 10.5: The neurocardiovascular graph during surgery on VA-ECMO. A clot was developed in the arterial canula, shortly after the procedure ended, which was consequently removed by the surgeon. The signals and graphs are presented as a median in 5 and 30 min windows, respectively. If a node is not displayed, the signal was not available in the corresponding time window, and thus, no interaction values could be computed.

selected for thoracoscopic repair were the most cardiopulmonary stable patients (Table 10.1). The conversion group was characterized by a larger connectivity compared with the open repair OR group, most likely because the neonates in the conversion group were clinically more stable (Table 10.1). Yet, the open repair OR group was the only group in which all CBF regulation mechanisms remained intact. Of all groups, the open repair NICU group had the largest NVC values, while the ECMO group had a significantly larger interaction among the vital parameters intraoperatively. CAR remained stable in all groups (Table 10.3). NVC remained functioning in all groups, except during thoracoscopic surgery.

**anesthesia** The majority of the drugs used at NICUs are unlicensed or off-label [77, 188]. Intravenous midazolam for sedation has been used for decades in the NICUs [294]. Nonetheless, a recent Cochrane review raised concerns about the safety of midazolam in neonates [285]. An included study reported statistically significant higher rates of adverse neurological events (death, grade III or IV IVH, PVL) in neonates treated with midazolam compared to morphine [14]. Two studies observed a (transient) decrease in middle cerebral artery blood flow velocity and transient cerebral hypoperfusion after a bolus of midazolam in preterm neonates [156, 414]. Our data suggest a more impaired CAR with increasing midazolam dose.

In general, literature reports a negative effect of general anesthesia on the neonatal physiology [251]. In the present study, we observed a stronger BR and less HRP with increasing sevoflurane dose during sevoflurane anesthesia, which might indicate that a higher sevoflurane dosage does not adversely affect regulation. Sevoflurane mediates a decrease in myocardial contractility and MABP [300]. In the brain, sevoflurane mediates vasodilation, suppresses somatosensory-evoked potentials and reduces cerebral metabolism [389].

Increasing fentanyl dosage during induction, however, was associated with a more pronounced HRP, a more impaired CAR and a stronger, directed coupling between EEG and MABP in the intraoperative period, which are all aspects associated with adverse outcome in neonates [358, 24, 262].

**Surgery** Thoracoscopic surgery is popular due to its potential benefits, including fewer postoperative ventilator days, lesser need for analgesics and a shorter hospital stay [83, 145, 424, 406]. A drawback is that an artificial CO<sub>2</sub>-pneumothorax is needed to create surgical workspace, which can result in hypercapnia and acidosis [39]. Signal interaction was highly affected during thoracoscopic surgery, which might be due to increased CO<sub>2</sub> or the increased intrathoracic pressure which affects venous return. An increase in PaCO<sub>2</sub>

correlated with a less functioning BR, and a more pronounced HRP. The observed increase in HR might indicate a comprised venous return, although MABP did not decrease (Figure 10.3). Open surgery gives fewer oxygenation and ventilation problems for the anesthesiologist to deal with, but our data suggest that graph connectivity decreased anyway. Although ECMO is associated with (intracranial) hemorrhagic and thrombotic complications, our results might indicate that ECMO might help to preserve the signal interactions intraoperatively.

**Events** In the run-up to CPR, we observed a decreased coupling strength of HR indicated a decoupling of this signal from the physiological network (Figure 10.4). This phenomenon started around 1.5 hours before CPR, and thus, long before the HR dropped in amplitude. In addition, a pronounced change in EEG dynamics was observed. In baseline behavior, EEG changes direct the network: changes in EEG trigger changes in all other signals of the neurocardiovascular graph. After CPR, however, this directionality was observed to be reserved, which points to a strongly disrupted network. In the postoperative period, the directionality restored to baseline behavior.

We hypothesize that the postoperatively observed subdural hemorrhages in the patient who developed a clot in the arterial canula of the VA-ECMO might be triggered by that event (Figure 10.5). This hypothesis was reinforced by the observed changes in the neurocardiovascular graphs. After clot formation, the graph connectivity changed drastically. A disrupted network, even for a small period of time, might be associated with pathological events, since the physiological interactions are disturbed, creating a loss in homeostasis. In this context, note especially the increase in interaction values corresponding to HRP and CAR. Impairment in both regulation mechanisms is associated with poor outcome in neonates [254]. After the clot was removed, the structure of the network steadily shifted again to baseline behavior, although the connectivity of the neurocardiovascular graph was observed to be significantly larger compared to the preoperative graphs. In the postoperative setting, the very large and highly directed coupling between EEG and MABP catches the eye. Remarkably, such strong, directed coupling was found to be related to lower CRIB II scores, which is in turn related to outcome [358].

**Importance** Perioperative management, including ICU management, anesthesia and surgery, could cause undesirable changes in the neonatal physiology, which might trigger perioperative brain injury [388, 387, 228]. So far, most of the studies on this subject have focused on the analysis of one of the CBF regulation mechanisms, and lack information about other physiology parameters. Advanced

computational approaches need to be developed to quantify and understand the impact of perioperative management on the neonatal physiology [163]. In this study, we applied a computational framework (with visual and graphic feedback) that allowed to handle multiple concomitant signals, and thereby to study all major regulation mechanisms in one straightforward model.

As numerous signals are measured from the same physiological system, a strong, coordinated interaction should exist between them [35]. The neurocardiovascular graph captures continuous information about the ability of the autonomic nervous system to react on changes in MABP (BR), and about the ability of the brain to regulate CBF, independently of fluctuations in MABP (CAR) and dependently of the cerebral metabolism (NVC). Therefore, it provides insights in cerebral perfusion. As HR, MABP and SpO<sub>2</sub> are included, the coordinated interactions between the brain and the cardiopulmonary systems can also be analyzed.

Clinical decisions should be based on precise, qualified, and selected information. Information overload in perioperative medicine is a major concern [348]. New monitoring strategies which integrate different information sources in one straightforward, visual model could help to reduce information overload. The neurocardiovascular graphs provided new information on how the neonatal physiology and the CBF regulation mechanisms are affected by the actions of the clinicians, even in the most cardiorespiratory stable patients. Therefore, this approach could assist clinicians in making timely decisions about the optimal surgical and anesthesiological approach, thereby making clinical practice more patient-specific and potentially preventing brain injury [163].

**Limitations** The framework was applied in a very specific pathology during major, non-cardiac, high-risk surgery. This approach needs further validation in other pathologies as well as in cardiorespiratory healthy neonates with and without anesthesia. The severity of the critical illness also differed between the groups, in addition to the surgical and the anesthesiological approach. Exposure to medication was compared based on dosages instead of its plasma concentrations.

## 10.6 Conclusions

In this chapter, we showed that the neurocardiovascular graph provides a new way to look at the effect of the perioperative management on the pathophysiology of surgical neonates. The neonate's clinical condition and the surgical and anesthesiological approach affected the neonatal physiology and CBF regulation

mechanisms at different levels. This new direction could assist clinicians in making patient-specific decisions about the optimal perioperative management, aiming to prevent brain injury and possibly impaired neurodevelopmental outcome. At this stage, however, given the patient numbers in each group and the novelty of our approach, it is still too early to couple our results directly to changes in clinical management.

P A

R T



CON-  
CLUSION

conclusion



# **Conclusion and future research directions**



## 11.1 Conclusions

In the introduction, two main goals of this thesis have been defined. Our first goal was to develop a new marker for neurovascular coupling, based on nonlinear interactions. The second goal of this thesis was to serve as a proof-of-concept for our signal interaction graph model capturing neurocardiovascular interactions. In the next sections, we will summarize the main findings of the presented research in relation to these objectives.

### 11.1.1 Marker for neurovascular coupling

The first objective of this thesis was the development of a new marker for neurovascular coupling. We successfully designed and validated a marker based on nonparametric TE. To the best of our knowledge, this marker is the first marker for NVC that takes into account nonlinear interactions.

During the last decades, there is an increased interest in monitoring regulation of CBF in the neonate. Although CAR is the most popular regulation mechanism, NVC is starting to become studied more and more as well [163]. In comparison with CAR, NVC markers have the additional difficulty that the temporal scales of the signals under study (EEG and rScO<sub>2</sub>) need to be matched. Therefore, they are more challenging from a signal processing point of view; they are characterized by more degrees of freedom, which have to be validated properly. Existing studies are based on (wavelet) coherence [67, 246] and linear TE [62].

In our analysis, we took a more general, nonparametric, nonlinear approach using advances in the field of information theory, where TE showed promising value in neurophysiology and in capturing the brain–heart interaction. In this work, we adapted this measure to capture NVC. Although validated in a small cohort of neonates, promising results were obtained, unraveling differences in the magnitude of the coupling in neonates with and without brain abnormalities. However, there are some limitations in the proposed approach that should be taken into account: we focused on a very specific clinical setting (propofol administration) and only a small number of neonates were studied.

### 11.1.2 Model for (neuro)cardiovascular interactions

The second objective of this thesis was to validate our signal interaction graph model, designed to capture (neuro)cardiovascular interactions, in various clinical settings. Although the size of the datasets used in this thesis was limited, these

studies can be used as a proof-of-concept, motivating further testing and large-scale validation.

In a first study (Chapter 8), we looked at cardiovascular interactions during immediate transition after birth. Due to the short length of the data, we adapted our framework and used the linear and nonlinear correlation coefficient to measure coupling. A significant coupling between HR and  $r\text{ScO}_2$  was found in all neonates, indicating that HR might have a key influence on cerebral hemodynamics in (pre)term infants. In addition, our data-driven clustering approach unraveled an age-dependency in the  $\text{SpO}_2$ - $r\text{ScO}_2$  coupling: as GA increases, the coupling between  $\text{SpO}_2$  and  $r\text{ScO}_2$  seems to decrease in magnitude, while becoming more and more nonlinear.

In a second study (Chapter 9), we quantified neurocardiovascular interaction explicitly using graph theory for the first time. This was the first validation study for the proposed model. For our propofol case study, we derived that the overall signal interaction pattern after propofol administration was highly influenced by both MABP and EEG. MABP dynamics were observed to recover first, followed by a much slower recovery of the EEG signal, meaning that MABP dynamics are recovered while EEG metabolism is still down. When EEG dynamics finally recover, MABP can adapt to supply new needs of the brain in order to sustain its function. Overall, the extent of loss in coupling observed after propofol administration was found to be determined only by propofol dose, not by age. Propofol was found to affect signal dynamics with an overall recovery time of around 90 min, after which the interaction curves reached steady baseline with a high degree of signal interaction.

In a third and final study (Chapter 10), the graph model was applied in different perioperative settings. In this study, the neonate's clinical condition and the surgical and anesthesiological approach affected the neonatal physiology and CBF regulation mechanisms at different levels. This study further indicated that the new direction in neuromonitoring, based on signal interaction graphs, could assist clinicians in making patient-specific decisions about the optimal perioperative management, ultimately aiming to prevent brain injury and possibly impaired neurodevelopmental outcome.

### 11.1.3 Other findings

In the perioperative period of CDH and EA neonates, we also conducted a univariate analysis in addition to the bivariate and multivariate analysis. The main goal of this analysis was to obtain more background information to understand the graph models better from a clinical perspective. Sevoflurane-based anesthesia resulted in increased cerebral oxygenation and decreased

brain activity, suggesting adequate anesthesia (Chapter 6). In addition, HRV decreased during sevoflurane-based anesthesia, and the contribution of the sympathetic and parasympathetic branch decreased and increased, respectively, reflecting the desired effect of anesthesia, which is to reduce stress (Chapter 5). Midazolam-based anesthesia, on the other hand, led to alarmingly low  $rScO_2$  values, below the threshold of hypoxia, and increased values of EEG power during the first 30 min of surgery, which might indicate the conscious experience of pain (Chapter 6). Following these limitations of midazolam, we argued that current perioperative medication strategies with midazolam and analgesia might not be sufficient for perioperative anesthesia.

## 11.2 Future directions

Before the neurocardiovascular graph can be introduced in clinical practice, numerous challenges need to be tackled. First of all, the measured signal modalities are highly sensitive to artifacts, especially in long recordings. Numerous methods exist to remove artifacts from biosignals, but they often lack the precision to be fully reliable in clinical practice. Second, from a signal processing point of view, many methodologies exist to quantify coupling, which often present different coupling values. Guidelines on which tool should be used in which setting are not (yet) available. Third, from a clinical perspective, research on the various CBF regulation mechanisms is still ongoing with many questions that still need to be answered. Examples include the effect of medication on regulation of CBF and the evolution of the CBF regulation mechanisms as a function of maturation. In addition, it is not yet known whether the CBF regulation mechanisms can recover if they develop later than planned, which is often the case in preterm neonates, or whether there is a very specific time frame in which the development needs to happen. Although these are all fundamental research questions, they all have a direct impact on the patient and the care given. Finally, many challenges arise when translating the model from a research setting into a tool that is used in clinical practice, where the physician can use it for his/her interpretation in diagnostics.

### 11.2.1 Artifact removal

In general, biomedical data recordings are susceptible to artifacts, which must be removed before the data can be used for processing. Current approaches rely on simple detection measurements, such as the moving standard deviation [351], and often require additional signal modalities, such as accelerometers [260], which is not practical in the NICU setting. In addition, these methods

lack precision in order to be fully reliable. Therefore, in most studies, only clean data segments are selected, which increases bias. In order to solve this, better, more robust methods to detect and correct artifacts have to be developed.

## 11.2.2 Multiscale analysis

Research on the coupling between EEG and rScO<sub>2</sub> to measure NVC is a growing field. From a clinical perspective, numerous questions still have to be answered regarding the exact nature of the interaction and the different physiological mechanisms behind regulation. In order to answer these questions, it is important to get more insight into coupling between EEG and rScO<sub>2</sub>. For this, new methodologies need to be developed based on a multiscale analysis. By decomposing the signals into different scales and consequently analyzing the resulting interactions between different scales, we can localize the coupling in time and frequency. In addition, this framework will allow us to detect nonlinearities in a straightforward way, which are present as even and odd harmonics in the frequency spectrum [323].

The methods that are currently available in literature are all based on coarse graining to compute the different scales. We propose to replace this procedure by the discrete wavelet transform (DWT), which provides perfect reconstruction and less redundancy compared to coarse graining. This will allow faster computation times, which will be important in future online applications. Formally, the DWT can be used to compute the projection of a signal  $x(t)$  (with length  $2^n$ ) onto a (predefined) wavelet  $\psi(t)$ . In general, wavelet coefficients  $\gamma_{jk}$  are defined as:

$$\gamma_{jk} = \int_{-\infty}^{\infty} x(t) \frac{1}{\sqrt{2^j}} \psi \left( \frac{t - k2^j}{2^j} \right) dt. \quad (11.1)$$

For a given scale  $j$ ,  $\gamma_{jk}$  is a function of  $k$  only and can be interpreted as a convolution of  $x(t)$  with a dilated, reflected, and normalized version of the mother wavelet  $\psi(t)$ , sampled at points  $1, 2^j, 2^{2j}, \dots, 2^n$ , which corresponds to a filter. In practice, the DWT is implemented using a filter bank with lowpass and highpass filters  $h$  and  $g$  that are related to  $\psi(t)$ .

A first analysis showed excellent multiscale decomposition performance using the Daubechies family of wavelets. Daubechies wavelets are a family of orthogonal wavelets, characterized by a maximal number of vanishing moments for a given (finite) support. A vanishing moment limits the wavelets ability to represent polynomial behaviour or information in a signal. More vanishing moments means that complex functions can be represented with a sparser set of wavelet coefficients. Like many other wavelets, Daubechies wavelets are defined by

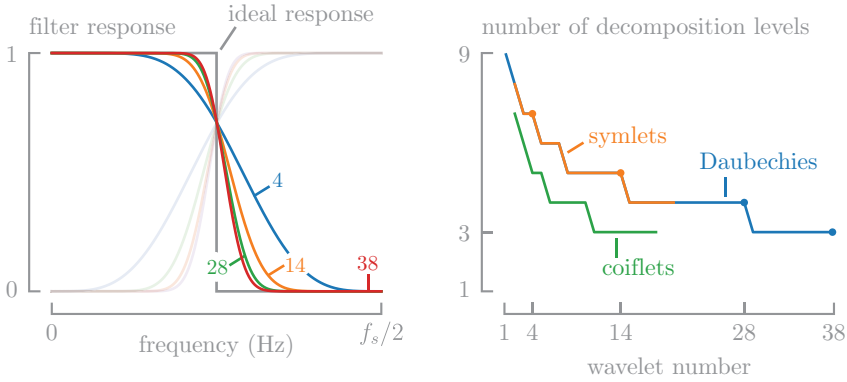


Figure 11.1: Composition using the DWT. Left: the filter response becomes steeper with increasing wavelet index, approximating the ideal step response (filter response corresponding to Daubies wavelets 4, 14, 28, and 38). Right: the number of decomposition levels decreases with increasing wavelet index.

an index, which refers to the number of coefficients. A larger index leads to a steeper frequency response (Figure 11.1). In an ideal world, we want the frequency response to approximate a step function, to avoid spectral leakage between different frequency bands in a multiscale decomposition. Therefore, we want the wavelet index to be as large as possible. In practice, however, the number of decomposition levels decreases as the index increases, which results in a less detailed multiscale decomposition, since the filter length increases. Therefore, the index has to be defined as a trade-off. The Daubechies wavelet with index 28 provides a good trade-off between the aforementioned factors (Figure 11.1).

Figure 11.2 presents an example of the multiscale decomposition for one patient in the propofol dataset using three different coupling measures: the linear correlation, the nonlinear correlation and normalized TE. The coupling was assessed between aEEG and rScO<sub>2</sub>. From the grids, it is clear that linear correlation can only capture linear interactions, interactions between bands of the same frequencies (on-diagonal elements). Naturally, nonlinear interaction measures also allow to detect nonlinear components of the interaction, if present. These nonlinear components present as off-diagonal elements. From Figure 11.2, it is clear that the aEEG-rScO<sub>2</sub> coupling is characterized by a degree of nonlinearity, as indicated by the substantial amount of off-diagonal values. Since these off-diagonal elements are mainly located in the lower right triangle

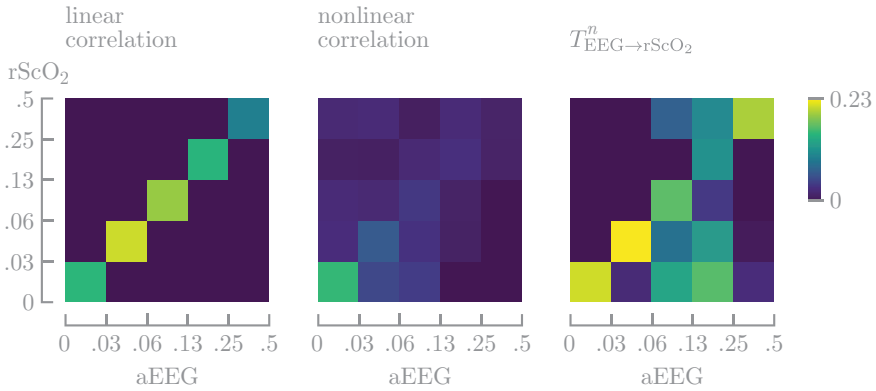


Figure 11.2: Example of a multiscale decomposition, for one patient (propofol dataset). The median grid is shown for the entire recording of six hours. The coupling is characterized by a degree of nonlinearity, as indicated by the substantial amount of off-diagonal values. Since these off-diagonal elements are mainly located in the lower right triangle of the grid, we can conclude that aEEG mainly modulates slower rScO<sub>2</sub> rhythms.

of the grid, we can conclude that faster aEEG components mainly modulate slower rScO<sub>2</sub> rhythms.

The proposed framework has three main strengths. First, both the EEG and the rScO<sub>2</sub> signal can be directly fed into the algorithm, without the need for preprocessing of the EEG. This removes the bias that can result from the different preprocessing algorithms. Second, the developed multiscale framework is not specific to NVC and can be generalized and transferred to other fields, such as CAR research. Third, the framework can be used to transform the neurocardiovascular graphs from 2D into more advanced and detailed 3D models. Since the framework localizes the coupling in time and in frequency, rScO<sub>2</sub> signals with a higher sampling rate might be interesting to investigate. In this context, it might be an opportunity to explore new measurement systems, such as the OxyPREM, which measure rScO<sub>2</sub> at a much higher sampling frequency.

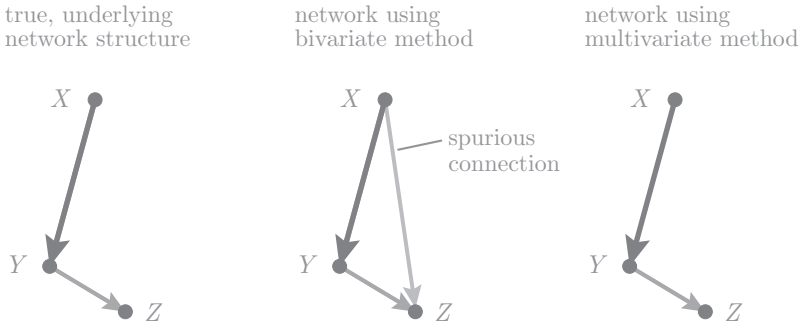


Figure 11.3: A disadvantage of bivariate coupling measures is that we risk to detect spurious connectivities in a multivariate setting. Multivariate methods have an improved accuracy (no spurious connections), but also a larger complexity (more free parameters and longer computational time).

### 11.2.3 Detection and removal of spurious connections

In this thesis, the interaction between the physiological signals was only studied in a pairwise fashion, using bivariate techniques (Section 3.4), including the linear and nonlinear correlation (Chapter 8), the RBF kernel function (Chapter 9) and TE (Chapters 7 and 10). These methods risk to detect spurious connections, which can be thought of as false positives. That is, some connections can be detected that are not there in practice. An example: if  $x$  causes  $y$ , and  $y$  causes  $z$ , a pairwise method risks to detect a coupling between  $x$  and  $z$ , even though there is no direct relation between these two signals (Figure 11.3).

This problem can be solved by moving from bivariate methods to multivariate methods. These methods model the dependency between all signals under study directly, and therefore reduce the risk of detecting spurious connections. In information dynamics, a multivariate extension of TE exists, which is defined as:

$$T_{X \rightarrow Y|Z} = H(Y_n|Y_n^-, \mathbf{Z}_n^-) - H(Y_n|X_n^-, Y_n^-, \mathbf{Z}_n^-) \quad (11.2)$$

where  $H(\cdot)$  denotes Shannon entropy,  $X$  and  $Y$  denote two discrete-time signals, and  $\mathbf{Z}$  presents a (collection of) signal(s), different from  $X$  and  $Y$ . As before, the minus superscript denotes the past of the signal (Section 3.4.4). The main advantage of using multivariate TE over bivariate TE is improved accuracy. The main disadvantage is a considerably larger complexity: the dimension of the

PDFs grow compared to bivariate TE. In addition, computation of multivariate TE requires significantly more computational power, forcing one to GPU-based computing.

Another strategy to reduce spurious connectivities is based on learning the underlying graph structure directly from the signals, based on the assumption of smoothness of signals on graphs [190]. In short, these methods solve a regularized optimization problem, that leads to naturally sparse solutions. This characteristic might be beneficial, since it might remove spurious connections, while being computationally less expensive than the multivariate extension of TE. A main disadvantage of this framework is that the resulting graphs are undirected as opposed to the directed graphs that result from TE computations.

### 11.2.4 Validation

In this thesis, the (neuro)cardiovascular graph model was applied in three different clinical settings on a small scale. In these settings, we illustrated that the connectivity of the (neuro)cardiovascular graph reflected age, the effect of various drugs frequently used in the NICU (propofol, midazolam, sevoflurane), and different types of perioperative management. These results suggest that the graphs might be useful in other applications such as sleep analysis and sleep staging. In addition, features derived from the graphs showed discriminative power between neonates with and without brain injury, indicating that graph topology markers can be used to detect neonates at risk for brain injury. In order to assess the true power of these graph models, further validation is needed. For this, large datasets are needed to accurately study how the graph structure responds to changes in physiological condition. In addition, neonates with normal clinical outcome and term newborns need to be included in these validation studies, since this allows to contrast the graph structure with healthy controls.

### 11.2.5 Functional growth charts of neural development

The neonatal brain is characterized by a marked development of the anatomical structure in the brain between 24 and 36 weeks of PMA, which corresponds to the time in which preterm infants are cared for in the NICU [107]. A dramatic development in brain volume and cortical surface takes place during this period, together with a marked increase in functional brain connectivity and organization. These anatomical changes affect the brain hemodynamics, and therefore, the changes in brain anatomy are expected to lead to changes in CBF regulation as well. Studying how the healthy human brain develops

is important to understand early pathological mechanisms and to assess the influence of fetal or perinatal events on later life [107].

In clinical practice, functional growth charts are very important in the identification of infants at risk of suffering from brain injury [319]. They allow to study the evolution of brain markers over time, which is important since some infants normalize over time while others remain abnormal. Due to the increase in blood pressure and the development of brain anatomy and functional connectivity, the CAR scores are expected to change with age. Baroreflex was found to change with PMA, suggesting a progressive vagal maturation [19]. Therefore, it is important to describe the maturation of CAR and NVC in future research. This can be done on an individual level (considering each regulation mechanism separately) and on an integrated level (using neurocardiovascular graphs).

### **11.2.6 Clinical support system**

The different models described in this thesis and in the current discussion on future directions will finally need to be combined in a clinical decision support system. Based on the results presented in this thesis, various features derived from these models (pairwise coupling, graph topology and connectivity) are expected to be associated with a large prognostic value. The integration into a clinical decision support system is however not trivial: a lot of information needs to be integrated and the resulting tool has to be user-friendly and easy-to-access for the medical doctors and nurses. Therefore, designing a tool that is of added value in daily clinical care is challenging and requires a close collaboration with the medical team for its design. In order to build a robust, reliable and future-proof tool, the human-in-the-loop approach, which is currently emerging in (interactive) machine learning seems like the right candidate for this job. Using such models, both engineers and medical doctors will be able to interact with the decision tool in a straightforward way, enabling the final tool to learn from the data as well as from a multidisciplinary team.



# Bibliography

- [1] Photograph of pyramidal neurons in the cerebral cortex. <https://www.pinterest.com/pin/129971139216847071/>. Accessed: 2021-10-05.
- [2] ÄÄRIMAA, T., OJA, R., ANTILA, K., AND VÄLIMÄKI, I. Interaction of heart rate and respiration in newborn babies. *Pediatric Research* 24, 6 (1988), 745–750.
- [3] AARNOUDSE-MOENS, C. S. H., WEISGLAS-KUPERUS, N., VAN GOUDOEVER, J. B., AND OOSTERLAAN, J. Meta-analysis of neurobehavioral outcomes in very preterm and/or very low birth weight children. *Pediatrics* 124, 2 (aug 2009), 717–728.
- [4] AASLID, R., LINDEGAARD, K. F., SORTEBERG, W., AND NORNES, H. Cerebral autoregulation dynamics in humans. *Stroke* 20, 1 (1989), 45–52.
- [5] ABREU, R., LEAL, A., AND FIGUEIREDO, P. EEG-Informed fMRI: A Review of Data Analysis Methods. *Frontiers in Human Neuroscience* 12 (feb 2018), 29.
- [6] AKRAWI, W. P., DRUMMOND, J. C., KALKMAN, C. J., AND PATEL, P. M. A comparison of the electrophysiologic characteristics of EEG burst-suppression as produced by isoflurane, thiopental, etomidate and propofol. *J. of Neurosur. Anesth.* 8, 1 (1996), 40–46.
- [7] ALDERLIESTEN, T., DIX, L., BAERTS, W., CAICEDO, A., VAN HUFFEL, S., NAULAERS, G., GROENENDAAL, F., VAN BEL, F., AND LEMMERS, P. Reference values of regional cerebral oxygen saturation during the first 3 days of life in preterm neonates. *Pediatric Research* 79, 1 (2016), 55–64.
- [8] ALDERLIESTEN, T., LEMMERS, P. M., SMARIUS, J. J., VAN DE VOSSE, R. E., BAERTS, W., AND VAN BEL, F. Cerebral oxygenation, extraction, and autoregulation in very preterm infants who develop periventricular hemorrhage. *Journal of Pediatrics* 162, 4 (2013).

- [9] ALLEGAERT, K., HOON, J. D., VERBESSELT, R., NAULAERS, G., AND MURAT, I. Maturational pharmacokinetics of single intravenous bolus of propofol. *Paediatric Anaesthesia* 17, 11 (2007), 1028–1034.
- [10] ALLEGAERT, K., PEETERS, M. Y., VERBESSELT, R., TIBBOEL, D., NAULAERS, G., DE HOON, J. N., AND KNIBBE, C. A. Inter-individual variability in propofol pharmacokinetics in preterm and term neonates. *British Journal of Anaesthesia* 99, 6 (2007), 864–870.
- [11] ALLIN, M., ROONEY, M., CUDDY, M., WYATT, J., WALSH, M., RIFKIN, L., AND MURRAY, R. Personality in Young Adults Who Are Born Preterm. *Pediatrics* 117, 2 (feb 2006), 309–316.
- [12] ALTMAN, D. I., POWERS, W. J., PERLMAN, J. M., HERSCOVITCH, P., VOLPE, S. L., AND VOLPE, J. J. Cerebral blood flow requirement for brain viability in newborn infants is lower than in adults. *Annals of Neurology* 24, 2 (1988), 218–226.
- [13] ALY, S. A., ZURAKOWSKI, D., GLASS, P., SKUROW-TODD, K., JONAS, R. A., AND DONOFRIO, M. T. Cerebral tissue oxygenation index and lactate at 24 hours postoperative predict survival and neurodevelopmental outcome after neonatal cardiac surgery. *Congenital Heart Disease* 12, 2 (2017), 188–195.
- [14] ANAND, K. J., MCINTOSH, N., LAGERCRANTZ, H., PELAUSA, E., YOUNG, T. E., AND VASA, R. Analgesia and sedation in preterm neonates who require ventilatory support: Results from the NOPAIN trial. *Archives of Pediatrics and Adolescent Medicine* 153, 4 (1999), 331–338.
- [15] ANAND, K. J., SIPPPELL, W. G., AND AYNLEY-GREEN, A. Randomised trial of fentanyl anaesthesia in preterm babies undergoing surgery: effects on the stress response. *The Lancet* 329, 8524 (1987), 62–66.
- [16] ANDESCAVAGE, N. N., DU PLESSIS, A., MCCARTER, R., SERAG, A., EVANGELOU, I., VEZINA, G., ROBERTSON, R., AND LIMPEROPOULOS, C. Complex Trajectories of Brain Development in the Healthy Human Fetus. *Cerebral Cortex* 27, 11 (2017), 5274–5283.
- [17] ANDRÉ, M., LAMBLIN, M. D., D'ALLEST, A. M., CURZI-DASCALOVA, L., MOUSSALLI-SALEFRANQUE, F., NGUYEN THE TICH, S., VECCHIERINI-BLINEAU, M. F., WALLOIS, F., WALLS-ESQUIVEL, E., AND PLOUIN, P. Electroencephalography in premature and full-term infants. Developmental features and glossary. *Neurophysiol Clin* 40, 2 (may 2010), 59–124.

- [18] ANDRIESEN, P., KOOLEN, A. M. P., BERENDSEN, R. C. M., WIJN, P. F. F., TEN BROEKE, E. D. M., OEI, S. G., AND BLANCO, C. E. Cardiovascular Fluctuations and Transfer Function Analysis in Stable Preterm Infants. *Pediatric Research* 53, 1 (2003), 89–97.
- [19] ANDRIESEN, P., OETOMO, S. B., PETERS, C., VERMEULEN, B., WIJN, P. F., AND BLANCO, C. E. Baroreceptor reflex sensitivity in human neonates: The effect of postmenstrual age. *Journal of Physiology* 568, 1 (2005), 333–341.
- [20] ANDRZEJAK, R. G., KRASKOV, A., STÖGBAUER, H., MORMANN, F., AND KREUZ, T. Bivariate surrogate techniques: Necessity, strengths, and caveats. *Physical Review E - Statistical Physics, Plasmas, Fluids, and Related Interdisciplinary Topics* 68, 6 (2003).
- [21] ANSARI, A. H., DE WEL, O., PILLAY, K., DEREYMAEKER, A., JANSEN, K., VAN HUFFEL, S., NAULAERS, G., AND DE VOS, M. A convolutional neural network outperforming state-of-the-art sleep staging algorithms for both preterm and term infants. *Journal of Neural Engineering* 17, 1 (2020).
- [22] ARICHI, T., FAGIOLO, G., VARELA, M., MELENDEZ-CALDERON, A., ALLIEVI, A., MERCHANT, N., TUSOR, N., COUNSELL, S. J., BURDET, E., BECKMANN, C. F., AND EDWARDS, A. D. Development of BOLD signal hemodynamic responses in the human brain. *NeuroImage* 63, 2 (nov 2012), 663–673.
- [23] ARICHI, T., MORAUX, A., MELENDEZ, A., DORIA, V., GROPPA, M., MERCHANT, N., COMBS, S., BURDET, E., LARKMAN, D. J., COUNSELL, S. J., BECKMANN, C. F., AND EDWARDS, A. D. Somatosensory cortical activation identified by functional MRI in preterm and term infants. *NeuroImage* 49, 3 (feb 2010), 2063–2071.
- [24] ARMSTEAD, W. M. Cerebral Blood Flow Autoregulation and Dysautoregulation. *Anesthesiology Clinics* 34, 3 (sep 2016), 465–477.
- [25] ARTHURS, O. J., EDWARDS, A., AUSTIN, T., GRAVES, M. J., AND LOMAS, D. J. The challenges of neonatal magnetic resonance imaging. *Pediatric Radiology* 42, 10 (aug 2012), 1183–1194.
- [26] AZHAN, A., AND WONG, F. Y. Challenges in understanding the impact of blood pressure management on cerebral oxygenation in the preterm brain. *Frontiers in Physiology* 3 (2012).
- [27] BAIK, N., URLESBERGER, B., SCHWABERGER, B., SCHMÖLZER, G. M., AVIAN, A., AND PICHLER, G. Cerebral haemorrhage in preterm neonates:

- Does cerebral regional oxygen saturation during the immediate transition matter? *Archives of Disease in Childhood: Fetal and Neonatal Edition* 100, 5 (2015), F422–F427.
- [28] BAIK, N., URLESBERGER, B., SCHWABERGER, B., SCHMÖLZER, G. M., MILEDER, L., AVIAN, A., AND PICHLER, G. Reference Ranges for Cerebral Tissue Oxygen Saturation Index in Term Neonates during Immediate Neonatal Transition after Birth. *Neonatology* 108, 4 (2015), 283–286.
- [29] BAIK-SCHNEDITZ, N., PICHLER, G., SCHWABERGER, B., BINDER-HESCHL, C., MILEDER, L., REISS, I. K., AVIAN, A., GREIMEL, P., KLARITSCH, P., AND URLESBERGER, B. Effect of Intrauterine Growth Restriction on Cerebral Regional Oxygen Saturation in Preterm and Term Neonates during Immediate Postnatal Transition. *Neonatology* 117, 3 (2020), 324–330.
- [30] BAIK-SCHNEDITZ, N., SCHWABERGER, B., MILEDER, L., HÖLLER, N., AVIAN, A., URLESBERGER, B., AND PICHLER, G. Cardiac output and cerebral oxygenation in term neonates during neonatal transition. *Children* 8, 6 (2021).
- [31] BALLABH, P. Intraventricular hemorrhage in premature infants: Mechanism of disease. *Pediatric Research* 67, 1 (jan 2010), 1–8.
- [32] BARBEAU, D. Y., AND WEISS, M. D. Sleep Disturbances in Newborns. *Children* 4, 10 (oct 2017), 90.
- [33] BARFIELD, C. P., YU, V. Y., NOMA, O., KUKITA, J., CUSSEN, L. J., OATES, A., AND WALKER, A. M. Cerebral blood volume measured using near-infrared spectroscopy and radiolabels in the immature lamb brain. *Pediatric Research* 46, 1 (1999), 50–56.
- [34] BARSTOW, T. J. Understanding near infrared spectroscopy and its application to skeletal muscle research. *Journal of Applied Physiology* 126, 5 (2019), 1360–1376.
- [35] BARTSCH, R. P., LIU, K. K., BASHAN, A., AND IVANOV, P. C. Network physiology: How organ systems dynamically interact. *PLoS ONE* 10, 11 (2015).
- [36] BASHAN, A., BARTSCH, R. P., KANTELHARDT, J. W., HAVLIN, S., AND IVANOV, P. C. Network physiology reveals relations between network topology and physiological function. *Nature Communications* 3 (2012).

- [37] BERTINIERI, G., DI RIENZO, M., CAVALLAZZI, A., FERRARI, A. U., PEDOTTI, A., AND MANCIA, G. Evaluation of baroreceptor reflex by blood pressure monitoring in unanesthetized cats. *American Journal of Physiology - Heart and Circulatory Physiology* 254, 2 (1988).
- [38] BHATTACHARYA, J., PEREDA, E., AND PETSCHKE, H. Effective detection of coupling in short and noisy bivariate data. *IEEE Transactions on Systems, Man, and Cybernetics, Part B: Cybernetics* 33, 1 (jan 2003), 85–95.
- [39] BISHAY, M., GIACOMELLO, L., RETROSI, G., THYOKA, M., GARRIBOLI, M., BRIERLEY, J., HARDING, L., SCUPLAK, S., CROSS, K. M., CURRY, J. I., KIELY, E. M., DE COPPI, P., EATON, S., AND PIERRO, A. Hypercapnia and acidosis during open and thoracoscopic repair of congenital diaphragmatic hernia and esophageal atresia: Results of a pilot randomized controlled trial. *Annals of Surgery* 258, 6 (dec 2013), 895–900.
- [40] BLACKBURN, S. T. *Maternal, Fetal & Neonatal Physiology: A Clinical Perspective*, 3 ed. Elsevier, St. Louis, MO, 2007.
- [41] BLANCO, S., FIGLIOLA, A., QUIROGA, R. Q., ROSSO, O. A., AND SERRANO, E. Time-frequency analysis of electroencephalogram series. III. Wavelet packets and information cost function. *Physical Review E - Statistical Physics, Plasmas, Fluids, and Related Interdisciplinary Topics* 57, 1 (jan 1998), 932–940.
- [42] BLASI, A., PHILLIPS, D., LLOYD-FOX, S., KOH, P. H., AND ELWELL, C. E. Automatic detection of motion artifacts in infant functional optical topography studies. In *Advances in Experimental Medicine and Biology* (2010), vol. 662, Adv Exp Med Biol, pp. 279–284.
- [43] BLENCOWE, H., COUSENS, S., OESTERGAARD, M., CHOU, D., MOLLER, A., NARWAL, R., ADLER, A., VERA GARCIA, C., ROHDE, S., SAY, L., AND LAWN, J. National, regional, and worldwide estimates of preterm birth rates in the year 2010 with time trends since 1990 for selected countries: a systematic analysis and implications. *Lancet (London, England)* 379, 9832 (2012), 2162–2172.
- [44] BOCCALETTI, S., KURTHS, J., OSIPOV, G., VALLADARES, D. L., AND ZHOU, C. S. The synchronization of chaotic systems. *Physics Report* 366, 1-2 (aug 2002), 1–101.
- [45] BOLISSETTY, S., DHAWAN, A., ABDEL-LATIF, M., BAJUK, B., STACK, J., AND LUI, K. Intraventricular hemorrhage and neurodevelopmental outcomes in extreme preterm infants. *Pediatrics* 133, 1 (jan 2014), 55–62.

- [46] BONIFACIO, S., GONZALEZ, F., AND FERRIERO, D. Diseases of the Newborn. In *Central nervous system injury and neuroprotection*, 9th ed. Elsevier, Philadelphia, 2012, p. 869–891.
- [47] BONNER, R. F., NOSSAL, R., HAVLIN, S., AND WEISS, G. H. Model for photon migration in turbid biological media. *Journal of the Optical Society of America A* 4, 3 (mar 1987), 423.
- [48] BORN, P., LETH, H., MIRANDA, M. J., ROSTRUP, E., STENSGAARD, A., PEITERSEN, B., LARSSON, H. B. W., AND LOU, H. C. Visual Activation in Infants and Young Children Studied by Functional Magnetic Resonance Imaging. *Pediatric Research* 1998 44:4 44, 4 (1998), 578–583.
- [49] BOUYSSI-KOBAR, M., DU PLESSIS, A. J., MCCARTER, R., BROSSARD-RACINE, M., MURNICK, J., TINKLEMAN, L., ROBERTSON, R. L., AND LIMPEROPOULOS, C. Third trimester brain growth in preterm infants compared with in utero healthy fetuses. *Pediatrics* 138, 5 (2016).
- [50] BOZDOGAN, H. Model selection and Akaike’s Information Criterion (AIC): The general theory and its analytical extensions. *Psychometrika* 52, 3 (1987), 345–370.
- [51] BRADY, K. M., MYTAR, J. O., KIBLER, K. K., HOGUE, C. W., LEE, J. K., CZOSNYKA, M., SMIELEWSKI, P., AND EASLEY, R. B. Noninvasive autoregulation monitoring with and without intracranial pressure in the naïve piglet brain. *Anesthesia and Analgesia* 111, 1 (2010), 191–195.
- [52] BRAZY, J. E., AND LEWIS, D. V. Changes in cerebral blood volume and cytochrome aa3 during hypertensive peaks in preterm infants. *The Journal of Pediatrics* 108, 6 (1986), 983–987.
- [53] BRESESTI, I., AVIAN, A., BRUCKNER, M., BINDER-HESCHL, C., SCHWABERGER, B., BAIK-SCHNEDITZ, N., SCHMÖLZER, G., PICHLER, G., AND URLESBERGER, B. Impact of bradycardia and hypoxemia on oxygenation in preterm infants requiring respiratory support at birth. *Resuscitation* 164 (2021), 62–69.
- [54] BREW, N., WALKER, D., AND WONG, F. Y. Cerebral vascular regulation and brain injury in preterm infants. *American Journal of Physiology - Regulatory Integrative and Comparative Physiology* 306, 11 (2014), 773–786.
- [55] BROWN, D. W., PICOT, P. A., NAEINI, J. G., SPRINGETT, R., DELPY, D. T., AND LEE, T. Y. Quantitative near infrared spectroscopy measurement of cerebral hemodynamics in newborn piglets. *Pediatric Research* 51, 5 (2002), 564–570.

- [56] BROWN, E. N., LYDIC, R., AND SCHIFF, N. D. General anesthesia, sleep, and coma. *N. Engl. J. Med.* 363, 27 (2010), 2638–2650.
- [57] BRUNS, N., BLUMENTHAL, S., MEYER, I., KLOSE-VERSCHUUR, S., FELDERHOFF-MÜSER, U., AND MÜLLER, H. Application of an amplitude-integrated EEG monitor (cerebral function monitor) to neonates. *Journal of Visualized Experiments* 2017, 127 (2017).
- [58] BUCHER, H. U., EDWARDS, A. D., LIPP, A. E., AND DUC, G. Comparison between near infrared spectroscopy and 133xenon clearance for estimation of cerebral blood flow in critically III preterm infants. *Pediatric Research* 33, 1 (1993), 56–60.
- [59] BURTIN, P., JACQZ-AIGRAIN, E., GIRARD, P., LENCLÉN, R., MAGNY, J., BETREMIEUX, P., TEHIRY, C., DESPLANQUES, L., AND MUSSAT, P. Population pharmacokinetics of midazolam in neonates. *Clinical Pharmacology & Therapeutics* 56, 6 (1994), 615–625.
- [60] CAICEDO, A., DE SMET, D., NAULAERS, G., AMEYE, L., VANDERHAEGEN, J., LEMMERS, P., VAN BEL, F., AND VAN HUFFEL, S. Cerebral tissue oxygenation and regional oxygen saturation can be used to study cerebral autoregulation in prematurely born infants. *Pediatric Research* 69, 6 (jun 2011), 548–553.
- [61] CAICEDO, A., NAULAERS, G., LEMMERS, P., VAN BEL, F., WOLF, M., AND VAN HUFFEL, S. Detection of cerebral autoregulation by near-infrared spectroscopy in neonates: performance analysis of measurement methods. *J of Biomed Optics* 17, 11 (2012), 117003.
- [62] CAICEDO, A., THEWISSEN, L., SMITS, A., NAULAERS, G., ALLEGAERT, K., AND VAN HUFFEL, S. Changes in oxygenation levels precede changes in amplitude of the EEG in premature infants. In *Advances in Experimental Medicine and Biology* (2016), vol. 923, Adv Exp Med Biol, pp. 143–149.
- [63] CAICEDO, A., THEWISSEN, L., SMITS, A., NAULAERS, G., ALLEGAERT, K., AND VAN HUFFEL, S. Relation between EEG activity and brain oxygenation in preterm neonates. *Advances in Experimental Medicine and Biology* 977 (2017), 133–139.
- [64] CALDERON-ARNULPHI, M., ALARAJ, A., AND SLAVIN, K. V. Near infrared technology in neuroscience: Past, present and future. *Neurological Research* 31, 6 (jul 2009), 605–614.
- [65] CAMFFERMAN, F. A., DE GOEDEREN, R., GOVAERT, P., DUDINK, J., VAN BEL, F., PELLICER, A., COOLS, F., AGUT, T., ALARCON, A.,

- ARENA, R., BARTOCCI, M., BRAVO, M., CABAÑAS, F., CARRERAS, N., CLARIS, O., DUDINK, J., FUMAGALLI, M., GOVAERT, P., HORSCH, S., PARODI, A., PELLICER, A., RAMENGI, L., ROEHR, C. C., STEGGERDA, S., AND VALVERDE, E. Diagnostic and predictive value of Doppler ultrasound for evaluation of the brain circulation in preterm infants: a systematic review. *Pediatric Research* 87, 1 (mar 2020), 50–58.
- [66] CAO, L. Practical method for determining the minimum embedding dimension of a scalar time series. *Physica D: Nonlinear Phenomena* 110, 1-2 (dec 1997), 43–50.
- [67] CHALAK, L. F., TIAN, F., ADAMS-HUET, B., VASIL, D., LAPTOOK, A., TARUMI, T., AND ZHANG, R. Novel Wavelet Real Time Analysis of Neurovascular Coupling in Neonatal Encephalopathy. *Scientific Reports* 7, 1 (apr 2017), 1–8.
- [68] CHANCE, B., DAIT, M. T., ZHANG, C., HAMAOKA, T., AND HAGERMAN, F. Recovery from exercise-induced desaturation in the quadriceps muscles of elite competitive rowers. *American Journal of Physiology - Cell Physiology* 262, 3 31-3 (1992).
- [69] CHANG, T., AND DU PLESSIS, A. Neurodiagnostic techniques in neonatal critical care. *Current Neurology and Neuroscience Reports* 12, 2 (2012), 145–152.
- [70] CHERIAN, P. J., SWARTE, R. M., AND VISSER, G. H. Technical standards for recording and interpretation of neonatal electroencephalogram in clinical practice. *Annals of Indian Academy of Neurology* 12, 1 (jan 2009), 58–70.
- [71] CHINGA, S., PURDONA, P. L., VIJAYAND, S., KOPELLD, N. J., AND BROWN, E. N. A neurophysiological-metabolic model for burst suppression. *PNAS* 109, 8 (2012), 3095–3100.
- [72] CHOCK, V. Y., RAMAMOORTHY, C., AND VAN MEURS, K. P. Cerebral autoregulation in neonates with a hemodynamically significant patent ductus arteriosus. *Journal of Pediatrics* 160, 6 (2012), 936–942.
- [73] CIMATTI, A. G., MARTINI, S., GALLETTI, S., VITALI, F., ACETI, A., FRABONI, G., FALDELLA, G., AND CORVAGLIA, L. Cerebral Oxygenation and Autoregulation in Very Preterm Infants Developing IVH During the Transitional Period: A Pilot Study. *Frontiers in Pediatrics* 8 (2020).
- [74] CLAEYS, M. A., GEPTS, E., AND CAMU, F. Haemodynamic changes during anaesthesia induced and maintained with propofol. *Br. J. Anaesth.* 60 (1988), 3–9.

- [75] CLAIRAMBAULT, J., CURZI-DASCALOVA, L., KAUFFMANN, F., MÉDIGUE, C., AND LEFFLER, C. Heart rate variability in normal sleeping full-term and preterm neonates. *Early Human Development* 28, 2 (1992), 169–183.
- [76] CLEMSON, P., LANCASTER, G., AND STEFANOVSKA, A. Reconstructing Time-Dependent Dynamics. *Proceedings of the IEEE* 104, 2 (feb 2016), 223–241.
- [77] CONROY, S., MCINTYRE, J., AND CHOONARA, I. Unlicensed and off label drug use in neonates. *Archives of Disease in Childhood: Fetal and Neonatal Edition* 80, 2 (1999), F142.
- [78] COOPER, C. E., AND SPRINGETT, R. Measurement of cytochrome oxidase and mitochondrial energetics by near-infrared spectroscopy. *Philosophical Transactions of the Royal Society B: Biological Sciences* 352, 1354 (1997), 669.
- [79] COOPER, R. J., SELB, J., GAGNON, L., PHILLIP, D., SCHYTZ, H. W., IVERSEN, H. K., ASHINA, M., AND BOAS, D. A. A systematic comparison of motion artifact correction techniques for functional near-infrared spectroscopy. *Frontiers in Neuroscience* 0, OCT (2012), 147.
- [80] CORNELISSEN, L., KIM, S. E., LEE, J. M., BROWN, E. N., PURDON, P. L., AND BERDE, C. B. Electroencephalographic markers of brain development during sevoflurane anaesthesia in children up to 3 years old. *British Journal of Anaesthesia* 120, 6 (2018), 1274–1286.
- [81] COSTA, M., GOLDBERGER, A. L., AND PENG, C. K. Multiscale entropy analysis of biological signals. *Physical Review E - Statistical, Nonlinear, and Soft Matter Physics* 71, 2 (feb 2005).
- [82] COSTERUS, S., VLOT, J., VAN ROSMALEN, J., WIJNEN, R., AND WEBER, F. Effects of Neonatal Thoracoscopic Surgery on Tissue Oxygenation: A Pilot Study on (Neuro-) Monitoring and Outcomes. *European Journal of Pediatric Surgery* 29, 2 (2019), 166–172.
- [83] COSTERUS, S., ZAHN, K., VAN DE VEN, K., VLOT, J., WESSEL, L., AND WIJNEN, R. Thoracoscopic versus open repair of CDH in cardiovascular stable neonates. *Surgical Endoscopy* 30, 7 (jul 2016), 2818–2824.
- [84] COSTERUS, S. A., KORTENBOUT, A. J., VOS, H. J., GOVAERT, P., TIBBOEL, D., WIJNEN, R. M., DE JONG, N., BOSCH, J. G., AND DE GRAAFF, J. C. Feasibility of Doppler Ultrasound for Cortical Cerebral Blood Flow Velocity Monitoring During Major Non-cardiac Surgery of Newborns. *Frontiers in Pediatrics* 9 (mar 2021), 203.

- [85] COSTERUS, S. A., VAN HOORN, C. E., HENDRIKX, D., KORTENBOUT, J., HUNFELD, M., VLOT, J., NAULAERS, G., TIBBOEL, D., AND DE GRAAFF, J. C. Towards integrative neuromonitoring of the surgical newborn: A systematic review. *European Journal of Anaesthesiology* 37, 8 (2020), 701–712.
- [86] COUGHTREY, H., RENNIE, J. M., AND EVANS, D. H. Variability in cerebral blood flow velocity: observations over one minute in preterm babies. *Early Human Development* 47, 1 (1997), 63–70.
- [87] CURZI-DASCALOVA, L. [Development of the sleep and autonomic nervous system control in premature and full-term newborn infants]. *Archives de pediatrie : organe officiel de la Societe francaise de pediatrie* (1995).
- [88] D’ALESSANDRO, A., DZIECIATKOWSKA, M., NEMKOV, T., AND HANSEN, K. C. Red blood cell proteomics update: Is there more to discover? *Blood Transfusion* 15, 2 (2017), 182–187.
- [89] D’ANDREA, A., CONTE, M., SCARAFILE, R., RIEGLER, L., COCCHIA, R., PEZZULLO, E., CAVALLARO, M., CARBONE, A., NATALE, F., RUSSO, M. G., GREGORIO, G., AND CALABRÒ, R. Transcranial Doppler ultrasound: Physical principles and principal applications in Neurocritical care unit. *Journal of Cardiovascular Echography* 26, 2 (apr 2016), 28–41.
- [90] DANZER, E., GERDES, M., D’AGOSTINO, J. A., HOFFMAN, C., BERNBAUM, J., BEBBINGTON, M. W., SIEGLE, J., SULKOWSKI, J., RINTOUL, N. E., FLAKE, A. W., SCOTT ADZICK, N., AND HEDRICK, H. L. Longitudinal neurodevelopmental and neuromotor outcome in congenital diaphragmatic hernia patients in the first 3 years of life. *Journal of Perinatology* 33, 11 (nov 2013), 893–898.
- [91] DARBELLAY, G. A., AND VAJDA, I. Estimation of the information by an adaptive partitioning of the observation space. *IEEE Transactions on Information Theory* 45, 4 (1999), 1315–1321.
- [92] DAVID, M., HIRSCH, M., KARIN, J., TOLEDO, E., AND AKSELROD, S. An estimate of fetal autonomic state by time-frequency analysis of fetal heart rate variability. *Journal of Applied Physiology* 102, 3 (mar 2007), 1057–1064.
- [93] DAWSON, J. A., DAVIS, P. G., O’DONNELL, C. P., KAMLIN, C. O., AND MORLEY, C. J. Pulse oximetry for monitoring infants in the delivery room: A review. *Archives of Disease in Childhood: Fetal and Neonatal Edition* 92, 1 (2007).

- [94] DE LA MONTE, S. M., HSU, F. I., HEDLEY-WHYTE, E. T., AND KUPSKY, W. Morphometric Analysis of the Human Infant Brain: Effects of Intraventricular Hemorrhage and Periventricular Leukomalacia. *Journal of Child Neurology* 5, 2 (1990), 101–110.
- [95] DE WEL, O., LAVANGA, M., CAICEDO, A., JANSEN, K., NAULAERS, G., AND VAN HUFFEL, S. Decomposition of a multiscale entropy tensor for sleep stage identification in preterm infants. *Entropy* 21, 10 (2019).
- [96] DEBOER, R. W., KAREMAKER, J. M., AND STRACKEE, J. Hemodynamic fluctuations and baroreflex sensitivity in humans: A beat-to-beat model. *American Journal of Physiology - Heart and Circulatory Physiology* 253, 3 (1987).
- [97] DELPRAT, N., GUILLEMAIN, P., ESCUDIE, B., KRONLAND-MARTINET, R., TCHAMITCHIAN, P., AND TORRESANI, B. Asymptotic Wavelet and Gabor Analysis: Extraction of Instantaneous Frequencies. *IEEE Transactions on Information Theory* 38, 2 (1992), 644–664.
- [98] DELPY, D. T., AND COPE, M. Quantification in tissue near-infrared spectroscopy. *Philosophical Transactions of the Royal Society B: Biological Sciences* 352, 1354 (1997), 649–659.
- [99] DELPY, D. T., COPE, M., VAN DER ZEE, P., ARRIDGE, S., WRAY, S., AND WYATT, J. Estimation of optical pathlength through tissue from direct time of flight measurement. *Physics in Medicine & Biology* 33, 12 (dec 1988), 1433.
- [100] DENG, W., PLEASURE, J., AND PLEASURE, D. Progress in periventricular leukomalacia. *Archives of Neurology* 65, 10 (oct 2008), 1291–1295.
- [101] DEREYMAEKER, A., KOOLEN, N., JANSEN, K., VERVISCH, J., ORTIBUS, E., DE VOS, M., VAN HUFFEL, S., AND NAULAERS, G. The suppression curve as a quantitative approach for measuring brain maturation in preterm infants. *Clinical Neurophysiology* 127, 8 (2016), 2760–2765.
- [102] DEREYMAEKER, A., PILLAY, K., VERVISCH, J., DE VOS, M., VAN HUFFEL, S., JANSEN, K., AND NAULAERS, G. Review of sleep-EEG in preterm and term neonates. *Early Human Development* 113 (oct 2017), 87–103.
- [103] DETTMERS, C., CONNELLY, A., STEPHAN, K. M., TURNER, R., FRISTON, K. J., FRACKOWIAK, R. S., AND GADIAN, D. G. Quantitative comparison of functional magnetic resonance imaging with positron emission tomography using a force-related paradigm. *NeuroImage* 4, 3 (1996), 201–209.

- [104] DIX, L. M. L., VAN BEL, F., AND LEMMERS, P. M. A. Monitoring cerebral oxygenation in neonates: An update. *Frontiers in Pediatrics* 5 (2017).
- [105] DONDERS, F. Bewegungen des gehirns und die veränderungen der gefässfüllung der pia mater. *Schmid's Fahrbücher*, 69 (1851), 5.
- [106] DOYLE, O. M., KOROTCHIKOVA, I., LIGHTBODY, G., MARNANE, W., KERINS, D., AND BOYLAN, G. B. Heart rate variability during sleep in healthy term newborns in the early postnatal period. *Physiological Measurement* 30, 8 (2009), 847–860.
- [107] DUBOIS, J., DEHAENE-LAMBERTZ, G., KULIKOVA, S., POUPON, C., HÜPPI, P. S., AND HERTZ-PANNIER, L. The early development of brain white matter: A review of imaging studies in fetuses, newborns and infants. *Neuroscience* 276 (2014).
- [108] DUERDEN, E. G., TAYLOR, M. J., AND MILLER, S. P. Brain development in infants born preterm: Looking beyond injury. *Seminars in Pediatric Neurology* 20, 2 (2013), 65–74.
- [109] DULLENKOPF, A., KOLAROVA, A., SCHULZ, G., FREY, B., BAENZIGER, O., AND WEISS, M. Reproducibility of cerebral oxygenation measurement in neonates and infants in the clinical setting using the NIRO 300 oximeter. *Pediatric Critical Care Medicine* 6, 3 (2005), 344–347.
- [110] DUNCAN, A., MEEK, J. H., CLEMENCE, M., ELWELL, C. E., TYSZCZUK, L., COPE, M., AND DELPY, D. Optical pathlength measurements on adult head, calf and forearm and the head of the newborn infant using phase resolved optical spectroscopy. *Physics in Medicine and Biology* 40, 2 (1995), 295–304.
- [111] DUNSMORE, I. R., BHATTACHARYYA, G. K., AND JOHNSON, R. A. Statistical Concepts and Methods. *Journal of the Royal Statistical Society. Series A (General)* 141, 2 (1978), 262.
- [112] EDWARDS, A. D., RICHARDSON, C., COPE, M., WYATT, J. S., DELPY, D. T., AND REYNOLDS, E. O. Cotside measurement of cerebral blood flow in ill newborn infants by near infrared spectroscopy. *The Lancet* 332, 8614 (1988), 770–771.
- [113] ELEVELD, D. J., COLIN, P., ABSALOM, A. R., AND STRUYS, M. M. Pharmacokinetic–pharmacodynamic model for propofol for broad application in anaesthesia and sedation. *British Journal of Anaesthesia* 120, 5 (mar 2018), 942–959.

- [114] ELLIS, C. T., SKALABAN, L. J., YATES, T. S., BEJANKI, V. R., CÓRDOVA, N. I., AND TURK-BROWNE, N. B. Re-imagining fMRI for awake behaving infants. *Nature Communications* 11, 1 (sep 2020), 1–12.
- [115] ELLIS, C. T., AND TURK-BROWNE, N. B. Infant fMRI: A Model System for Cognitive Neuroscience. *Trends in Cognitive Sciences* 22, 5 (2018), 375–387.
- [116] ERBERICH, S. G., PANIGRAHY, A., FRIEDLICH, P., SERI, I., NELSON, M. D., AND GILLES, F. Somatosensory lateralization in the newborn brain. *NeuroImage* 29, 1 (jan 2006), 155–161.
- [117] FABRIZI, L., VERRIOTIS, M., WILLIAMS, G., LEE, A., MEEK, J., OLHEDE, S., AND FITZGERALD, M. Encoding of mechanical nociception differs in the adult and infant brain. *Scientific Reports* 6 (2016).
- [118] FAES, L., NOLLO, G., AND PORTA, A. Non-uniform multivariate embedding to assess the information transfer in cardiovascular and cardiorespiratory variability series. *Computers in Biology and Medicine* 42, 3 (mar 2012), 290–297.
- [119] FALLANI, F. D., COSTA, L. D., RODRIGUEZ, F. A., ASTOLFI, L., VECCHIATO, G., TOPPI, J., BORGHINI, G., CINCOTTI, F., MATTIA, D., SALINARI, S., ISABELLA, R., AND BABILONI, F. A graph-theoretical approach in brain functional networks. Possible implications in EEG studies. *Nonlinear Biomedical Physics* 4, SUPPL. 1 (2010).
- [120] FARRARO, R., FATHI, O., AND CHOI, B. Handheld, point-of-care laser speckle imaging. *Journal of Biomedical Optics* 21, 9 (aug 2016), 094001.
- [121] FAUST, O., ACHARYA, U. R., ADELI, H., AND ADELI, A. Wavelet-based EEG processing for computer-aided seizure detection and epilepsy diagnosis. *Seizure* 26 (mar 2015), 56–64.
- [122] FIELDS, R. D., ARAQUE, A., JOHANSEN-BERG, H., LIM, S. S., LYNCH, G., NAVE, K. A., NEDERGAARD, M., PEREZ, R., SEJNOWSKI, T., AND WAKE, H. Glial biology in learning and cognition. *Neuroscientist* 20, 5 (2014), 426–431.
- [123] FRANCESCHINI, M. A., RADHAKRISHNAN, H., THAKUR, K., WU, W., RUVINSKAYA, S., CARP, S., AND BOAS, D. A. The effect of different anesthetics on neurovascular coupling. *NeuroImage* 51, 4 (jul 2010), 1367–1377.
- [124] FRASER, A. M., AND SWINNEY, H. L. Independent coordinates for strange attractors from mutual information. *Physical Review A* 33, 2 (feb 1986), 1134–1140.

- [125] FRIEDMAN, W. F. The intrinsic physiologic properties of the developing heart. *Progress in Cardiovascular Diseases* 15, 1 (1972), 87–111.
- [126] FRISTON, K. J. Functional and Effective Connectivity: A Review. *Brain Connectivity* 1, 1 (jun 2011), 13–36.
- [127] FRITSCH, J. M., REA, R. F., AND ECKBERG, D. L. Carotid baroreflex resetting during drug-induced arterial pressure changes in humans. *American Journal of Physiology - Regulatory Integrative and Comparative Physiology* 256, 2 (1989).
- [128] FYFE, K. L., YIALLOUROU, S. R., WONG, F. Y., ODOI, A., WALKER, A. M., AND HORNE, R. S. Gestational age at birth affects maturation of baroreflex control. *Journal of Pediatrics* 166, 3 (2015), 559–565.
- [129] GAIES, M. G., GURNEY, J. G., YEN, A. H., NAPOLI, M. L., GAJARSKI, R. J., OHYE, R. G., CHARPIE, J. R., AND HIRSCH, J. C. Vasoactive-inotropic score as a predictor of morbidity and mortality in infants after cardiopulmonary bypass. *Pediatric Critical Care Medicine* 11, 2 (2010), 234–238.
- [130] GALDERISI, A., BRIGADOI, S., CUTINI, S., MORO, S. B., LOLLI, E., MECONI, F., BENAVIDES-VARELA, S., BARALDI, E., AMODIO, P., COBELLI, C., TREVISANUTO, D., AND DELL’ACQUA, R. Long-term continuous monitoring of the preterm brain with diffuse optical tomography and electroencephalography: a technical note on cap manufacturing. *Neurophotonics* 3, 4 (dec 2016), 045009.
- [131] GALKA, A. *Topics in Nonlinear Time Series Analysis*, vol. 14 of *Advanced Series in Nonlinear Dynamics*. WORLD SCIENTIFIC, feb 2000.
- [132] GAO, W., GILMORE, J. H., GIOVANELLO, K. S., SMITH, J. K., SHEN, D., ZHU, H., AND LIN, W. Temporal and spatial evolution of brain network topology during the first two years of life. *PLoS ONE* 6, 9 (2011).
- [133] GARVEY, A. A., AND DEMPSEY, E. M. Applications of near infrared spectroscopy in the neonate. *Current Opinion in Pediatrics* 30, 2 (apr 2018), 209–215.
- [134] GAY, A. N., LAZAR, D. A., STOLL, B., NAIK-MATHURIA, B., MUSHIN, O. P., RODRIGUEZ, M. A., BURRIN, D. G., AND OLUTOYE, O. O. Near-infrared spectroscopy measurement of abdominal tissue oxygenation is a useful indicator of intestinal blood flow and necrotizing enterocolitis in premature piglets. *Journal of Pediatric Surgery* 46, 6 (jun 2011), 1034–1040.

- [135] GERSTNER, B., DESILVA, T. M., GENZ, K., ARMSTRONG, A., BREHMER, F., NEVE, R. L., FELDERHOFF-MUESER, U., VOLPE, J. J., AND ROSENBERG, P. A. Hyperoxia causes maturation-dependent cell death in the developing white matter. *Journal of Neuroscience* 28, 5 (2008), 1236–1245.
- [136] GHANTA, S., ABDEL-LATIF, M. E., LUI, K., RAVINDRANATHAN, H., AWAD, J., AND OEI, J. Propofol compared with the morphine, atropine, and suxamethonium regimen as induction agents for neonatal endotracheal intubation: A randomized, controlled trial. *Pediatrics* 119, 6 (2007).
- [137] GLASS, H. C., COSTARINO, A. T., STAYER, S. A., BRETT, C., CLADIS, F., AND DAVIS, P. J. Outcomes for Extremely Premature Infants. *Anesthesia and analgesia* 120, 6 (jun 2015), 1337.
- [138] GLEASON, C. A., HAMM, C., AND JONES, M. D. Effect of acute hypoxemia on brain blood flow and oxygen metabolism in immature fetal sheep. *American Journal of Physiology - Heart and Circulatory Physiology* 258, 4 27-4 (1990).
- [139] GLOVER, G. H. Overview of Functional Magnetic Resonance Imaging. *Neurosurgery clinics of North America* 22, 2 (apr 2011), 133.
- [140] GO, J. L. Neuroradiology Companion: Methods, Guidelines, and Imaging Fundamentals, 3rd ed. *American Journal of Roentgenology* 188, 1 (2007), W100–W100.
- [141] GODDARD-FINEGOLD, J., LOUIS, P. T., RODRIGUEZ, D. L., DAVID, Y., CONTANT, C. F., AND ROLFE, P. Correlation of near infrared spectroscopy cerebral blood flow estimations and microsphere quantitations in newborn piglets. *Biology of the Neonate* 74, 5 (1998), 376–384.
- [142] GONG, Q. Y., ROBERTS, N., GARDEN, A. S., AND WHITEHOUSE, G. H. Fetal and fetal brain volume estimation in the third trimester of human pregnancy using gradient echo MR imaging. *Magnetic Resonance Imaging* 16, 3 (1998), 235–240.
- [143] GONZÁLEZ, J. J., MAÑAS, S., DE VERA, L., MÉNDEZ, L. D., LÓPEZ, S., GARRIDO, J. M., AND PEREDA, E. Assessment of electroencephalographic functional connectivity in term and preterm neonates. *Clinical Neurophysiology* 122, 4 (apr 2011), 696–702.
- [144] GOURÉVITCH, B., AND EGGERMONT, J. J. Evaluating information transfer between auditory cortical neurons. *Journal of Neurophysiology* 97, 3 (mar 2007), 2533–2543.

- [145] GOURLAY, D. M., CASSIDY, L. D., SATO, T. T., LAL, D. R., AND ARCA, M. J. Beyond feasibility: a comparison of newborns undergoing thoracoscopic and open repair of congenital diaphragmatic hernias. *Journal of Pediatric Surgery* 44, 9 (2009), 1702–1707.
- [146] GOURNAY, V., DROUIN, E., AND ROZÉ, J. C. Development of baroreflex control of heart rate in preterm and full term infants. *Archives of Disease in Childhood: Fetal and Neonatal Edition* 86, 3 (2002).
- [147] GOVINDAN, R. B., AL-SHARGABI, T., MASSARO, A. N., METZLER, M., ANDESCAVAGE, N. N., JOSHI, R., DAVE, R., AND DU PLESSIS, A. Baroreflex dysfunction in sick newborns makes heart rate an unreliable surrogate for blood pressure changes. *Pediatric Research* 79, 6 (2016), 929–933.
- [148] GREISEN, G. Autoregulation of cerebral blood flow in newborn babies. *Early Human Development* 81, 5 (may 2005), 423–428.
- [149] GREISEN, G., LEUNG, T., AND WOLF, M. Has the time come to use near-infrared spectroscopy as a routine clinical tool in preterm infants undergoing intensive care? *Philosophical Transactions of the Royal Society A: Mathematical, Physical and Engineering Sciences* 369, 1955 (nov 2011), 4440–4451.
- [150] GRIFFIN, M. P., AND MOORMAN, J. R. Toward the early diagnosis of neonatal sepsis and sepsis-like illness using novel heart rate analysis. *Pediatrics* 107, 1 (2001), 97–104.
- [151] GRUBB, R. L., RAICHLER, M. E., EICHLING, J. O., AND TER-POGOSSIAN, M. M. The effects of changes in PaCO<sub>2</sub> on cerebral blood volume, blood flow, and vascular mean transit time. *Stroke* 5, 5 (1974), 630–639.
- [152] GRUBER, E. M., LAUSSEN, P. C., CASTA, A., ANDREW ZIMMERMAN, A., ZURAKOWSKI, D., REID, R., ODEGARD, K. C., CHAKRAVORTI, S., DAVIS, P. J., MCGOWAN, F. X., HICKEY, P. R., AND HANSEN, D. D. Stress response in infants undergoing cardiac surgery: A randomized study of fentanyl bolus, fentanyl infusion, and fentanyl-midazolam infusion. *Anesthesia and Analgesia* 92, 4 (2001), 882–890.
- [153] GUPTA, P., SODHI, K. S., SAXENA, A. K., KHANDELWAL, N., AND SINGHI, P. Neonatal cranial sonography: A concise review for clinicians. *Journal of Pediatric Neurosciences* 11, 1 (jan 2016), 7–13.
- [154] HANSEN, A., LEVITON, A., PANETH, N., REUSS, M. L., SUSSER, M., ALLRED, E. N., DAMMANN, O., KUBAN, K., PAGANO, M., BANOGAN, P., COLLINS, M., GENEST, D., HELLER, D., SHEN-SCHWARZ, S., ABIRI,

- M., DISALVO, D., DOUBILET, P., KAIRAM, R., KAZAM, E., KIRPEKAR, M., ROSENFELD, D., SANOCKA, U., SCHONFELD, S., SHARE, J., HEGYI, T., HIATT, M., SHAHRIVAR, F., VAN MARTER, L. J., AND HSU, I. The correlation between placental pathology and intraventricular hemorrhage in the preterm infant. *Pediatric Research* 43, 1 (1998), 15–19.
- [155] HARRIS, J. J., JOLIVET, R., AND ATTWELL, D. Synaptic Energy Use and Supply. *Neuron* 75, 5 (2012), 762–777.
- [156] HARTE, G. J., GRAY, P. H., LEE, T. C., STEER, P. A., AND CHARLES, B. G. Haemodynamic responses and population pharmacokinetics of midazolam following administration to ventilated, preterm neonates. *Journal of Paediatrics and Child Health* 33, 4 (1997), 335–338.
- [157] HATA, M., KAZUI, H., TANAKA, T., ISHII, R., CANUET, L., PASCUAL-MARQUI, R. D., AOKI, Y., IKEDA, S., KANEMOTO, H., YOSHIYAMA, K., IWASE, M., AND TAKEDA, M. Functional connectivity assessed by resting state EEG correlates with cognitive decline of Alzheimer’s disease - An eLORETA study. *Clinical Neurophysiology* 127, 2 (2016), 1269–1278.
- [158] HEAD, G. A., LUKOSHKOVA, E. V., BURKE, S. L., MALPAS, S. C., LAMBERT, E. A., AND JANSSEN, B. J. Comparing spectral and invasive estimates of baroreflex gain: Can power spectral analysis reproducibly estimate changes in baroreflex sensitivity? *IEEE Engineering in Medicine and Biology Magazine* 20, 2 (2001), 43–52.
- [159] HEEKEREN, H. R., OBRIG, H., WENZEL, R., EBERLE, K., RUBEN, J., VILLRINGER, K., KURTH, R., AND VILLRINGER, A. Cerebral haemoglobin oxygenation during sustained visual stimulation - A near-infrared spectroscopy study. *Philosophical Transactions of the Royal Society B: Biological Sciences* 352, 1354 (1997), 743–750.
- [160] HEEP, A., SCHEEF, L., JANKOWSKI, J., BORN, M., ZIMMERMANN, N., SIVAL, D., BOS, A., GIESEKE, J., BARTMANN, P., SCHILD, H., AND BOECKER, H. Functional magnetic resonance imaging of the sensorimotor system in preterm infants. *Pediatrics* 123, 1 (jan 2009), 294–300.
- [161] HELLSTRÖM-WESTAS, L., AND ROSÉN, I. Continuous brain-function monitoring: State of the art in clinical practice. *Seminars in Fetal and Neonatal Medicine* 11, 6 (dec 2006), 503–511.
- [162] HELLSTRÖM-WESTAS, L., ROSEN, I., DE VRIES, L. S., AND GREISEN, G. Amplitude-integrated EEG Classification and Interpretation in Preterm and Term Infants. *NeoReviews* 7, 2 (feb 2006), e76–e87.

- [163] HENDRIKX, D., SMITS, A., LAVANGA, M., DE WEL, O., THEWISSEN, L., JANSEN, K., CAICEDO, A., VAN HUFFEL, S., AND NAULAERS, G. Measurement of neurovascular coupling in neonates. *Frontiers in Physiology* 10, FEB (2019).
- [164] HENDRIKX, D., THEWISSEN, L., SMITS, A., NAULAERS, G., ALLEGAERT, K., VAN HUFFEL, S., AND CAICEDO, A. Using graph theory to assess the interaction between cerebral function, brain hemodynamics, and systemic variables in premature infants. *Complexity* 2018 (2018).
- [165] HEROLD, S., BROZOVIC, M., GIBBS, J., LAMMERTSMA, A. A., LEENDERS, K. L., CARR, D., FLEMING, J. S., AND JONES, T. Measurement of regional cerebral blood flow, blood volume and oxygen metabolism in patients with sickle cell disease using positron emission tomography. *Stroke* 17, 4 (1986), 692–698.
- [166] HILLMAN, E. M. Coupling mechanism and significance of the BOLD signal: A status report. *Annual Review of Neuroscience* 37 (2014), 161–181.
- [167] HLAVÁČKOVÁ-SCHINDLER, K., PALUŠ, M., VEJMEJKA, M., AND BHATTACHARYA, J. Causality detection based on information-theoretic approaches in time series analysis. *Physics Reports* 441, 1 (mar 2007), 1–46.
- [168] HONZÍKOVÁ, N., FISER, B., AND HONZÍK, J. Noninvasive determination of baroreflex sensitivity in man by means of spectral analysis. *Physiological research / Academia Scientiarum Bohemoslovaca* 41, 1 (1992), 31–37.
- [169] HOSHI, Y. Functional near-infrared optical imaging: Utility and limitations in human brain mapping. *Psychophysiology* 40, 4 (2003), 511–520.
- [170] HOUSTON, S. M., HERTING, M. M., AND SOWELL, E. R. The neurobiology of childhood structural brain development: Conception through adulthood. *Current Topics in Behavioral Neurosciences* 16 (2014), 3–17.
- [171] HUG JR, C. C., MCLESKEY, C. H., NAHRWOLD, M. L., ROIZEN, M. F., STANLEY, T. H., THISTED, R. A., WALAWANDER, C. A., WHITE, P. F., APFELBAUM, J. L., AND GRASELA, T. H. Hemodynamic effects of propofol: data from over 25,000 patients. *Anesth. Analg.* 77, 4 (1993), S21–S29.
- [172] HUNEAU, C., BENALI, H., AND CHABRIAT, H. Investigating human neurovascular coupling using functional neuroimaging: A critical review of dynamic models. *Frontiers in Neuroscience* 9, DEC (2015).

- [173] HUNG, Y. C., HUANG, C. J., KUOK, C. H., AND CHEN, C. C. The effect of hemodynamic changes induced by propofol induction on cerebral oxygenation in young and elderly patients. *Clin. Anesth.* 17 (2005), 353–357.
- [174] HUNTER, C. L., OEI, J. L., LUI, K., AND SCHINDLER, T. Cerebral oxygenation as measured by near-infrared spectroscopy in neonatal intensive care: correlation with arterial oxygenation. *Acta Paediatrica, International Journal of Paediatrics* 106, 7 (2017), 1073–1078.
- [175] HYDER, F., ROTHMAN, D. L., AND BENNETT, M. R. Cortical energy demands of signaling and nonsignaling components in brain are conserved across mammalian species and activity levels. *Proceedings of the National Academy of Sciences of the United States of America* 110, 9 (2013), 3549–3554.
- [176] IKEDA, K., MACLEOD, D. B., GROCOTT, H. P., MORETTI, E. W., AMES, W., AND VACCHIANO, C. The accuracy of a near-infrared spectroscopy cerebral oximetry device and its potential value for estimating jugular venous oxygen saturation. *Anesthesia and Analgesia* 119, 6 (dec 2014), 1381–1392.
- [177] ISHIMARU, A. Diffusion of a pulse in densely distributed scatterers. *J Opt Soc Am* 68, 8 (1978), 1045–1050.
- [178] J. A., B., AND U. S. R., M. *Graph theory with applications*. Elsevier Science Publishing Co., Inc., 1982.
- [179] JANAILLAC, M., BEAUSOLEIL, T. P., BARRINGTON, K. J., RABOISSON, M. J., KARAM, O., DEHAES, M., AND LAPOINTE, A. Correlations between near-infrared spectroscopy, perfusion index, and cardiac outputs in extremely preterm infants in the first 72 h of life. *European Journal of Pediatrics* 177, 4 (2018).
- [180] JARY, S., KMITA, G., WROBLEWSKA, J., AND WHITELAW, A. Quantitative cranial ultrasound prediction of severity of disability in premature infants with post-haemorrhagic ventricular dilatation. *Archives of Disease in Childhood* 97, 11 (2012), 955–959.
- [181] JAVORKA, K., LEHOTSKA, Z., KOZAR, M., UHRIKOVA, Z., KOLAROVSKZI, B., JAVORKA, M., AND ZIBOLEN, M. Heart rate variability in newborns. *Physiological Research* 66, 2 (2017), S203–S214.
- [182] JENKINS, A., GREENBLATT, E. P., FAULKNER, H. J., BERTACCINI, E., LIGHT, A., LIN, A., ANDREASEN, A., VINER, A., TRUDELL, J. R., AND HARRISON, N. L. Evidence for a common binding cavity for three general

- anesthetics within the GABAA receptor. *The Journal of neuroscience : the official journal of the Society for Neuroscience* 21, 6 (2001).
- [183] JENKINS, J. G., REID, M. M. C., AND MCCLURE, B. G. Study of heart rate variability in sick newborn infants. *Acta Pædiatrica* 69, 3 (1980), 393–396.
- [184] JESSEN, K. R., AND MIRSKY, R. Glial cells in the enteric nervous system contain glial fibrillary acidic protein. *Nature* 286, 5774 (1980), 736–737.
- [185] JÖBSIS, F. F. Noninvasive, infrared monitoring of cerebral and myocardial oxygen sufficiency and circulatory parameters. *Science* 198, 4323 (1977), 1264–1266.
- [186] JOHN MIHIC, S., YE, Q., WICK, M. J., KOLTCHINE, V. V., KRASOWSKI, M. D., FINN, S. E., MASCIA, M. P., FERNANDO VALENZUELA, C., HANSON, K. K., GREENBLATT, E. P., ADRON HARRIS, R., AND HARRISON, N. L. Sites of alcohol and volatile anaesthetic action on GABA(A) and glycine receptors. *Nature* 389, 6649 (1997), 385–389.
- [187] JONES, M. D., TRAYSTMAN, R. J., SIMMONS, M. A., AND MOLteni, R. A. Effects of changes in arterial O<sub>2</sub> content on cerebral blood flow in the lamb. *American Journal of Physiology - Heart and Circulatory Physiology* 9, 2 (1981).
- [188] JONG, G., VAN DER LINDEN, P., BAKKER, E., VAN DER LELY, N., ELAND, I., STRICKER, B., AND VAN DEN ANKER, J. Unlicensed and off-label drug use in a paediatric ward of a general hospital in the Netherlands. *European Journal of Clinical Pharmacology* 58, 4 (2002), 293–297.
- [189] JUHÁSZ, C., CHUGANI, D. C., MUZIK, O., WATSON, C., SHAH, J., SHAH, A., AND CHUGANI, H. T. Relationship between EEG and positron emission tomography abnormalities in clinical epilepsy. *Journal of Clinical Neurophysiology* 17, 1 (2000), 29–42.
- [190] KALOFOLIAS, V. How to learn a graph from smooth signals. In *Proceedings of the 19th International Conference on Artificial Intelligence and Statistics, AISTATS 2016* (2016).
- [191] KAMLIN, C. O. F., O'DONNELL, C. P., DAVIS, P. G., AND MORLEY, C. J. Oxygen saturation in healthy infants immediately after birth. *Journal of Pediatrics* 148, 5 (2006), 585–589.
- [192] KANTZ, H., AND SCHREIBER, T. *Nonlinear Time Series Analysis*, 2 ed. Cambridge University Press, nov 2003.

- [193] KAREN, T., MORREN, G., HAENSSE, D., BAUSCHATZ, A. S., BUCHER, H. U., AND WOLF, M. Hemodynamic response to visual stimulation in newborn infants using functional near-infrared spectroscopy. *Human Brain Mapping* 29, 4 (apr 2008), 453–460.
- [194] KENET, G., KUPERMAN, A. A., STRAUSS, T., AND BRENNER, B. Neonatal IVH - Mechanisms and management. *Thrombosis Research* 127, SUPPL. 3 (feb 2011), S120–S122.
- [195] KENNY, J. D., GARCIA-PRATS, J. A., HILLIARD, J. L., CORBET, A. J., AND RUDOLPH, A. J. Hypercarbia at birth: A possible role in the pathogenesis of intraventricular hemorrhage. *Pediatrics* 62, 4 (1978), 465–467.
- [196] KHWAJA, O., AND VOLPE, J. J. Pathogenesis of cerebral white matter injury of prematurity. *Archives of Disease in Childhood: Fetal and Neonatal Edition* 93, 2 (2008).
- [197] KIDOKORO, H., INDER, T., OKUMURA, A., AND WATANABE, K. What does cyclicity on amplitude-integrated EEG mean. *Journal of Perinatology* 32, 8 (aug 2012), 565–569.
- [198] KINNEY, H., HAYNES, R., AND FOLKERTH, R. White matter lesions in the perinatal period. In *Pathology and Genetics: Acquired and Inherited Diseases of the Developing Nervous System*. ISN Neuropathology Press, Basel, 2004, p. 156–170.
- [199] KINNEY, H. C. The Near-Term (Late Preterm) Human Brain and Risk for Periventricular Leukomalacia: A Review. *Seminars in Perinatology* 30, 2 (apr 2006), 81–88.
- [200] KISHI, K., KAWAGUCHI, M., YOSHITANI, K., NAGAHATA, T., AND FURUYA, H. Influence of patient variables and sensor location on regional cerebral oxygen saturation measured by INVOS 4100 near-infrared spectrophotometers. *Journal of Neurosurgical Anesthesiology* 15, 4 (2003), 302–306.
- [201] KISSACK, C. M., GARR, R., WARDLE, S. P., AND WEINDLING, A. M. Cerebral fractional oxygen extraction is inversely correlated with oxygen delivery in the sick, newborn, preterm infant. *Journal of Cerebral Blood Flow and Metabolism* 25, 5 (may 2005), 545–553.
- [202] KIYMIK, M. K., GÜLER, I., DIZIBÜYÜK, A., AND AKIN, M. Comparison of STFT and wavelet transform methods in determining epileptic seizure activity in EEG signals for real-time application. *Computers in Biology and Medicine* 35, 7 (2005), 603–616.

- [203] KLEBERMASS-SCHREHOF, K., CZABA, C., OLISCHAR, M., FUIKO, R., WALDHOER, T., RONA, Z., POLLAK, A., AND WENINGER, M. Impact of low-grade intraventricular hemorrhage on long-term neurodevelopmental outcome in preterm infants. *Child's Nervous System* 28, 12 (2012), 2085–2092.
- [204] KLEIGER, R. E., STEIN, P. K., BOSNER, M. S., AND ROTTMAN, J. N. Time domain measurements of heart rate variability. *Cardiology Clinics* 10, 3 (1992), 487–498.
- [205] KLEISER, S., NASSERI, N., ANDRESEN, B., GREISEN, G., AND WOLF, M. Comparison of tissue oximeters on a liquid phantom with adjustable optical properties. *Biomedical Optics Express* 7, 8 (2016), 2973.
- [206] KLEISER, S., OSTOJIC, D., ANDRESEN, B., NASSERI, N., ISLER, H., SCHOLKMANN, F., KAREN, T., GREISEN, G., AND WOLF, M. Comparison of tissue oximeters on a liquid phantom with adjustable optical properties: an extension. *Biomedical Optics Express* 9, 1 (2018), 86.
- [207] KLEISER, S., OSTOJIC, D., AND NASSERI, N. In vivo precision assessment of a near-infrared spectroscopy-based tissue oximeter (OxyPrem v1.3) in neonates considering systemic hemodynamic fluctuations. *Journal of Biomedical Optics* 23, 06 (2018), 1.
- [208] KNYAZEVA, G. G. EEG delta oscillations as a correlate of basic homeostatic and motivational processes. *Neuroscience and Biobehavioral Reviews* 36, 1 (jan 2012), 677–695.
- [209] KOEHLER, R. C., JONES, M. D., AND TRAYSTMAN, R. J. Cerebral circulatory response to carbon monoxide and hypoxic hypoxia in the lamb. *American Journal of Physiology - Heart and Circulatory Physiology* 12, 1 (1982).
- [210] KOOLEN, N., JANSEN, K., VERVISCH, J., MATIC, V., DE VOS, M., NAULAERS, G., AND VAN HUFFEL, S. Line length as a robust method to detect high-activity events: Automated burst detection in premature EEG recordings. *Clinical Neurophysiology* 125, 10 (2014), 1985–1994.
- [211] KORNER, P. I., WEST, M. J., SHAW, J., AND UTHER, J. B. 'Steady-state' properties of the baroreceptor-heart rate reflex in essential hypertension in man. *Clinical and Experimental Pharmacology and Physiology* 1, 1 (1974), 65–76.
- [212] KOZAR, M., TONHAJZEROVA, I., MESTANIK, M., MATASOVA, K., ZIBOLEN, M., CALKOVSKA, A., AND JAVORKA, K. Heart rate variability

- in healthy term newborns is related to delivery mode: A prospective observational study. *BMC Pregnancy and Childbirth* 18, 1 (2018).
- [213] KOZBERG, M. G., CHEN, B. R., DELEO, S. E., BOUCHARD, M. B., AND HILLMAN, E. M. C. Resolving the transition from negative to positive blood oxygen level-dependent responses in the developing brain. *Proceedings of the National Academy of Sciences* 110, 11 (mar 2013), 4380–4385.
- [214] KOZBERG, M. G., AND HILLMAN, E. Neurovascular coupling and energy metabolism in the developing brain. *Progress in Brain Research* 225 (2016), 213–242.
- [215] KOZBERG, M. G., AND HILLMAN, E. M. C. Neurovascular coupling develops alongside neural circuits in the postnatal brain. *Neurogenesis* 3, 1 (2016).
- [216] KRASKOV, A. *Synchronization and Interdependence Measures and their Applications to the Electroencephalogram of Epilepsy Patients and Clustering of Data*. PhD thesis, 2004.
- [217] KRASKOV, A., STÖGBAUER, H., AND GRASSBERGER, P. Estimating mutual information. *Physical Review E - Statistical Physics, Plasmas, Fluids, and Related Interdisciplinary Topics* 69, 6 (2004), 16.
- [218] KUBAN, K. C., EPI, S. M., AND VOLPE, J. J. Intraventricular hemorrhage: An update. *Journal of Intensive Care Medicine* 8, 4 (jul 1993), 157–176.
- [219] KUEBLER, W. M., SCKELL, A., HABLER, O., KLEEN, M., KUHNLE, G. E. H., WELTE, M., MESSMER, K., AND GOETZ, A. E. Noninvasive Measurement of Regional Cerebral Blood Flow by Near-Infrared Spectroscopy and Indocyanine Green. *Journal of Cerebral Blood Flow & Metabolism* 18, 4 (1998), 445–456.
- [220] KUPERMAN, A. A., BRENNER, B., AND KENET, G. Intraventricular hemorrhage in preterm infants and coagulation - Ambivalent perspectives? *Thrombosis Research* 131, SUPPL.1 (2013).
- [221] KUUSELA, T. Methodological aspects of heart rate variability analysis. In *Heart Rate Variability (HRV) Signal Analysis: Clinical Applications*, M. Kamath, M. Watanabe, and A. Upton, Eds., 1st editio ed. CRC Press, 2016, ch. Methodolog, pp. 9–42.
- [222] LALLY, K. P., LASKY, R. E., LALLY, P. A., BAGOLAN, P., DAVIS, C. F., FRENCKNER, B. P., HIRSCHL, R. M., LANGHAM,

- M. R., BUCHMILLER, T. L., USUI, N., TIBBOEL, D., AND WILSON, J. M. Standardized reporting for congenital diaphragmatic hernia - An international consensus. In *Journal of Pediatric Surgery* (dec 2013), vol. 48, J Pediatr Surg, pp. 2408–2415.
- [223] LAOPRASERT, P. Artifacts. In *Atlas of Pediatric EEG*. McGraw Hill Medical, 2011, ch. 2, pp. 125–200.
- [224] LAVANGA, M., DE WEL, O., CAICEDO, A., JANSEN, K., DEREYMAEKER, A., NAULAERS, G., AND VAN HUFFEL, S. A brain-age model for preterm infants based on functional connectivity. *Physiological Measurement* 39, 4 (2018).
- [225] LAVANGA, M., HEREMANS, E., MOEYERSONS, J., BOLLEN, B., JANSEN, K., ORTIBUS, E., NAULAERS, G., VAN HUFFEL, S., AND CAICEDO, A. Maturation of the Autonomic Nervous System in Premature Infants: Estimating Development Based on Heart-Rate Variability Analysis. *Frontiers in Physiology* 11 (2021), 581250.
- [226] LEE, J. K., KIBLER, K. K., BENNI, P. B., EASLEY, R. B., CZOSNYKA, M., SMIELEWSKI, P., KOEHLER, R. C., SHAFFNER, D. H., AND BRADY, K. M. Cerebrovascular reactivity measured by near-infrared spectroscopy. *Stroke* 40, 5 (2009), 1820–1826.
- [227] LEE, J. Y., KIM, H. S., JUNG, E., KIM, E. S., SHIM, G. H., LEE, H. J., LEE, J. A., CHOI, C. W., KIM, E. K., KIM, B. I., AND CHOI, J. H. Risk factors for periventricular-intraventricular hemorrhage in premature infants. *Journal of Korean Medical Science* 25, 3 (mar 2010), 418–424.
- [228] LEEUWEN, L., SCHILLER, R. M., RIETMAN, A. B., VAN ROSMALEN, J., WILDSCHUT, E. D., HOUMES, R. J. M., TIBBOEL, D., AND IJSSELSTIJN, H. Risk factors of impaired neuropsychologic outcome in school-Aged survivors of neonatal critical illness. *Critical Care Medicine* 46, 3 (2018), 401–410.
- [229] LEMMERS, P. M., TOET, M. C., AND VAN BEL, F. Impact of patent ductus arteriosus and subsequent therapy with indomethacin on cerebral oxygenation in preterm infants. *Pediatrics* 121, 1 (2008), 142–147.
- [230] LEMMERS, P. M., AND VAN BEL, F. Left-to-right differences of regional cerebral oxygen saturation and oxygen extraction in preterm infants during the first days of life. *Pediatric Research* 65, 2 (2009), 226–230.
- [231] LIAO, S. M., GREGG, N. M., WHITE, B. R., ZEFF, B. W., BJERKAAS, K. A., INDER, T. E., AND CULVER, J. P. Neonatal hemodynamic response to visual cortex activity: high-density near-infrared spectroscopy study. *Journal of Biomedical Optics* 15, 2 (2010), 026010.

- [232] LIBENSON, M. H. The electroencephalogram of the newborn. In *Practical Approach to Electroencephalography*. Elsevier Health Sciences, 2010, ch. 13, pp. 301–328.
- [233] LIEM, K. D., AND GREISEN, G. Monitoring of cerebral haemodynamics in newborn infants. *Early Human Development* 86, 3 (2010), 155–158.
- [234] LINCHANG, Y., HONGWEI, H., CHANGQING, J., AND LUMING, L. Preliminary study on processing local field potential with smoothed pseudo Wigner-Ville distribution for epileptic seizure detection. In *2010 4th International Conference on Bioinformatics and Biomedical Engineering, iCBBE 2010* (2010).
- [235] LINDAUER, U., LEITHNER, C., KAASCH, H., ROHRER, B., FODDIS, M., FÜCHTEMEIER, M., OFFENHAUSER, N., STEINBRINK, J., ROYL, G., KOHL-BAREIS, M., AND DIRNAGL, U. Neurovascular coupling in rat brain operates independent of hemoglobin deoxygenation. *Journal of Cerebral Blood Flow and Metabolism* 30, 4 (apr 2010), 757–768.
- [236] LINKENKAER-HANSEN, K., NIKOULINE, V. V., PALVA, J. M., AND ILMONIEMI, R. J. Long-range temporal correlations and scaling behavior in human brain oscillations. *Journal of Neuroscience* 21, 4 (feb 2001), 1370–1377.
- [237] LIPPMAN, N., STEIN, K. M., AND LERMAN, B. B. Comparison of methods for removal of ectopy in measurement of heart rate variability. *American Journal of Physiology - Heart and Circulatory Physiology* 267, 1 36-1 (1994).
- [238] LIU, B. Kernel discrimination via oblique projection. In *Proceedings of 2011 International Conference on Image Analysis and Signal Processing, IASP 2011* (2011), pp. 707–711.
- [239] LOGITHARAJAH, P., RUTHERFORD, M. A., AND COWAN, F. M. Hypoxic-ischemic encephalopathy in preterm infants: Antecedent factors, brain imaging, and outcome. *Pediatric Research* 66, 2 (2009), 222–229.
- [240] LONGIN, E., GERSTNER, T., SCHAIBLE, T., LENZ, T., AND KÖNIG, S. Maturation of the autonomic nervous system: Differences in heart rate variability in premature vs. term infants. *Journal of Perinatal Medicine* 34, 4 (2006), 303–308.
- [241] LOPES DA SILVA, F., PIJN, J. P., AND BOEIJINGA, P. Interdependence of EEG signals: Linear vs. nonlinear Associations and the significance of time delays and phase shifts. *Brain Topography* 2, 1-2 (sep 1989), 9–18.

- [242] LOU, H. C., LASSEN, N. A., AND FRIIS-HANSEN, B. Impaired autoregulation of cerebral blood flow in the distressed newborn infant. *The Journal of Pediatrics* 94, 1 (1979), 118–121.
- [243] LOUIS, E. K. S., AND FREY, L. C. *Electroencephalography - An introductory text*. American Epilepsy Society, 2016.
- [244] MADDEROM, M. J., TOUSSAINT, L., VAN DER CAMMEN-VAN ZIJP, M. H., GISCHLER, S. J., WIJNEN, R. M., TIBBOEL, D., AND IJSSELSTIJN, H. Congenital diaphragmatic hernia with(out) ECMO: Impaired development at 8 years. *Archives of Disease in Childhood: Fetal and Neonatal Edition* 98, 4 (2013).
- [245] MÄENPÄÄ, M., PENTTILÄ, J., LAITIO, T., KAISTI, K., KUUSELA, T., HINKKA, S., AND SCHEININ, H. The effects of surgical levels of sevoflurane and propofol anaesthesia on heart rate variability. *European Journal of Anaesthesiology* 24, 7 (2007), 626–633.
- [246] MAHMOUDZADEH, M., DEHAENE-LAMBERTZ, G., KONGOLO, G., FOURNIER, M., GOUDJIL, S., AND WALLOIS, F. Consequence of intraventricular hemorrhage on neurovascular coupling evoked by speech syllables in preterm neonates. *Developmental Cognitive Neuroscience* 30 (apr 2018), 60–69.
- [247] MALIK, M., JOHN CAMM, A., THOMAS BIGGER, J., BREITHARDT, G., CERUTTI, S., COHEN, R. J., COUMEL, P., FALLEN, E. L., KENNEDY, H. L., KLEIGER, R. E., LOMBARDI, F., MALLIANI, A., MOSS, A. J., ROTTMAN, J. N., SCHMIDT, G., SCHWARTZ, P. J., AND SINGER, D. H. Heart rate variability: Standards of measurement, physiological interpretation, and clinical use. *Circulation* 93, 5 (1996), 1043–1065.
- [248] MARCH OF DIMES, THE PARTNERSHIP FOR MATERNAL, NEWBORN & CHILD HEALTH, SAVE THE CHILDREN, AND WHO. Born too soon: the global action report on preterm birth.
- [249] MARIN, T., AND MOORE, J. Understanding near-infrared spectroscopy. *Advances in Neonatal Care* 11, 6 (dec 2011), 382–388.
- [250] MARMARELIS, V. Linear and Nonlinear Modeling of Cerebral Flow Autoregulation Using Principal Dynamic Modes. *The Open Biomedical Engineering Journal* 6, 1 (may 2012), 42–55.
- [251] MARTIN, L. D., DISSEN, G. A., MCPIKE, M. J., AND BRAMBRINK, A. M. Effects of anesthesia with isoflurane, ketamine, or propofol on physiologic parameters in neonatal rhesus macaques (*Macaca mulatta*). *Journal of the American Association for Laboratory Animal Science* 53, 3 (2014), 290–300.

- [252] MASSARO, A. N., GOVINDAN, R. B., AL-SHARGABI, T., ANDESCAVAGE, N. N., METZLER, M., CHANG, T., GLASS, P., AND DU PLESSIS, A. J. Heart rate variability in encephalopathic newborns during and after therapeutic hypothermia. *Journal of Perinatology* 34, 11 (2014), 836–841.
- [253] MAYNARD, D., PRIOR, P. F., AND SCOTT, D. F. Device for Continuous Monitoring of Cerebral Activity in Resuscitated Patients. *British Medical Journal* 4, 5682 (1969), 545–546.
- [254] MAZURSKY, J. E., BIRKETT, C. L., BEDELL, K. A., BEN-HAIM, S. A., AND SEGAR, J. L. Development of baroreflex influences on heart rate variability in preterm infants. *Early Human Development* 53, 1 (nov 1998), 37–52.
- [255] MCCANN, M. E., AND SCHOUTEN, A. N. Beyond survival; Influences of blood pressure, cerebral perfusion and anesthesia on neurodevelopment. *Paediatric Anaesthesia* 24, 1 (2014), 68–73.
- [256] MEEK, J. H., FIRBANK, M., ELWELL, C. E., ATKINSON, J., BRADDICK, O., AND WYATT, J. S. Regional hemodynamic responses to visual stimulation in awake infants. *Pediatric Research* 43, 6 (1998), 840–843.
- [257] MEIJLER, G., AND STEGGERDA, S. J. Transcranial Doppler Sonography in Neonates. In *Neonatal Cranial Ultrasonography*. Springer, Cham, 2019, pp. 219–257.
- [258] MESSER, J., HADDAD, J., AND CASANOVA, R. Transcranial Doppler evaluation of cerebral infarction in the neonate. *Neuropediatrics* 22, 3 (1991), 147–151.
- [259] MESSERE, A., AND ROATTA, S. Influence of cutaneous and muscular circulation on spatially resolved versus standard Beer-Lambert near-infrared spectroscopy. *Physiological Reports* 1, 7 (dec 2013), e00179.
- [260] METZ, A. J., WOLF, M., ACHERMANN, P., AND SCHOLKMANN, F. A new approach for automatic removal of movement artifacts in near-infrared spectroscopy time series by means of acceleration data. *Algorithms* 8, 4 (nov 2015), 1052–1075.
- [261] MINTZER, J. P., AND MOORE, J. E. Regional tissue oxygenation monitoring in the neonatal intensive care unit: evidence for clinical strategies and future directions. *Pediatric Research* 86, 3 (2019), 296–304.
- [262] MITRA, S., CZOSNYKA, M., SMIELEWSKI, P., O'REILLY, H., BRADY, K., AND AUSTIN, T. Heart rate passivity of cerebral tissue oxygenation is associated with predictors of poor outcome in preterm infants. *Acta Paediatrica, International Journal of Paediatrics* 103, 9 (2014).

- [263] MOEYERSONS, J., AMONI, M., HUFFEL, S. V., WILLEMS, R., AND VARON, C. R-DECO: An open-source Matlab based graphical user interface for the detection and correction of R-peaks. *PeerJ Computer Science* 2019, 10 (2019).
- [264] MOEYERSONS, J., SMETS, E., MORALES, J., VILLA, A., DE RAEDT, W., TESTELMANS, D., BUYSE, B., VAN HOOF, C., WILLEMS, R., VAN HUFFEL, S., AND VARON, C. Artefact detection and quality assessment of ambulatory ECG signals. *Computer Methods and Programs in Biomedicine* 182 (2019).
- [265] MOLAVI, B., DUMONT, G., AND SHADGAN, B. Motion artifact removal from muscle NIR Spectroscopy measurements. In *Canadian Conference on Electrical and Computer Engineering* (2010).
- [266] MOORE, G. P., LEMYRE, B., BARROWMAN, N., AND DABOVAL, T. Neurodevelopmental outcomes at 4 to 8 years of children born at 22 to 25 weeks' gestational age: A meta-analysis. *JAMA Pediatrics* 167, 10 (oct 2013), 967–974.
- [267] MORAN, M., MILETIN, J., PICOVA, K., AND DEMPSEY, E. M. Cerebral tissue oxygenation index and superior vena cava blood flow in the very low birth weight infant. *Acta Paediatrica, International Journal of Paediatrics* 98, 1 (2009), 43–46.
- [268] MORAN, M. M., GUNN-CHARLTON, J. K., WALSH, J. M., CHEONG, J. L., ANDERSON, P. J., DOYLE, L. W., GREAVES, S., AND HUNT, R. W. Associations of Neonatal Noncardiac Surgery with Brain Structure and Neurodevelopment: A Prospective Case-Control Study. *Journal of Pediatrics* 212 (sep 2019), 93–101.
- [269] MUKERJI, A., SHAH, V., AND SHAH, P. S. Periventricular/intraventricular hemorrhage and neurodevelopmental outcomes: A meta-analysis. *Pediatrics* 136, 6 (dec 2015), 1132–1143.
- [270] MULKEY, S. B., AND DÚ PLESSIS, A. The Critical Role of the Central Autonomic Nervous System in Fetal-Neonatal Transition. *Seminars in Pediatric Neurology* 28 (2018), 29–37.
- [271] MULKEY, S. B., AND DU PLESSIS, A. J. Autonomic nervous system development and its impact on neuropsychiatric outcome. *Pediatric Research* 85, 2 (2019), 120–126.
- [272] MULLAART, R. A., HOPMAN, J. C., ROTTEVEEL, J. J., DANIËLS, O., STOELINGA, G. B., AND DE HAAN, A. F. Cerebral blood flow fluctuation in neonatal respiratory distress and periventricular haemorrhage. *Early Human Development* 37, 3 (1994), 179–185.

- [273] MULLINGER, K., AND BOWTELL, R. Combining EEG and fMRI. *Methods in Molecular Biology* 711 (2011), 303–326.
- [274] MUZI, M., BERENS, R. A., KAMPINE, J. P., AND EBERT, T. J. Venodilation contributes to propofol-mediated hypotension in humans. *Anesth. Analg.* 74, 6 (1992), 877–883.
- [275] NAGARAJ, S. B., STEVENSON, N. J., MARNANE, W. P., BOYLAN, G. B., AND LIGHTBODY, G. Robustness of time frequency distribution based features for automated neonatal EEG seizure detection. In *2014 36th Annual International Conference of the IEEE Engineering in Medicine and Biology Society, EMBC 2014* (nov 2014), Institute of Electrical and Electronics Engineers Inc., pp. 2829–2832.
- [276] NAGDYMAN, N., EWERT, P., PETERS, B., MIERA, O., FLECK, T., AND BERGER, F. Comparison of different near-infrared spectroscopic cerebral oxygenation indices with central venous and jugular venous oxygenation saturation in children. *Paediatric Anaesthesia* 18, 2 (2008), 160–166.
- [277] NAKAMURA, S., WALKER, D. W., AND WONG, F. Y. Cerebral haemodynamic response to somatosensory stimulation in near-term fetal sheep. *The Journal of Physiology* 595, 4 (feb 2017), 1289–1303.
- [278] NAULAERS, G. *Non-invasive measurements of the neonatal cerebral and splanchnic circulation by near-infrared spectroscopy*. PhD thesis, KU Leuven, 2003.
- [279] NAULAERS, G., MEYNS, B., MISEREZ, M., LEUNENS, V., VAN HUFFEL, S., CASAER, P., AND DEVLIEGER, H. Measurement of the liver tissue oxygenation by near-infrared spectroscopy. *Intensive Care Medicine* 31, 1 (jan 2005), 138–141.
- [280] NAULAERS, G., MEYNS, B., MISEREZ, M., LEUNENS, V., VAN HUFFEL, S., CASAER, P., WEINDLING, M., AND DEVLIEGER, H. Use of tissue oxygenation index and fractional tissue oxygen extraction as non-invasive parameters for cerebral oxygenation: A validation study in piglets. *Neonatology* 92, 2 (2007), 120–126.
- [281] NAULAERS, G., MORREN, G., VAN HUFFEL, S., CASAER, P., AND DEVLIEGER, H. Cerebral tissue oxygenation index in very premature infants. *Archives of Disease in Childhood: Fetal and Neonatal Edition* 87, 3 (2002).
- [282] NAVARRO, X., PORÉE, F., KUCHENBUCH, M., CHAVEZ, M., BEUCHÉE, A., AND CARRAULT, G. Multi-feature classifiers for burst detection in single EEG channels from preterm infants. *Journal of Neural Engineering* 14, 4 (2017).

- [283] NETOFF, T. I., AND SCHIFF, S. J. Decreased neuronal synchronization during experimental seizures. *Journal of Neuroscience* 22, 16 (aug 2002), 7297–7307.
- [284] NEUKIRCHEN, M., AND KIENBAUM, P. Sympathetic nervous system: Evaluation and importance for clinical general anesthesia. *Anesthesiology* 109, 6 (2008), 1113–1131.
- [285] NG, E., TADDIO, A., AND OHLSSON, A. Intravenous midazolam infusion for sedation of infants in the neonatal intensive care unit. *Cochrane Database of Systematic Reviews* 2012, 6 (jun 2012).
- [286] NGUYEN, T. Total Number of Synapses in the Adult Human Neocortex. *Undergraduate Journal of Mathematical Modeling: One + Two* 3, 1 (2013).
- [287] OATES, J., KARMILOFF-SMITH, A., AND JOHNSON, M. Developing brains. *Early Childhood in Focus*, 7 (2012).
- [288] OKADA, E., AND DELPY, D. T. Near-infrared light propagation in an adult head model I Modeling of low-level scattering in the cerebrospinal fluid layer. *Applied Optics* 42, 16 (jun 2003), 2906.
- [289] OPPENHEIM, A. V., AND SCHAFER, R. W. *Digital signal processing*. Prentice-Hall, 1975.
- [290] ORTIBUS, E., DE COCK, P., AND LAGAE, L. Visual perception in preterm children: what are we currently measuring? *Pediatric neurology* 45, 1 (jul 2011), 1–10.
- [291] ORTINAU, C., AND NEIL, J. The neuroanatomy of prematurity: Normal brain development and the impact of preterm birth. *Clinical Anatomy* 28, 2 (mar 2015), 168–183.
- [292] O'TOOLE, J. M., BOYLAN, G. B., LLOYD, R. O., GOULDING, R. M., VANHATALO, S., AND STEVENSON, N. J. Detecting bursts in the EEG of very and extremely premature infants using a multi-feature approach. *Medical Engineering and Physics* 45 (2017), 42–50.
- [293] OWENS, R. Intraventricular hemorrhage in the premature neonate. *Neonatal network : NN* 24, 3 (2005), 55–71.
- [294] PACIFICI, G. M. Clinical Pharmacology of Midazolam in Neonates and Children: Effect of Disease—A Review. *International Journal of Pediatrics* 2014 (2014), 1–20.
- [295] PAKKENBERG, B., AND GUNDERSEN, H. J. G. Neocortical neuron number in humans: Effect of sex and age. *Journal of Comparative Neurology* 384, 2 (1997), 312–320.

- [296] PALUŠ, M. Detecting nonlinearity in multivariate time series. *Physics Letters, Section A: General, Atomic and Solid State Physics* 213, 3-4 (apr 1996), 138–147.
- [297] PANERAI, R. B., SIMPSON, D. M., DEVERSON, S. T., MAHONY, P., HAYES, P., AND EVANS, D. H. Multivariate dynamic analysis of cerebral blood flow regulation in humans. *IEEE Transactions on Biomedical Engineering* 47, 3 (2000), 419–423.
- [298] PAPILE, L. A., BURSTEIN, J., BURSTEIN, R., AND KOFFLER, H. Incidence and evolution of subependymal and intraventricular hemorrhage: A study of infants with birth weights less than 1,500 gm. *The Journal of Pediatrics* 92, 4 (apr 1978), 529–534.
- [299] PAPOFF, P., MANCUSO, M., CARESTA, E., AND MORETTI, C. Effectiveness and safety of propofol in newborn infants. *Pediatrics* 121 (2008), 448–449.
- [300] PATEL, S. S., AND GOA, K. L. Sevoflurane. A Review of its Pharmacodynamic and Pharmacokinetic Properties and its Clinical Use in General Anaesthesia. *Drugs* 51 (1996), 658–700.
- [301] PAVLIDIS, E., LLOYD, R. O., AND BOYLAN, G. B. EEG-A Valuable Biomarker of Brain Injury in Preterm Infants. *Developmental Neuroscience* 39, 1-4 (2017), 23–35.
- [302] PAVLOPOULOS, G. A., SECRIER, M., MOSCHOPOULOS, C. N., SOLDATOS, T. G., KOSSIDA, S., AERTS, J., SCHNEIDER, R., AND BAGOS, P. G. Using graph theory to analyze biological networks. *BioData Mining* 4, 1 (2011).
- [303] PENIDO, M. G., DE OLIVEIRA SILVA, D. F., TAVARES, E. C., AND E SILVA, Y. P. Propofol versus midazolam for intubating preterm neonates: a randomized controlled trial. *J. of Perinatology* 31 (2011), 256–360.
- [304] PEREDA, E., QUIROGA, R. Q., AND BHATTACHARYA, J. Nonlinear multivariate analysis of neurophysiological signals. *Progress in Neurobiology* 77, 1-2 (sep 2005), 1–37.
- [305] PEREDA, E., RIAL, R., GAMUNDI, A., AND GONZÁLEZ, J. Assessment of changing interdependencies between human electroencephalograms using nonlinear methods. *Physica D: Nonlinear Phenomena* 148, 1-2 (2001), 147–158.

- [306] PERLMAN, J. M., MCMENAMIN, J. B., AND VOLPE, J. J. Fluctuating Cerebral Blood-Flow Velocity in Respiratory-Distress Syndrome. *New England Journal of Medicine* 309, 4 (jan 1983), 204–209.
- [307] PETROVA, A., AND MEHTA, R. Near-infrared spectroscopy in the detection of regional tissue oxygenation during hypoxic events in preterm infants undergoing critical care. *Pediatric Critical Care Medicine* 7, 5 (sep 2006), 449–454.
- [308] PETROVA, A., AND MEHTA, R. Regional tissue oxygenation in association with duration of hypoxaemia and haemodynamic variability in preterm neonates. *Archives of Disease in Childhood: Fetal and Neonatal Edition* 95, 3 (2010).
- [309] PFURTSCHELLER, K., BAUERNFEIND, G., MÜLLER-PUTZ, G. R., URLESBERGER, B., MÜLLER, W., AND PFURTSCHELLER, G. Correlation between EEG burst-to-burst intervals and HR acceleration in preterm infants. *Neuroscience* 437, 2 (may 2008), 103–106.
- [310] PHILLIPS, A. A., CHAN, F. H., ZHENG, M. M. Z., KRASSIOUKOV, A. V., AND AINSLIE, P. N. Neurovascular coupling in humans: Physiology, methodological advances and clinical implications. *Journal of Cerebral Blood Flow and Metabolism* 36, 4 (2015), 647–664.
- [311] PICHLER, G., AVIAN, A., BINDER, C., ZOTTER, H., SCHMÖLZER, G. M., MORRIS, N., MÜLLER, W., AND URLESBERGER, B. AEEG and NIRS during transition and resuscitation after birth: Promising additional tools; an observational study. *Resuscitation* 84, 7 (2013), 974–978.
- [312] PICHLER, G., BINDER, C., AVIAN, A., BECKENBACH, E., SCHMÖLZER, G. M., AND URLESBERGER, B. Reference ranges for regional cerebral tissue oxygen saturation and fractional oxygen extraction in neonates during immediate transition after birth. *Journal of Pediatrics* 163, 6 (2013), 1558–1563.
- [313] PICHLER, G., CHEUNG, P. Y., AZIZ, K., URLESBERGER, B., AND SCHMÖLZER, G. M. How to monitor the brain during immediate neonatal transition and resuscitation? A systematic qualitative review of the literature. *Neonatology* 105, 3 (2014), 205–210.
- [314] PICHLER, G., SCHMÖLZER, G. M., AND URLESBERGER, B. Cerebral tissue oxygenation during immediate neonatal transition and resuscitation. *Frontiers in Pediatrics* 5 (2017).
- [315] PICHLER, G., URLESBERGER, B., BAIK, N., SCHWABERGER, B., BINDER-HESCHL, C., AVIAN, A., PANSY, J., CHEUNG, P. Y., AND

- SCHMÖLZER, G. M. Cerebral Oxygen Saturation to Guide Oxygen Delivery in Preterm Neonates for the Immediate Transition after Birth: A 2-Center Randomized Controlled Pilot Feasibility Trial. *Journal of Pediatrics* 170 (2016), 73–78.e4.
- [316] PICHLER, G., WOLF, M., ROLL, C., WEINDLING, M. A., GREISEN, G., WARDLE, S. P., ZARAMELLA, P., NAULAERS, G., PELLICER, A., AUSTIN, T., BARTOCCI, M., AND URLESBERGER, B. Recommendations to increase the validity and comparability of peripheral measurements by near infrared spectroscopy in neonates: 'Round table', section of haematology, oxygen transport and microcirculation, 48th annual meeting of ESPR, Prague 2007. *Neonatology* 94, 4 (nov 2008), 320–322.
- [317] PIJN, J. P. M., VEILS, D. N., VAN DER HEYDEN, M. J., DEGOEDE, J., VAN VEELLEN, C. W., AND LOPES DA SILVA, F. H. Nonlinear dynamics of epileptic seizures on basis of intracranial EEG recordings. *Brain Topography* 9, 4 (1997), 249–270.
- [318] PIKOVSKY, A., ROSENBLUM, M., KURTHS, J., AND HILBORN, R. C. Synchronization: A Universal Concept in Nonlinear Science. *American Journal of Physics* 70, 6 (2002), 655–655.
- [319] PILLAY, K., DEREYMAEKER, A., JANSEN, K., NAULAERS, G., AND DE VOS, M. Applying a data-driven approach to quantify EEG maturational deviations in preterms with normal and abnormal neurodevelopmental outcomes. *Scientific Reports* 10, 1 (2020).
- [320] PILLAY, K., DEREYMAEKER, A., JANSEN, K., NAULAERS, G., VAN HUFFEL, S., AND DE VOS, M. Automated EEG sleep staging in the term-age baby using a generative modelling approach. *Journal of Neural Engineering* 15, 3 (2018).
- [321] PINCUS, S. M. Approximate entropy as a measure of system complexity. In *Proceedings of the National Academy of Sciences of the United States of America* (1991), vol. 88, pp. 2297–2301.
- [322] PINCUS, S. M., GLADSTONE, I. M., AND EHRENKRANZ, R. A. A regularity statistic for medical data analysis. *Journal of Clinical Monitoring* 7, 4 (oct 1991), 335–345.
- [323] PINTELON, R., AND SCHOUKENS, J. *System Identification: A Frequency Domain Approach, Second Edition*. 2012.
- [324] POWERS, W. J., HIRSCH, I. B., AND CRYER, P. E. Effect of stepped hypoglycemia on regional cerebral blood flow response to physiological brain activation. *American Journal of Physiology - Heart and Circulatory Physiology* 270, 2 39-2 (1996).

- [325] QUIAN QUIROGA, R., KRASKOV, A., KREUZ, T., AND GRASSBERGER, P. Performance of different synchronization measures in real data: A case study on electroencephalographic signals. *Physical Review E - Statistical Physics, Plasmas, Fluids, and Related Interdisciplinary Topics* 65 (2002), 14.
- [326] QUINN, R. Comparing rat's to human's age: How old is my rat in people years? *Nutrition* 21, 6 (jun 2005), 775–777.
- [327] QUIROGA, R. Q., ARNHOLD, J., AND GRASSBERGER, P. Learning driver-response relationships from synchronization patterns. *Physical Review E - Statistical Physics, Plasmas, Fluids, and Related Interdisciplinary Topics* 61, 5 (2000), 5142–5148.
- [328] RABI, Y., YEE, W., CHEN, S. Y., AND SINGHAL, N. Oxygen saturation trends immediately after birth. *Journal of Pediatrics* 148, 5 (2006), 590–594.
- [329] RADIC, J. A., VINCER, M., AND MCNEELY, P. D. Temporal trends of intraventricular hemorrhage of prematurity in Nova Scotia from 1993 to 2012. *Journal of Neurosurgery: Pediatrics* 15, 6 (jun 2015), 573–579.
- [330] RAGWITZ, M., AND KANTZ, H. Markov models from data by simple nonlinear time series predictors in delay embedding spaces. *Physical Review E - Statistical Physics, Plasmas, Fluids, and Related Interdisciplinary Topics* 65, 5 (apr 2002), 12.
- [331] RAICHLE, M. E., AND GUSNARD, D. A. Appraising the brain's energy budget. *Proceedings of the National Academy of Sciences of the United States of America* 99, 16 (2002), 10237–10239.
- [332] RANGAYAN, R. M. *Biomedical signal analysis: Second edition*. Wiley-IEEE Press, apr 2015.
- [333] RAWLINGS, J. O., PANTULA, S. G., AND DICKEY, D. A. *Applied Regression Analysis*. Springer-Verlag, 1998.
- [334] REES, S., HARDING, R., AND WALKER, D. The biological basis of injury and neuroprotection in the fetal and neonatal brain. *International Journal of Developmental Neuroscience* 29, 6 (2011), 551–563.
- [335] REES, S., AND INDER, T. Fetal and neonatal origins of altered brain development. *Early Human Development* 81, 9 (2005), 753–761.
- [336] RHEE, C. J., DA COSTA, C. S., AUSTIN, T., BRADY, K. M., CZOSNYKA, M., AND LEE, J. K. Neonatal cerebrovascular autoregulation. *Pediatric Research* 84, 5 (nov 2018), 602–610.

- [337] RHONDALI, O., JUHEL, S., MATHEWS, S., CELLIER, Q., DESGRANGES, F. P., MAHR, A., DE QUEIROZ, M., POUYAU, A., RHZIOUAL-BERRADA, K., AND CHASSARD, D. Impact of sevoflurane anesthesia on brain oxygenation in children younger than 2 years. *Paediatric Anaesthesia* 24, 7 (2014), 734–740.
- [338] RICHMAN, J. S., AND MOORMAN, J. R. Physiological time-series analysis using approximate and sample entropy. *American Journal of Physiology - Heart and Circulatory Physiology* 278, 6 47-6 (2000).
- [339] RISBERG, J., ANCRI, D., AND INGVAR, D. H. Correlation between cerebral blood volume and cerebral blood flow in the cat. *Experimental Brain Research* 8, 4 (1969), 321–326.
- [340] ROBBE, H. W., MULDER, L. J., RÜDDEL, H., LANGEWITZ, W. A., VELDMAN, J. B., AND MULDER, G. Assessment of baroreceptor reflex sensitivity by means of spectral analysis. *Hypertension* 10, 5 (1987), 538–543.
- [341] ROBERTS, I., FALLON, P., KIRKHAM, F., LLOYD-THOMAS, A., COOPER, C., MAYNARD, R., ELLIOT, M., AND EDWARDS, A. D. Estimation of cerebral blood flow with near infrared spectroscopy and indocyanine green. *The Lancet* 342, 8884 (1993), 1425.
- [342] ROCHE-LABARBE, N., WALLOIS, F., PONCHEL, E., KONGOLO, G., AND GREBE, R. Coupled oxygenation oscillation measured by NIRS and intermittent cerebral activation on EEG in premature infants. *NeuroImage* 36, 3 (jul 2007), 718–727.
- [343] ROLAND, E. H., AND HILL, A. Germinal matrix-intraventricular hemorrhage in the premature newborn: Management and outcome. *Neurologic Clinics* 21, 4 (2003), 833–851.
- [344] ROMERO-GUZMAN, G., AND LOPEZ-MUNOZ, F. Prevalence and risk factors for periventricular leukomalacia in preterm infants. a systematic review. *Rev Neurol* 65, 2 (jul 2017), 57–62.
- [345] ROSENGARTEN, B., SCHERMULY, R., VOSWINCKEL, R., KOHSTALL, M., OLSCHIEWSKI, H., WEISSMANN, N., SEEGER, W., KAPS, M., GRIMMINGER, F., AND GHOFRANI, H. Sildenafil Improves Dynamic Vascular Function in the Brain: Studies in Patients with Pulmonary Hypertension. *Cerebrovascular Diseases* 21, 3 (feb 2006), 194–200.
- [346] SAKATANI, K., CHEN, S., LICHTY, W., ZUO, H., AND PING WANG, Y. Cerebral blood oxygenation changes induced by auditory stimulation in newborn infants measured by near infrared spectroscopy. *Early Human Development* 55, 3 (jul 1999), 229–236.

- [347] SAYERS, E. W., BECK, J., BRISTER, J. R., BOLTON, E. E., CANESE, K., COMEAU, D. C., FUNK, K., KETTER, A., KIM, S., KIMCHI, A., KITTS, P. A., KUZNETSOV, A., LATHROP, S., LU, Z., MCGARVEY, K., MADDEN, T. L., MURPHY, T. D., O'LEARY, N., PHAN, L., SCHNEIDER, V. A., THIBAUD-NISSEN, F., TRAWICK, B. W., PRUITT, K. D., AND OSTELL, J. Database resources of the National Center for Biotechnology Information. *Nucleic Acids Research* 48, D1 (2020), D9–D16.
- [348] SBAFFI, L., WALTON, J., BLENKINSOPP, J., AND WALTON, G. Information overload in emergency medicine physicians: A multisite case study exploring the causes, impact, and solutions in Four North England national health service trusts. *Journal of Medical Internet Research* 22, 7 (jul 2020).
- [349] SCHILLER, R., IJSSELSTIJN, H., HOSKOTE, A., WHITE, T., VERHULST, F., VAN HEIJST, A., AND TIBBOEL, D. Memory deficits following neonatal critical illness: a common neurodevelopmental pathway. *The Lancet Child and Adolescent Health* 2, 4 (apr 2018), 281–289.
- [350] SCHMIDT, L. A., MISKOVIC, V., BOYLE, M. H., AND SAIGAL, S. Shyness and timidity in young adults who were born at extremely low birth weight. *Pediatrics* 122, 1 (jul 2008), e181–e187.
- [351] SCHOLKMANN, F., SPICHTIG, S., MUEHLEMANN, T., AND WOLF, M. How to detect and reduce movement artifacts in near-infrared imaging using moving standard deviation and spline interpolation. *Physiological Measurement* 31, 5 (2010), 649–662.
- [352] SCHREIBER, T. Measuring information transfer. *Physical Review Letters* 85, 2 (2000), 461–464.
- [353] SCHULZ, G., WEISS, M., BAUERSFELD, U., TELLER, J., HAENSSE, D., BUCHER, H., AND BAENZIGER, O. Liver tissue oxygenation as measured by near-infrared spectroscopy in the critically ill child in correlation with central venous oxygen saturation. *Intensive Care Medicine* 28, 2 (2002), 184–189.
- [354] SCHWABERGER, B., PICHLER, G., BINDER-HESCHL, C., BAIK, N., AVIAN, A., AND URLESBERGER, B. Transitional Changes in Cerebral Blood Volume at Birth. *Neonatology* 108, 4 (2015), 253–258.
- [355] SCHWABERGER, B., PICHLER, G., BINDER-HESCHL, C., BAIK-SCHNEDITZ, N., AVIAN, A., AND URLESBERGER, B. Cerebral blood volume during neonatal transition in term and preterm infants with and without respiratory support. *Frontiers in Pediatrics* 6 (2018).

- [356] SCHWARTZ, T. H. Neurovascular Coupling and Epilepsy: Hemodynamic Markers for Localizing and Predicting Seizure Onset. <https://doi.org/10.1111/j.1535-7511.2007.00183.x> 7, 4 (jul 2007), 91–94.
- [357] SCOTT, S., KNAPP, M., HENDERSON, J., AND MAUGHAN, B. Financial cost of social exclusion: follow up study of antisocial children into adulthood. *BMJ* 323, 7306 (jul 2001), 191.
- [358] SEMENOVA, O., O'TOOLE, J. M., BOYLAN, G. B., DEMPSEY, E., AND TEMKO, A. Modelling interactions between blood pressure and brain activity in preterm neonates. *Engineering in Medicine and Biology Society (EMBC), 2017 39th Annual International Conference of the IEEE* (2017).
- [359] SHAFER, A. Metaphor and anesthesia. *Anesthesiology* 83 (1995), 1331–1342.
- [360] SHAFFER, F., AND GINSBERG, J. P. An Overview of Heart Rate Variability Metrics and Norms. *Frontiers in Public Health* 5 (2017).
- [361] SHAFFER, F., MCCRATY, R., AND ZERR, C. L. A healthy heart is not a metronome: an integrative review of the heart's anatomy and heart rate variability. *Frontiers in Psychology* 5 (2014).
- [362] SHAH, P. S., SANKARAN, K., AZIZ, K., ALLEN, A. C., SESHIA, M., OHLSSON, A., AND LEE, S. K. Outcomes of preterm infants 29 weeks gestation over 10-year period in Canada: A cause for concern. In *Journal of Perinatology* (2012), vol. 32, Nature Publishing Group, pp. 132–138.
- [363] SHANNON, C. E. A Mathematical Theory of Communication. *Bell System Technical Journal* 27, 3 (1948), 379–423.
- [364] SHIMIZU, N., GILDER, F., BISSONNETTE, B., COLES, J., BOHN, D., AND MIYASAKA, K. Brain tissue oxygenation index measured by near infrared spatially resolved spectroscopy agreed with jugular bulb oxygen saturation in normal pediatric brain: A pilot study. *Child's Nervous System* 21, 3 (2005), 181–184.
- [365] SHIN, J., VON LÜHMANN, A., KIM, D.-W., MEHNERT, J., HWANG, H.-J., AND MÜLLER, K.-R. Simultaneous acquisition of EEG and NIRS during cognitive tasks for an open access dataset. *Scientific Data* 2018 5:1 5, 1 (feb 2018), 1–16.
- [366] SHINEBOURNE, E. A., VAPAAVUORI, E. K., WILLIAMS, R. L., HEYMANN, M. A., AND RUDOLPH, A. M. Development of baroreflex activity in unanesthetized fetal and neonatal lambs. *Circulation research* 31, 5 (1972), 710–718.

- [367] SHUMAN, R. M., AND SELEDNIK, L. J. Periventricular Leukomalacia: A One-Year Autopsy Study. *Archives of Neurology* 37, 4 (1980), 231–235.
- [368] SIDDIQUEE, M. R., MARQUEZ, J. S., ATRI, R., RAMON, R., PERRY MAYRAND, R., AND BAI, O. Movement artefact removal from NIRS signal using multi-channel IMU data. *Biomedical engineering online* 17, 1 (sep 2018), 120.
- [369] SIEGEL, G. J., AGRANOFF, B. W., ALBERS, R. W., FISHER, S. K., AND UHLER, M. D.
- [370] SIMONS, S. H. P., VAN DER LEE, R., REISS, I. K. M., AND VAN WEISSENBRUCH, M. M. Clinical evaluation of propofol as sedative for endotracheal intubation in neonates. *Acta Paediatr.* 102 (2013), 487–492.
- [371] SINGH, H., COOPER, R. J., WAI LEE, C., DEMPSEY, L., EDWARDS, A., BRIGADOI, S., AIRANTZIS, D., EVERDELL, N., MICHELL, A., HOLDER, D., HEBDEN, J. C., AND AUSTIN, T. Mapping cortical haemodynamics during neonatal seizures using diffuse optical tomography: A case study. *NeuroImage: Clinical* 5 (jan 2014), 256–265.
- [372] SKOV, L., PRYDS, O., AND GREISEN, G. Estimating cerebral blood flow in newborn infants: Comparison of near infrared spectroscopy and 133xe clearance. *Pediatric Research* 30, 6 (1991), 570–573.
- [373] SMITH, S. L., HALEY, S., SLATER, H., AND MOYER-MILEUR, L. J. Heart rate variability during caregiving and sleep after massage therapy in preterm infants. *Early Human Development* 89, 8 (2013), 525–529.
- [374] SMITHA, K. A., AKHIL RAJA, K., ARUN, K. M., RAJESH, P. G., THOMAS, B., KAPILAMOORTHY, T. R., AND KESAVADAS, C. Resting state fMRI: A review on methods in resting state connectivity analysis and resting state networks. *Neuroradiology Journal* 30, 4 (2017), 305–317.
- [375] SMITS, A., THEWISSEN, L., CAICEDO, A., NAULAERS, G., AND ALLEGAERT, K. Propofol Dose-Finding to Reach Optimal Effect for (Semi-)Elective Intubation in Neonates. *Journal of Pediatrics* 179 (dec 2016), 54–60.e9.
- [376] SMITS, A., THEWISSEN, L., DEREYMAEKER, A., DEMPSEY, E., CAICEDO, A., AND NAULAERS, G. The Use of Hemodynamic and Cerebral Monitoring to Study Pharmacodynamics in Neonates. *Current Pharmaceutical Design* 23, 38 (feb 2018), 5955–5963.
- [377] SMYTH, H. S., SLEIGHT, P., AND PICKERING, G. W. Reflex regulation of arterial pressure during sleep in man. A quantitative method of assessing baroreflex sensitivity. *Circulation research* 24, 1 (1969), 109–121.

- [378] SNOEK, K. G., REISS, I. K., GREENOUGH, A., CAPOLUPO, I., URLESBERGER, B., WESSEL, L., STORME, L., DEPREST, J., SCHAIBLE, T., VAN HEIJST, A., TIBBOEL, D., ALLEGAERT, K., DEBEER, A., KEIJZER, R., BENACHI, A., TISSIERES, P., KIPFMUELLER, F., SCHAIBLE, T., BREATNACH, C., PATEL, N., LEVA, E., CIRALLI, F., BAGOLAN, P., DOTTA, A., MORINI, F., DI PEDE, A., EMBLEM, R., ERTESVAG, K., MIGDAL, M., PIOTROWSKI, A., FRENCKNER, B., MESAS, C., ELORZA, D., MARTINEZ, L., SCHARBATKE, H., COHEN-OVERBEEK, T., EGGINK, A. J., KRAEMER, U. S., TIBBOEL, D., WIJNEN, R. M., DEPREST, J., DE COPPI, P., EATON, S., AND DAVENPORT, M. Standardized postnatal management of infants with congenital diaphragmatic hernia in Europe: The CDH EURO Consortium Consensus - 2015 Update. *Neonatology* 110, 1 (2016), 66–74.
- [379] SORENSEN, L. C., AND GREISEN, G. Precision of measurement of cerebral tissue oxygenation index using near-infrared spectroscopy in preterm neonates. *Journal of Biomedical Optics* 11, 5 (2006), 054005.
- [380] SORENSEN, L. C., AND GREISEN, G. The brains of very preterm newborns in clinically stable condition may be hyperoxygenated. *Pediatrics* 124, 5 (2009).
- [381] SORENSEN, L. C., LEUNG, T. S., AND GREISEN, G. Comparison of cerebral oxygen saturation in premature infants by near-infrared spatially resolved spectroscopy: observations on probe-dependent bias. *Journal of Biomedical Optics* 13, 6 (2008), 064013.
- [382] SOUL, J. S., HAMMER, P. E., TSUJI, M., SAUL, J. P., BASSAN, H., LIMPEROPOULOS, C., DISALVO, D. N., MOORE, M., AKINS, P., RINGER, S., VOLPE, J. J., TRACHTENBERG, F., AND DU PLESSIS, A. J. Fluctuating pressure-passivity is common in the cerebral circulation of sick premature infants. *Pediatric Research* 61, 4 (2007), 467–473.
- [383] SPITTLE, A., AND TREYVAUD, K. The role of early developmental intervention to influence neurobehavioral outcomes of children born preterm. *Seminars in Perinatology* 40, 8 (dec 2016), 542–548.
- [384] STIENSTRA, R. M., AND MCHONEY, M. Near-infrared spectroscopy (NIRS) measured tissue oxygenation in neonates with gastroschisis: a pilot study. *Journal of Maternal-Fetal and Neonatal Medicine* (2021).
- [385] STILES, J., AND JERNIGAN, T. L. The basics of brain development. *Neuropsychology Review* 20, 4 (dec 2010), 327–348.
- [386] STOLL, B. J., HANSEN, N. I., BELL, E. F., SHANKARAN, S., LAPTOOK, A. R., WALSH, M. C., HALE, E. C., NEWMAN, N. S., SCHIBLER, K.,

- CARLO, W. A., KENNEDY, K. A., POINDEXTER, B. B., FINER, N. N., EHRENKRANZ, R. A., DUARA, S., SÁNCHEZ, P. J., O'SHEA, T. M., GOLDBERG, R. N., VAN MEURS, K. P., FAIX, R. G., PHELPS, D. L., FRANTZ, I. D., WATTERBERG, K. L., SAHA, S., DAS, A., AND HIGGINS, R. D. Neonatal outcomes of extremely preterm infants from the NICHD Neonatal Research Network. *Pediatrics* 126, 3 (sep 2010), 443–456.
- [387] STOLWIJK, L. J., KEUNEN, K., DE VRIES, L. S., GROENENDAAL, F., VAN DER ZEE, D. C., VAN HERWAARDEN, M. Y., LEMMERS, P. M., AND BENDERS, M. J. Neonatal Surgery for Noncardiac Congenital Anomalies: Neonates at Risk of Brain Injury. *Journal of Pediatrics* 182 (mar 2017), 335–341.e1.
- [388] STOLWIJK, L. J., LEMMERS, P. M., HARMSSEN, M., GROENENDAAL, F., DE VRIES, L. S., VAN DER ZEE, D. C., BENDERS, M. J., AND VAN HERWAARDEN-LINDEBOOM, M. Y. Neurodevelopmental outcomes after neonatal surgery for major noncardiac anomalies. *Pediatrics* 137, 2 (feb 2016).
- [389] STOLWIJK, L. J., WEEKE, L. C., DE VRIES, L. S., VAN HERWAARDEN, M. Y., VAN DER ZEE, D. C., VAN DER WERFF, D. B., BENDERS, M. J., TOET, M., AND LEMMERS, P. M. Effect of general anesthesia on neonatal aEEG — A cohort study of patients with non-cardiac congenital anomalies. *PLoS ONE* 12, 8 (aug 2017).
- [390] SUZUKI, S., TAKASAKI, S., OZAKI, T., AND KOBAYASHI, Y. Tissue oxygenation monitor using NIR spatially resolved spectroscopy. *Optical Tomography and Spectroscopy of Tissue III* 3597 (jul 1999), 582–592.
- [391] SYNNEs, A., LUU, T. M., MODDEMANN, D., CHURCH, P., LEE, D., VINCER, M., BALLANTYNE, M., MAJNEMER, A., CREIGHTON, D., YANG, J., SAIGAL, S., SHAH, P. S., LEE, S. K., HARRISON, A., TING, J., YEE, W., AZIZ, K., TOYE, J., KALAPESI, Z., SANKARAN, K., DASPAL, S., SESHIA, M., ALVARO, R., SHIVANANDA, S., DA SILVA, O., NWAESEI, C., LEE, K. S., DUNN, M., ROUVINEZ-BOUALI, N., DOW, K., PELAUSA, E., KOVACS, L., BARRINGTON, K., DROLET, C., PIEDBOEUF, B., RILEY, S. P., CLAVEAU, M., FAUCHER, D., BERTELLE, V., MASSE, E., CANNING, R., MAKARY, H., OJAH, C., MONTERROSA, L., ANDREWS, W., DESHPANDEY, A., MCMILLAN, D., AFIFI, J., PILLAY, T., SAUVÉ, R., REICHERT, A., BODANI, J., DABOVAL, T., LY, L., KELLY, E., EL HELOU, S., LEVEBVRE, F., DEMERS, C., BÉLANGER, S., MURPHY, P., AND SAUVE, R. Determinants of developmental outcomes in a very preterm Canadian cohort. *Archives of Disease in Childhood: Fetal and Neonatal Edition* 102, 3 (may 2017), F235–F243.

- [392] SZTAJZEL, J. Heart rate variability: A noninvasive electrocardiographic method to measure the autonomic nervous system. *Swiss Medical Weekly* 134, 35-36 (2004), 514–522.
- [393] TACHTSIDIS, I. *Experimental measurements of cerebral haemodynamics and oxygenation and comparisons with a computational model: a near-infrared spectroscopy investigation*. PhD thesis, University College London, 2005.
- [394] TAKENS, F. Detecting strange attractors in turbulence. Springer, Berlin, Heidelberg, 1981, pp. 366–381.
- [395] TAO, J. D., AND MATHUR, A. M. Using amplitude-integrated EEG in neonatal intensive care. *Journal of Perinatology* 30, SUPPL. 1 (2010).
- [396] TATARANNO, M. L., ALDERLIESTEN, T., DE VRIES, L. S., GROENENDAAL, F., TOET, M. C., LEMMERS, P. M. A., VAN DE, R. E. V., VAN BEL, F., AND BENDERS, M. J. N. L. Early Oxygen-Utilization and Brain Activity in Preterm Infants. *PLoS ONE* 10, 5 (may 2015), e0124623.
- [397] TAUSSKY, P., O’NEAL, B., DAUGHERTY, W. P., LUKE, S., THORPE, D., POOLEY, R. A., EVANS, C., HANEL, R. A., AND FREEMAN, W. D. Validation of frontal near-infrared spectroscopy as noninvasive bedside monitoring for regional cerebral blood flow in brain-injured patients. *Neurosurgical Focus* 32, 2 (feb 2012).
- [398] TEAM, R. C. R: A language and environment for statistical computing, 2020.
- [399] THEWISSEN, L. *Near-infrared spectroscopy in the neonatal intensive care unit: can it change treatment decision?* PhD thesis, KU Leuven, 2019.
- [400] THEWISSEN, L., CAICEDO, A., LEMMERS, P., VAN BEL, F. V., VAN HUFFEL, S. V., AND NAULAERS, G. Measuring near-infrared spectroscopy derived cerebral autoregulation in neonates: From research tool toward bedside multimodal monitoring. *Frontiers in Pediatrics* 6 (2018).
- [401] THORUP, L., KOCH, K. U., UPTON, R. N., ØSTERGAARD, L., AND RASMUSSEN, M. Effects of Vasopressors on Cerebral Circulation and Oxygenation: A Narrative Review of Pharmacodynamics in Health and Traumatic Brain Injury. *Journal of Neurosurgical Anesthesiology* 32, 1 (2020), 18–28.
- [402] TIAN, F., TARUMI, T., LIU, H., ZHANG, R., AND CHALAK, L. Wavelet coherence analysis of dynamic cerebral autoregulation in neonatal hypoxic-ischemic encephalopathy. *NeuroImage: Clinical* 11 (2016), 124–132.

- [403] TINA, L., FRIGIOLA, A., ABELLA, R., ARTALE, B., PULEO, G., D'ANGELO, S., MUSMARRA, C., TAGLIABUE, P., LI VOLTI, G., FLORIO, P., AND GAZZOLO, D. Near Infrared Spectroscopy in Healthy Preterm and Term Newborns: Correlation with Gestational Age and Standard Monitoring Parameters. *Current Neurovascular Research* 6, 3 (2009), 148–154.
- [404] TOET, M. C., AND LEMMERS, P. M. Brain monitoring in neonates. *Early Human Development* 85, 2 (2009), 77–84.
- [405] TOKARIEV, A., VIDEMAN, M., PALVA, M. J., AND VANHATALO, S. Functional brain connectivity develops rapidly around term age and changes between vigilance states in the human newborn. *Cerebral Cortex* 26, 12 (2016), 4540–4550.
- [406] TSAO, K. J., LALLY, P. A., AND LALLY, K. P. Minimally invasive repair of congenital diaphragmatic hernia. *Journal of Pediatric Surgery* 46, 6 (2011), 1158–1164.
- [407] TSUJI, M., DUPLESSIS, A., TAYLOR, G., CROCKER, R., AND VOLPE, J. J. Near infrared spectroscopy detects cerebral ischemia during hypotension in piglets. *Pediatric Research* 44, 4 (1998), 591–595.
- [408] UNDERWOOD, M. A., MILSTEIN, J. M., AND SHERMAN, M. P. Near-infrared spectroscopy as a screening tool for patent ductus arteriosus in extremely low birth weight infants. *Neonatology* 91, 2 (2007), 134–139.
- [409] URLESBERGER, B., GROSSAUER, K., POCIVALNIK, M., AVIAN, A., MÜLLER, W., AND PICHLER, G. Regional oxygen saturation of the brain and peripheral tissue during birth transition of term infants. *Journal of Pediatrics* 157, 5 (2010), 740–744.
- [410] VAN BEL, F., LEMMERS, P., AND NAULAERS, G. Monitoring neonatal regional cerebral oxygen saturation in clinical practice: Value and pitfalls. *Neonatology* 94, 4 (nov 2008), 237–244.
- [411] VAN BEL, F., VAN DE BOR, M., STIJNEN, T., BAAN, J., AND RUYS, J. H. Aetiological Rôle Of Cerebral Blood-Flow Alterations In Development And Extension Of Peri-Intraventricular Haemorrhage. *Developmental Medicine & Child Neurology* 29, 5 (1987), 601–614.
- [412] VAN DEN BERG, E., LEMMERS, P. M. A., TOET, M. C., KLAESSENS, J. H. G., AND VAN BEL, F. Effect of the "InSurE" procedure on cerebral oxygenation and electrical brain activity of the preterm infant. *Arch Dis Child Fetal Neonatal Ed* 95 (2010), F53–F58.

- [413] VAN RAVENSWAAIJ-ARTS, C. M., HOPMAN, J. C., KOLLÉE, L. A., VAN AMEN, J. P., STOELINGA, G. B., AND VAN GEIJN, H. P. The influence of respiratory distress syndrome on heart rate variability in very preterm infants. *Early Human Development* 27, 3 (1991), 207–221.
- [414] VAN STRAATEN, H. L., RADEMAKER, C. M., AND DE VRIES, L. S. Comparison of the effect of midazolam or vecuronium on blood pressure and cerebral blood flow velocity in the premature newborn. *Developmental Pharmacology and Therapeutics* 19, 4 (1992), 191–195.
- [415] VAN VONDEREN, J. J., ROEST, A. A., SIEW, M. L., WALTHER, F. J., HOOPER, S. B., AND TE PAS, A. B. Measuring physiological changes during the transition to life after birth. *Neonatology* 105, 3 (2014), 230–242.
- [416] VAN WEZEL-MEIJLER, G., STEGGERDA, S. J., AND LEIJSER, L. M. Cranial Ultrasonography in Neonates: Role and Limitations. *Seminars in Perinatology* 34, 1 (feb 2010), 28–38.
- [417] VANDERHAEGEN, J., DEHING, L., NAULAERS, G., DEVLIEGER, H., AL-OLAYET, Y., PENNINGCKX, F., AND MISEREZ, M. Use of the liver tissue oxygenation index as a noninvasive parameter of intestinal ischemia in rabbits. *World Journal of Surgery* 31, 12 (dec 2007), 2359–2362.
- [418] VANDERHAEGEN, J., NAULAERS, G., VAN HUFFEL, S., VANHOLE, C., AND ALLEGAERT, K. Cerebral and systemic hemodynamic effects of intravenous bolus administration of propofol in neonates. *Neonatology* 98, 1 (2010), 57–63.
- [419] VANHATALO, S., ALNAJJAR, A., NGUYEN, V. T., COLDITZ, P., AND FRANSSON, P. Safety of EEG-fMRI recordings in newborn infants at 3T: A study using a baby-size phantom. *Clinical Neurophysiology* 125, 5 (may 2014), 941–946.
- [420] VARDI, A., SALEM, Y., PADEH, S., PARET, G., AND BARZILAY, Z. Is propofol safe for procedural sedation in children? A prospective evaluation of propofol versus ketamine in pediatric critical care. *Crit Care Med* 30, 6 (2002), 1231–1236.
- [421] VERRIOTIS, M., FABRIZI, L., LEE, A., COOPER, R. J., FITZGERALD, M., AND MEEK, J. Mapping Cortical Responses to Somatosensory Stimuli in Human Infants with Simultaneous Near-Infrared Spectroscopy and Event-Related Potential Recording. *eNeuro* 3, 2 (mar 2016), 663–673.
- [422] VESOULIS, Z. A., AND MATHUR, A. M. Cerebral autoregulation, brain injury, and the transitioning premature infant. *Frontiers in Pediatrics* 5 (apr 2017), 64.

- [423] VESOULIS, Z. A., MINTZER, J. P., AND CHOCK, V. Y. Neonatal NIRS monitoring: recommendations for data capture and review of analytics. *Journal of Perinatology* 41, 4 (feb 2021), 675–688.
- [424] VIJFHUIZE, S., DEDEN, A. C., COSTERUS, S. A., SLOOTS, C. E., AND WIJNEN, R. M. Minimal access surgery for repair of congenital diaphragmatic hernia: Is it advantageous? - An open review. *European Journal of Pediatric Surgery* 22, 5 (2012), 364–373.
- [425] VILLA, M. P., CALCAGNINI, G., PAGANI, J., PAGGI, B., MASSA, F., AND RONCHETTI, R. Effects of sleep stage and age on short-term heart rate variability during sleep in healthy infants and children. *Chest* 117, 2 (2000), 460–466.
- [426] VÖLLER, S., FLINT, R. B., BEGGAH, F., REISS, I., ANDRIESSEN, P., ZIMMERMANN, L. J., VAN DEN ANKER, J. N., LIEM, K. D., KOCH, B. C., DE WILDT, S., KNIBBE, C. A., AND SIMONS, S. H. Recently Registered Midazolam Doses for Preterm Neonates Do Not Lead to Equal Exposure: A Population Pharmacokinetic Model. *Journal of Clinical Pharmacology* 59, 10 (2019), 1300–1308.
- [427] VOLPE, J., INDER, T., DARRAS, B., DE VRIES, L., DU PLESSIS, A., NEIL, J., AND PERLMAN, J. *Volpe’s Neurology of the Newborn - 6th Edition*. Elsevier, 2017.
- [428] VOLPE, J. J. Intraventricular hemorrhage in the premature infant—current concepts. Part II. *Annals of Neurology* 25, 2 (feb 1989), 109–116.
- [429] VOLPE, J. J. Brain injury in premature infants: a complex amalgam of destructive and developmental disturbances. *The Lancet Neurology* 8, 1 (2009).
- [430] VOLPE, J. J. Confusions in Nomenclature: “Periventricular Leukomalacia” and “White Matter Injury”—Identical, Distinct, or Overlapping? *Pediatric Neurology* 73 (aug 2017), 3–6.
- [431] VOLPE, J. J., AND ZIPURKSY, A. Neurobiology of periventricular leukomalacia in the premature infant. *Pediatric Research* 50, 5 (2001), 553–562.
- [432] WANG, J., ZUO, X., AND HE, Y. Graph-based network analysis of resting-state functional MRI. *Frontiers in Systems Neuroscience* 4 (2010).
- [433] WARDLE, S. P., YOXALL, C. W., AND WEINDLING, A. M. Peripheral oxygenation in hypotensive preterm babies. *Pediatric Research* 45, 3 (1999), 343–349.

- [434] WARDLE, S. P., YOXALL, C. W., AND WEINDLING, A. M. Determinants of cerebral fractional oxygen extraction using near infrared spectroscopy in preterm neonates. *Journal of Cerebral Blood Flow and Metabolism* 20, 2 (2000), 272–279.
- [435] WATZMAN, H. M., KURTH, C. D., MONTENEGRO, L. M., ROME, J., STEVEN, J. M., AND NICOLSON, S. C. Arterial and venous contributions to near-infrared cerebral oximetry. *Anesthesiology* 93, 4 (2000), 947–953.
- [436] WEHRWEIN, E. A., ORER, H. S., AND BARMAN, S. M. Overview of the Anatomy, Physiology, and Pharmacology of the Autonomic Nervous System. *Comprehensive Physiology* 6, 3 (2016), 1239–1278.
- [437] WEINDLING, M., AND PAIZE, F. Peripheral haemodynamics in newborns: Best practice guidelines. *Early Human Development* 86, 3 (2010), 159–165.
- [438] WEISS, M., DULLENKOPF, A., KOLAROVA, A., SCHULZ, G., FREY, B., AND BAENZIGER, O. Near-infrared spectroscopic cerebral oxygenation reading in neonates and infants is associated with central venous oxygen saturation. *Paediatric Anaesthesia* 15, 2 (2005), 102–109.
- [439] WELZING, L., KRIBS, A., EIFINGER, F., HUENSELER, C., OBERTHUER, A., AND ROTH, B. Profol as an induction agent for endotracheal intubation can cause significant arterial hypotension in preterm neonates. *Paediatr. Anaesth.* 20 (2010), 605–611.
- [440] WHITEHEAD, K., PRESSLER, R., AND FABRIZI, L. Characteristics and clinical significance of delta brushes in the EEG of premature infants. *Clinical Neurophysiology Practice* 2 (2016).
- [441] WHO. The European Perinatal Health Report 2010.
- [442] WILSON, R. J. *Introduction to Graph Theory*, 4 ed. Prentice Hall, 1996.
- [443] WITCOMBE, N. B., YIALLOUROU, S. R., SANDS, S. A., WALKER, A. M., AND HORNE, R. S. Preterm birth alters the maturation of baroreflex sensitivity in sleeping infants. *Pediatrics* 129, 1 (2012).
- [444] WOLF, M., FERRARI, M., AND QUARESIMA, V. Progress of near-infrared spectroscopy and topography for brain and muscle clinical applications. *Journal of Biomedical Optics* 12, 6 (nov 2007), 062104.
- [445] WOLF, M., AND GREISEN, G. Advances in Near-Infrared Spectroscopy to Study the Brain of the Preterm and Term Neonate. *Clinics in Perinatology* 36, 4 (dec 2009), 807–834.

- [446] WOLF, T., LINDAUER, U., VILLRINGER, A., AND DIRNAGL, U. Excessive oxygen or glucose supply does not alter the blood flow response to somatosensory stimulation or spreading depression in rats. *Brain Research* 761, 2 (jul 1997), 290–299.
- [447] WOLFSBERGER, C. H., BRUCKNER, M., BAIK-SCHNEDITZ, N., SCHWABERGER, B., MILEDER, L. P., AVIAN, A., URLESBERGER, B., AND PICHLER, G. Fetal Inflammatory Response Syndrome and Cerebral Oxygenation During Immediate Postnatal Transition in Preterm Neonates. *Frontiers in Pediatrics* 8 (2020).
- [448] WONG, F. Y., ALEXIOU, T., SAMARASINGHE, T., BRODECKY, V., AND WALKER, A. M. Cerebral arterial and venous contributions to tissue oxygenation index measured using spatially resolved spectroscopy in newborn lambs. *Anesthesiology* 113, 6 (2010), 1385–1391.
- [449] WONG, F. Y., BARFIELD, C. P., HORNE, R. S., AND WALKER, A. M. Dopamine therapy promotes cerebral flow-metabolism coupling in preterm infants. *Intensive Care Medicine* 35, 10 (oct 2009), 1777–1782.
- [450] WONG, F. Y., LEUNG, T. S., AUSTIN, T., WILKINSON, M., MEEK, J. H., WYATT, J. S., AND WALKER, A. M. Impaired autoregulation in preterm infants identified by using spatially resolved spectroscopy. *Pediatrics* 121, 3 (mar 2008).
- [451] WOYTHALER, M., MCCORMICK, M. C., MAO, W. Y., AND SMITH, V. C. Late preterm infants and neurodevelopmental outcomes at kindergarten. *Pediatrics* 136, 3 (sep 2015), 424–431.
- [452] WYATT, J. S., COPE, M., DELPY, D. T., RICHARDSON, C. E., EDWARDS, A. D., WRAY, S., AND REYNOLDS, E. O. Quantitation of cerebral blood volume in human infants by near-infrared spectroscopy. *Journal of Applied Physiology* 68, 3 (1990), 1086–1091.
- [453] YAMADA, H., SEDATO, N., KONISHI, Y., KIMURA, K., TANAKA, M., YONEKURA, Y., AND ISHII, Y. A rapid brain metabolic change in infants detected by fMRI. *Neuroreport* 136, 8 (1997), 3775–3778.
- [454] YARDLEY, R. W., BOWES, G., WILKINSON, M., CANNATA, J. P., MALONEY, J. E., RITCHIE, B. C., AND WALKER, A. M. Increased arterial pressure variability after arterial baroreceptor denervation in fetal lambs. *Circulation Research* 52, 5 (1983), 580–588.
- [455] YEO, K. T., LEE, Q. Y., QUEK, W. S., WANG, Y. A., BOLISSETY, S., AND LUI, K. Trends in morbidity and mortality of extremely preterm multiple gestation newborns. *Pediatrics* 136, 2 (aug 2015), 263–271.

- [456] YIALLOUROU, S. R., SANDS, S. A., WALKER, A. M., AND HORNE, R. S. Postnatal development of baroreflex sensitivity in infancy. *Journal of Physiology* 588, 12 (2010), 2193–2203.
- [457] YIALLOUROU, S. R., WALKER, A. M., AND HORNE, R. S. Validation of a new noninvasive method to measure blood pressure and assess baroreflex sensitivity in preterm infants during sleep. *Sleep* 29, 8 (2006), 1083–1088.
- [458] YIALLOUROU, S. R., WALKER, A. M., AND HORNE, R. S. Effects of sleeping position on development of infant cardiovascular control. *Archives of Disease in Childhood* 93, 10 (2008), 868–872.
- [459] YOUNGE, N., SMITH, P. B., GUSTAFSON, K. E., MALCOLM, W., ASHLEY, P., COTTEN, C. M., GOLDBERG, R. N., AND GOLDSTEIN, R. F. Improved survival and neurodevelopmental outcomes among extremely premature infants born near the limit of viability. *Early Human Development* 95 (2016), 5–8.
- [460] YOXALL, C. W., AND WEINDLING, A. M. Measurement of cerebral oxygen consumption in the human neonate using near infrared spectroscopy: Cerebral oxygen consumption increases with advancing gestational age. *Pediatric Research* 44, 3 (1998), 283–290.
- [461] ZANELLI, S. A., ABUBAKAR, M., ANDRIS, R., PATWARDHAN, K., FAIRCHILD, K. D., AND VESOULIS, Z. A. Early Vital Sign Differences in Very Low Birth Weight Infants with Severe Intraventricular Hemorrhage. *American Journal of Perinatology* (2021).
- [462] ZARAMELLA, P., FREATO, F., AMIGONI, A., SALVADORI, S., MARANGONI, P., SUPPJEI, A., SCHIAVO, B., AND CHIANDETTI, L. Brain auditory activation measured by near-infrared spectroscopy (NIRS) in neonates. *Pediatric Research* 49, 2 (2001), 213–219.
- [463] ZEHENDNER, C. M., TSOHATARIDIS, S., LUHMANN, H. J., AND YANG, J. W. Developmental switch in neurovascular coupling in the immature rodent barrel cortex. *PLoS ONE* 8, 11 (2013).
- [464] ZOCCOLI, G., ANDREOLI, E., BOJIC, T., CIANCI, T., FRANZINI, C., PREDIERI, S., AND LENZI, P. Central and baroreflex control of heart rate during the wake-sleep cycle in rat. *Sleep* 24, 7 (2001), 753–758.



# Curriculum vitae

Dries Hendrikx was born in Genk, Belgium on May 17, 1994.

In September 2012, he started studying engineering at KU Leuven, Belgium. Following his strong interests in medicine and the human body in general, he started a master in Biomedical Engineering in 2015. During his master thesis, entitled *Assessment of the effects of propofol in the cerebral hemodynamic regulation mechanisms of premature neonates using graphs*, he explored the use of graph theory for monitoring the interaction in the neurocardiovascular system. He received a M.Sc. degree in Biomedical Engineering (cum laude) in September 2017.

In September 2017, he joined STADIUS, Department of Electrical Engineering (ESAT), KU Leuven, Belgium as a PhD student under the joint supervision of Prof. dr. ir. Sabine Van Huffel, Prof. dr. Gunnar Naulaers and Prof. dr. ir. Alexander Caicedo Dorado. In his research, he developed an integrated model to study CBF regulation in the neonatal brain. This model was validated in close collaboration with the medical teams from the University Hospitals Leuven, Belgium, and the Sophia Children's Hospital, Erasmus Medical Center, Rotterdam, The Netherlands.

During his PhD, he was active as a youngster member in the National Committee on Biomedical Engineering, which organizes a yearly event titled *The National Day on Biomedical Engineering*. He was awarded with the *Duane Bruley Travel Award*, which he received at the 46th Annual Meeting of the International Society on Oxygen Transport to Tissue (ISOTT).



# List of publications

## Articles in internationally reviewed journals

1. **Hendriks, D.**, Thewissen, L., Smits, A., Naulaers, G., Allegaert, K., Van Huffel, S. and Caicedo, A. Using Graph Theory to Assess the Interaction Between Cerebral Function, Brain Hemodynamics and Systemic Variables in Premature Infants. *Complexity* 2018 (2018), 6504039.
2. **Hendriks, D.**, Thewissen, L., Smits, A., Naulaers, G., Allegaert, K., Van Huffel, S. and Caicedo A. Nonlinear Transfer Entropy to Assess the Neurovascular Coupling in Premature Neonates. *Advances in Experimental Medicine and Biology* 1232 (2020), 11–17.
3. **Hendriks, D.**, Smits, A., Lavanga, M., De Wel, O., Thewissen, L., Jansen, K., Caicedo, A., Van Huffel, S. and Naulaers, G. Measurement of Neurovascular Coupling in Neonates. *Frontiers in Physiology* 10 (2019), 65.
4. Thewissen, L., Naulaers, G., **Hendriks, D.**, Caicedo, A., Barrington, K., Boylan, G., Cheung, P.-Y., Corcoran, D., El-Khuffash, A., Garvery, A., Macko, J., Marlow, N., Miletin, J., O'Donnell, C.P.F., O'Toole, J., Strak, Z., Van Laere, D., Wiedermannova, H. and Dempsey, E. Cerebral oxygen saturation and autoregulation during hypotension in extreme preterm infants: a nested study within a randomized clinical trial. *Pediatric Research* 90, 2 (2021), 373–380.
5. Costerus, S., van Hoorn, C., **Hendriks, D.**, Kortenbout, J., Hunfeld, M., Vlot, J., Naulaers, G., Tibboel, D. and de Graaff, J. Towards integrative neuromonitoring of the non-cardiac surgical newborn; a systematic review. *European Journal of Anaesthesiology* 37, 8 (2020), 701–712.

6. **Hendriks, D.\***, Costerus, S.\*, Caicedo, A., Zahn, K., Perez-Ortiz, A., Van Huffel, S., de Graaff, J., Wijnen, R., Wessel, L., Tibboel, D. and Naulaers, G. Neurocardiovascular coupling; revealing insight in perioperative neonatal physiology. Accepted for publication in *European Journal of Anaesthesiology* (2021).  
(\*: joint first author)
7. **Hendriks, D.\***, Costerus, S.\*, IJsselmuiden, J., Zahn, K., Perez-Ortiz, A., Van Huffel, S., Flint, R., Caicedo, A., Wijnen, R., Wessel, L., de Graaff, J., Tibboel, D. and Naulaers, G. Cerebral oxygenation and activity during surgical repair of neonates with congenital diaphragmatic hernia: a comparative analysis. Accepted for publication in *Frontiers in Pediatrics* (2021).  
(\*: joint first author)

## Submitted articles

1. **Hendriks, D.\***, Costerus, S.\*, Van Huffel, S., de Graaff, J., Wijnen, R., Caicedo, A., Tibboel, D., Naulaers, G. Heart rate variability during non-cardiac-major surgery. Submitted (2021).  
(\*: joint first author)
2. **Hendriks, D.**, Caicedo, A., Van Huffel, S., Naulaers, G., Wolfsberger, C., Urlesberger, B., and Pichler, G. Coupling between regional oxygen saturation of the brain and vital signs during immediate transition after birth. Submitted to *Neonatology* (2021).

## Papers in proceedings of international conferences

1. Varon, C., Deviaene, M., **Hendriks, D.**, Van de Putte, S., Testelmans, D., Buyse, B. and Van Huffel, S. The Cardiorespiratory Graph in Sleep Apnea and Associated Comorbidities. *Computing in Cardiology* 45 (2018), 1–4. Maastricht, The Netherlands. ISSN: 2325-887X. DOI: 10.22489/CinC.2018.192
2. Varon, C., **Hendriks, D.**, Bolea, J., Laguna, P. and Bailon, R. Quantification of Linear and Nonlinear Cardiorespiratory Interactions Under Autonomic Nervous System Blockade. *Computing in Cardiology* (2019), 1–4. Singapore, Republic of Singapore. ISSN: 2325-887X. DOI: 10.23919/CinC49843.2019.9005628.

## Abstracts in proceedings of (inter)national conferences

1. **Hendrikkx, D.**, Caicedo, A., Thewissen, L., Smits, A., Naulaers, G., Allegaert, K. and Van Huffel, S. Assessment of the effects of propofol on the cerebral hemodynamic regulation mechanisms of premature neonates using graphs. 10th International Conference on Brain Monitoring and Neuroprotection in the Newborn. Killarney, Ireland. October 5 to 7, 2017. Poster presentation.
2. **Hendrikkx, D.**, Caicedo, A., Thewissen, L., Smits, A., Naulaers, G., Allegaert, K. and Van Huffel, S. Assessment of the effects of propofol on the cerebral hemodynamic regulation mechanisms of premature neonates using graphs. 16th Belgian National Day on Biomedical Engineering. Brussels, Belgium. December 1, 2017. Poster presentation.
3. **Hendrikkx, D.**, Thewissen, L., Smits, A., Naulaers, G., Allegaert, K., Van Huffel, S. and Caicedo, A. Nonlinear Transfer Entropy to Assess the Neurovascular Coupling in Premature Neonates. Annual meeting of the International Society on Oxygen Transport to Tissue (ISOTT). Seoul, South Korea. July 1 to 5, 2018. Poster presentation.
4. **Hendrikkx, D.**, Thewissen, L., Smits, A., Naulaers, G., Allegaert, K., Van Huffel, S. and Caicedo, A. Nonlinear Transfer Entropy to Assess the Neurovascular Coupling in Premature Neonates. 7th Dutch Bio-Medical Engineering Conference. Egmond aan Zee, The Netherlands. January 24 to 25, 2019. Oral presentation.
5. **Hendrikkx, D.**, Thewissen, L., Smits, A., Naulaers, G., Allegaert, K., Van Huffel, S. and Caicedo, A. Nonlinear Transfer Entropy to Assess the Neurovascular Coupling in Premature Neonates. 11th International Conference on Brain Monitoring and Neuroprotection in the Newborn. Clearwater, Florida, United States of America. January 7 to 9, 2019. Oral presentation.
6. **Hendrikkx, D.**, Costerus, S., Caicedo, A., Tibboel, D., de Graaff, J, Naulaers, G. and Van Huffel, S. Neurocardiovascular interactions before, during and after open surgery for congenital diaphragmatic hernia. 2nd International Summer Institute on Network Physiology. Como, Italy. July 28 to August 2, 2019. Poster presentation.
7. **Hendrikkx, D.**, Costerus, S., Caicedo, A., Tibboel, D., de Graaff, J, Naulaers, G. and Van Huffel, S. Neurocardiovascular graphs: creating

understanding about neonatal physiology in the perioperative period. 11th European congress for Paediatric Anaesthesiology, organized by the European Society for Paediatric Anaesthesiology (ESPA). Rotterdam, The Netherlands. September 19 to 21, 2019. Poster presentation.

8. **Hendriks, D.**, Costerus, S., Caicedo, A., Tibboel, D., de Graaff, J, Naulaers, G. and Van Huffel, S. Neurocardiovascular graphs: creating understanding about neonatal physiology in the perioperative period. Annual IEEE EMBS Benelux Chapter Symposium: Artificial Intelligence in Healthcare. Leuven, Belgium. November 28. Poster presentation.
9. **Hendriks, D.**, Costerus, S., Caicedo, A., Tibboel, D., de Graaff, J, Naulaers, G. and Van Huffel, S. Neurocardiovascular coupling: Revealing insight in perioperative neonatal physiology. 8th Dutch Bio-Medical Engineering Conference. Online. January 28 to 29, 2021. Oral presentation.



FACULTY OF ENGINEERING SCIENCE  
DEPARTMENT OF ELECTRICAL ENGINEERING  
STADIUS CENTER FOR DYNAMICAL SYSTEMS, SIGNAL PROCESSING AND DATA ANALYTICS  
Kasteelpark Arenberg 10  
B-3001 Leuven  
dries.hendrixx@kuleuven.be  
<http://www.esat.kuleuven.be/stadius>

